R-11-10

Bedrock Hydrogeology – Groundwater flow modelling

Site investigation SFR

Johan Öhman, Geosigma AB

Sven Follin, SF GeoLogic AB

Magnus Odén, SKB

May 2013

Svensk Kärnbränslehantering AB
Swedish Nuclear Fuel
and Waste Management Co

Box 250, SE-101 24 Stockholm
Phone +46 8 459 84 00

ISSN 1402-3091
SKB R-11-10
ID 1288394

Bedrock Hydrogeology – Groundwater flow modelling

Site investigation SFR

Johan Öhman, Geosigma AB

Sven Follin, SF GeoLogic AB

Magnus Odén, SKB

May 2013

Keywords: Kravdatabas SFR-utbyggnad (N2-273).

Abstract

The hydrogeological model developed for the SFR extension project (PSU) consists of 40 geologically modelled deformation zones (DZ) and 8 sub-horizontal structural-hydraulic features, called SBA-structures, not defined in the geological model. However, some of the SBA-structures coincide with what is defined as unresolved possible deformation zones (Unresolved PDZ) in the geological modelling. In addition, the hydrogeological model consists of a stochastic discrete fracture network (DFN) model intended for the less fractured rock mass volumes (fracture domains) between the zones and the SBA-structures, and a stochastic fracture model intended to handle remaining Unresolved PDZs in the geological modelling not modelled as SBA-structures in the hydrogeological modelling. The four structural components of the bedrock in the hydrogeological model, i.e. DZ, SBA, Unresolved PDZ and DFN, are assigned hydraulic properties in the hydrogeological model based on the transmissivities interpreted from single-hole hydraulic tests.

The main objective of the present work is to present the characteristics of the hydrogeological model with regard to the needs of the forthcoming safety assessment SR-PSU. In concrete words, simulated data are compared with measured data, i.e. hydraulic heads in boreholes and tunnel inflow to the existing repository (SFR).

The calculations suggest that the available data for flow model calibration cannot be used to motivate a substantial adjustment of the initial hydraulic parameterisation (assignment of hydraulic properties) of the hydrogeological model. It is suggested that uncertainties in the hydrogeological model are studied in the safety assessment SR-PSU by means of a large number of calculation cases. These should address hydraulic heterogeneity of deterministic structures (DZ and SBA) and realisations of stochastic fractures/fracture networks (Unresolved PDZ and DFN) within the entire SFR Regional model domain.

Sammanfattning

En hydrogeologisk modell har tagits fram inom Projektet SFR Utbyggnad (PSU). Modellen består av 40 geologiskt modellerade deformationszoner (DZ), samt 8 subhorisontella strukturer, så kallade SBA-strukturer (*Eng.* Shallow Bedrock Aquifer structures), vilka inte ingår i den geologiska modellen. Några av SBA strukturerna sammanfaller emellertid med det som kallas för PDZ-intervall i den geologiska modellen (*Eng.* Unresolved Possible Deformation Zones). Vidare består den hydrogeologiska modellen av en stokastisk spricknätverksmodell (*Eng.* Discrete Fracture Network model; DFN), som är avsedd för att beskriva/modellera grundvattenflödet i bergmassan mellan deformationszoner och SBA-strukturer, samt en stokastisk sprickmodell för att hantera de PDZ-intervall som inte modelleras som SBA-strukturer. De fyra byggstenarna för att beskriva/modellera bergets egenskaper, dvs DZ, SBA, Unresolved PDZ och DFN, har i den hydrogeologiska modellen tilldelats hydrauliska egenskaper baserat på de transmissivitetsdata som tolkats från hydrotester.

Huvudsyftet med föreliggande rapport är att redovisa den hydrogeologiska modellens egenskaper med tanke på behoven i den kommande säkerhetsredovisningen SR-PSU. Resultat från olika flödesmodellberäkningar jämförs i denna rapport med uppmätta grundvattennivåer i borrhål och tunnelinflöden till befintligt förvar (SFR).

Beräkningarna visar att befintliga mätdata för modellkalibrering inte kan åberopas för en justering av den hydrogeologiska modellens initiala parameterisering (tilldelning av hydrauliska egenskaper). För att hantera osäkerheter av strukturell-hydraulisk karaktär i den kommande säkerhetsanalysen SR-PSU föreslås därför att ett stort antal beräkningsfall studeras i syfte att identifiera tänkbara ytterlighetsfall. Beräkningsfallen bör studera hydraulisk heterogenitet hos deterministiskt modellerade strukturer (DZ och SBA) samt realiseringar av stokastiska sprickor/spricknätverk (Unresolved PDZ och DFN) inom SFR:s regionaldomän.

Contents

1 Introduction

1.1 Context

The first stage of the underground facility SFR (final repository for low and intermediate level radioactive operational waste) was constructed and taken into operation in 1987. During 2008, SKB (the Swedish Nuclear Fuel and Waste Management Company) initiated an investigation programme for a future extension of the existing SFR. The project managing the activities associated with extension of SFR is referred to as PSU. The extension of SFR is necessitated by the pending decommissioning of the closed nuclear reactors Barsebäck, Studsvik, and Ågesta, the additional amounts of operational waste associated with the extended operating time of the remaining nuclear power plants, as well as the future decommission of running nuclear power plants Oskarshamn, Forsmark, and Ringhals (SKB 2008). The overall purpose of the recent site investigation is to develop a Site Descriptive Model (SDM-PSU) for the bedrock volume hosting both the existing SFR as well as the planned extension (Figure 1-1).

As part of SDM-PSU, a hydrogeological model has been established for the SFR Regional model domain shown in Figure 1-2, based on analysis of available structural, hydraulic and chemical data (Öhman et al. 2012). This report describes a groundwater flow model implementation of the hydrogeological model. The output from the groundwater flow simulations, groundwater levels (hydraulic heads) and tunnel inflows are compared with available data (measurements).

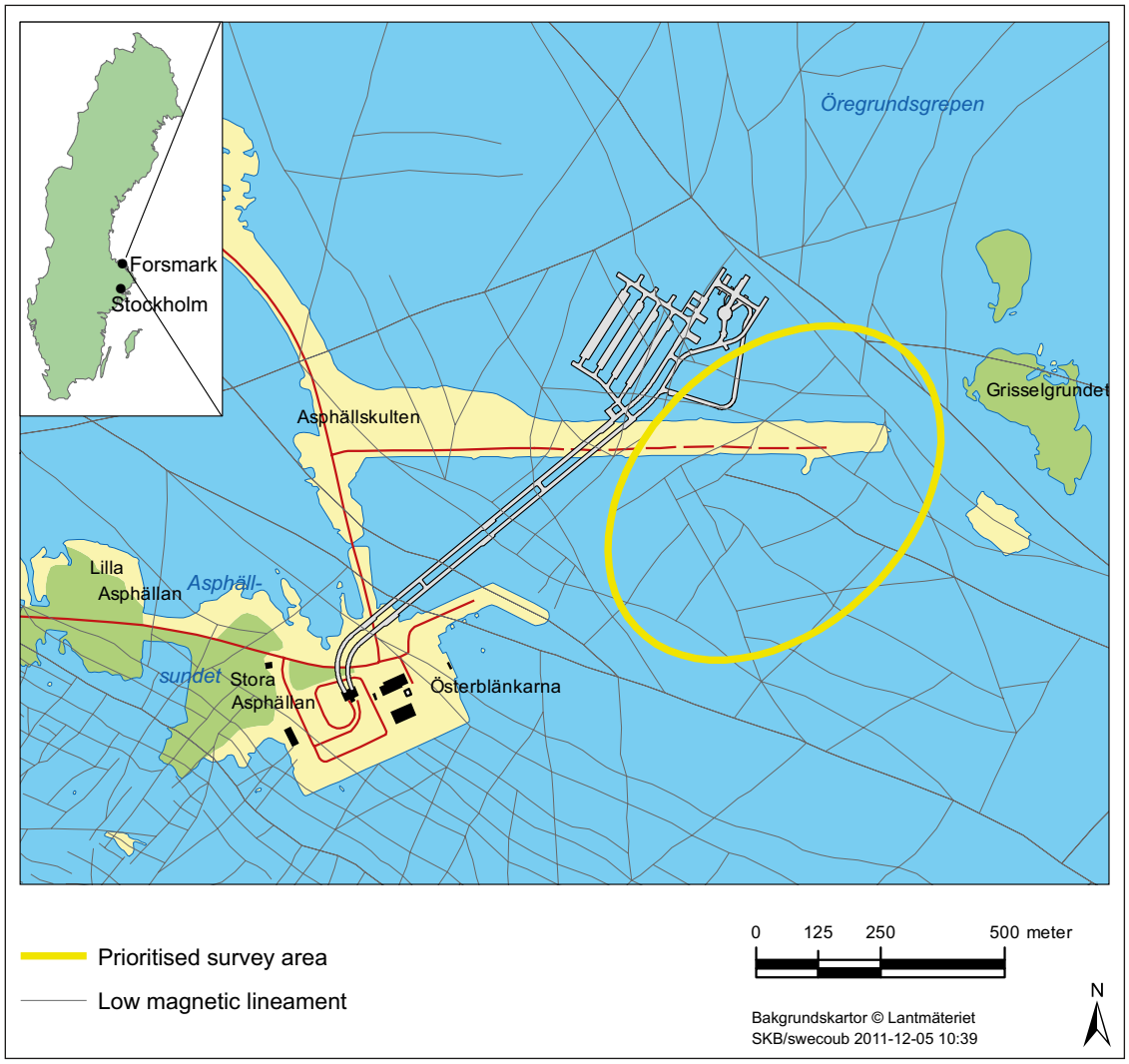

Figure 1-1. *Map showing the Forsmark-SFR area, the location of the existing SFR and the prioritised survey area for an extension of SFR.*

The work reported here was carried out in accordance with activity plan AP SFR-10-001. The controlling documents for performing this activity are listed in Table 1-1. Both the activity plan and the method descriptions are SKB's internal controlling documents.

Table 1-1. Controlling documents for the performance of the activity reported here.

Activity plan	Number	Version
Platsmodellering Hydrogeologi 1.0	AP SFR-10-001	1.0
Method descriptions	**Number**	**Version**
Hantering av data och modeller inom SFR – utbyggnad	SKB MD SDU-203	1.0
Hantering av primärdata vid platsundersökningar	SKB MD SDK-508	

1.2 Scope of SDM-PSU and role the hydrogeological model

The purpose of SDM-PSU is to provide means for an integrated evaluation of the suitability of the investigated site to host an extension of the existing SFR repository. The integrated evaluation involves sub-models from several disciplines, i.e. geology, rock mechanics, hydrogeology, hydrogeochemistry and surface hydrology/near-surface hydrogeology. As such, the development of a hydrogeological model for the bedrock is an important component (sub-model). The hydrogeological model presented in Öhman et al. (2012) is built from quality-assured geological, hydrogeological, and hydrogeochemical data stored in SKB's database Sicada, as well as geometric models for the crystalline rock and the Quaternary deposits formed in GIS (Geographical Information System) and Rock Visualisation System (RVS).

The purpose of the site descriptive model SDM-PSU is to provide input to repository layout design, safety assessment, and environmental impact assessment. The role of a hydrogeological model for the bedrock is to describe the current status of the subsurface part of hydrological cycle.

1.3 Objectives and strategy

The main objective of the present work is to study the hydrogeological model presented in Öhman et al. (2012) with regard to the needs of the forthcoming safety assessment SR-PSU. In concrete words, we compare simulated data with measured data available for flow model calibration (hydraulic heads in boreholes and tunnel inflow), and address potential obstacles and uncertainties in using this information. Section 1.7 provides an overview of the conducted flow simulations.

1.4 Scales and volumes

Two different model scales for the SFR site descriptive modelling have been defined by the geoscientific programme (SKB 2008); a local scale and a regional scale. The local scale covers the volume that is expected to host the SFR extension, whereas the regional scale covers a larger volume that places the description of the local volume in a larger scale context. The two SFR model areas (local and regional) are shown in Figure 1-2 together with the borehole coverage. The SFR local model volume extends from +100 m elevation to –300 m elevation, while the regional model volume extends from +100 m to –1,100 m elevation. The RT 90 coordinates defining the horizontal extent of the model volumes are provided in Table 1-2. All elevations refer to the former elevation system RHB 70.

Table 1-2. Coordinates defining the SFR model areas in metres.

Regional model volume (m, RT90 2.5 gon W)		Local model volume (m, RT90 2.5 gon W)	
Easting	Northing	Easting	Northing
1631920.0000	6701550.0000	1632550.0000	6701880.0000
1633111.7827	6702741.1671	1633059.2484	6702388.9854
1634207.5150	6701644.8685	1633667.2031	6701780.7165
1633015.7324	6700453.7014	1633157.9547	6701271.7311

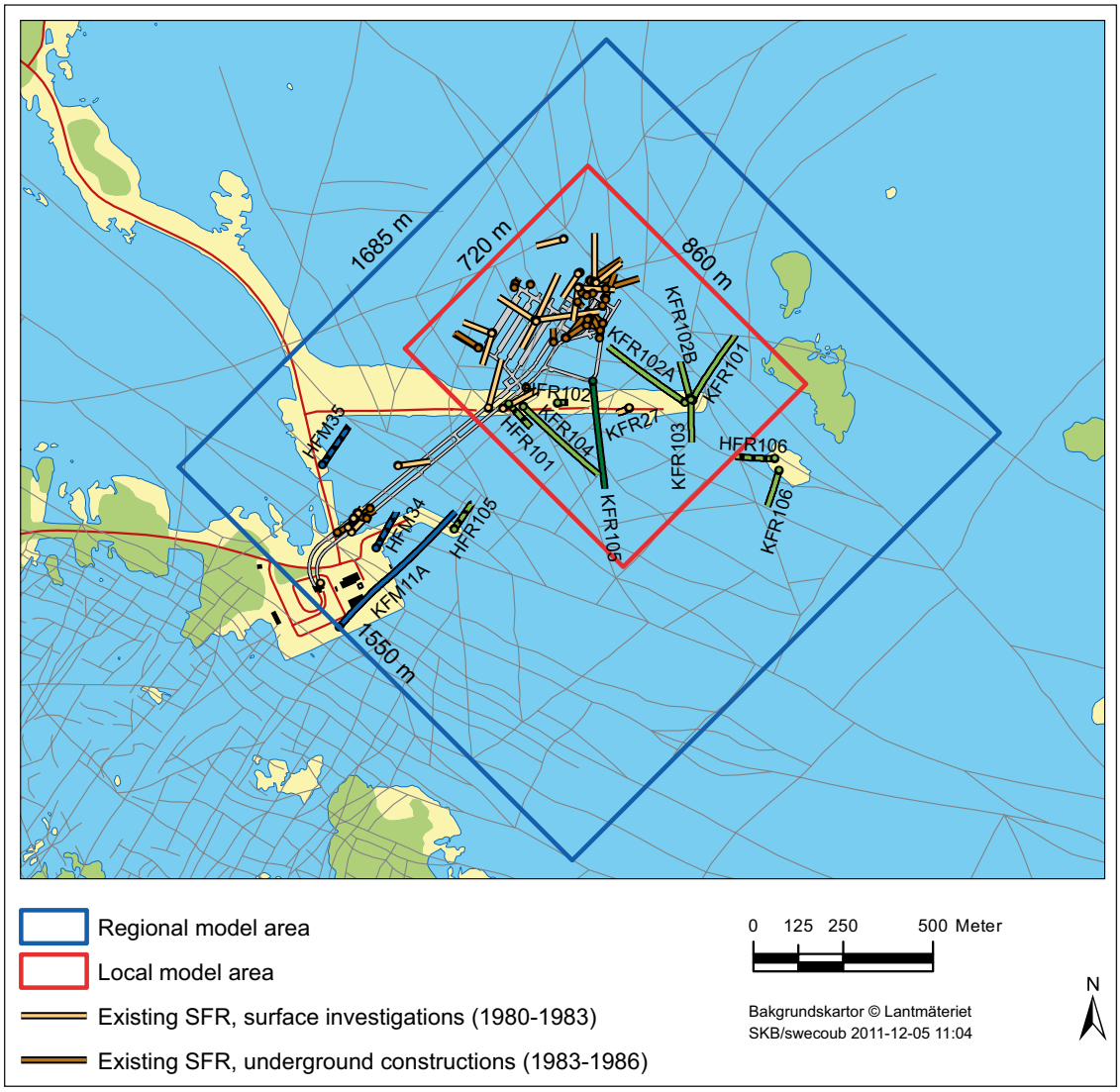

Figure 1-2. *Map visualising the borehole coverage within the regional (blue border) and local (red border) model areas, respectively. Boreholes are colour coded by investigation project/period. Cored boreholes (KFRXX) are solid colour; percussion (HFRXX) boreholes have black dots. The horizontal component of inclined boreholes is shown.*

It should be emphasised that the distinct rectangular volumes (Figure 1-2 and Table 1-2) do not conform to hydrogeological boundaries, but primarily concern the development of the updated geological model. Three geological units defined in the geological model of the SFR area v. 1.0 (Curtis et al. 2011) provide the fundaments of the conceptual hydrogeological model (Öhman et al. 2012). These are (1) a Central block, which is bounded by (2) a Southern boundary belt (the Singö deformation zone and associated zones) and (3) a Northern boundary belt (previously known as Zone 8).

The area defined for groundwater flow and solute transport modelling was delineated based on surface-water divides interpreted from topographical data (Figure 1-3). The parts of the model area that are currently below sea level were chosen with respect to future topographical divides, as well as the deep seafloor trench (the so-called Gräsörännan). The topographical data are available as a Digital Elevation Model (DEM) with a spatial resolution of 20 m scale in the horizontal plane. The hydrogeological model volume extends vertically from +100 m to –1,100 m elevation.

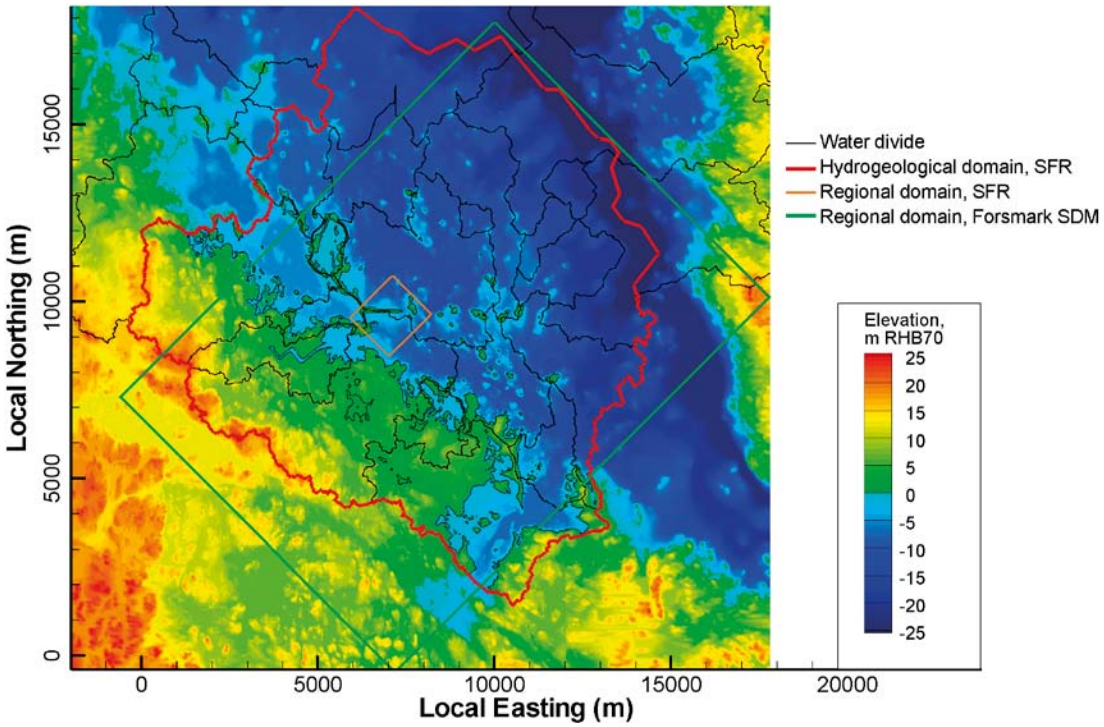

Figure 1-3. *Hydrogeological model area SFR (red) defined by surface-water divides. The Regional domain of the SFR structural model (orange) is a sub-volume of the Regional model domain used in the Forsmark site investigation (green). Local coordinate system is set to (0, 0) at RT 90 coordinates Northing = 6,692,000, Easting = 1,626,000.*

1.5 Data used

The data used in this report are summarised in Table 1-3. These are traceable in SKB's GIS and Sicada databases (specified data deliveries) or the SKBdoc model database (as indicated by footnotes).

Table 1-3. Data used in this report.

Hydraulic data	Boreholes	Source
plu_pfl_diff_seq_flo.xls	KFR101-106, KFR27, KFM11A	Sicada_2010_106
p_transmissivity.xls	KFR101-106, KFR27, KFM11A, HFR101, HFR105, HFR106, HFM33-35	Sicada_2010_106
plu_pfl_inferr_anom.xls		
pfl_anom_crush_id.xls		
pfl_anom_fract_id.xls	KFR101-106, KFR27, KFM11A	Sicada_2010_079
plu_impeller_anomaly.xls	HFR101, HFR105, HFR106, HFM33-35	Sicada_2010_079
Old hydraulic data set[1]	Screened hydraulic data from the historic data set (obtained during the construction of SFR 1980–1986), see Öhman and Follin (2010a).	See footnote
Groundwater levels (HMS)	Measured groundwater levels in the HMS database (quality-assured data in Sicada were unavailable at time of the data delivery)	Sicada_2011_064
SFR tunnel inflow	Measurements of groundwater inflow to different parts of SFR	Sicada_11_076
Hydraulic interferences		
HFM33	Table 6-149 (Gokall-Norman and Ludvigson 2008)	
Geological model files		
Deformation zone model[2]	Three-dimensional geometry of deformation zones, as modelled in RVS (combined version of Regional and Local deformation zones)	

Hydraulic data	Boreholes	Source
Deformation zone intercepts[3,4]	Tabulated deformation zone intercepts in boreholes	
Deformation zone model bridges[5]	Three-dimensional geometric elements to fill in artificial gaps between the Forsmark v. 2.2 and the SFR v. 1.0 Geological models, as modelled in RVS	
Non-deterministic PDZ intercepts[6]	Tabulated intercepts of “possible deformation zones” in boreholes that were not included in the deterministic deformation zone model.	
Hydrogeological structures		
081006_sheet_joints_v5.ifz	Sheet joints from SDM-Site Forsmark (geomtrery and hydraulic hydraulic parameterisation; SKB -TRAC)	
SBA-structures	Deterministic planar structures representing networks of interconnected, sub-horizontal, transmissive fractures inside the SFR Regional domain, defined in Öhman et al. (2012).	
Possible stress-relief structure[7]	Borehole intercepts of possible stress-relief structure (referred to as SBA7), based on the original interpretation of Zone H1 and Zone H3, by Carlsson et al. (1985)	
Hydro-DFN outside the SFR Regional domain[8]	Imported from SDM-Site Forsmark	
Geometric data		
object_location.xls	Sicada_2011_029	
Existing SFR tunnels and disposal facilities[9] (tunnels and disposal facilities in CAD STL format)	Laser-scanned geometry of the existing SFR	
861006_DZ_PFM_REG_v22_SJ.dt	Deformation-zone model for SDM-Site Forsmark (geomtrery and hydraulic hydraulic parameterisation; SKB -TRAC)	
SDEADM.UMEU_FM_HOJ_4528, SDEADM.UMEU_FM_HOJ_4529	Surface topography (DEM)	GIS_08_62
GIS_request09_26.mxd	Regolith depth model (RDM)	GIS_09_26
koderz1_srsite[10]		
QD_codes_z5_(SDM)_with_till_from_SR-site	Spatial soiltype distribution in layers Z1 and z5	

1 SKBdoc 1233724 – Hydraulic data used for hydrogeological model v.0.1, Version 1.0, 2010-05-25.
2 SKBdoc 1244246 – SFR_DZ_MASTER_v1.0, Version 1.0, 2010-06-21.
3 SKBdoc 1246851 – DZ_by_DZ_after_review_100615, Version 1.0, 2010-08-19.
4 SKBdoc 1246852 – BH_by_BH_after_review_100615, Version 1.0, 2010-08-19.
5 SKBdoc 1282650 – SFR DZ MASTER v1.0-bridges.xml
6 SKBdoc 1246849 – SFR_DZ_V1.0_PDZs_not_linked_to_DZs, Version 1.0, 2010-08-19.
7 SKBdoc 1246853 – SFR_DZ_V1.0_Possible_stress_relief_structures, Version 1.0, 2010-08-19.
8 SRS-FFM01-06_v4_alterFinal_nocpm_r1_sets1-65_all_96.asc, delivered from Serco.
9 SKBdoc 1223130 – Befintligt skannat SFR i STL-format, Version 0.1, 2010-06-08.
10 SKBdoc 1282649 – Mike_SHE_filer_använda_i_SFR_DT-simulations_110520.

1.6 Modelling tools

1.6.1 FracMan

FracMan is based on the Discrete Fracture Network (DFN) approach, where flow in a complex three-dimensional fracture-network geometry is solved (Dershowitz et al. 1998). The appeal of the DFN approach is that it allows a realistic fracture representation, which, in a statistical sense, is consistent with borehole data. One benefit of the DFN approach is that it does not rely on the so-called continuum approximation (see below), which makes it appropriate for fracture-flow modelling in sparsely fractured bedrock with low-permeable matrix One drawback of the DFN approach is that its detailed resolution of fracture geometry become computationally demanding in large models. In this study, FracMan is used to simulate transient pressure responses in deterministic structures (Chapter 6).

1.6.2 DarcyTools

DarcyTools is based on the Continuum Porous-Medium (CPM) representation (Svensson et al. 2010), according to which the hydraulic properties of a flowing fracture network are approximated by those of a porous medium. DarcyTools allows transferring fracture-network characteristics onto its computational grid by means of geometric up-scaling. The up-scaled properties are referred to as Equivalent Continuous Porous Medium (ECPM) properties. As the ECPM approach is based on an underlying stochastic DFN model, the resulting ECPM properties are also stochastic. The uncertainty related to variability in hydraulic properties should therefore be handled by addressing multiple realisations.

The ECPM approach is computationally more efficient than the DFN approach. Geometric up-scaling does not always ensure *hydraulic* consistency between the complex heterogeneity of the underlying flowing fracture network and the approximated ECPM. Thus, "Equivalent" implies a fine resolution of the computational grid in order to be valid. In this study, DarcyTools is used to test parameter sensitivity in a perturbation analysis (Chapter 5) and to explore flow paths under different flow regimes (Chapter 7).

1.7 This report

The overall approach is described in Chapter 2, together with the concepts, assumptions, limitations, and uncertainties that were important for formulating the approach. The parameterisation of the hydraulic domains is described in Chapter 3. Chapter 4 describes the implementation of the hydrogeological model in DarcyTools and how the performance of the flow model is compared with data, groundwater levels (hydraulic head) and inflow.

The flow simulations are divided into three parts:

In the first part, the sensitivity of the hydraulic parameterisation is explored, see Chapter 5. This is done in a sequence of Model Exercises and leads to the final parameterisation of deformation zones (Appendix A).

In the second part, two interference tests are simulated by means of a simplified model setup, see Chapter 6. These simulations are based on the adjustments made in Chapter 5.

In the third part, the difference in flow regime between the current, open SFR facility and a future, re-saturated SFR facility, is demonstrated in Chapter 7 by means of particle tracking and identification of recharge/discharge locations.

A summary of the study and the conclusions drawn are presented in Chapter 8.

1.7.1 Nomenclature

This report contains several terms and acronyms that are rarely used outside SKB and makes several references to site-specific deformation zones. To facilitate the readability of the report these are listed in Table 1-4.

Table 1-4. Terminology, acronyms and structures frequently referred to in the report.

Central notations used in the hydrogeological modelling	
Shallow Bedrock Aquifer (SDM-Site Forsmark)	Originally, a concept that describes the hydraulic character of the uppermost c 150 m of rock modelled in SDM-Site Forsmark. This shallow realm is hydraulically dominated by large, sub-horizontal, transmissive structures, i.e. sheet joints.
Sheet joints (SDM-Site Forsmark)	Deformations caused by stresses/stress releases following glaciations/ deglaciations. In the flow model for SDM-Site Forsmark, the hydraulic impact of sheet joints is accounted for in terms of three hydraulically heterogeneous horizons, which can be highly transmissive locally (Figure 3-10).
SBA, SBA-structure (SDM-PSU)	Network of interconnected, sub-horizontal, transmissive features (T $>10^{-6}$ m^2/s) that is geometrically represented by a plane for deterministic modelling purposes. Inside the SFR Regional domain, eight structures are modelled in the upper 200 m bedrock (SBA1 to SBA8 in Figure 3-11). The term *SBA-structure* is used at SFR to emphasise that these structures are of lesser size and of less significant hydraulic nature as compared to the *sheet joints* modelled in SDM-Site Forsmark. Data suggest that hydraulic contrast between the SBA-structures at SFR and the sheet joints at Forsmark is c. one to two orders of magnitude.
PDZ, Unresolved PDZ	In the conceptual geological modelling, all borehole intervals interpreted to have "deformation-zone like characteristics" are initially referred to as Possible Deformation Zones (PDZ) In the three-dimensional geological modelling, deterministic structures (ZFMxxx) are modelled by linking PDZs to surface lineaments. Remaining PDZs, which cannot be linked to lineaments, are referred to as "Unresolved PDZs" (Figure 3-12).
Central block	The volume of rock in the centre of the SFR Regional domain that is enclosed by the Northern and Southern boundary belts (Curtis et al. 2011). The Central block has considerably less evidence of transmissive SBA-structures.
Northern boundary belt	The geologic model (Curtis et al. 2011) defines a northern belt of deformation zones acting as a geological boundary in the SFR model (ZFMNW0805A/B).
Southern boundary belt	The geologic model (Curtis et al. 2011) defines a southern belt of deformation zones acting as a geological boundary in the SFR model (the Singö deformation zone and splays). It is judged likely that the Southern boundary belt also has a wider influence range on the rock mass outside its deformation zones, although this hypothesis was not confirmed in the hydrogeological modelling due to lack of borehole support.

Acronym	Stands for	Explanation
Boremap	Borehole mapping	Database for fractures mapped in boreholes.
DEM	Digital Elevation Model	Topographical data of the Forsmark area, covering both land and seafloor with a spatial resolution of 20 m scale in the horizontal plane.
DFN	Discrete Fracture Network	Description of the fractures contained in the rock mass. DFN fractures are typically resolved as a network of planar geologic features.
ECPM	Equivalent Continuous Porous Medium	A hydrogeological modelling concept, according to which the hydraulic properties of a conductive fracture network is approximated by those of a porous medium. ECPM does not resolve fracture flow explicitly, and hence is useful in large scale simulations.
FWH	Fresh-water head [m]	Groundwater level expressed in terms of a freshwater column, see Equation 2-1.
GEHYCO	GEnerate HYdraulic COnductivity	A DarcyTools module used to translate the hydraulic properties of a geometric DFN into an ECPM (Svensson et al. 2010)
HCD	Hydraulic Conductor Domain	Hydraulic domain representing deformation zones (Figure 2-1)
HFM	Hammarborrhål Forsmark	Percussion-drilled borehole, drilled during the investigations for SDM-Site Forsmark.
HFR	Hammarborrhål SFR	Percussion-drilled borehole in the SFR area. Only data from boreholes drilled during the investigations for SDM-PSU (2008–2009) are included in the present study.
HMS	Hydro Monitoring System	Database storing e.g. measured groundwater level data. In a second step, quality assured data are transferred from HMS to SKB's primary database Sicada.
HRD	Hydraulic Rock mass Domain	Hydraulic representation of rock between deformation zones (Figure 2-1)

Acronym	Stands for	Explanation
HSD	Hydraulic Soil Domain	Hydraulic representation of Quaternary deposits (Figure 2-1)
HTHB	Hydraulisk Test Hammar borrhål	Hydraulic test method used in percussion boreholes, based on a combination of impeller flow logging and pump tests. Considerably lower resolution and higher detection limit than the method used in core boreholes (see PFL).
KFM	Kärnborrhål Forsmark	Core-drilled borehole, drilled during the SDM-Site Forsmark investigations.
KFR	Kärnborrhål SFR	Core-drilled borehole, drilled for the SFR investigations; a historic data set exists from the construction of SFR (1982 to 1987), as well as, a recent data set drilled during the investigations for the SFR extension (2008–2009).
M0 to M7	Model Exercises	A sequence of model setups used to analyse the constraining power of available data, and the prospect of stepwise improvement of model parameterisation.
NBT	Nedre Byggunneln	A lower tunnel section in SFR where inflow is measured.
PFL	Posiva Flow Logging method	Hydraulic test method used in core boreholes designed to detect *continuously flowing fractures*. The method has a considerably higher spatial resolution and a lower hydraulic detection limit than the hydraulic test method used in percussion-drilled boreholes (see HTHB).
PFL-f	Discrete inflow detected by the Posiva Flow Logging method	A discrete borehole inflow expressed in term of transmissivity. Used as input for the DFN model after it is coupled to Boremap feature.
PWH	Point-water head [m]	Groundwater level expressed in terms of a point-water column, see Equation 2-1, where the columns has the same fluid density as the water in the bedrock at the “point of reference”. Column/Reference fluid densities are measured for each section.
RHB 70	z, elevation [m]	The national levelling system used by SKB in PSU.
RVS	Rock Visualization System	Tool for modelling the geometry of geological structures
SDM	Site-Descriptive Model	Integrated, multi-disciplinary, evaluation of site data
SHI	Single-hole Interpretation	A methodology used by SKB to analyse borehole databased on a selection of geological and geophysical parameters.
SFR	Slutförvaret för kortlivat radioaktivt driftavfall	The existing final repository for short-lived low and intermediate level radioactive material
SKB	Svensk Kärnbränslehantering AB	The Swedish Nuclear Fuel and Waste Management Company
ZFM	Deformation zone in the Forsmark area	Deterministically modelled deformation zone in the geological model. Modelled by linking borehole intercepts with “deformation-zone like characteristics” to surface lineaments (see acronym PDZ).

Key deformation zones, modelled in RVS (Deterministic structures of the Geological model SFR v 1.0)		**Alternatively known as:** (Structures in previous SFR modelling)
ZFMWNW0001	Key deformation zone of the Southern boundary belt	Singö deformation zone
ZFMNW0805A/B	Key deformation zone of the Northern boundary belt	Zone 8
ZFMNNW1034	Deformation zone of high transmissivity intersection the wedge between the Northern and Southern boundary belts	Not modelled in previous SFR models
ZFM871	Gently dipping deformation zone below the existing SFR facility	Zone H2
ZFMENE3115	Deformation zone that terminates ZFM871 to the southeast	Not modelled in previous SFR models
ZFMNE0870	Low-transmissive deformation zone running parallel to the access tunnel “ByggTunnel” (BT)	Zone 9
ZFMNNE0869	High-transmissive deformation zone intersecting access tunnels	Zone 3
ZFMNNW1209	Deformation zone that intersects the SFR disposal facilities (rock caverns)	Zone 6
ZFMWNW1035	Deformation zone located At the northern rim of the Sothern Belt	Zone 1

2 Methodology and assumptions made

2.1 Geology

Based on the geological model version 1.0 (Curtis et al. 2011), a hydrogeological model has been formulated for the SFR Regional model domain (Öhman et al. 2012). A Central block is defined between two geological boundaries called the Southern and Northern boundary belts, respectively. The Central block is characterised by a lower density of flowing fractures and has a restricted vertical hydraulic connection to the sea. The vertical hydraulic connectivity to the overlying sea is interpreted to be along the Southern and Northern boundary belts, which act as key hydraulic features in the SFR area. The Central block is interpreted to be connected to the two boundary belts via a sub-horizontal, transmissive fracture network. The more prominent hydraulic connections have been modelled explicitly in the hydrogeological model, where they are referred to as SBA-structures (see Section 3.4.3 and Appendix B). Another important gently dipping structure is the deformation zone ZFM871, which is located below the existing SFR. The spatial extension of ZFM871 is uncertain. Other deformation zones within the Central block are modelled as steeply dipping. The majority of these have a comparatively minor role for the hydrogeological system.

The Northern boundary belt is geologically defined by ZFMNW0805A/B. The Southern boundary belt is geologically defined by ZFMWNW0001, ZFMWNW3259, ZFMWNW0813, ZFMNW0002, and to a lesser extent ZFMWNW1035. The hydraulic connection of the Northern boundary belt to the sea is expected to better than that of the Southern boundary belt, which is potentially constrained by overlying sediments (Figure 3-3). The hydraulic connection to the Forsmark inland, i.e. perpendicular to the Southern boundary belt, is not fully clear. For instance, the Southern boundary belt may be hydraulically heterogeneous due intersecting sheet joints (Section 3.4.1).

The two belts form a wedge. The size of the Central block narrows as the point of observation gets closer to the wedge vertex. In between the vertex and the existing SFR facility, the Central block is intersected by ZFMNNW1034, which is interpreted to have an essential hydrogeological role within the SFR area.

The modelling approach is described in Section 2.3. The approach taken has been setup in context of important concepts, necessary assumptions, and data interpretations, which are described in Sections 2.4 to 2.8.

2.2 Systems approach

Following SKB methodology (Rhén et al. 2003), the hydrogeological system is conceptually divided into three types of hydraulic domains (Figure 2-1):

- HSD (Hydraulic Soil Domain) represents the regolith[1]
- HCD (Hydraulic Conductor Domain) represents deformation zones, and
- HRD (Hydraulic Rock mass Domain) represents the less fractured bedrock outside deformation zones.

This division into hydraulic domains constitutes the basis for the conceptual and numerical modelling. The hydrogeological model consists of: 1) the geometry of these hydraulic domains, and 2) their hydraulic parameterisation. The hydraulic parameterisation is based on the hydraulic investigations conducted in cored boreholes, percussion boreholes, and stand pipes. The geometries of the hydraulic domains are coherent with the geometries of the geological features, and their hydraulic properties reflect the anisotropy and spatial variability observed during the hydraulic investigations. Each of the three hydraulic domains can be split into sub-domains, e.g. different regolith layers (HSD), individual zones (HCD), and fracture domains (HRD), respectively. The hydraulic parameterisation is described in Chapter 3.

[1] Regolith include any loose material covering the bedrock, e.g. Quaternary deposits, artificial filling material, and weathered rock, see Section 3.1.

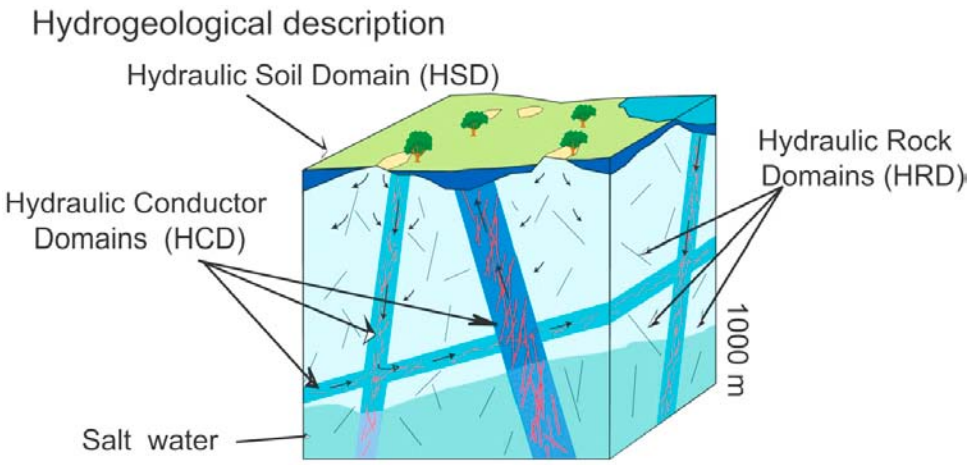

Figure 2-1. *The hydraulic sub domains of a hydrogeological model; taken from Rhen et al. (2003).*

The hydrogeological modelling of the shallow bedrock realm at Forsmark required an updated modelling strategy to handle a frequent occurrence of transmissive, sub-horizontal sheet joints (see Follin et al. 2007a) and Section 3.4.1). Effectively, the uppermost c 150 m of rock is referred to as a Shallow Bedrock Aquifer (SBA). In PSU, interpreted sheet joints in the SFR area are called SBA-structures (see Appendix B in Öhman et al. 2012, and Section 3.4.3).

2.3 Approach

In theory, measured data could be used for flow model calibration. Flow modelling is therefore used in this work to study the parameterisation of the hydrogeological model defined in Öhman et al. (2012). Earlier work, where the focus was directed towards the existing SFR, have applied tunnel-inflow simulations to parameterise the hydraulic domains (Holmén and Stigsson 2001, Holmén 2005). The tunnel-inflow calibration method was not applied in this study, primarily for the following reasons:

Target volume: Tunnel inflow data provide little constraining power for structures lacking direct contact to the existing SFR. In the present geological model for SFR, 35 out of 40 deformation zones and 7 of 8 SBA-structures lack direct contact with the existing SFR facility. In the previous model of Holmén and Stigsson (2001), only 1 out of 5 deformation zones lacked direct contact.

Limitations in constraining data: The head and inflow data change with time (Section 2.7) and represent a disturbed hydrogeological system, which raise concerns regarding their usefulness for the derivation of a flow model that assess the natural state (hydraulic properties in the future, re-saturated system). The calibration becomes dependent on an assumed relation between skin (Section 2.5) and transient inflow phenomena (Section 2.8). Furthermore, several data uncertainties and necessary simplifications in the model setup are discussed in Section 4.4.

Owing to the circumstances discussed above, the available data are judged insufficient for providing a well-constrained tunnel-inflow calibration of the hydrogeological model. Instead, the model performance is demonstrated by means of forward modelling, i.e. for a number of parameterisation setups and compared to present-day data (inflow, head, and observed interferences). The flow simulations are therefore intended as tests of model performance in relation to limitations and uncertainty in constraining data.

The simulations are divided into three parts:

1) The first part examines the sensitivity of the implemented flow model being exposed to a series of parameter perturbations (Section 2.3.1). These simulations are performed with an increasing level of detail, using the equivalent continuous porous media modelling tool (DarcyTools (Svensson 2010)).

2) The second part focuses on two hydraulic interference tests carried out at the site (Section 2.3.2). These simulations are performed with a simplistic model setup using the discrete fracture network model modelling tool FracMan (Dershowitz et al. 1998).

3) Finally, the difference in flow regimes between the open repository (current state) and the re-saturated repository (future state) are exemplified by a particle tracking exercise using DarcyTools (Chapter 7).

The interference-test simulations (part 2 in the list) are based on the results of the previous modelling part, and provide similar results; the reason for using a different flow concept and computer code is that it more efficiently handles the transient test responses.

2.3.1 Model Exercises investigating model performance

Comparison between tunnel inflow simulations and measured data are complicated by the impact of local flow resistances close to the tunnel wall, so-called tunnel-wall skin (see Section 2.5). Tunnel-wall skin censors the hydraulic inferences (responses) in the surrounding rock. The lack of uniqueness in model interpretation arising from skin can – to some extent – be overcome by combining the two following data types:

1) Spatially distributed tunnel inflow (Sections 2.7.2 and 4.4.1).

2) Monitored head in surrounding borehole sections (Sections 2.7.1 and 4.4.2).

However, a complication in using the measured data at SFR for comparisons with flow model simulations is that the measured data are not at steady-state (Section 2.7). Hence, a fundamental decision must be taken whether steady-state flow modelling can be used and, if so, which data should be compared to the steady-state solution; the *early* data, or the *late* data.

The cause(s) for the on-going transient development remain unclear (Section 2.8). It can be assumed to reflect:

1) a leaky, compartmentalised natural fracture system dominated sub-horizontal fractures, and/or

2) a transient alteration of the fracture properties of the rock mass in the vicinity of the existing SFR.

It is obviously more rational to use the early data set, since this is more representative of the virgin-state rock mass. Nevertheless, it was decided to use the most recent data in the present work. The motive for this decision is that the recent data set provides considerably more data, both in terms of monitored heads from the area where the SFR extension is planned (Figure 1-1 and Figure 1-2), but also an improved spatial resolution of inflow data.

Owing to the concerns raised regarding the representativeness of the recent data set for flow model calibration, the numerical simulations are not used for direct model calibration. Instead, the objective here is to address various conceptual uncertainties and to evaluate the hydraulic significance of geological structures, as parameterised by hydraulic data. In operation, seven Model Exercises were defined and tested. These are referred to as M0 to M7, where M0 is the most simplistic model, and M7 is the most complex model. Finally, the results from a model setup, referred to as M8, are compared with the estimated initial inflow (i.e. at time t = 0, prior to alteration of the hydraulic properties; Section 2.8.1).

The model set-ups are specified in more detail in Chapter 5 (summarised in Table 5-1), and the model results are presented and discussed in more detail in Appendix C.

2.3.2 Transient simulation of interference tests

Interference tests provide useful information on large-scale, hydraulically significant structures. For instance, the tests conducted in SDM-Site Forsmark provided key evidence for the identification and characterisation of so-called sheet joints. Therefore, hydraulic interferences have been evaluated also during the SFR extension investigations (Walger et al. 2010). It should be noted that the interference tests conducted occur in bedrock below the Baltic Sea, in the vicinity of an open underground facility, which is an unusual situation for this type of analysis.

Hydraulic interferences/responses observed at SFR during the drilling activities (Walger et al. 2010) led to the definition of the so-called SBA-structures, see Appendix B in Öhman et al. (2012). Unfortunately, disturbances cause by drilling activities are difficult to evaluate hydraulically and difficult to simulate numerically. However, three controlled interference tests were also performed, out of which two were simulated with a simplistic model setup, where only deterministic structures (selected HCDs and SBAs) were included. The limitations of the two tests are the following:

1) They have a relatively short duration (one day and three days, respectively), which necessitates transient simulation and introduces additional uncertainty related to storage (storativity parameterisation).
2) Their location in the Central block is of high relevance to the SFR extension, but provides little confirmatory evidence for the concept of SBA-structures (which are imagined to be more dominant closer to the Northern boundary belt and to zone ZFMNNW1034).

As stated earlier, the objective of these simulations is *not* to fine-tune the hydrogeological model parameterisation, but to study the proposed conceptual model in order to gain further insight and confidence.

Neglecting the fractures in the rock between deformation zones (HRD) in the simplistic model setup implies a significant underrepresentation of potential flow paths. However, the HRD is represented by a stochastic Hydro-DFN model in the hydrogeological model developed by Öhman et al. (2012), which adds on additional complexities. Therefore, it was decided to only include deterministic structures, i.e. deformation zones (HCD) and SBA-structures, where the latter represents sub-horizontal hydraulic connectivity, since almost all deformation zones are steeply dipping. The simulations are described in more detail in Chapter 6.

2.4 Alternative parameterisation methods

2.4.1 Tunnel inflow calibration

In the work by Holmén and Stigsson (2001), the hydraulic properties of modelled deformation zones (HCD) and the bedrock between zones (HRD) were calibrated to match SFR inflow measurements. A drawback of this calibration method is that it is produces non-unique solutions, since the tunnel-wall skin allows for a range of possible parameter combinations of the HCDs and HRDs to be fitted. (Tunnel-wall skin represents locally lower hydraulic conductivity of the rock in the vicinity of the tunnel wall, Section 2.5.) To mitigate this uncertainty, Holmén (2005) determined ensembles of possible HCD and HRD parameter combinations that reproduce inflow data.

Notwithstanding, t he significance of tunnel-wall skin and its role in controlling tunnel inflow is not readily assessed (Section 2.8), since the true *non-disturbed* hydraulic properties of the HCDs and HRDs cannot be differentiated from effects of tunnel-wall skin. Further, when the repository is closed and the tunnels are fully saturated, the tunnel-wall skin may disappear, implying greater hydraulic conductivity.

2.4.2 Borehole data parameterisation

In the current study, the deformation zones are parameterised based on hydraulic data from borehole investigations (Section 3.2). The primary reason for this is that the target area for the SFR extension includes structures that are located farther away from the existing SFR facility, with a subordinate role in the present SFR inflow, and consequently cannot be well-constrained by tunnel inflow calibration. A possible drawback of this strategy is that borehole data could be subject to local-scale heterogeneity and hence less representative of the effective large-scale hydraulic properties of zones. However, the features identified in the boreholes with PFL logging are envisaged as *continuously* flowing features (i.e. large-scale flow paths). This is different from the short-term measurements characterising the historic data set of PSS data, which are expected to also include data from borehole intervals intersected by fractures that are not necessarily connected on a large scale (compartmentalisation). The general notion is that the HCD parameterisation based on historic hydraulic data provides an upper estimate of HCD transmissivity and therefore is more conservative than tunnel-inflow calibration.

Both methods have their merits and drawbacks. The experiences of Holmén and Stigsson (2001) are taken into account in the flow simulations reported here. However, the transient behaviour of inflow and head data (Section 2.7) complicates a direct transfer of experience from the earlier models. Indeed, the SFR inflow calibration by Holmén and Stigsson (2001) was based on inflow measurements conducted 1997, which had a total of 469.5 L/min. The latest inflow measurements at hand, 2010, has reduced to a total of 286 L/min (i.e. approximately 60% of the measurements in 1997). In other words, the relevance of the calibrated HCD and HRD values in Holmén and Stigsson (2001) must discussed while analysing the current situation.

2.5 Skin factor

Underground constructions and drilled boreholes may affect the hydraulic properties of the rock . The penetration depth of the alteration is often referred to as "skin zone". Skin can be *positive*, which implies a locally lower hydraulic conductivity (or increased flow resistance), or *negative*, which implies a locally enhanced hydraulic conductivity. In most cases, tunnel-wall skin is found to be positive, resulting in considerably smaller tunnel inflows than expected, e.g. compared to predictions based on borehole investigation. A key concern is then how representative the measured tunnel inflow is for flow model calibration of the natural (undisturbed) rock. Several potential physical explanations have been suggested for positive skin (see discussion in Section 2.8). Due to practical limitations and lack of data-inferred evidence, these physical phenomena cannot be modelled in detail. Instead, tunnel-wall skin (skin factor) is typically implemented as a fitting parameter in a groundwater flow model, and calibrated to reproduce measured tunnel inflow.

In addition to the natural processes contributing to skin, the tunnel-wall flow resistance is also altered by engineering techniques. Bolt boreholes, drilled for rock stabilisation during tunnel constructions, are reported to substantially increase the tunnel inflow, at least during an initial stage. Several tunnel sections of the existing SFR have been grouted and the major grouting efforts were made at deformation zone intercepts (Öhman et al. 2012). In the early construction stage, standard cement was used as grouting material (before and during the penetration of the Singö deformation zone in the upper part of the SFR access tunnel). Standard cement is not expected to reduce the hydraulic conductivity much below c 10^{-6} m/s. However, a finer grouting material became available during the later stage of the tunnel constructions (*in Swedish:* finmalen anläggningscement), which potentially reduced the hydraulic conductivity about an order of magnitude. On the other hand, the extent of grout degradation over the last 25 years is not fully clear. Calibrated skin in earlier SFR models have been interpreted to primarily reflect grouting of deformation zone intercepts. Note that these values are not directly applicable to the current flow model as they relate to a higher inflow (1997) and an earlier structural model, and also depend on a different discretisation of the computational grid (e.g. Figure 2-2).

Tunnel inflow potentially provides constraining criteria for the parameterisation of the hydrogeological model during open repository conditions. However, it is possible that the tunnel-wall skin is *reversible* after closure of the underground system. That is, the skin-affected rock mass will eventually resume its original properties after re-saturation.

In this study, the tunnel-wall resistance (including both skin and grouting) is implemented in the groundwater flow model as a low hydraulic conductivity, K_{skin}. This conductivity value is applied over a single computational cell (in the current flow model, the tunnel wall cell size is 2.0 m (Figure 2-2), which implies that the major head drop takes place adjacent to the tunnel wall. In reality, the thickness of the skin zone varies in space and locally it could extend much farther into the rock. Keeping the pressure drop the same over a larger distance from the tunnel wall, e.g. 20 m, implies an order of magnitude lower gradient. In order to maintain the same flux to the tunnel in the flow model, the corresponding K_{skin} would need to be an order of magnitude higher.

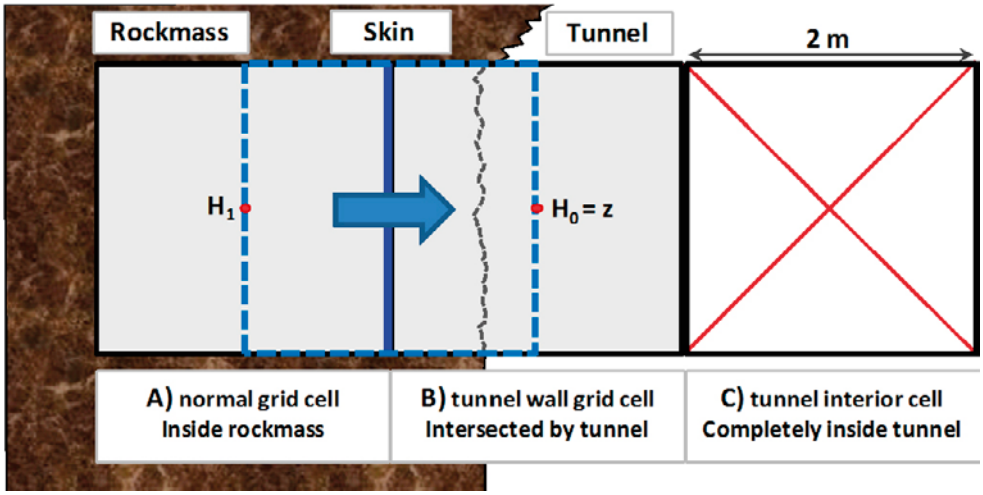

Figure 2-2. *Conceptual illustration of inflow calculation. Grid cells completely inside the tunnel are removed (i.e. red cross, cell C). Grid cells intersected by the tunnel wall are prescribed an atmospheric pressure (i.e. cell B is assigned atmospheric pressure, $H_0 = z$ m). The cell wall between an intersected cell and its adjacent cell in the rock mass (i.e. illustrated by the blue line between cells A and B) are identified as an inflow surface. Such cell walls are classified by inflow area (Table 4-3) and assigned skin values.*

2.6 Groundwater levels, heads and uniform-density flow

Two types of groundwater levels, or head data, are measured at SFR: *fresh-water head* (FWH; in underground boreholes) and *point-water head* (PWH; in surface boreholes). *FWH* is calculated for an assumed fresh-water density of $\rho = 1{,}000$ kg/m^3, whereas *PWH* is calculated based on the measured fluid density inside the borehole (cf. Follin 2008).

$$H_i = \frac{P}{g\,\rho} + z \qquad (2\text{-}1)$$

where P is the measure fluid pressure, g is the gravitational acceleration, and z is the elevation of the monitoring interval. Variations in the water density may cause a discrepancy between the two data types and direct comparisons between FWH data and PWH data should be made with caution. On the other hand, the significance of this discrepancy depends on the context of application.

This study addresses the disturbed flow system around SFR, which is dominated by tunnel inflows, large head decreases, and high gradients directed towards the SFR facility. Compared to the observed magnitudes of head decrease (see Section 2.7), density effects on head data are relatively small at the shallow depths of interest (c 100 m elevation). Moreover, necessary geometric simplifications in the numerical model lead to inexact comparisons between simulated and measured head data (Section 4.4.2).

Consequently, a *uniform-density system* is assumed in the flow simulations. The overlying Baltic Sea is included in this assumed uniform-density system (or put in other words, the groundwater density is assumed to be similar to the Baltic Sea). This assumption allows prescribing, H = 0 m, as a constant-head boundary condition along the seafloor. The measured head data are briefly presented in Section 2.7.

2.7 Overview of constraining head and inflow data

Measured inflow and head data are used for model performance evaluation. The usage differs somewhat between the tunnel-inflow simulations and the interference test simulations. The handling also depends on the software used (DarcyTools and FracMan); details are therefore described in Sections 4.4 and 6.2.

It is important to note that the measured inflow and head data are both in a transient state despite c 25 years of operation. The interpretation of this condition necessitates fundamental decisions on assumptions, model simplifications, as well as formulating an approach for the flow simulations.

Therefore, data are briefly presented in this section, followed by hypotheses concerning the causes for the transient state (Section 2.8).

2.7.1 Measured head and evolution over time

In total, 95 monitored borehole sections are available for the evaluation of the simulated head decrease around SFR.

- Thirty-nine monitored sections were installed in 12 underground boreholes drilled during the construction of SFR (Figure 2-3). Recorded absolute pressures are expressed as fresh-water heads (FWH) assuming a freshwater density of $\rho = 1{,}000$ kg/m^3. The long-term groundwater pressure evolution around the SFR facility has been monitored in the tunnel boreholes since the construction in 1985. The observed general behaviour was an initial rapid drop in head during the construction period and the first time thereafter. The head quickly stabilised in the largest zones ZFMWNW0001 and ZFMNW0805A,B (the Singö zone and Zone 8). In the less conductive rock there has been a slow, relatively constant, declining trend in most borehole sections since 1987–1988 (Figure 2-3b and Figure 2-4).
- Fifty-six monitored sections were installed either during the SDM-Site Forsmark investigations, or during the SDM-PSU investigations (Figure 2-5). Monitored sections in surface boreholes are expressed in terms of point-water heads (PWH), where the reference density is that of the actual fluid in the borehole interval. However, KFR105 is an underground borehole and the pressure measured in this borehole is expressed in terms of FWH.

In the light of the strong gradients around the SFR facility, the relative shallow depths, model uncertainties and necessary simplifications made, the distinction between FWH and PWH is regarded as of minor significance for this study (see discussion in Section 2.6). The approach taken to evaluate model performance in terms of head is explained in Section 4.4.2.

2.7.2 Measured inflow over time

The total inflow has declined gradually over time since the completion of excavations, from 720 L/min (1988) to about 285 L/min (2010). This corresponds to a 60% decrease over a period of 23 years (Figure 2-6). A declining inflow with time is not unique to SFR, but follows the general observations in underground facilities. For example, similar observations have been made at the Stripa Mine and the Äspö Hard Rock Laboratory (Jarsjö and Destouni 2000).

Besides a transient decline in total inflow, there is also a transient evolution in the inflow pattern and the magnitudes of mapped specific inflow locations between the years 1988 and 1993 were partially re-distributed by Axelsson et al. (2002).

The significant decrease in total inflow poses a main concern to which inflow data is the most representative for the safety assessment. A calibrated flow model that matches present-day radial inflow data to an unsaturated repository is not necessarily representative for regional flow conditions, saturated rock, and a weathered grouting.

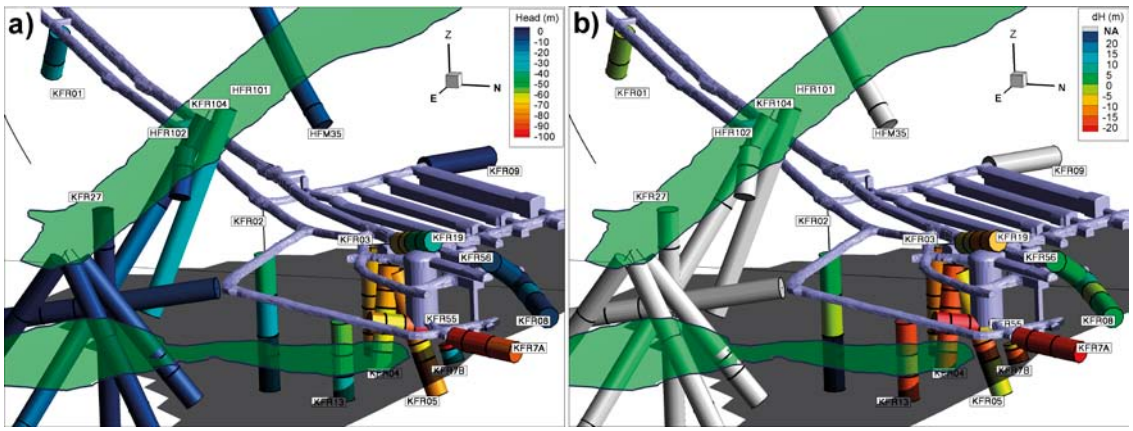

Figure 2-3. *Head in SFR tunnel boreholes; a) 2010 and b) change in head between year 1988 and 2010. The reference year 1988 was chosen since it has been a relatively constant, declining trend in most borehole sections since then.*

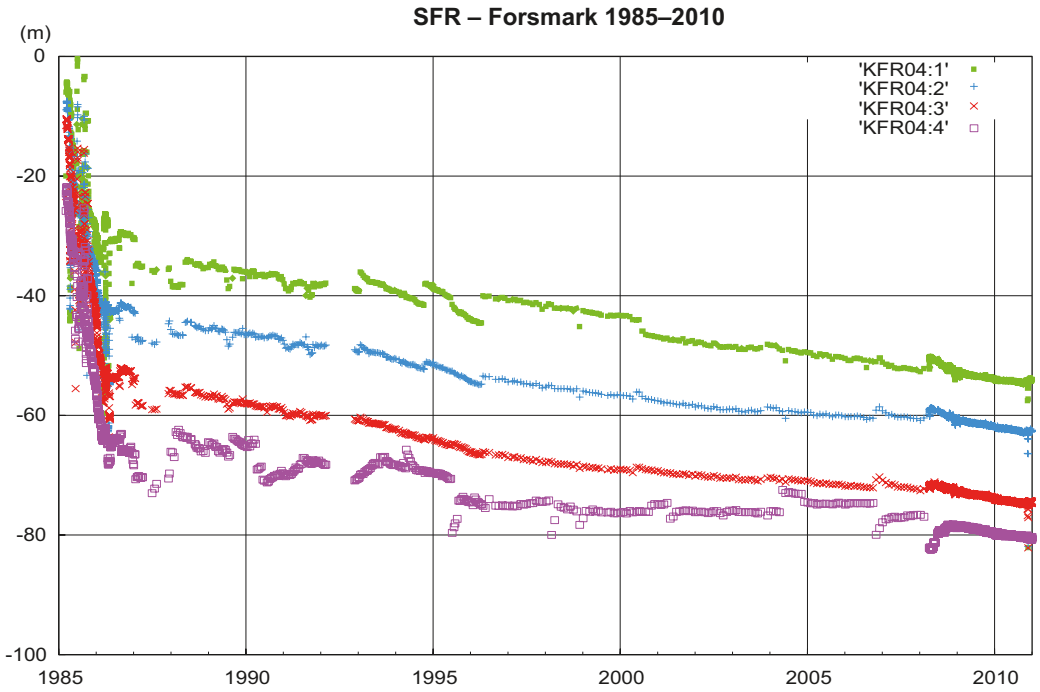

Figure 2-4. *Examples of time series showing the trend in hydraulic head in borehole KFR04. The monitored borehole sections in KFR04 are located at distances between 16 and 42 m from the SFR facility.*

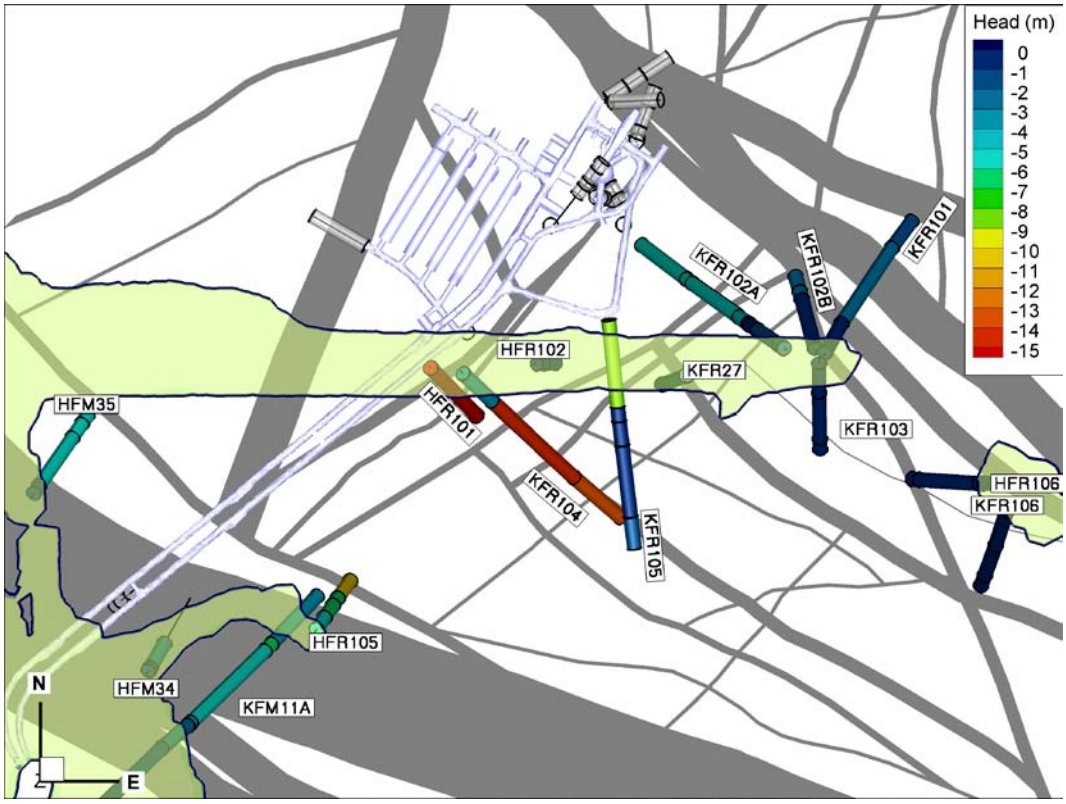

Figure 2-5. *Estimated heads in recently installed borehole sections. The borehole sections installed during the construction of SFR are included for reference. Note that the head cannot be measured in deepest section of HFM34, but is known to be below –14 m.*

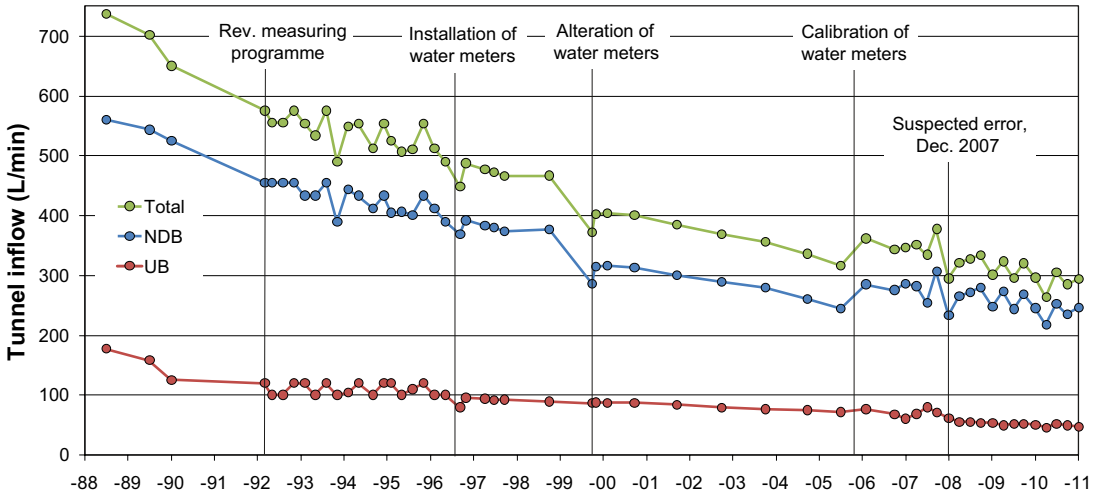

Figure 2-6. *Declining SFR inflow measured in pump pits UB and NDB, since June 1988. Besides inflow to the two pump pits, more differentiated information is also available for a number of tunnel subareas; these are specified in Section 4.4.1. The approach taken to evaluate model performance in terms of differentiated tunnel subarea inflow is also explained in Section 4.4.1.*

2.8 Hypotheses on transient coupled decreasing inflow and head

It is remarkable that steady state flow conditions (constant inflow rates and constant groundwater levels in the monitored borehole section) are not established despite 25 years of operation. After all, SFR is located c 60 m below the Baltic Sea and the majority of the deformation zones surrounding SFR are steeply dipping, i.e. outcropping at the sea bottom.

The interpretation of a simultaneous decrease in total inflow and surrounding heads is a key conceptual question, the answer of which has implications to formulating the approach for groundwater flow modelling. A decision must be taken on to how to relate inflow data to hydraulic properties of the *undisturbed* rock mass away from the SFR. Two interpretation alternatives are identified. These are not exclusive, however, i.e. combinations of the two are probable.

Compartmentalisation: If some fractures are more transmissive than others, but the overall fracture networks in the rock mass and in the deformation zones, respectively, are compartmentalised (poorly connected), the early large inflow could reflect the transient release of water stored of transmissive and connected fractures intersecting the tunnel walls. The low inflow during the later stage could reflect impact of hydraulic chokes due to the compartmentalisation.

Sealing phenomena: The open tunnels cause large perturbations to the hydrogeological system, in terms of e.g. unsaturated flow and capillary fringe near the tunnel walls, changed head gradients with different stress levels in the surrounding rock mass, and new hydrochemical mixing conditions including precipitation and microbial growth conditions on tunnel walls. Such perturbations are known to alter the hydraulic properties of the rock mass around an underground construction (Gustafson 2009). Four such sealing phenomena are considered in Öhman et al. (2012):

1) **Unsaturated fracture flow:** Close to the tunnel wall, air may enter dewatered fractures. Even at some distance away from the tunnel walls, the decreasing groundwater pressure around an underground facility may cause dissolved gases to come out of solution (Jarsjö and Destouni 2000). Degassing may cause unsaturated fracture flow with a reduction on flow. For instance, at fracture scale, trapped air bubbles may form along conductive flow paths and partially block the flow. This phenomenon is coupled to declining head and does not necessarily occur close to the tunnel walls.
2) **Particle clogging:** Tunnel inflow may transport sediment particles from the seafloor into the fracture system, or cause existing fracture filling (sediments, gouge, clay, etc) to re-suspend and clog hydraulic paths. This phenomenon does not necessarily occur close to the tunnel walls.
3) **Fracture sealing due to chemical precipitation and microbial growth:** Tunnel inflow cause disturbances to the natural groundwater conditions, which may cause mineral precipitation/dissolution, as well as microbial growth on fracture walls (Laaksoharju et al. 2009). Sealing of fractures is known to decrease conductivity and cause re-distribution of flow paths, but primarily in the immediate vicinity of tunnel walls.

4) **Hydro-mechanical fracture closure:** Fracture transmissivity is related to the normal stress. Hydraulic data measured before and after the Silo construction demonstrated a local conductivity reduction as the result of increasing stress in the walls of the Silo (Carlsson et al. 1986). This indicates that fracture transmissivity at SFR is sensitive to normal loading, i.e. fractures have low fracture stiffness with regard to the changes in hydraulic head. The dewatering of conductive fractures during tunnel inflow implies increasing effective normal stress, causing fracture closure and decreasing fracture transmissivity, which in turn reduces tunnel inflow. The reduction in flow will slow down the propagation of the low-pressure front, appearing as a very slow, transient head decrease process. This phenomenon is coupled to declining head and does not necessarily occur close to the tunnel walls.

It has not been possible to fully resolve whether the declining inflow relates more to compartmentalisation than to sealing, or if both processes are equally present. Alone, the latter alternative, the sealing phenomenon, would imply that the *undisturbed* fracture network is more transmissive and better connected than is revealed by the inflow measurements; it is therefore a more pessimistic interpretation from a safety assessment point of view. By the same token, it is more pessimistic to assume that the causes for the sealing phenomenon are reversible, implying that in future the rock mass around the saturated tunnel will resume its original hydraulic properties once the repository tunnels are saturated and the grouting has weathered.

2.8.1 Estimation of initial inflow

To put the declining inflow patterns in context with the sealing phenomenon discussed above, it is necessary to estimate a value for the initial inflow (i.e. prior to sealing phenomenon occurs). The construction phase lasted almost 3 years (from the autumn of 1983 through the spring in 1986). The earliest documented total inflow measurement is from June 1988, two years after the completion of SFR (May 1986). Thus, the sealing phenomena may gradually have developed during this time, and in effect, inflow from the unaltered rock mass may be larger than the earliest inflow record in 1988. On the other hand, some of processes discussed above take time to develop.

For the purpose of the work reported here, a logarithmic function was fitted to the inflow data and extrapolated backwards in time. Two main hydraulic disturbances can be identified, which are associated to large tunnel inflows:

- the penetration of the Singö deformation zone, and
- the penetration of the gently dipping deformation zone below SFR, ZFM871 (Figure 2-7).

The extrapolation suggests an inflow of c 1,000 L/min at time $t = t_0$ (i.e. the instantaneous inflow). This value provides an estimate of the inflow upper bound, where the influence of skin effects is at minimum. It is a useful ball-park estimate in evaluation of simulated inflow, in which the transient development during the gradual construction progress is neglected.

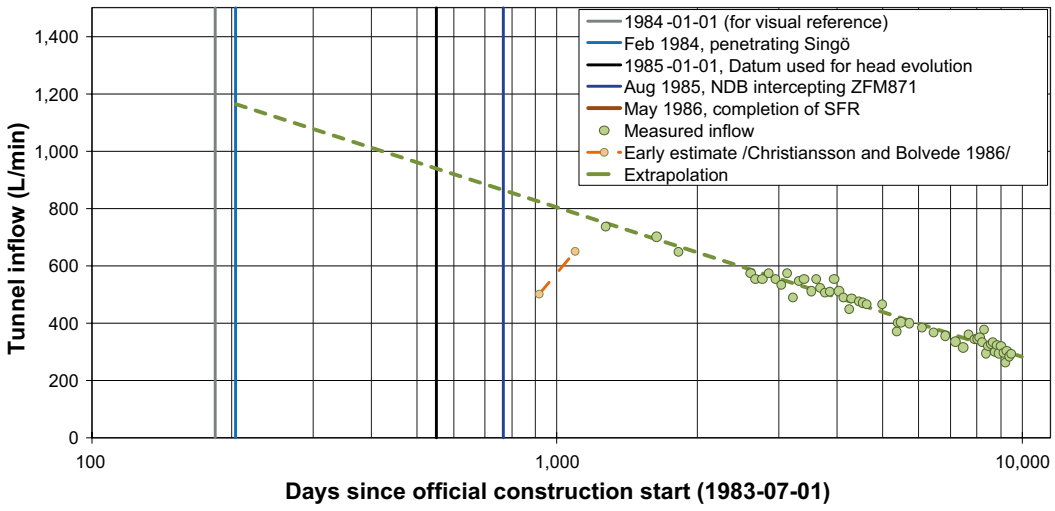

Figure 2-7. *Extrapolation of declining inflow over time in order to estimate a theoretical initial total inflow depending. The tunnel construction was gradually introduced as a sink term to the hydrogeological system over a time span of c three years.*

3 Parameterisation of hydraulic model domains

The concept of Hydraulic Domains HSD, HCD, and HRD is presented in Section 2.2. This chapter describes the hydraulic parameterisation of these units (Sections 3.1 to 3.3). The separate handling of structures falling between the resolution level of the geological model (Curtis et al. 2011) and stochastic fractures represented in the DFN model, are described in Section 3.4.

3.1 Hydraulic Soil Domain (HSD)

The regolith in the Forsmark area was deposited during the Quaternary period. Most of the Quaternary deposits were deposited during or after the latest deglaciation. During SDM-Site Forsmark, a conceptual model of the distribution of Quaternary deposits was developed, which covers the Forsmark inland as well as marine sediments above SFR (Hedenström and Sohlenius 2008, Hedenström et al. 2008). The marine sediments above SFR potentially have an important role in the flow model if they control the hydraulic connection between the sea and the underlying bedrock.

The conceptual model for the regolith consists of nine layers (L1–L3, Z1–Z6; see Figure 3-1 and Table 3-1). Not all layers exist everywhere, and the spatially variable thickness was modelled with a horizontal spatial resolution of 20×20 m. The total thickness of the Quaternary deposits varies from less than a decimetre to a maximum of 42 m (Hedenström et al. 2008).

Anisotropic, effective conductivity values have been calibrated for each of the different regolith layers by means of surface hydrological modelling (Bosson et al. 2010). Additionally, layer Z1, and to some extent layers Z5 and L1, are modelled taking into account spatially variable soil types within the layer (Table 3-1). The numerical implementation of the HSD model in flow simulations is facilitated by means of indicator flags (integer codes), which are used to identify the spatial distribution of soil types and their corresponding conductivity values (see Table 3-1 and Figure 3-2). Indicator flags are not used for homogeneous layers.

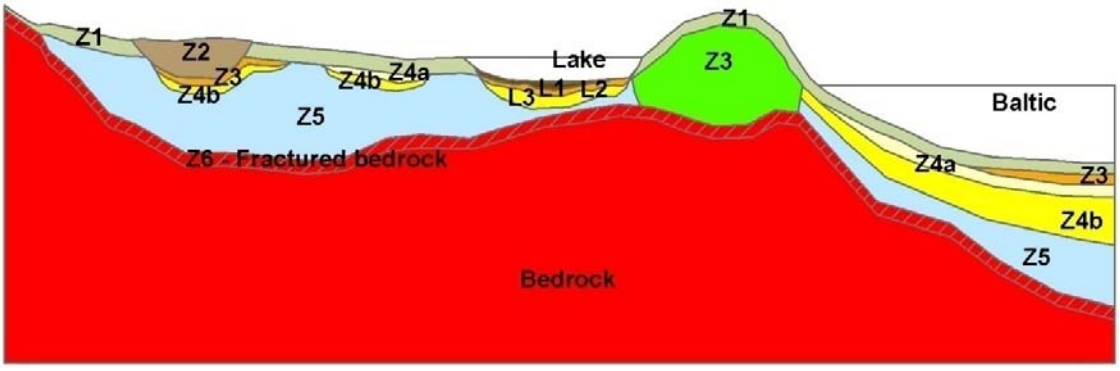

Figure 3-1. *Conceptual model for the layering of Quaternary deposits. The different layers are described in Table 3-1.*

Table 3-1. Quaternary deposits layers (Hedenström et al. 2008), with calibrated effective conductivity values (Bosson et al. 2010).

Layer	Description	Flag	K_H (m/s)	K_V (m/s)
Lake lenses L1 to L3. Only present below lakes (on land)				
L1	Gyttja/mud/clay		3E-7	3.E-7
	Peat (if Flag = 6 in **Z1**)		1E-6	1.E-6
L2	Sand/gravel		2E-4	2.E-4
L3	Glacial and postglacial clay		2.E-8	2E-8
HSD layers Z1 to Z7. Values assumed equal on land and below sea				
Z1	Surface-affected layer. Covers most of the model domain with a thickness of 0.6 m.			
	Spatially distributed, with soil type indicated by Flags.			
	Artificial fill (e.g. the SFR Pier)	1	2E-4	2E-5
	Bedrock outcrop (see **Z7**)	2	1E-7	1E-7
	Clay-Gyttja	3	3E-7	3E-7
	Glacial clay	4	5E-6	5E-7
	Glaciofluvial sediments	5	8E-4	8E-5
	Peat	6	5E-6	5E-7
	Post glacial clay	7	5E-6	5E-7
	Sand	8	8E-4	8E-5
	Coarse and fine till	9	2E-4	2E-5
	Clay till	10	2E-4	2E-5
	Till (Eckarfjärden; if Flag = 20 in **Z5**)	–	8E-4	8E-6
	Glacial clay	100	5E-6	5E-7
	Glaciofluvial sediments	200	8E-4	8E-5
	Bedrock	300	1E-7	1E-7
	Till	400	2E-4	2E-5
	Postglacial sand	500	8E-4	8E-5
	Postglacial clay	600	5E-6	5E-7
	Postglacial sand/gravel	700	8E-4	8E-5
	Postglacial silt	800	5E-6	5E-7
Z2	Peat (only on land, rare, above **Z1**)		3.E-7	3E-7
Z3	Glaciofluvial deposit (rare)		2.E-4	2E-4
Z4	Glacial and postglacial clay		2.E-8	2E-8
Z5	Fine till	10	5E-7	5E-8
	Coarse till	9	8E-6	8E-7
	Till (Eckarfjärden drainage area)	20	2E-5	8E-7
Z6	Uppermost 0.5 m of HRD		2.E-6	2E-6
Z7	Uppermost 4 m of HRD (if Flag = 2 in **Z1**)[1]		1.E-7	1E-7

1 Layer Z7 does not exist in the Regolith model. It was created in the flow modelling conducted with MKE SHE to handle data transfer issues between different flow models in SDM-Site, see Bosson et al. (2008) (SF: R-08-09).

It is assumed in the work reported here that the calibrated effective parameters for HSD on land are also valid for offshore, marine sediments at SFR. That is, the Quaternary deposits above, respectively, below the current sea level are assigned similar hydraulic properties in the flow modelling. However, it is noted that the offshore sediments have not been exposed to landscape dynamic processes that occur on land; these include erosion (shoreline wave erosion and topographical surface runoff), biological activity (such as increased porosity from wormholes and tree roots), and frost heaving.

3.1.1 HSD implementation in DarcyTools

In order to accomplish a realistic numerical implementation of the regolith in the flow model, the part of the computational grid covering HSD was refined (Table 4-1). In spite of the refinement, geometric inconsistencies arise between the Cartesian grid and the regolith layers (Table 3-1). Therefore, the uppermost HSD layer (Z1, Z2, or L1) and the uppermost HRD layer (Z6) were implemented as *contiguous layers*; all grid cells intersected by either of these two layers were *directly* assigned

the conductivity from Table 3-1. Any grid cell located between these two contiguous layers was assigned an upscaled conductivity value weighted by on the fraction of contribution from intersecting Regolith layers. The flow model is set up in a rotated coordinate system (Section 4.3) and therefore the grid cell coordinates required back-rotation in order to determine the intersection between grid cells and the Regolith layers. HSD conductivity upscaling was performed differently in the vertical, respectively, horizontal directions.

The arithmetic mean of different regolith layers was applied to upscale HSD conductivity in the horizontal direction:

$$K_H^{cell} = \frac{\Sigma \left(b\, K_H\right)^i}{\Sigma\, b^i}, \qquad (3\text{-}1)$$

where K_H^{cell} is the upscaled horizontal conductivity of a HSD grid cell, K_H^i is the horizontal conductivity of Regolith layer *i*, and b^i is the partial thickness of Regolith layer *i* intersecting the cell.

The harmonic mean of different regolith layers was applied to upscale HSD conductivity in the vertical direction:

$$K_Z^{cell} = \frac{\sum b^i}{\sum\left(b^i \big/ K_Z^i\right)}, \qquad (3\text{-}2)$$

where K_Z^{cell} is the upscaled vertical conductivity of a HSD grid cell, K_Z^i is the vertical conductivity of regolith layer *i*, and b^i is the partial thickness of regolith layer *i* intersecting the cell. An example of the HSD implementation in the numerical model is presented in (Figure 3-3).

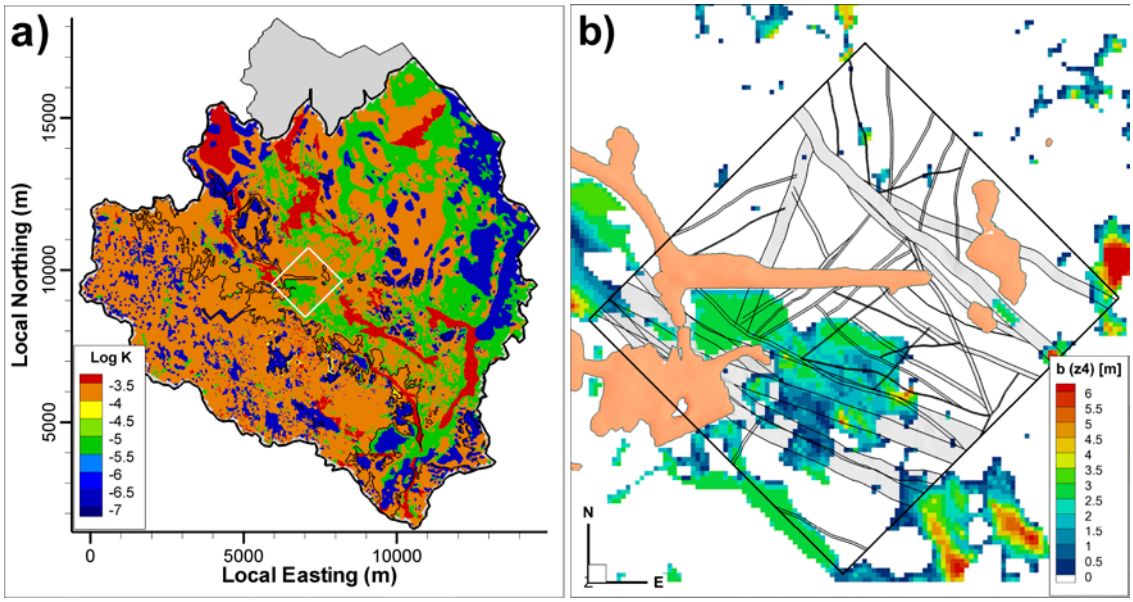

Figure 3-2. *Parameterisation of the upper grid layer in DarcyTools simulations; a) inside the entire flow model domain used and b) glacial clay thickness in the SFR near-field. The upper HSD layer is highly conductive. Vertical cross sections of the SFR near-field are shown in Figure 3-3.*

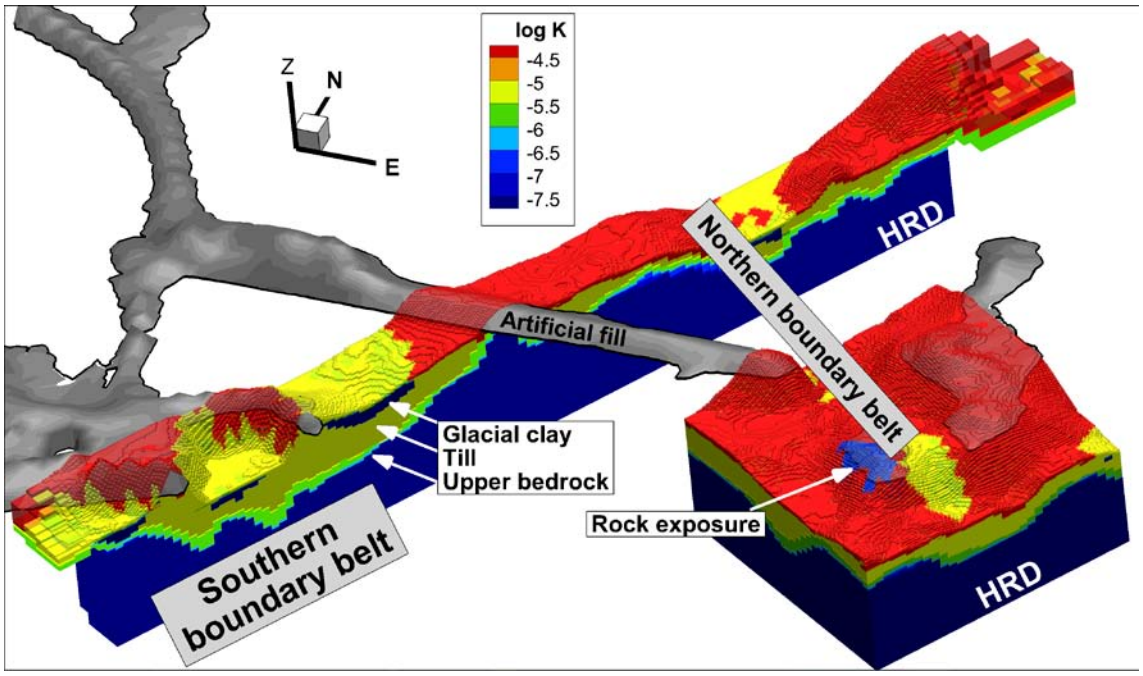

Figure 3-3. *HSD parameterisation in DarcyTools simulations in the SFR near-field. With the exception of occurrences of Glacial clay ($K_z = 2 \cdot 10^{-8}$ m/s), the HSD conductivity is considerably higher than that of the underlying bedrock ($K_{HRD} = 6.5 \cdot 10^{-9}$ m/s). HCD conductivity is not included in the figure. Vertical exaggeration factor = 10.*

3.2 Hydraulic Conductor Domain (HCD)

3.2.1 Merging the geological models for Forsmark-Lens and Forsmark-SFR

All HCDs outside the SFR Regional domain are taken directly from SDM-Site Forsmark. Inside the SFR Regional domain the HCD geometry is taken from the SFR Geological model v. 1.0 (Curtis et al. 2011). These are parameterised based on hydraulic borehole data inside deformation zone intercepts, following the methodology described in Follin (2008). Due to different versions of underlying lineament data in the Forsmark and SFR geological models, minor "gaps" may occur at the interface between the two models. In order to ensure hydraulic continuity in the HCDs across the boundary between the two model domains, the gaps are overcome by so-called "bridges". The purpose is to circumvent geometric inconsistencies that are due to different model objectives and versions. (It should be noted, however, that a few gaps were intentionally left without using "bridges", since inclusion of too large bridges may, in itself, introduce a hydraulic model artefact along the SFR Regional model domain.)

Six deformation zones inside the SFR Regional domain terminate at the model boundary and lack geometric definitions outside the SFR Regional domain: ZFMNNW3113, ZFMNNW0999, ZFMNS3154, ZFMNNE3266, ZFMNNE3265, and ZFMNNE3264. These zones are of low geological confidence, but are included in the hydrogeological model for the sake of safety assessment modelling at later stages of land-lift. It is recommended that the six zones are extended according to lineament data in the forthcoming safety assessment.

3.2.2 Data-based HCD parameterisation

The SFR data set is composed of data from two periods:

- historic data (collected during the construction of SFR 1980 to 1987), and
- recent data set from the SFR extension site investigations (see Öhman and Follin 2010a, respectively, Öhman et al. 2012).

The two data sets are of different quality and cover different parts of the model domain; the old data set covers the near-field of the existing SFR, while the new data set cover the area of the planned extension. The old data set is dominated by short-term hydraulic tests performed over an interval length of 3 m and are therefore expected to include compartmentalised fracture transmissivity, as well as, effects of short-circuited flow to the borehole. Thus, HCD transmissivity in the SFR near-field is expected to be overestimated, as it is parameterised based on old data with lower quality. The more recent data set from the Forsmark and SFR extension investigations, are based on PFL-f and HTHB data; these data reflect sustained flow after several days pumping with the entire borehole acting as a line sink (and effectively eliminates compartmentalised transmissivity and the risk of short-circuiting).

Some of the HCDs inside the SFR Regional domain were included in SDM-Site Forsmark (Follin 2008). However, no SFR-specific data were used at the time; instead the transmissivities of these HCDs were pooled from data inside the Forsmark Site (see Table 3-2). The Forsmark and SFR sites have a common geological history, but differ in some aspects; most notably the tectonic lens and the highly transmissive upper bedrock (Curtis et al. 2011). It is nevertheless of interest to put the current HCD parameterisation into context of the inflow-calibrated parameterisation of Holmén and Stigsson (2001), as well as, the hydraulic-databased parameterisation in SDM-Site Forsmark (Follin 2008) (Table 3-2). The HCD parameterisation reported in Table 3-2 was established in three phases, referred to as the *initial*, *revised* and *final* parameterisation (Table A-1).

3.2.3 HCD depth trend

Data analyses indicate decreasing transmissivity with depth, both outside and inside deformation zones (Öhman et al. 2012). However, in the light of heterogeneity, sample size and data elevation range, it was concluded that a site-specific depth-dependency relationship in HCD transmissivity cannot be determined for the SFR data set with confidence. On the other hand, a depth-dependency concept and relationship has been developed for HCD transmissivity for the nearby Forsmark Site (e.g. Follin et al. 2007b and Follin 2008). The Forsmark Site has characteristics that differ from SFR; its depth trend may be accentuated due to the low transmissivity at depth, inside the Tectonic lens, and excessively high transmissivity in the shallow bedrock.

Although it is conceptually more appealing to express the trends in terms of depth below ground, it is more practical to use elevation, z. The topography within the model domain is shallow (ranging from 7 to -16 m elevation), so the difference is small. Based on observations made in maximum HCD transmissivity in Forsmark as a function of depth, the depth dependency in HCD transmissivity is assumed to follow an exponential model:

$$T(z) = T_0 10^{z/k} \qquad (3\text{-}3)$$

where $T(z)$ is transmissivity at elevation z (m elevation), T_0 is the expected transmissivity at zero elevation, and k is the depth interval over which transmissivity decreases one order of magnitude. The value of $T_0 = T(0)$ can be calculated by inserting a measured value $T(z')$ at its reference elevation z'.

$$T_0 = T(z')10^{-z'/k} \qquad (3\text{-}4)$$

Details on the interpretation of different intercepts, T_0, are described in Appendix A (see further details in Öhman et al. 2012). Effective HCD transmissivity values, $T_{eff}(0)$, are determined for each of the 40 HCDs, as defined at the reference level 0 m elevation according to the principles established during Site Investigation Forsmark (Follin et al. 2007b). In cases where hydraulic data are available at several intercepts of a zone, $T_{eff}(0)$ is calculated as the geometric mean of all depth-adjusted intercepts (i.e. individual T_0 values presented in Table A-3). If no intercepts are available, $T_{eff}(0)$ is *either* based on pooled T_0 for a group of HCDs with similar orientation, *or* taken from SDM-Site Forsmark (see comments in Table 3-2).

Table 3-2. Final parameterisation of deformation zones inside the SFR Regional model domain (cf. Table A-1).

Deformation zone	Hydraulic width[1)]	No. intcps[2)]	No. cond. points[6)]	$T_{eff}(0)$[7)] (m^2/s)	log $T_{eff}(0)$	Standard deviation σ(log $T_{eff}(0)$)[5)]	Forsmark SDM, log $T_{eff}(0)$	SFR 2001[4)], log T	Calculation of $T_{eff}(0)$
ZFM871	11.3	19 (4)	15	Not defined		0.81	–3.6	–5.8	A special depth-trend relations for transmissivity is fitted based on all 19 intercepts (5 of these are not included in the geological model; see Figure 3-4), log T = z/30 –0.699 (bounded by –7 ≤ log $T_{eff}(0)$ ≤ –3.699).
ZFMA1	40.0	None	None	1.59E-5	–4.8	(0.55)	–4.8		Taken from SDM-Site Forsmark
ZFMB10	7.2	None	None	1.59E-5	–4.8	(0.55)			Aassumed equal to ZFMA1 (i.e. taken from SDM-Site Forsmark)
ZFMENE3115	4.8	3	3	3.50E-7	–6.5	0.91			Taken as average from all 3 intercepts.
ZFMENE3135	3.6	None	None	1.92E-7	–6.7	(0.55)			Taken as pooled average of the NNE to ENE set (only based on new data)
ZFMENE3151	3.6	None	None	1.92E-7	–6.7	(0.55)			Taken as pooled average of the NNE to ENE set (only based on new data)
ZFMENE8031	3.6	None	None	1.92E-7	–6.7	(0.55)			Taken as pooled average of the NNE to ENE set (only based on new data)
ZFMENE8034	7.2	None	None	1.92E-7	–6.7	(0.55)			Taken as pooled average of the NNE to ENE set (only based on new data)
ZFMNE0870	12.0	8 (5)	7	5.11E-7	–6.3	0.46	–7.4	–7.7	Taken as average from all 8 intercepts. Evaluated transmissivity at intercepts are exaggerated by unfavourable borehole orientations, causing long intercepts.
ZFMNE3112	7.4	4	4	2.67E-7	–6.6	0.62			Taken as average from all 4 intercepts.
ZFMNE3118	6.2	3 (2)	3 (1)	2.38E-7	–6.6	0.29			Taken as average of all 3 intercepts, weighted by low-transmissive tunnel intercept[3)].
ZFMNE3134	3.6	None	None	1.92E-7	–6.7	(0.55)			Pooled average of the NNE to ENE set (only based on new data)
ZFMNE3137	5.0	4	4	5.48E-8	–7.3	0.30			Taken as average from all 4 intercepts.
ZFMNNE0725	12.0	None	None	1.11E-4	–4.0	(0.55)	–4.0		Taken from SDM-Site Forsmark
ZFMNNE0869	41.7	4	4	2.72E-5	–4.6	0.28	–6.1	–4.7	Taken as average from all 4 intercepts
ZFMNNE2308	15.0	None	None	8.26E-7	–6.1	(0.55)	–6.1		Taken from SDM-Site Forsmark
ZFMNNE3130	3.6	None	None	1.92E-7	–6.7	(0.55)			Taken as pooled average of the NNE to ENE set (only based on new data)
ZFMNNE3264	7.2	None	None	1.92E-7	–6.7	(0.55)			Taken as pooled average of the NNE to ENE set (only based on new data)
ZFMNNE3265	7.2	None	None	1.92E-7	–6.7	(0.55)			Taken as pooled average of the NNE to ENE set (only based on new data)
ZFMNNE3266	7.2	None	None	1.92E-7	–6.7	(0.55)			Taken as pooled average of the NNE to ENE set (only based on new data)
ZFMNNW0999	3.6	0 (1)	None	1.76E-8	–7.8	(0.55)			Rejected intercept. Value taken from pooled average of NNW group in SDM-Site Forsmark
ZFMNNW1034	13.7	3	3	3.74E-5	–4.4	0.27			Taken as average from all 3 intercepts.
ZFMNNW1209	15.8	2	2 (4)	1.28E-6	–5.9	(0.55)	–7.8	–5.7	Taken as average from both 2 intercepts. The zone is interpreted as highly heterogeneous, and therefore the zone is conditioned at its intersections with the four disposal facilities.
ZFMNNW3113	3.6	None	None	1.76E-8	–7.8	(0.55)			Taken from SDM-Site Forsmark, pooled average of NNW group
ZFMNS3154	7.2	None	None	3.74E-5	–4.4	(0.55)			Assumed similar to ZFMNNW1034, based on location and orientation.
ZFMNW0002	50.0	1 (2)	1	2.45E-5	–4.6	(0.55)	–4.6		Rejected intercept. Value taken from SDM-Site Forsmark

Deformation zone	Hydraulic width[1)]	No. intcps[2)]	No. cond. points[6)]	$T_{eff}(0)$[7)] (m^2/s)	log $T_{eff}(0)$	Standard deviation $\sigma(\log T_{eff}(0))$ [5)]	Forsmark SDM, log $T_{eff}(0)$	SFR 2001[4)], log T	Calculation of $T_{eff}(0)$
ZFMNW0805A	37.6	6 (2)	6	1.83E-5	–4.7	0.55	–4.6	–5.5	Taken as average of all 6 intercepts.
ZFMNW0805B	21.7	7 (1)	7 (2)	3.40E-6	–5.5	0.48			Taken as average of 7 intercepts and 2 low-transmissive tunnel intercepts[3)].
ZFMWNW0001	108.0	3 (9)	3	1.32E-4	–3.9	0.56	–4.6	–3.3	Taken as average from 3 intercepts: KFR71, HFM34, and KFM11A render $T_{eff}(0) = 1.3\cdot10^{-3}$ m^2/s or log $T_{eff}(0) = –2.9$. The value was lowered one order of magnitude as a result of flow simulations.
ZFMWNW0813	72.7	1	1 (1)	1.16E-6	–5.9	(0.55)	–7.1		KFM11A, weighted by low-transmissive tunnel intercept[3)]
ZFMWNW0835	15.1	1	2	6.30E-6	–5.2	0.71	–7.1		Taken as average of the 2 intercepts in KFR27
ZFMWNW0836	36.0	0 (2)	None	7.92E-8	–7.1	(0.55)	–7.1		Two rejected intercepts. Value taken from SDM-Site Forsmark
ZFMWNW1035	10.8	2 (2)	4	1.08E-5	–5.0	0.64			Only two intercepts used: HFM35, HFR105. This renders $T_{eff}(0) = 1.1\cdot10^{-4}$ m^2/s or log $T_{eff}(0) = –4.0$. The value was lowered one order of magnitude as a result of flow simulations.
ZFMWNW1056	10.0	None	None	7.92E-8	–7.1	(0.55)	–7.1		Taken from SDM-Site Forsmark
ZFMWNW3259	49.0	1	1 (1)	5.18E-6	–5.3	(0.55)			KFM11A, weighted by low-transmissive tunnel intercept[3)]
ZFMWNW3262	1.4	2	2	2.80E-5	–4.6	(0.55)			Average of both intercepts
ZFMWNW3267	12.3	2	2	2.13E-7	–6.7	(0.55)			Average of both intercepts.
ZFMWNW3268	3.6	None	None	1.44E-6	–5.8	(0.55)			Taken as pooled average of the WNW to NW set (only based on new data).
ZFMWNW8042	4.3	1	1	1.05E-6	–6.0	(0.55)			Single intercept used. The zone is well-supported by sub-parallel PFL-f data.
ZFMWNW8043	7.2	None	None	3.06E-7	–6.5	(0.55)			Taken as pooled average of the WNW to NW set (only based on new data).

1) Average hydraulic thickness calculated as the average true thickness (intersection-angle compensated) of all intercepts. For HCDs without intercepts the hydraulic width is taken as 72% of the geological envelope, based on pooling of HCDs that have intercepts. For HCDs that exist inside SDM-Site Forsmark and where no additional information has been gained from the SFR investigations, the thickness is taken directly from SDM-Site Forsmark.

2) Number of intercepts with hydraulic data that are judged representative for the HCD. The number in brackets indicate that additional intercepts exist, but that hydraulic data are unavailable, or judged to be misleading due to junction with other deformation zones that may dominate.

3) Intercepts with the SFR tunnel without record grouting of specific fracture inflow are weighted equal to a single borehole intercept. Such low-transmissive tunnel intercepts were assumed equal to the background conductivity used in Holmén and Stigsson (2001) (i.e. the intercept was set to $T = 6.5\cdot10^{-9}$ m/s multiplied by the hydraulic width).

4) Reported transmissivity values in Holmén and Stigsson (2001). These values do not refer to $T_{eff}(0)$, as no depth trend was implemented in the SFR 2001 model. Approximately 0.4 should be added to these log T-values for direct comparison to the T_0-concept (i.e. extrapolated from the SFR depth level).

5) Following the established SKB methodology (Follin 2008), the standard deviation in modelled logarithmic transmissivity values is estimated as $(\log T_{0,max} – \log T_{0,min})/4$ (i.e. assuming that the range in evaluated log $T_{eff}(0)$ corresponds to $\pm2\sigma$). For zones with less than 3 intercepts, the standard deviation is assumed equal to 0.55 (indicated by parentheses) taken from the average of zones with more than 3 intercepts.

6) Number of conditional points for the particular HCD. The number in brackets indicates additional intercepts with the SFR tunnel that have no record of inflow. Low-transmissive tunnel intercepts were set equal to the background conductivity used in Holmén and Stigsson (2001) (i.e. set to $T = 6.5\cdot10^{-9}$ m/s multiplied by the hydraulic width).

7) Calculation of ground-surface transmissivity, $T_{eff}(0)$, is described in the comment field. In principle, determined as geometric mean of available T_0, according to Equation 3-4, see Table A-1 and Table A-3. For zones without hydraulic data support, $T_{eff}(0)$ is based on pooled deformation zone-set statistics, or values from SDM-Site Forsmark. However, $T_{eff}(0)$ is reduced for ZFMWNW1035, ZFMWNW0001, and ZFM871, based on results of Model Exercise M6.

3.2.4 Depth trend in ZFM871

ZFM871, the gently dipping deformation zone below SFR, has several borehole intercepts, which allows a separate depth-trend analysis. It has earlier been described as less transmissive towards the Southeast (Carlsson et al. 1987). With consideration to its dip, this observed trend can equally well be described as a strong depth trend (Öhman and Follin 2010a). The same trend can also be envisaged as declining laterally with distance from the junction of ZFMNNE0869 and ZFMNW0805A. A visual fit was made to all 15 intercepts (black solid line in Figure 3-4a), defined as log T = z/30, with a minimum value of –7 and a maximum value of –3. The trend fitted to borehole intercepts is here referred to as the "revised" parameterisation (black line in Figure 3-4b). Previous parameterisations of ZFM871 are included for reference, indicating a considerably weaker depth-dependency in SDM-Site Forsmark and a constant value in the SFR 2001 model (dashed lines in Figure 3-4a). Four intercepts outside the geologically modelled termination of ZFM871 (grey dots marked as "low confidence" in Figure 3-4a) are included based on hydrogeological indications of its possible extension beyond ZFMNNE0869 and ZFMNW0805B (see Appendix A).

In the geological model, ZFM871 is described by a stepped geometry of lenses with increased fracturing. Hydraulic data, interference tests, and hydrochemistry suggest that ZFM871 is highly heterogeneous, with local channelling and also containing compartmentalised volumes of stagnant water. As part of Model Exercise M6 (Chapter 5), the transmissivity of ZFM871 was reduced to the alternatively fitted trend (brown solid line in Figure 3-4a), which was defined as log T = z/30 – 0.7, with a minimum value of –7 and a maximum value of -3.7. At the interception point with the SFR tunnel (c –140 m elevation), this alternative trend is more similar to the SFR 2001 model.

3.2.5 Local borehole conditioning

The HCD transmissivity, as defined by $T_{eff}(0)$ in Table 3-2, reflect an averaged, large-scale property, as estimated from underlying borehole data. Local information can be honoured by conditioning the HCD transmissivity at borehole intercepts (intercepts listed in Table A-3). The extrapolation distance from a given conditional point cannot be deduced from data, but must be assumed (i.e. over what extent of a deformation zone hydraulic data are representative, and how far away from the intercept it is reasonable to extrapolate data). In SDM-Site Forsmark, the conditional data were extrapolated along the entire deformation zone laterally, but no more than 100 m vertically (Follin 2008).

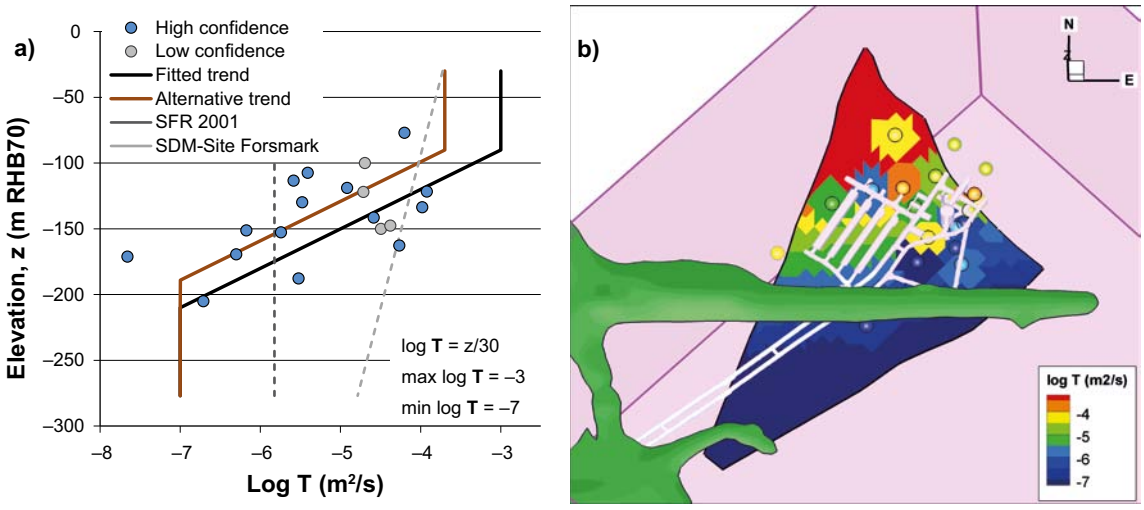

Figure 3-4. *Parameterisation of ZFM871; a) two depth trends fitted to borehole intercept transmissivity and b) "Fitted trend" applied to the triangulated surface representing ZFM871, conditioned at borehole intercepts. Four intercepts outside the geologically modelled termination of ZFM871 (grey dots marked as "low confidence", details in Appendix A) are included in the depth trend.*

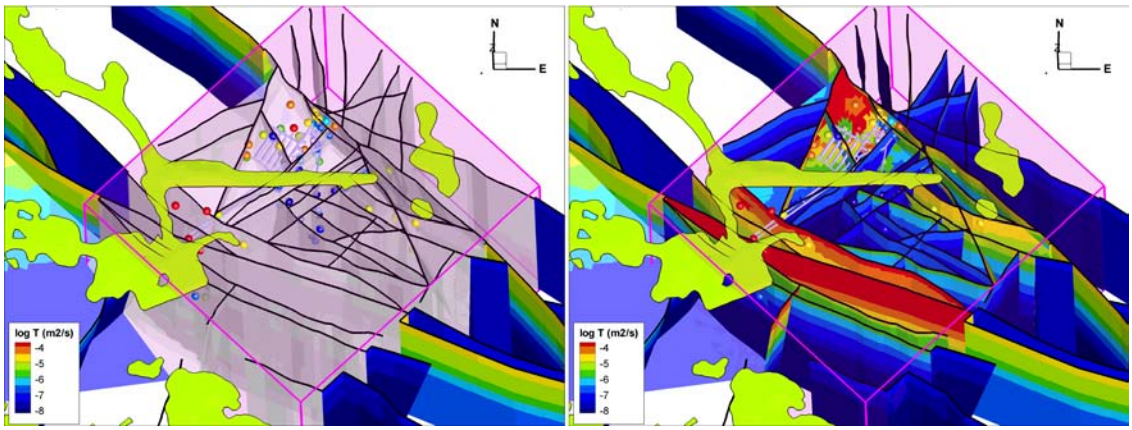

Figure 3-5. *Parameterisation of the SFR HCDs and geometric merging with the surrounding HCDs defined in SDM-Site Forsmark. In some cases, the difference in model versions causes discontinuities over the SFR Regional domain boundary. Such discontinuities are filled-in by so-called "bridges" (left). Conditional borehole intercepts are shown as spheres coloured by transmissivity.*

A variance analysis of ZFM871 intercepts (Öhman and Follin 2010a, Section 5.3.4) suggests that it is reasonable to apply conditioning data within a 50 m radius around the borehole intercept. The reason for choosing ZFM871 is that it has a large data set of closely located borehole intercepts (see Figure 3-4b). The disadvantage of inferring characteristics from ZFM871 is that the zone is not expected to be representative of the general characteristics of deformation zones (i.e. primarily steeply dipping). In lack of contradicting data, it was decided to apply the 50 m conditioning radius as a general rule except in the following cases made:

- ZFMNW0805A/B: conditioning radius = 25 m, in order to reduce transmissivity along junction with ZFM871 (see Model Exercise M5, described in Section 5.6).
- ZFMNNW1209: conditioning radius = 30 m, based on separation distance between SFR disposal tunnels.
- ZFMWNW0835 and ZFMENE3115: conditioning radius = 100 m, as explained below.

Owing to their location in the Central block, the parameterisation of ZFMWNW0835 and ZFMENE3115 is expected to be of particular significance for the planned SFR extension (Figure 3-6). The supporting data for these two structures exhibit an unusual pattern with depth (discussed in Öhman et al. 2012, Section 5.2.3). The shallow intercepts have short lengths and are low-transmissive, while the deep intercepts are comparatively long and high-transmissive (Table 3-3). The difference between shallow and deep intercepts accentuates, if discussed in terms of depth-adjusted transmissivity, T_0, Equation 3-4. The reason for this pattern cannot be resolved from available data; the shallow intercepts agree with the overall interpretation of the Central block, while the deep intercepts are partly the result of sub-parallel intersection, but lack reference data from similar depth levels. In order to honour local data in the Repository depth interval (z = –60 to –200 m elevation), it was considered more realistic to apply the larger conditioning radius, 100 m, for ZFMENE3115 and ZFMWNW0835 (Figure 3-6b).

Table 3-3. Hydraulic data in borehole intercepts of zones ZFMENE3115 and ZFMWNW0835.

Structure	Borehole	Transmissivity (m^2/s)	Log T_0	Elevation range (m)	
				From	To
ZFMENE3115	KFR105	$6.1 \cdot 10^{-9}$	–7.7	–114.61	–115.80
ZFMENE3115	KFR104	$8.6 \cdot 10^{-9}$	–7.6	–117.66	–121.63
ZFMWNW0835	KFR27	$8.1 \cdot 10^{-8}$	–6.6	–105.12	–117.12
ZFMENE3115	KFR102A	$1.7 \cdot 10^{-6}$	–4.1	–379.20	–450.99
ZFMWNW0835	KFR27	$3.2 \cdot 10^{-6}$	–3.8	–319.49	–464.53

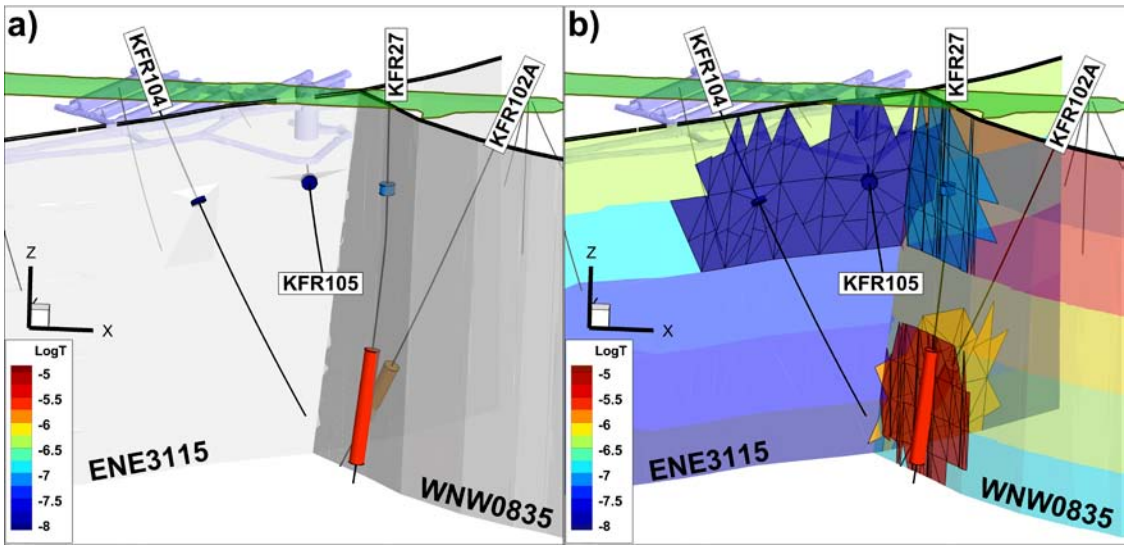

Figure 3-6. *Local conditioning of deformation zones with particular relevance for the planned SFR extension (ZFMENE3115 and ZFMWNW0835); a) deformation-zone intercepts (cylinders) and model geometry (central planes grey shaded), and b) HCD transmissivity (as parameterised according to Table 3-2) and local conditioning (triangulated areas).*

3.3 Hydraulic Rock mass Domain (HRD)

The Hydraulic Rock mass Domain is defined as the less fractured bedrock mass outside (between) deterministically modelled deformation zones (Figure 2-1). The HRD inside the SFR Regional domain has been parameterised by means of a stochastic Discrete Fracture Network model (details in Öhman et al. 2012 summarised in Section 3.3.2; Figure 3-7). DarcyTools is based on a Continuum Porous-Medium (CPM) representation, where the hydraulic properties of a flowing fracture network are approximated by those of a porous medium (Svensson et al. 2010). In order to account for fracture-network characteristics, DarcyTools allows geometric upscaling of fracture properties over grid cells according to which local fracture properties are transferred onto a computational grid. These upscaled properties are referred to as Equivalent Continuous Porous Medium (ECPM) properties (Section 3.3.2).

Depending on the purpose of simulations, the following HRD parameterisations are used in this study:

1) The principle of the perturbation analysis (Model Exercises in Chapter 5) is to use a simplistic model setup to test model sensitivity. For this purpose, a homogeneous, average rock mass conductivity, K_{CPM}, was used (see Section 3.3.1).
2) The HRD is assumed to have a minor contribution in short-term interference tests compared to the uncertainty in storativity; hence the HRD component is not included in the transient simulations (Chapter 6).
3) The fracture-network characteristics are of interest in the flow-path analysis (Chapter 7). For this study, the ECPM concept is used, K_{ECPM} (see Section 3.3.2), where conductivity is upscaled based on a single DFN realisation (shown in Figure 3-7).

3.3.1 Average HRD conductivity, K_{CPM}

The earlier tunnel inflow calibration by Holmén and Stigsson (2001) resulted in an average rock mass conductivity of $K_{CPM} = 6.5 \cdot 10^{-9}$ m/s. This value applies for a model domain which roughly corresponds to the SFR Regional domain (see Odén 2009). The authors also calibrated an average conductivity for the surrounding rock mass outside this model volume, $K_{CPM} = 1.5 \cdot 10^{-8}$ m/s. According to Holmén and Stigsson (2001) there are two reasons why this value is slightly larger: 1) It relates to bedrock located further away from the existing SFR where there is little influence of SFR and therefore flow is more uniform, 2) the structural model is less detailed far from SFR,

implying that minor structures not deterministically modelled are included in average "rock mass" conductivity. It should be noted that these values were calibrated to the 1997 inflow, which was 64% higher than the current inflow (Section 2.7.2).

The calibrated values of Holmén and Stigsson (2001) are taken as a starting point in this study. Inside the SFR Regional domain the average HRD conductivity is assumed to be $K_{CPM} = 6.5 \cdot 10^{-9}$ m/s, while outside SFR Regional domain it is assumed to be $K_{CPM} = 1.5 \cdot 10^{-8}$ m/s. These values are referred to as *default* HRD conductivity values. Various modifications of this average K_{CPM} are tested inside the SFR Regional domain (Model Exercises in Chapter 5); however, outside the default value is always retained. One of these modifications concern the hydraulic anisotropy discussed in Öhman et al. (2012). Effects of HRD anisotropy are tested in Chapter 5, by introducing a scaling factor a (where $a^2 = K_{XY}/K_Z$):

$$K_{XY} = a\, K_{CPM}, \quad K_Z = \frac{K_{CPM}}{a}. \tag{3-5}$$

Moreover, the effect of introducing a conductivity depth trend in HRD is also explored. The HRD depth dependence is assumed to obey the same trend as inferred for HCD, cf. Equation 3-3.

$$K_{CPM}(z) = K_0\, 10^{-z/k}, \tag{3-6}$$

where $k = 232.5$ m, and $K_0 = 1.8 \cdot 10^{-8}$ m/s, which corresponds to $K_{CPM} = 6.5 \cdot 10^{-9}$ m/s at the typical depth of disposal facilities (z = –70 m elevation).

3.3.2 Upscaled HRD conductivity, K_{ECPM}

The appeal of upscaling is that the approximated conductivity field bears hydraulic traits of the fracture network as parameterised from borehole data, for example anisotropic correlation structures and scale-dependent stochastic heterogeneity. Specifically, the heterogeneity depends on the cell size in the computational mesh. An example of ECPM upscaling is provided in Figure 3-8.

It should be noted that *geometric* up-scaling does not always ensure *hydraulic* consistency between the complex heterogeneity of the underlying flowing fracture network and the approximated ECPM. As the ECPM approach is based on an underlying stochastic DFN model, the resulting ECPM properties are also stochastic. The underlying DFN models for the SFR Regional domain and outside the SFR Regional domain, respectively, are described below.

3.3.3 Hydro-DFN inside the SFR Regional domain

The HRD is modelled as a fracture system of open connected fractures, and parameterised by means of a Hydro-DFN (Öhman et al. 2012). The Hydro-DFN provides a stochastic model representation of the flowing fracture network outside deterministically modelled structures (HCD and SBA). The Hydro-DFN is defined by a global orientation model consisting of five fracture sets: steeply dipping EW-, NW, and NE-striking, gently dipping, and sub-horizontal (see details in Öhman and Follin 2010b). A depth trend in hydraulic data has been identified both in the historic and the recent data sets (Öhman and Follin 2010a, b). This depth trend is numerically represented by dividing the bedrock mass into three depth domains:

- Shallow domain (0 to –60 m elevation),
- repository domain (–60 to –200 m elevation) and
- deep domain (below –200 m elevation).

Open fracture intensity, size, and transmissivity are parameterised, for each of the five fracture sets and for each of the three depth domains. To reduce the artificial overrepresentation of connectivity in the flow simulations, only the subset of connected open fractures is translated into ECPM conductivity. The connected fracture network is identified in a geometric analysis, involving the following pre-defined hydraulic structures:

1) Deformation zones, ZFM (Section 3.2),
2) SBA-structures (Section 3.4.3),
3) Unresolved PDZs (Section 3.4.4), and
4) the surrounding DFN (Figure 3-7).

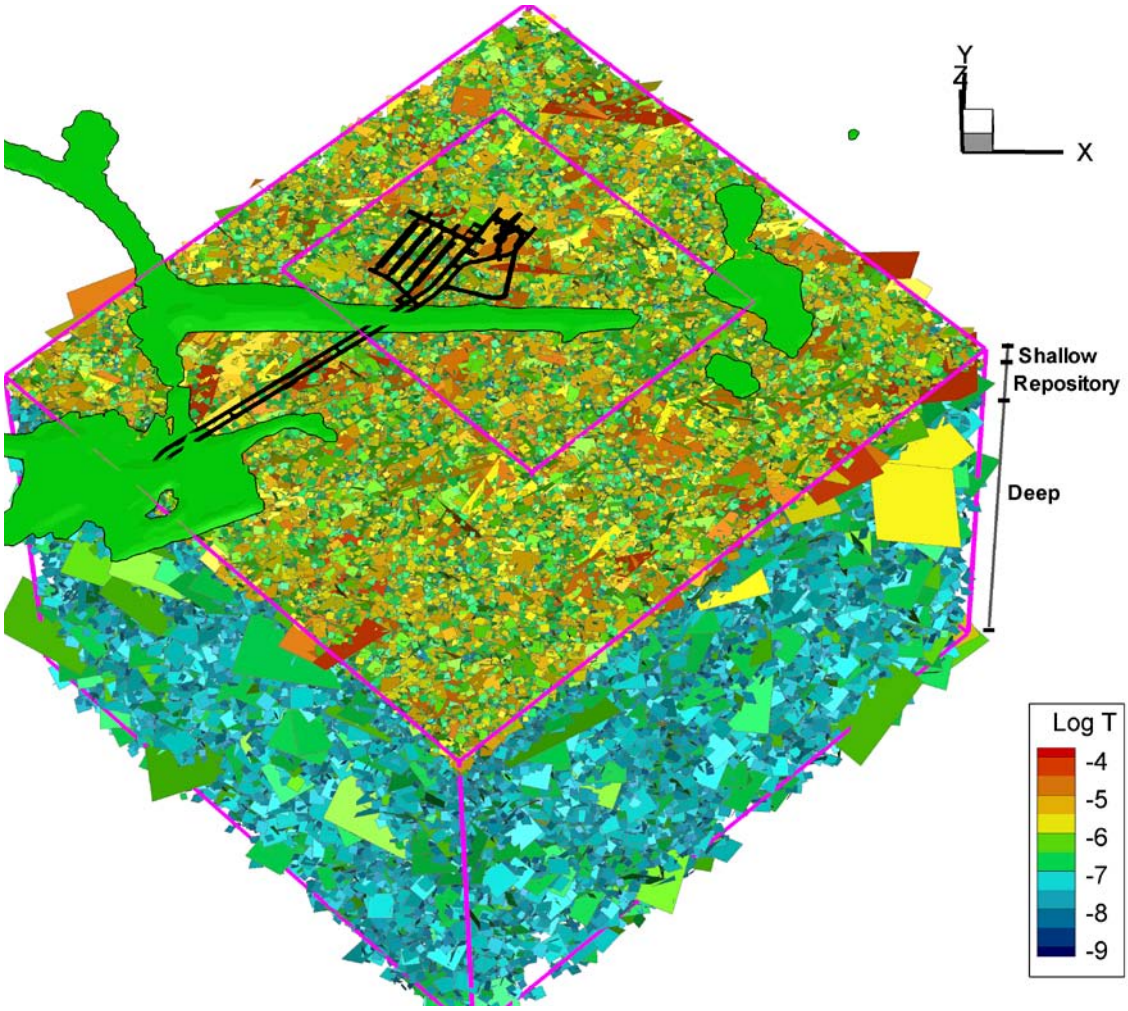

Figure 3-7. *Connected open fracture realisation in the Shallow, Repository, and Deep depth domains. The existing SFR facility is projected onto ground surface (black shade).*

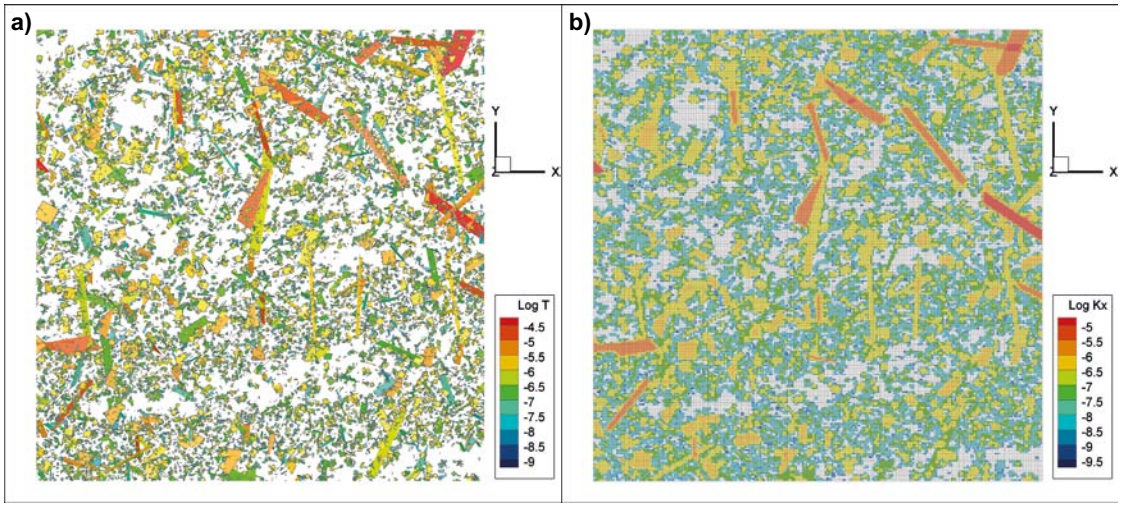

Figure 3-8. *ECPM translation of a horizontal slab at –60 m elevation inside the SFR Regional domain; a) connected fractures intersecting the slab for one realisation, and b) geometrically upscaled conductivity values. The slab has a resolution of 4 m and horizontal extents of 1,000 by 1,000 m^2.*

Fracture connectivity is largely controlled by fracture size parameterisation. Fracture size is assumed to be power-law distributed, defined by a size-scaling exponent, k_r, which is bounded by the interval, $r_0 = 0.038$ m to $r_{max} = 169$ m. Two alternative size models are considered, referred to as Connectivity analysis and Tectonic continuum (Öhman and Follin 2010b); the difference concerns the size of steeply dipping fractures.

Transmissivity, T, is assumed to be directly correlated to fracture radius, r (Follin et al. 2005):

$$T(r) = a\, r^b \qquad (3\text{-}7)$$

The two parameters, a and b, are calibrated by means of simulated borehole exploration of multiple realizations and conditioned, per set and depth domain to honour so-called PFL-f data (high-resolution hydraulic data on continuously flowing fractures). The final parameter setup of Hydro-DFN v. 1.0 is provided in Table 3-4.

3.3.4 Hydro-DFN outside the SFR Regional domain

The HRD parameterisation in model area outside the SFR Regional domain is imported from SDM-Site Forsmark (see Table 1-3). The tectonic lens south of Singö deformation zone (i.e. the low-transmissive, blue-to-green shaded fracture network; Figure 3-9) was parameterised in terms of fracture domains FFM01 to FFM06 (Follin 2008). The Forsmark site investigations were concentrated to the candidate site for the disposal of spent nuclear fuel (i.e. on land, just south of Singö), while considerably less information was available in the northern part of the hydrogeological model area.

Table 3-4. Hydro-DFN model parameterisation for alternative size models.

Set intensity[1]	Orientation[2]				Connectivity analysis Size ($T = a\, r^b$)			Tectonic continuum Size ($T = a\, r^b$)		
Shallow domain (z > -60 m elevation)										
Set	**P_{32}**	**Tr**	**Pl**	**Fisher κ**	**k_r**	**a**	**b**	**k_r**	**a**	**b**
EW	2.32	4.8	13.9	10.1	3.2	2.1E-8	1.3	2.694	1.6E-9	1.25
NW	0.99	233.8	7.2	13.7	3.2	5.3E-8	1.3	2.626	3.3E-9	1.2
NE	1.31	125.4	1.8	13.7	3.45	1.8E-8	1.0	2.778	1.2E-9	1.0
Gd	1.79	339.1	87	7.2	2.79	2.1E-8	1.09	2.79	2.1E-8	1.09
Hz	0.96	127.5	83.7	41.9	2.6	9.8E-8	1.32	2.60	9.8E-8	1.32
Repository domain (-60 ≥ z > -200 m elevation)										
Set	**P_{32}**	**Tr**	**Pl**	**Fisher κ**	**k_r**	**a**	**b**	**k_r**	**a**	**b**
EW	1.44	4.8	13.9	10.1	3.1	2.1E-9	1.1	2.63	7.9E-11	1.4
NW	0.81	233.8	7.2	13.7	3.0	1.1E-8	1.1	2.596	1.3E-9	1.1
NE	1.00	125.4	1.8	13.7	3.3	2.2E-9	1.3	2.752	8.6E-11	1.35
Gd	1.21	339.1	87	7.2	2.72	4.0E-9	0.8	2.72	4.0E-9	0.8
Hz	0.95	127.5	83.7	41.9	2.55	8.5E-10	1.35	2.55	8.5E-10	1.35
Deep domain (-200 ≥ z > -1,100 m elevation)										
Set	**P_{32}**	**Tr**	**Pl**	**Fisher κ**	**k_r**	**a**	**b**	**k_r**	**a**	**b**
EW	1.06	4.8	13.9	10.1	3.2	3.6E-9	1.6	2.585	7.1E-13	2.5
NW	0.67	233.8	7.2	13.7	3.15	4.7E-9	1.13	2.597	1.5E-10	1.31
NE	1.03	125.4	1.8	13.7	3.2	1.9E-9	1.0	2.75	1.6E-10	1.25
Gd	1.49	339.1	87	7.2	2.7	2.7E-10	1.6	2.7	1.4E-10	1.7
Hz	0.75	127.5	83.7	41.9	2.75	1.9E-9	1.15	2.75	1.3E-9	1.25

1) The intensity of open fractures reflects the size interval r_0 to r_{max}. The smallest modelled deterministic zones are on the order 300 m (SFR geological model v.1.0), corresponding to a radius of 169 m. Stochastic open fractures are therefore assumed to have a maximum radius of $r_{max} = 169$ m. The smallest fracture modelled are set equal to borehole radius, $r_0 = 0.038$ m.

2) Global orientation model used for all three depth domains. The same orientation model is used in both the Connectivity analysis and in the Tectonic continuum approach.

Hence, the HRD around SFR and to the north of SFR was conservatively parameterised (i.e. the orange-to-yellow shaded fracture network). The SDM-Site Forsmark model and the SFR hydrogeological models were merged, in a similar way as described for the HCD (Section 3.2). All fractures of the SDM-Site Forsmark model with centre-coordinates located inside the SFR Regional domain were excluded (the SFR Regional domain is indicated by white arrow in Figure 3-9a) and replaced by the DFN of the SFR hydrogeological model (e.g. Figure 3-7).

Unfortunately, the hydrogeological flow domains of the two site-descriptive models are not identical, which leaves the north-western and south-eastern parts of the SFR model domain undefined (pink areas in Figure 3-7a). These areas are of low-confidence due to lack of data support, but due to their remote location, they are assumed to be of lesser importance in simulations. The dilemma was therefore solved by a rather unsophisticated procedure. The approach can be described as follows:

1) Two subareas were assumed to be representative of the undefined areas (blue and grey areas, respectively, in Figure 3-7b).
2) Original fractures with centre-coordinates inside the grey areas are removed (i.e. boundaries are trimmed to avoid artificial overlap).
3) Fractures with centre-coordinates inside the blue areas are duplicated into the grey areas, as indicated by blue arrows.
4) In effect, the result of the procedure (Figure 3-7c) is an extension of the low-transmissive HRD characteristics to the east, while the more conservative parameterisation is extended to the north-west (potential future discharge area from SFR).

3.4 Specifically modelled structures

In the original SKB methodology (Rhén et al. 2003), the bedrock is divided into deterministic deformation zones (HCD) and the less fractured rock between (HRD; Figure 2-1). From a numerical modelling perspective, the classification of hydraulic domains primarily concerns if the structural geometry can be *deterministically* defined, or must be *stochastically* represented. The distinction is normally based on the resolution level of the geological model (i.e. the cut-off size for deterministically modelled structures). A drawback of the stochastic representation is that it is not very realistic for large, high-transmissive features (Section 3.3). The stochastic component in the model can therefore be reduced by providing alternative deterministic geometries for features identified as hydraulically significant in hydrogeological data. This section presents approaches taken to model particular structures falling between the resolution level of the geological model (Curtis et al. 2011) and stochastic fractures represented in the DFN model (Section 3.3).

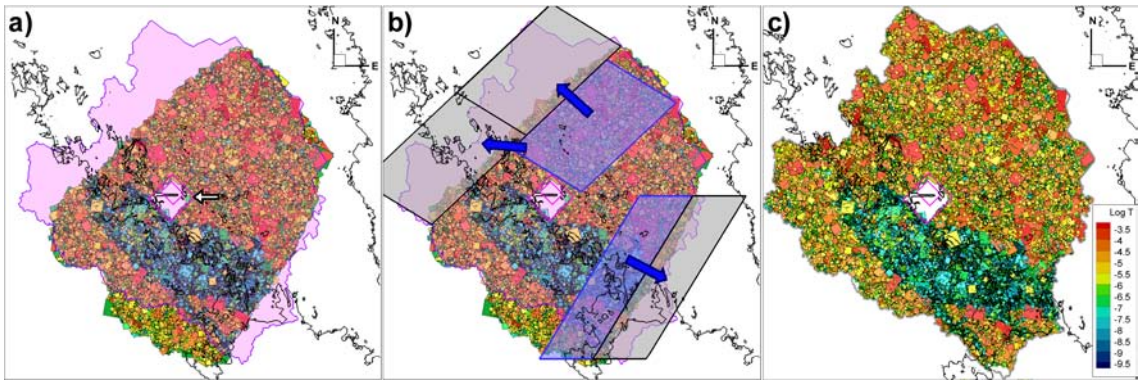

Figure 3-9. *DFN representation outside the SFR Regional domain; a) the SDM-Site Forsmark model domain does not fully cover the SFR hydrogeological domain, b) representative DFN subareas (blue shade) are duplicated into the uncovered areas (grey shade), and c) merged DFN representation.*

The Forsmark Site investigation lead to the introduction of deterministically modelled hydraulic features, referred to as *sheet joints* (Follin 2008). They are assumed to have formed from glacial loading/unloading and stress-relief and not due to tectonic deformation. Therefore, the sheet joints are not necessarily identifiable based on geological character (cf. deformation zone characteristics), in spite of their anomalous hydrogeological character. The significance of sheet joints was emphasized by referring to the superficial bedrock above the tectonic lens as a Shallow Bedrock Aquifer (SBA). To allude the previous experiences in SDM-Forsmark, the acronym SBA was used to denote anomalous hydraulic responses in the conceptual model of SFR (Öhman et al. 2012).

3.4.1 Sheet joints in the Forsmark lens

Field investigations in Forsmark, south of the SFR Regional domain, have demonstrated extraordinary well yields and rapid, large-scale hydraulic responses in the upper c 100 to 150 m of the bedrock (Follin et al. 2007a, b, c). Based on these findings, the shallow bedrock characteristics were interpreted to be hydraulically dominated by horizontal structures, referred to as *sheet joints* (Follin et al. 2007a) (Figure 3-10). Unfortunately, most core boreholes were cased in the uppermost c 100 m. Hence, the interpretation of sheet-joints was based on less detailed hydraulic data (primarily HTHB data from percussion boreholes, which are impeller-flow logging data combined with pumping tests (Follin et al. 2007c)). Owing this circumstance, it was decided to define a simplified geometric representation of sheet joints for numerical modelling purposes. The sheet joints in the Forsmark area were deterministically modelled as three large horizontal planes that undulate with topography and terminate against the southern side of the Singö deformation zone (Figure 3-10a). The sheet joint geometry was defined during an intermediate modelling stage of the SDM-Site Forsmark model (PFM 2.2), and paid little emphasis to the potential existence, or continuation, of structures inside the SFR model domain. This because it was assumed that there was no interference between SDM-Site and the SFR facility based on the results from the interference conducted in HFM33 (Gokall-Norman and Ludvigson 2008, Follin 2008). In the SDM-Forsmark model, the sheet joints cross the SFR tunnels on the southern side of the Singö deformation zone. This assumed model geometry constitutes a potential key component in SFR tunnel inflow modelling and may dominate the hydraulic communication between the Forsmark inland and the SFR model domain. Therefore, the modelled sheet joint/Singö junction is assessed in more detail, based on additional data.

3.4.2 Truncation of the sheet joint structures

The most critical issue in terms of SFR tunnel inflow concerns a geometric intersection between modelled sheet-joints and the SFR access tunnels in the vicinity of the Singö deformation zone (Figure 3-10a). This intercept is an artefact arising from the simplified geometric representation, and it is not supported by detailed tunnel mapping (Christiansson and Bolvede 1987). At the bare minimum, the sheet joint geometry must be revised so as to remove this artificial tunnel intercept.

Furthermore, subsequent to the development of the sheet-joint model a complementary interference test was performed in HFM33 (i.e. during the PFM 2.3 modelling stage) (Gokall-Norman and Ludvigson 2008). This interference test confirmed the primary objective of the test, i.e. to demonstrate a remote hydraulic communication with the Forsmark inland. Also, most remarkably, no responses were found in the nearby boreholes KFM11A, HFM34 and HFM35 (pink boreholes in Figure 3-10). There are two possible interpretations for this: 1) Singö acts as a constant head boundary, and/or 2) the sheet joints are poorly connected across the Singö zone. Both findings hamper the pressure propagation across the Singö zone. Noteworthy, KFM11A also indicates lack of hydraulic connection south of Singö (i.e. the upper part of KFM11A is located on the same side of Singö as the pumped borehole HFM33).

Moreover, flow simulations based on the original definition of the sheet joints (Model Exercises M0 to M5; see explanations in Section 5) cannot reproduce the measured large head decrease data in the Southern boundary belt without causing excessive simulated tunnel inflow. This also indicates that the upstream hydraulic connectivity is overrepresented (i.e. the contact between Singö and sheet joints). Consequently, as part of Model Exercise M6 (see explanations in Section 5), the transmissivity of the sheet joints is reduced in the vicinity of KFM11A and the tunnel intersections (inside the pink cylinder; Figure 3-10). More precisely, all elements of the triangulated mesh falling inside a 400 m radius from the point Northing = 6698449.8, Easting = 1635424.5 are set to $T = 10^{-7}$ m^2/s.

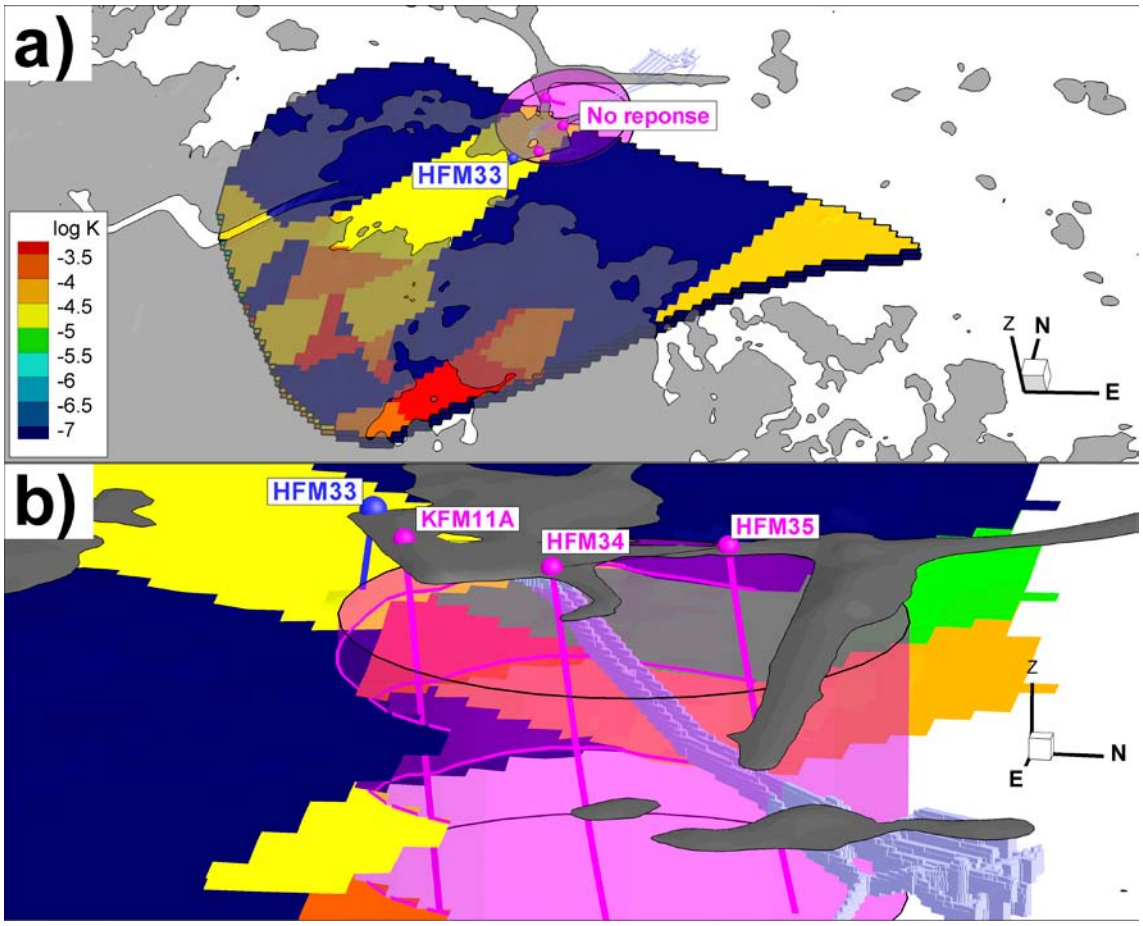

Figure 3-10. *Deterministic sheet joints modelled in SDM-Site Forsmark; a) top view and b) side-view of truncated geometry. Based on lack of responses from interference test in HFM33, the transmissivity of sheet joints is reduced to 10^{-7} m^2/s inside the pink cylinder.*

3.4.3 SBA (Shallow Bedrock Aquifer) structures in the SFR Regional domain

Hydrogeological data analyses indicate presence of sub-horizontal transmissive fractures in the shallow bedrock. Inference of hydraulic responses and cross-borehole data in the SFR model domain lead to the definition of eight deterministic, sub-horizontal structures, which are interpreted as hydraulically significant in uppermost part of the area of the planned SFR extension. In some aspects these structures resemble the Forsmark sheet joints (Section 3.4.1); however, they are of *considerably lesser hydraulic dignity,* and hence it was decided to elude the term "sheet joint".

To emphasize the difference in dignity, yet to allude the SBA annotation in SDM-Site Forsmark, the eight deterministically modelled structures were referred to as SBA1 to SBA8 (Figure 3-11). This does *not* mean that the superficial bedrock at SFR has "aquifer characteristics" outside these structures. The persistence of SBA-structures seems related to the Northern boundary belt and ZFMNNW1034. The existence of such features in the vicinity of the Southern boundary belt is plausible, but unclear.

There are four of key differences between the SBA-structures modelled in SDM-PSU (Forsmark-SFR) and the sheet joints modelled in SDM-Site (Forsmark-Lens):

- **Dignity:** The suggested deterministic SBA-structures at SFR are considerably smaller in terms of size, and of less extraordinary hydraulic nature, transmissivity and hydraulic response.
- **Visual confirmation:** The existence of sheet joints in the SDM-Site Forsmark model has been confirmed during the construction of the nuclear power plants and in the canal to the Baltic Sea. Only smaller horizontal structures were observed during construction of SFR, and most are *hydraulically insignificant*. Only two of these observed horizontal structures required substantial grouting (one of them leading to the definition of SBA8).

- **Data support and geometric representation:** The Forsmark sheet joints and the SBA-structures at SFR have different types of data support (level of resolution versus spatial coverage), as well as, different significance in safety assessment (owing to target depths). Consequently, their geometric representations are based on different methodologies. The modelled SBA-structures at SFR have more *detailed* support near borehole intercepts, but their areal extent outside borehole coverage is considerably more uncertain. The SBA geometry was modelled in a RVS-frame work, based on informed judgement of borehole intercepts and termination against steeply dipping zones.

It should be pointed out that in reality each modelled plane is believed to represent a network of connected sub-horizontal fractures, rather than a single fracture and that the extensions of the features outside the borehole intercepts are unknown. Note also that these structures are not expected to form perfect horizontal planes, but to bend and undulate, possibly related to topography. Also, the deterministically modelled structures are probably only a sub-set of the total number of horizontal hydraulic conductors in the model area, as only features intercepted by boreholes are detected. It cannot be excluded that the modelled structures, or other similar, should also occupy the southern uncharted part of the SFR model domain.

3.4.4 Unresolved Possible Deformation Zones

The starting point of the geological model (Curtis et al. 2011) is to define borehole intervals with "deformation-zone like characteristics", referred to as Possible Deformation Zones (PDZ), according to the established methodology Single Hole Interpretation (SHI). These PDZs are then linked to surface lineaments to form the deterministic structures of the geological model (Figure 3-5; Table 3-2). However, not all PDZs can be linked to lineaments and therefore lack deterministic definition in the geological model. In total, 31 PDZs were not included in the geological model; these remaining PDZs are referred to as "Unresolved PDZs".

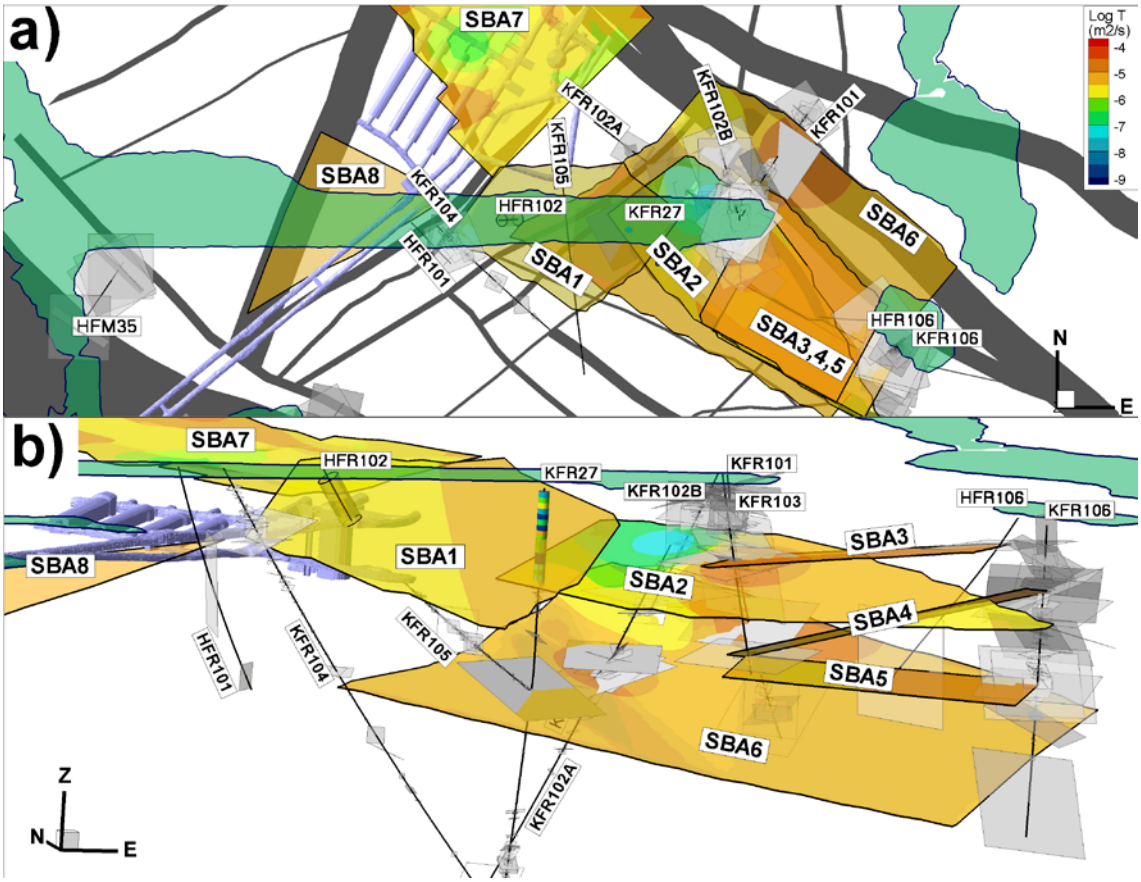

Figure 3-11. *Modelled SBA (Shallow Bedrock Aquifer) structures inside the SFR Regional domain; a) top view and b) side view from southwest. The structures are coloured by transmissivity interpolated from the transmissivity of the borehole intercepts.*

These Unresolved PDZs are the residue from the geological modelling, and therefore comprises a highly non-uniform data population. Firstly, these PDZs have varying confidence in existence (e.g. many have a low to medium confidence in existence). Secondly, they are interpreted to be of highly variable hydraulic significance in the hydrogeological modelling. Thirdly, the supporting data is of variable quality, which complicates modelling (PDZs in the historic data set lack orientation and some lack hydraulic data). It was therefore decided to screen the data set and develop a model for the subset of the Unresolved PDZs interpreted as the most hydraulically significant (Table 3-5; details in Öhman et al. (2012). The Unresolved PDZs that are not explicitly treated in this model are 1) deterministically interpreted as SBA-structures or splays of deformation zones, or 2) low-confidence and/or low-transmissive and is considered to be covered by the stochastic components of the hydrogeological model.

A stochastic model is defined based on the seven Unresolved PDZs listed in Table 3-5. The stochastic model has an assumed spatial inference to geological structures (Figure 3-12; a wedge between ZFMNNW1034 and the Northern boundary belt, as well as, ZFMWNW1035). The size distribution of Unresolved PDZs is estimated probabilistically, based on the following rules:

1) The feature has a maximum side-length of 300 m, as well as, a maximum ground-surface trace length equal to the resolution of the geological model (300 m).
2) The feature must *honour* its borehole intercept specified in Table 3-5.
3) The feature must have *direct contact* to the wedge between ZFMNNW1034 and the Northern boundary belt or to ZFMWNW1035 (Figure 3-12).
4) The feature must not violate information on *absence* of PDZs in adjacent boreholes.

The generation procedure can then be described as follows:

1) Each of the Unresolved PDZs in Table 3-5 are generated following a Poissonian distribution, but only those in direct contact to the wedge between ZFMNNW1034 and the Northern boundary belt or to ZFMWNW1035 are retained.
2) The generation stops when a retained feature is intersected by a borehole. The intersected feature is conditioned to its borehole intercept (i.e. it is replace by a valid realization, taken from the preceding size distribution estimation).

In summary, each realization of Unresolved PDZs honour the seven intercepts in Table 3-5 (Figure 3-12a), but also cover areas outside borehole coverage according to the assumed spatial inference to geological structures (Figure 3-12b).

Table 3-5. Modelled Unresolved PDZs (see also Figure 3-12a).

	Borehole length (m)		Elevation (m, elevation)		SHI conf. [1]	Orientation (Strike/Dip)		Dominant PFL-f	
	From	To	From	To		Geologic	PFL-f[2]	Log T	Set
KFR102B_DZ1	67	70	–51.9	–54.3	**3**	(098/81)	(95/79)	–6.1	EW
KFR102B_DZ3	149.5	150.5	–118.4	–119.2	**2**	(229/08)	(160/4)	–5.3	Hz
KFR103_DZ1	24.5	26.5	–17.5	–19.1	**3**	–	(336/29)	–6.6	Gd
KFR106_DZ1	15	20	–13.1	–17.8	**3**	(216/90)	(49/83)	–6.3	NE
KFR106_DZ2	36.5	52	–33.2	–47.8	2	–	(30/23)	–5.8	Hz
KFR106_DZ4	84.5	86	–78.3	–79.7	**3**	(181/14)	(125/7)	–4.8	Hz
KFR106_DZ5	100.5	101	–93.3	–93.7	**3**	(012/12)	(344/16)	–4.8	Hz

1) SHI confidence level: 1= low, 2 = medium, 3 = high.
2) Orientation estimated from PFL-f data.

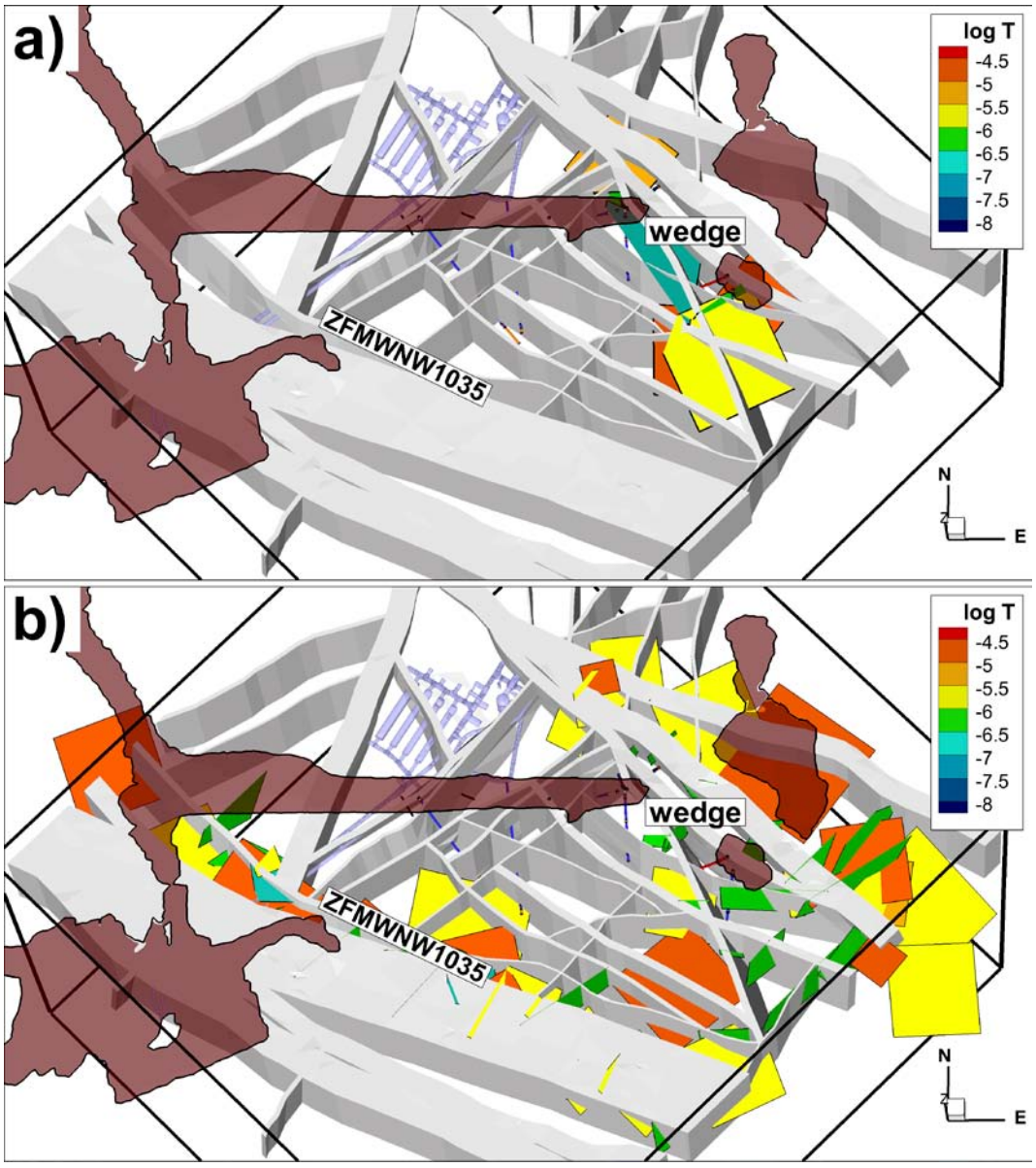

Figure 3-12. *Realisation of Unresolved PDZs; a) the seven structures conditioned at borehole intercepts (Table 3-5), and b) stochastic structures outside borehole coverage.*

4 Numerical model setup in DarcyTools

4.1 Boundary conditions of the flow model domain

Upper boundary

The topographical data are available as a DEM (Digital Elevation Model) with a horizontal spatial resolution of 20 m and where the seal level is the datum plane. The upper boundary of the flow model mesh was discretized with a minimum resolution in the vertical direction ranging from 1.0 to 0.25 m (Table 4-1). All cells located entirely above the DEM surface were removed. Sea-floor cells, located below the sea-level, are assigned a constant head equal to zero (i.e. neglecting the density effects of the overburden the Baltic Sea; Section 2.6). Land cells were assigned a prescribed head corresponding to a groundwater-table depth of 0.5 m below ground surface. More precisely, land cells are identified as cells where the uppermost grid layer intersect the DEM surface above the sea-level; these were prescribed head equal to z* – 0.5 m, where z* denotes the local ground-surface elevation according to the DEM. A pressure discontinuity near the shoreline was circumvented by setting the head equal to 0.0 m where $z < 0.5$ m.

4.1.1 Vertical boundaries

The flow model area is defined from surface-water divides of catchment areas and a deep seafloor trench (the so-called Gräsö-rännan; Figure 1-3). The surface-water divides are interpreted from topographical data, and are assumed to be valid also as divides for groundwater flow at depth. The parts of the model area that are currently below sea have been chosen with respect to future topographical divides.

The northern part of the flow domain (grey shaded area in Figure 4-1b) is important for free-groundwater surface modelling at 5000 AD (Öhman 2010). This downstream sub-catchment is not considered to be important for simulating the present state, and therefore it was not included in the current simulations.

No-flow boundaries were assigned to all vertical sides of the flow model.

4.1.2 Bottom boundary

The hydrogeological model volume extends down to –1,100 m elevation. No-flow was assigned to the bottom layer of the grid, based on assumptions of low conductivity at depth resulting in negligible flow.

4.1.3 Tunnels

Grid cells intersected by the SFR tunnel CAD file are identified as tunnel walls (see Figure 2-2). For open tunnel simulations, tunnel-wall grid cells are prescribed atmospheric pressure (i.e. head equal to the elevation of the grid cell centre). Grid cells located entirely inside the tunnel have no role in the flow solution, and are therefore removed. Tunnel-wall grid cells are cubic and have a side length of 2.0 m and are assigned a local skin resistance, referred to as K_{skin} (see Section 2.5).

In flow-field analyses for re-saturated tunnel conditions (Chapter 7), the prescribed-head condition and the skin are removed from tunnel-wall cells. The skin is replaced by a pessimistic high conductivity value (10^{-5} m/s; see Holmén and Stigsson 2001 and Odén 2009). Furthermore, all grid cells of the tunnel interior are restored to allow flow through the underground facility.

4.2 Discretisation in DarcyTools

The discretisation of the computational grid is specified as horizontal side-length of grid cells, ΔL_H, and vertical side-length of grid cells, ΔL_Z (Table 4-1). The discretisation can be summarised in the following steps:

1) Grid cells located outside the model domain are removed (note that also grid cells in the grey-shaded area in Figure 4-1 were removed, as it was primarily identified as important for simulating future stages of land lift, see Öhman (2010)).
2) Grid cells above the ground surface, as defined by the DEM (Figure 1-3), are removed.
3) Grid cells located above the bedrock surface (as well as grid cells intersected by the bedrock surface) are refined and identified as HSD (Table 4-1).
4) Grid cells in the area covered by sheet joints are refined to avoid short-circuiting the three deterministically modelled planes (Section 3.4.1).
5) Grid cells inside the SFR Regional domain (Figure 1-2) are refined to a maximum cell side-length of 16 m. Note that the HSD inside the SFR Regional domain has a vertical maximum cell side-length of 0.25 m.
6) Grid cells in the vicinity of the SFR tunnel is refined to a maximum side length of 2 m. Grid cells entirely located inside the tunnel are removed. Grid cells intersected by the tunnel wall are identified as a constant head boundary (i.e. atmospheric pressure, hydraulic head H = z), and also identified as different inflow areas (using "simulation area codes", see Table 4-3 and Figure 4-3). Tunnel wall cells are also classified as different areas of skin factors (Figure 5-1).
7) In the later modelling stages with stochastic SBA-structures, the upper 200 m of the SFR Regional domain was refined by maximum side-lengths of 4.0 m.

4.3 Orientation of computational mesh in DarcyTools

DarcyTools uses a fixed Cartesian computational grid, which in the present modelling study is aligned with the geographical axes (north, east and elevation). This is practical, as it allows addressing grid-cells by direction, for example: "east of a specified coordinate", or "below a certain level", etc. However, in other situations it may be preferable if the computational grid is aligned parallel to the dominating groundwater flow direction, in order to avoid artificially forcing the modelled flow into a zigzag pattern between grid cells. For example, in tunnel-flow calculations an unfavourably oriented computational mesh risks double-counting flow over the tunnel wall, see discussion in Odén (2009). Another example is artificial transversal spreading in particle tracking (i.e. in the DarcyTools cell-jump method), if the mesh is unfavourably orientated in relation to the regional hydraulic gradient.

Table 4-1. Grid construction.

Hydraulic domain	Location	Max. cell side length ΔL_H (m)	Max. cell side length ΔL_Z (m)
HRD, HCD	Outside SFR Regional domain	128	128
PFM Sheet joints	Outside SFR Regional domain	64	16
HSD	Outside SFR Regional domain	32	1
HRD, HCD	Inside SFR Regional domain	16	16
HSD	Inside SFR Regional domain	4	0.25
SFR tunnel	Inside SFR Regional domain	2	2
Shallow bedrock[1)]	Inside SFR Regional domain	8	8

1) Only applied in Model excises M6, and M7, as well as in flow-field analyses (Chapter 7) to honour the anisotropy of stochastic fractures. Only applied to z > –200 m elevation.

SFR was intentionally constructed *parallel* to the future flow field, and *orthogonal* to the major principal stress component as well as the dominant geological structures, i.e. the Southern and Northern boundary belts. Thus, a method to implement grid rotation in DarcyTools was developed in order to improve the performance of flow simulations of SFR (Öhman 2010). The method used here can be summarised as follows:

1) all input geometries (see complete list in Appendix D) are rotated into a local coordinate system [x´, y´], using Equation 4-1. In this rotated system, x´ is almost parallel to the Singö deformation zone (and the shoreline), while y´ is parallel to the regional hydraulic gradient and the repository tunnels.
2) The computational grid is constructed from rotated input geometries (Appendix D), and flow is solved within the local coordinate system [x´, y´].
3) The flow solution is transformed back into the original coordinate system (RT90 2.5 gon W).

The coordinate transformation was done by the following horizontal rotation:

$$\begin{bmatrix} x' \\ y' \end{bmatrix} = \begin{bmatrix} \cos\alpha & \sin\alpha \\ -\sin\alpha & \cos\alpha \end{bmatrix} \begin{bmatrix} x_p \\ y_p \end{bmatrix} + \begin{bmatrix} x_0 \\ y_0 \end{bmatrix}, \qquad (4\text{-}1)$$

where [x´, y´] is the rotated point in local coordinates, x_p = Easting – 1,632,400.0, y_p = Northing – 6,701,200.0, x_0 = 6,400.0, y_0 = 9,200.0, and the counter-clockwise rotation angle α = 32.58817°. The rotation angle α was calculated based on the SFR tunnel orientation in CAD, and is fairly close to the rotation angle for transformation between the RT90, 2.5 gon W and the T-U coordinate system (39.4118°). The rotation is illustrated in Figure 4-1.

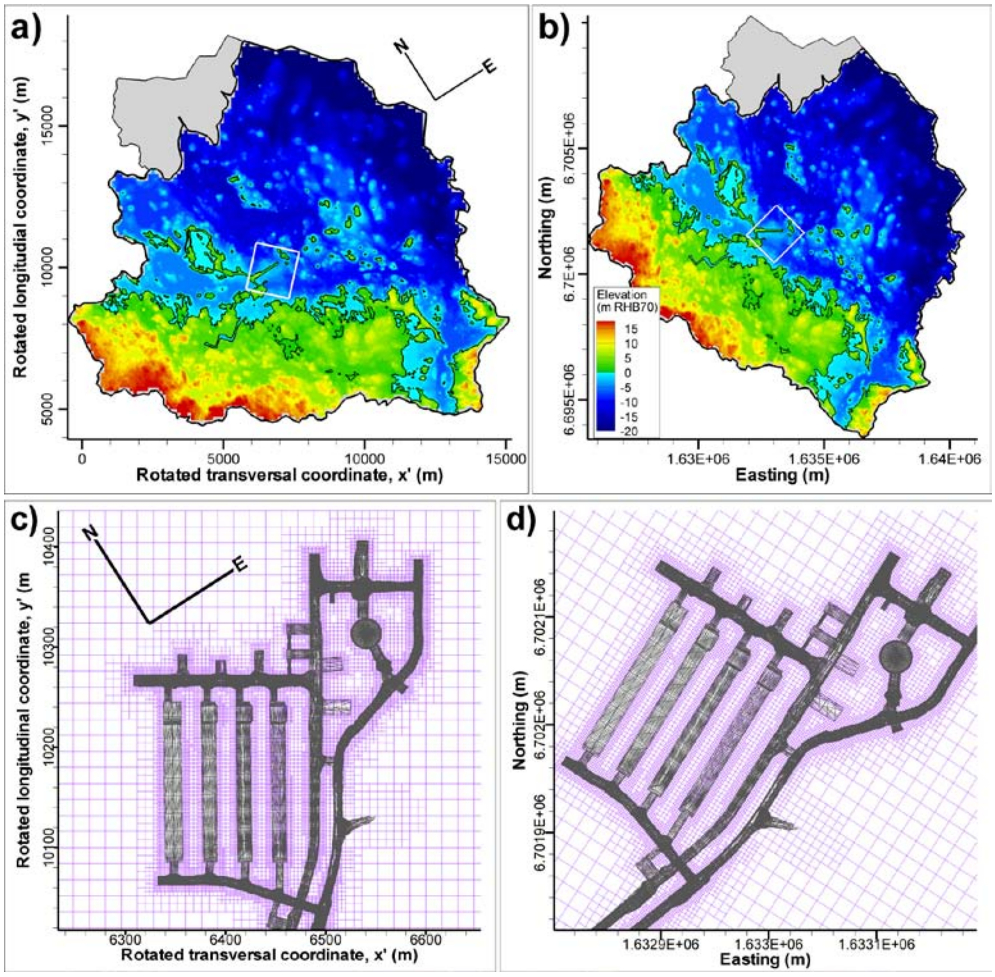

Figure 4-1. *Examples of the rotated computational mesh applied in flow simulations; a) flow model domain and c) horizontal cross-section of the SFR near-field at z = –80 m elevation, compared to grids back-rotated into the original RT90 coordinate system; b) flow model domain and c) the horizontal cross-section of the SFR near-field. The net effect is that the grid is parallel to the regional-scale flow pattern and disposal facility walls.*

4.4.1 Spatial differentiation of tunnel inflow

The average total inflow to SFR in 2010 was 286.4 L/min, being equal to the sum of inflows measured at the two pump pits UB and NDB (Figure 2-6). These pump pits collect drainage water from rather large parts of the SFR facility, which implies that the spatial resolution of inflow measurements is insufficient for evaluating details in the performance in flow simulations. However, additional information is provided for tributary tunnel sections that are part of the SFR control programme (Figure 4-2 and Table 4-2). For example, individual inflow measurements are made in the four storage caverns 1BTF, 2BTF, BLA, and BMA, from which drainage water is diverted to the pump pit UB. This information can, in turn, provide information on the inflow to tunnel sections *outside* the four storage caverns. Specifically, the inflow to the dark green area in Figure 4-2 can be calculated by subtracting the storage cavern inflows from the total inflow to pump pit UB.

This type of re-organisation in tunnel inflow data renders differentiated tunnel inflow for 10 defined areas that are applicable in simulations. These differentiated areas are assigned "simulation area codes" that are implemented in the flow modelling (numbered 11 to 20 in Table 4-2, shown in Figure 4-3). Note that the "simulation area codes" may be based on measurements, calculations, or estimations, while the SFR control program codes strictly refer to measurements. Estimated uncertainties are in specified Table 4-2 (taken from Carlsson and Christiansson 2007). It is quite possible that the uncertainties are underestimated; for example, it is unclear if all the water passes the measuring point in tributary areas. As a demonstrating example of this uncertainty, similar efforts of re-organising tunnel inflow in earlier work occasionally resulted in artificial *negative* values (Axelsson et al. 2002). Furthermore, due to temperature and moisture differences between the SFR facility and the surrounding open-air, the air ventilation system causes additional uncertainty to inflow data. The total contribution to flow measurements is expected to range from +30 L/min (moisture condensing during summer) to about -30 L/min (evaporation during dry winter months) (Öhman et al. 2012).

The re-organisation of inflow data is traceable via the conversion between SFR control program codes and the "simulation area codes" in Table 4-2 and Table 4-3, but also visualised (cf. Figure 4-2 and Figure 4-3). Note that simulation area code 20 (grey area in Figure 4-3) is based on an early estimate of inflow from the Singö zone and above, see Öhman et al. (2012). It should also be noted that the short entry tunnels to the storage facilities (simulation area code 21 shown by black areas in Figure 4-3) are not associated to any measured inflow; however, their total contribution is small in relation to uncertainties (typically ≤ 1 L/min) and it was therefore neglected.

In the simulations, the tunnel inflow is calculated separately for each of the 10 "simulation area codes" and directly compared to Table 4-3. It should be noted that these ten differentiated inflows relate to considerably different areas (Table 4-3) and therefore evaluation is also made in terms of specific inflow (i.e. area-normalised). A conceptual illustration of the discretised inflow across the tunnel wall is given in Figure 2-2.

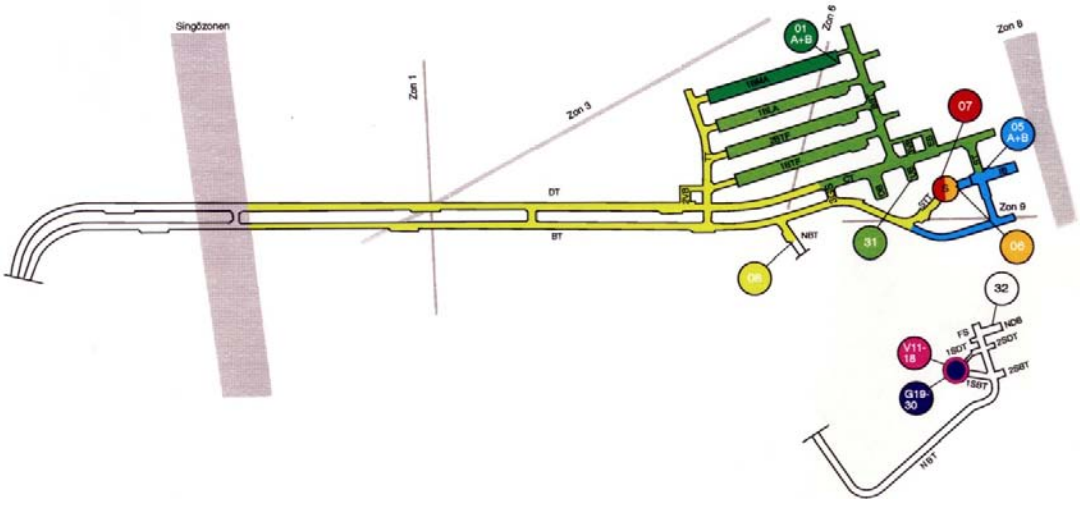

Figure 4-2. *Inflow measurement areas used in the SFR control program. The most recent values are specified in Table 4-2.*

Table 4-2. Tunnel inflow measurements (by the end of 2010).

Tunnel sections	Control program area code	Simulation area code	Measured flow (L/min)	Estimated uncertainty (L/min)
1BTF	[04]	11	**1.1**	±1
2BTF	[03]	12	**7.0**	±1
BLA	[02]	13	**0.0**	±1
BMA	[01A+B]	14	**4.0**	±1
Silo top	[V11–G31]	15	**0.0**	±0.1
Silo walls and bottom	[06+07]		**0.5**	±0.1
UB	[31B]	11,12,13,14, and 16	**48.8**	±1
Thompson weir NBT [BT+DT+STT+TT+2VB]	[08]	17 and 20	**161.6**	±10
[IB+part of ST&BT]	[05A+05B]	18	**2.8**	–
NDB	[32B]	15, 17, 18, 19, and 20	**237.6**	±10
Total UB+NDB			**286.4**	

Table 4-3. Re-organised tunnel inflow data (2010) used in flow simulations.

Inflow area	Simulation area code	Control program area code	Type	Flow (L/min)	Area[1] (m^2)
1BTF	11	[04]	Measured	**1.1**	9,096
2BTF	12	[03]	Measured	**7.0**	9,532
BLA	13	[02]	Measured	**0.0**	10,740
BMA	14	[01A+B]	Measured	**4.0**	13,172
Silo total	15	[V11–G31+06+07]	Summed	**0.5**	10,076
UB (without facilities)	16	[31B] – [01A+B+02+03+04]	Calculated	**36.7**	31,672
Access tunnels below Singö	17	70% of [08]	Assumed	**113.1**	87,876
[IB+part of ST&BT]	18	[05A+05B]	Measured	**2.8**	12,824
NBT	19	[32B] – [08+05A+05B+ V11–G31+06+07]	Calculated	**72.7**	25,784
Access tunnels above Singö	20	30% of [08]	Assumed	**48.5**	32,632
Connections to disposal facilities	21	Minor part of [08] and [31B]	Neglected	**–**	3,396
Sum of all inflow areas				**286.4**	**246,800**

1) Discretised cross-sectional area in the numerical flow model. In reality, the areas are somewhat smaller.

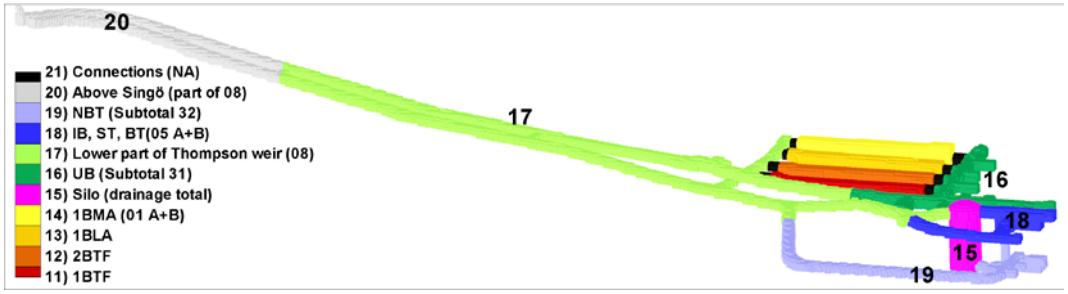

Figure 4-3. *SFR tunnel inflow subareas applied in simulations. The inflow data have been re-organised to some extent, by means of subtractions and estimates in order to provide more useful differentiation criteria.*

4.4.2 Evaluation of simulated head

In total, 95 monitored borehole sections are available for the evaluation of the simulated head decrease around SFR (see Section 2.7.1). Of these 95 borehole sections, 39 were installed during the construction of SFR (Figure 4-4), whereas 56 monitored sections were more recently installed (either during the Forsmark site investigations or during the recent SFR extension investigations; Figure 4-5). All underground boreholes (i.e. all boreholes of the old data set, but also the recently drilled KFR105) are monitored in terms of absolute pressure. The pressure is converted into a theoretical FWH, assuming a freshwater density of $\rho = 1{,}000$ kg/m^3, Equation 2-1. Monitored sections of surface boreholes are quantified in terms of PWH, with the actual fluid density in the borehole interval as reference density.

In context of the relative shallow depths, the large current head decrease, and strong gradients at SFR, a *uniform-density system* is assumed (Section 2.6) where the difference between FWH and PWH is regarded as of minor significance. A more serious concern in the head evaluation is related to the geometric resolution in DarcyTools modelling. The true geometry of borehole sections can be envisaged as long, thin cylinders (i.e. with a radius the order of a few centimetres and section lengths ranging from a few meters to a couple of hundred meters). Furthermore, the borehole opening short-circuits the flow and gradients between all features intersected by the borehole section, where the head value is largely determined by the most dominant structure.

This detailed geometry is computationally demanding to resolve in a regional-scale continuum model. The standard computational grid cells within the SFR Regional domain are cubic with a maximum side-length of 16 m (or 8 m in exercises M6 and M7), whereas closer to the existing SFR facility the side-length is refined to 2 m (Table 4-1). Thus, there is an evident geometric inconsistency, between the true, essentially linear-shaped, borehole sections and the large cubic grid cells used in simulations. The discrepancy is particularly large for long borehole sections (i.e. L > 100 m), over which the true hydraulic gradient is short-circuited (Table D-2). It was not considered possible to perform additional grid refinement in the vicinity of borehole sections. Instead, the borehole-section head data were compared directly with the simulated head in the grid cell that contains the mid-point of the true borehole section (Figure 4-4 and Figure 4-5). The numerically implemented head data are presented in Table D-2. The effect of geometric inconsistency is evident in the presence of a strong hydraulic gradient, such as near SFR (cf. Figure 4-4a and b).

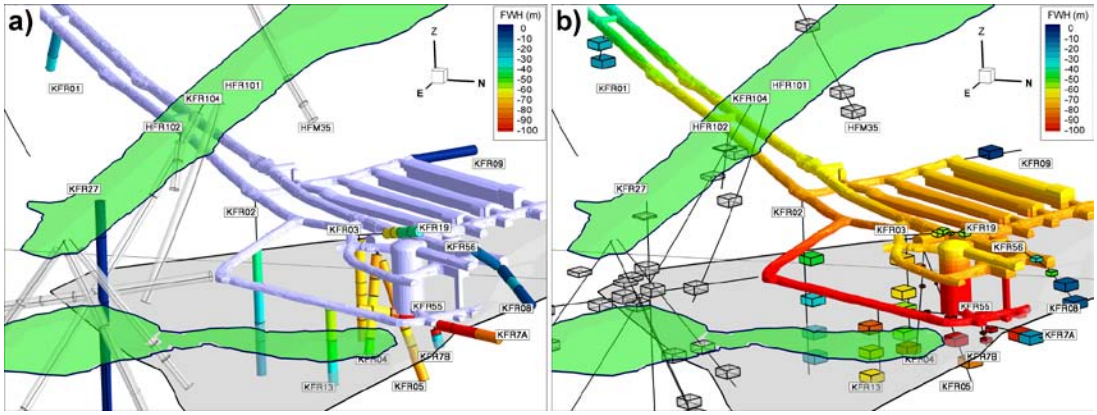

Figure 4-4. *Constraining head data in old boreholes; a) monitored head in boreholes, 2010 and b) simulated head in grid cells in DarcyTools (Model Exercise M2a). The prescribed head to the SFR tunnel is contoured for reference. Borehole sections of the recent data set and corresponding grid cells are included as transparent grey shades.*

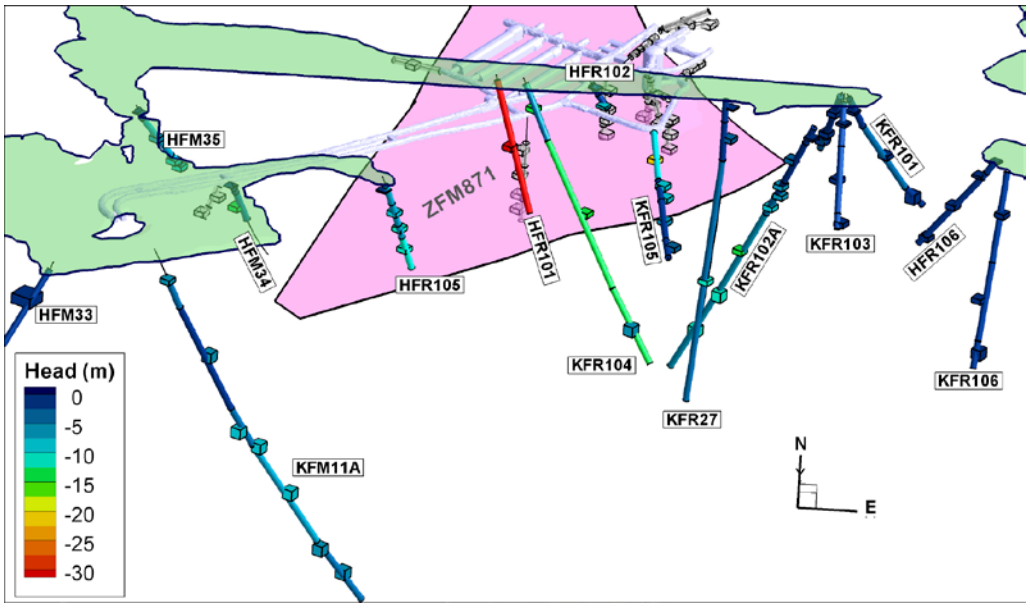

Figure 4-5. *Constraining head data in new boreholes; monitored PWH in borehole sections 2010 and simulated head of grid cells in DarcyTools (Model Exercise M2a). For reference, the old borehole sections and corresponding grid cells are included as transparent grey shades.*

5 Model Exercises

Shortcomings in constraining data and numerical implementation, discussed in Chapters 2 and 4, raise concerns regarding the possibilities to calibrate the groundwater flow model. Therefore, the performance of the groundwater flow model is instead explored by means of a perturbation analysis, where the output is placed in context of constraining data (measured inflow and monitored head). The main goal is to explore the potential in improving the hydraulic parameterisation (i.e. to weigh achievements in performance against the required additional level of complexity in parameterisation). The outcome of this analysis is the final HCD parameterisation (Table 3-2), which is primarily based on revised data interpretation in context of modelling results.

The parameterisation of the hydraulic domains (Chapter 3) is tested in a series of Model Exercises for open tunnel inflow simulations. The modelling sequence has a simplistic Initial Case as a starting point, referred to as Model Exercise M0. Increasing levels of complexity are sequentially included in the parameterisation, where the most advanced case is referred to as Model Exercise M7. The modelling sequence is summarised in Table 5-1. Model improvements (or the lack thereof) in more complex models are related to the Initial Case to judge the benefit/validity in adding more detail in the setup.

The goal of this study is to address the constraining power of data, the relative significance of hydraulic domain parameterisation, as well as specific conceptual uncertainties for the performance of the groundwater flow model. Model performance is evaluated by comparing simulation results to available head and inflow data (Section 4.4). A summary table for the evaluation of the model sequence M0 to M7 is provided in Table 5-2; this table is colour-coded such that yellow fields indicate a good agreement to available data. As a final step, the tunnel-wall skin is removed from the most advanced model setup, M7, and compared with the theoretical estimated initial inflow (i.e. at time t_0, prior to alteration of the hydraulic properties of the tunnel wall; Section 2.8.1).

It should be noted that the hydraulic parameterisation is only varied *inside* the SFR Regional domain; the hydraulic properties outside are consistently kept constant as defined in Chapter 3. The Model Exercises are presented in sequential order M0 to M7 in terms of *purpose*, *description*, and *expectations,* followed by a short summary of *observations made*. Simulation outputs are visualised in vertical cross sections along the SFR facility ($x' = 6{,}480$ in the local rotated coordinate system, see Section 4.3). More detailed results, discussions and conclusions are presented in Appendix C.

To facilitate discussions on the outcome of Model Exercises, the defined inflow areas of the SFR tunnel (Table 4-3) are visualised in the context of HCD intercepts (Figure 5-1). The tunnel-wall conductivity at deformation-zone intercepts in Figure 5-1c reflects the initial HCD parameterisation without skin (Öhman et al. 2012). Note that this parameterisation is adjusted in the Model Exercises presented below.

Table 5-1. Overview of model sequence with sequential complexity.

Exercise		Description	Parameterisation of hydraulic domains				
			HRD	HCD	Skin	HSD	SBA
M0	**Initial Case (no HSD)**						
	a	Average rock-mass conductivity, K_{CPM} = $6.5 \cdot 10^{-9}$ m/s					
	b	Doubled average rock-mass conductivity, K_{CPM} = $1.3 \cdot 10^{-8}$ m/s					
M1	**Introducing HSD, testing HRD anisotropy**						
	a	Isotropic, *a* = 1 (reference case for M1b and M1c)	$6.5 \cdot 10^{-9}$			SR-Site	
	b	Moderate HRD anisotropy, *a* = 3	Equation 3-5			SR-Site	
	c	High HRD anisotropy, *a* = 10	Equation 3-5			SR-Site	
M2	**Testing anisotropy with HRD, HSD, and HCD (initial, non-conditioned HCD)**						
	a	Isotropic, *a* = 1 (reference case for M2b and M2c)	$6.5 \cdot 10^{-9}$	Table A-1		SR-Site	
	b	Moderate anisotropy, *a* = 3	Equation 3-5	Equation 3-5		Equation 3-5	
	c	High anisotropy, *a* = 10	Equation 3-5	Equation 3-5		Equation 3-5	
M3	**Revised and conditioned HCD, introducing tunnel-wall skin**						
	a	Revised HCD, Conditioned at borehole and tunnel intercepts	$6.5 \cdot 10^{-9}$	Table A-1		SR-Site	
	b	Introducing tunnel-wall skin, K_{skin} = $6.5 \cdot 10^{-9}$ m/s	$6.5 \cdot 10^{-9}$	Table A-1	$6.5 \cdot 10^{-9}$	SR-Site	
M4	**Introducing deterministic SBA-structures**						
	a	Only SBA, HRD, and HSD (equivalent to M1a + SBA)	$6.5 \cdot 10^{-9}$			SR-Site	Deterministic
	b	Combining SBA-structures with HCD + skin (equivalent to M3b + SBA)	$6.5 \cdot 10^{-9}$	Table A-1	$6.5 \cdot 10^{-9}$	SR-Site	Deterministic
M5	**Exploring variants of M4b**						
	a	Reducing connectivity at junction between ZFM871 and ZFMNW0805B	$6.5 \cdot 10^{-9}$	Table A-1	$6.5 \cdot 10^{-9}$	SR-Site	Deterministic
	b	Introducing HRD depth trend	Equation 3-6	Table A-1	$6.5 \cdot 10^{-9}$	SR-Site	Deterministic
	c	Moderate global anisotropy, *a* = 3	Equation 3-5	Table A-1	$6.5 \cdot 10^{-9}$	SR-Site	Deterministic
	d	Choking sediments (reducing K_z by a factor of 10 in HSD)	$6.5 \cdot 10^{-9}$	Table A-1	$6.5 \cdot 10^{-9}$	Reduced K_z	Deterministic
M6	**Parameter optimisation (M5 as starting point)**						
	Various cases tested; the “optimised” setup is propagated to M7		Equation 3-6	Table 3-2	Table 5-3	Reduced K_z	Deterministic
M7	**Introducing stochastic SBA in areas outside borehole coverage**		Equation 3-6	Table 3-2	Table 5-3	Reduced K_z	Appendix B
Virgin inflow at time = t_0. Skin reflects grouting only.			Equation 3-6	Table 3-2	Grout	Reduced K_z	Det. + Stoch

Table 5-2. Summarised model performance in Model Exercise sequence M0 to M7 (see Table 5-1)

		Head evaluation for hydraulic units[1] (m)											Overall error estimates							
Data set		ALL	NEW				OLD													
		All data	Southern boundary belt	Northern boundary belt	Central block HCD	HRD	Southern boundary belt	Northern boundary belt	NE0869	ENE0870	ZFM871	HRD	Head (all boreholes)	Head (Old boreholes)	Head (New boreholes)	Flux, q (subarea 11–20)	ΔHead[3] (all boreholes)	Norm. ΔH[4] (Old boreholes)	Norm. ΔH[4] (New boreholes)	Ratio Q_{tot}[5] (Q_{sim} / Q_{data})
No. data		95	14	11	13	18	2	4	1	8	10	14								
Avg. r_{SFR} (m)			282	394	209	217	37	34	40	30	54	28								
Avg. head (m)		–25.6	–5.1	–1	–7.1	–1	–28.5	–11.9	–1.9	–69	–66.6	–66								
		Average head difference for hydraulic units[2] (m)											Coeff. determination, r^2							
M0a	Initial Case	–6.5	0.5	–3.3	–7.2	–5.1	4.8	–25.7	–22.3	–17.3	3.5	–13.2	0.81	0.51	0.4	0.61	11.1	0.35	1.35	0.45
M0b		–6.7	0.1	–3.5	–7.5	–5.2	4.6	–25.8	–22.5	–17.3	3.3	–13.3	0.81	0.51	0.4	0.61	11.2	0.36	1.38	0.89
M1a		–5.8	1.4	–2.9	–6.3	–4.3	5.7	–24.8	–21.2	–17	4	–12.7	0.81	0.51	0.39	0.67	10.8	0.35	1.25	0.47
M1b	Anisotropy	–7.4	–2.4	–7.7	–12.5	–10	10.4	–39.4	–39.5	–16.1	11	–3.3	0.74	0.44	0.2	0.45	13.7	0.35	2.7	0.38
M1c		–6.6	–5.4	–12.4	–15.3	–13	11.3	–47.1	–55.1	–10	20.4	8.2	0.57	0.31	0.07	0.21	18	0.44	3.77	0.5
M2a		–6.6	–3.1	–0.7	–3.7	–2.9	1	–17.3	–3.8	–17.5	–5.9	–14.5	0.82	0.54	0.64	0.14	10	0.34	0.93	29.1
M2b	HCD + anisotropy	–11.1	–7.9	–5	–10.6	–8.5	7.7	–31.1	–22.7	–24	–12.1	–11.2	0.82	0.57	0.48	0.2	13.2	0.35	2.41	28.8
M2c		–17.4	–13.3	–18.3	–20.1	–17.1	7.2	–44.7	–49.4	–27.7	–15	–7.8	0.77	0.53	0.17	0.23	19.4	0.39	4.99	26.8
M3a	Revised HCD	–4.7	–4	–0.8	–5	–3.1	3.2	–12.7	–0.9	–11.1	–1.9	–7.3	0.8	0.5	0.64	0.11	9.6	0.31	1.11	24.0
M3b	HCD + Skin	3.8	4.8	–0.4	–2.4	–1.5	28.2	–3.4	–0.2	–1.2	31.3	1	0.69	0.35	0.45	0.65	10.5	0.36	0.92	1.7
M4a	M1a + SBA	–4.9	1.4	–3.3	–4.4	–3.1	5.7	–23.7	–21.1	–16	5.2	–11.1	0.81	0.51	0.49	0.63	10.2	0.34	1.05	0.5
M4b	M3b + SBA	4.6	4.8	–0.2	–0.8	–0.8	28.2	–3.4	–0.2	–0.7	31.9	2.6	0.7	0.36	0.54	0.66	10.2	0.37	0.76	1.8
M5a	Choke WNW0805	4.5	4.8	–0.1	–0.6	–0.7	28.2	–3.2	–0.2	–0.9	31	2.4	0.7	0.35	0.55	0.68	10.2	0.37	0.75	1.8
M5b	HRD depth trend	4.7	4.8	0.2	0.2	–0.2	28.2	–2.8	0	–0.1	31.2	1.9	0.69	0.34	0.6	0.56	10.3	0.38	0.69	1.8
M5c	HRD anisotropy	5.6	4.8	–0.3	–2.7	–2	28.2	–4.6	–1.2	0	38.8	8.3	0.65	0.35	0.39	0.65	11.8	0.41	1.05	1.8
M5d	HSD anisotropy	4.3	4.2	–0.2	–0.9	–1	27.3	–3.8	–0.5	–0.9	31.6	2.4	0.7	0.36	0.57	0.67	10	0.36	0.71	1.7
M6	Optimisation	0.7	–0.2	0.1	–1.3	–0.4	17.7	–1.8	0.4	–4.7	8.3	1.3	0.85	0.59	0.74	0.65	7.4	0.27	0.52	1.5
M7a	Stochastic SBA	2.7	1.2	0	–1.4	–0.6	19.2	–0.4	0.3	–0.5	15.7	5.6	0.83	0.55	0.66	0.76	7.7	0.28	0.57	1.5
M7b	Merged SBA	0.7	0.2	0.3	0.2	0	17.8	–1.5	0.5	–8.4	8.6	0.9	0.83	0.55	0.74	0.79	7.7	0.28	0.48	1.3
M7c	Merged SBA	–0.2	0.2	0.2	0.1	–0.1	17.6	–0.7	0.5	–9.1	3	–0.7	0.85	0.6	0.72	0.77	7.5	0.27	0.5	1.2

1) Summary of data as subdivided into hydraulic units (Table D-2)

2) Average head difference for hydraulic units (simulated – monitored head). Colour scale reflects data agreement. Blue = too low, Yellow = best value, Red = too high.

3) Average head error of all N evaluation points (Σ(Hsim – Hdata)/N)

4) Normalised average head error (Σ(Hsim – Hdata)/ Σ(Hdata))

5) Ratio in total inflow (Qsim / Qdata), where data refers to year 2010, and "total" refers to all sections 11 to 21 in Figure 4-3.

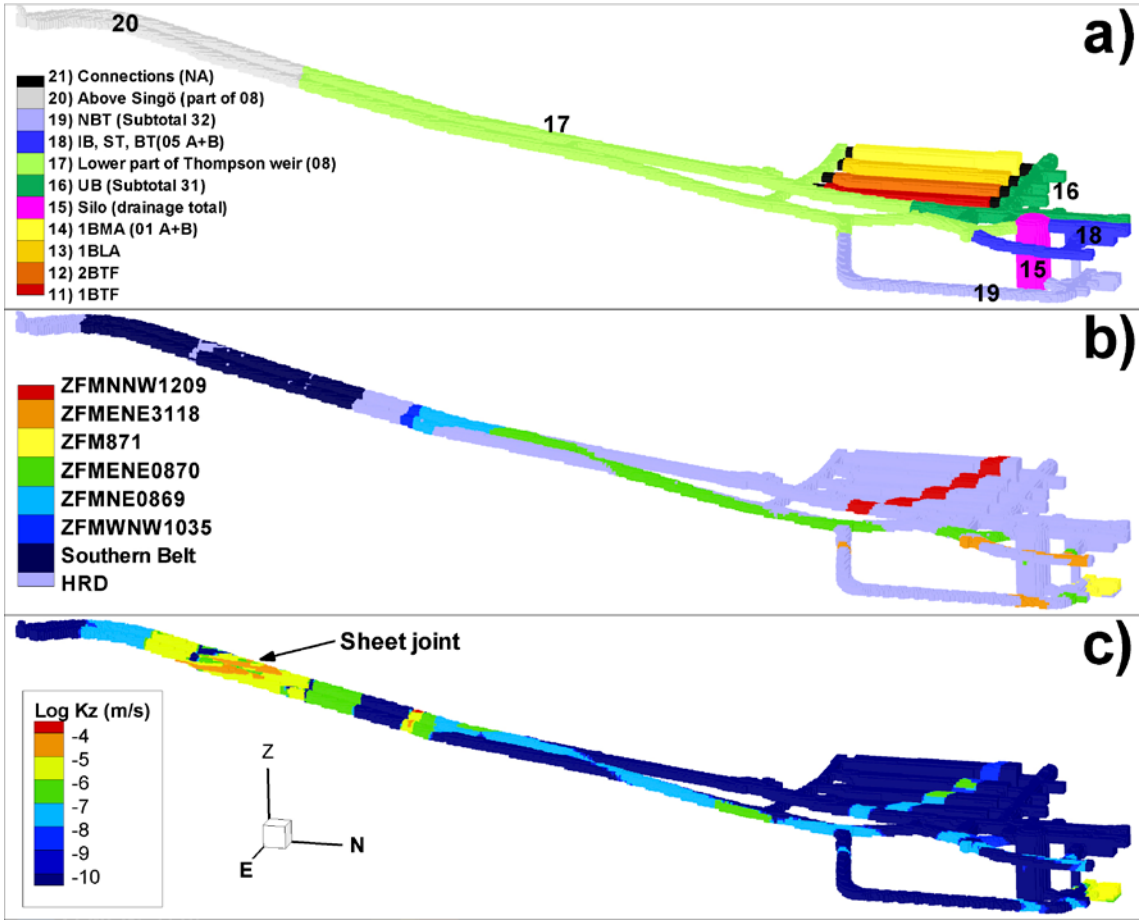

Figure 5-1. *Deformation-zone intercepts in the differentiated inflow of areas SFR tunnel; a) inflow of areas 11 to 21 used in calculations (cf. Table 4-3), b) HCD intercepts, and c) calculated conductivity of the SFR tunnel for initial HCD parameterisation, without skin. Note that the high hydraulic conductivity in the Southern boundary belt is caused by a sheet joint, defined in SDM-Site Forsmark (Follin et al. 2007b).*

5.1 M0: Average HRD conductivity (no HCD, HSD, or skin)

Model Exercise M0 is the simplest model setup and serves as a reference for evaluating the improvements (or lack thereof) in subsequent, more complex model setups. In the M0 model setup, the entire SFR Regional domain is represented by an average hydraulic conductivity (Figure 5-5). This conductivity is applied to all model cells inside the SFR Regional domain (i.e. HRD, HCD, HSD and tunnel-wall cells).

Two cases are compared:

M0a: $K_{CPM} = 6.5 \cdot 10^{-9}$ m/s (calibrated to tunnel inflow in 1997 (Holmén and Stigsson 2001)), and

M0b: $K_{CPM} = c \cdot (6.5 \cdot 10^{-9})$ m/s, where a constant c is scaled to reproduce recent total inflow (year 2010; Table 4-3).

The expectation is that M0a will underestimate the current inflow, as the deformation zones, which are not included in this model setup, had a significant role in the calibration of Holmén and Stigsson (2001). Hence, neglect of the HCD inflow component in M0a is expected to provide an underestimated inflow. The purpose of this test is to put the average rock-mass conductivity of Holmén and Stigsson (2001) in context of the recent inflow measurements as the inflow has declined since 1997.

The purpose of M0b is to provide a simulated inflow that is more readily comparable to recent inflow data. Expectations of M0b are the following: 1) the head field will be identical to M0a, as the hydraulic conductivity is re-scaled by a constant (c), and 2) although the total inflow is reproduced, the spatial patterns in inflow data cannot be reproduced in detail, i.e. they cannot reveal that the M0b parameterisation is too simple and thereby justify sophistication to the model setup.

5.1.1 Observations

In this simplistic model setup, the simulated head decrease has a smooth appearance that is clearly related to the geometry of the SFR facility and its location below sea (Figure 5-5). The hydraulic gradient is clearly stronger above SFR than it is below. Head decrease larger than, say, 40 m does not propagate far from the facility. Even so, comparison with data demonstrates that the simulated head decrease is too high, particularly in more remotely located borehole sections of the new data set (Figure 5-3b). This suggests that steep deformation zones, which are not included in this model setup, may have a significant role in controlling the lateral extent of head decrease. For example, hydraulic connection to the sea via ZFMNE3118 and ZFMENE3115 may dampen the propagation into the recently investigated area.

Simulated inflow (Figure 5-4a) is surprisingly proportional to measurements, in spite of the fact that HCDs are not included in this model setup. This suggests that the geometry of the quantified inflow areas (location and exposed tunnel-wall area) have a significant role in tunnel inflow, relatively to geological structures. The significance of cross-sectional area is demonstrated by the poorer correlation in terms of flux, q (area-normalised flow; Figure 5-4b). Notably, the experience from tunnel construction was, quite contradictory, that tunnel inflow was strongly correlated to deformation zone intercepts (Christiansson and Bolvede 1987). Thus, with consideration to the on-going decline in tunnel inflow, it is possible that the role of HCDs has diminished (i.e. perhaps the decline in tunnel inflow is partly due to dewatering of HCDs).

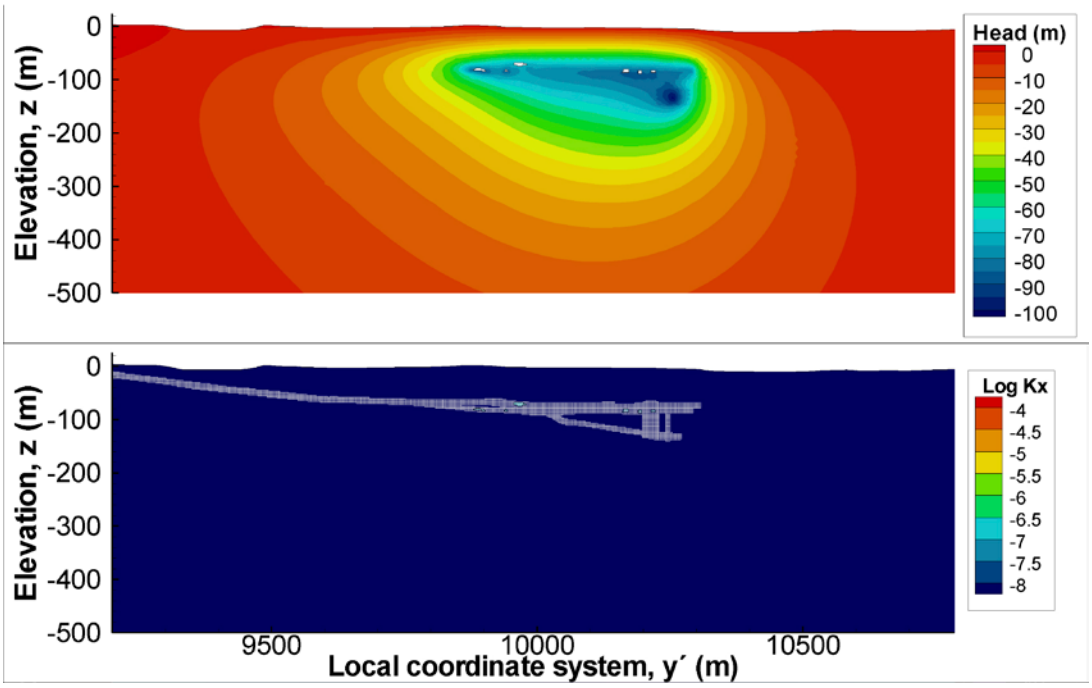

Figure 5-2. *Exercise M0a. Upper image: vertical cross section of simulated head. Lower image: parameterised conductivity (local coordinate x´= 6,480). Average, isotropic hydraulic conductivity, $K_{CPM} = 6.5 \cdot 10^{-9}$ m/s (taken from K_{HRD} in Holmén and Stigsson 2001).*

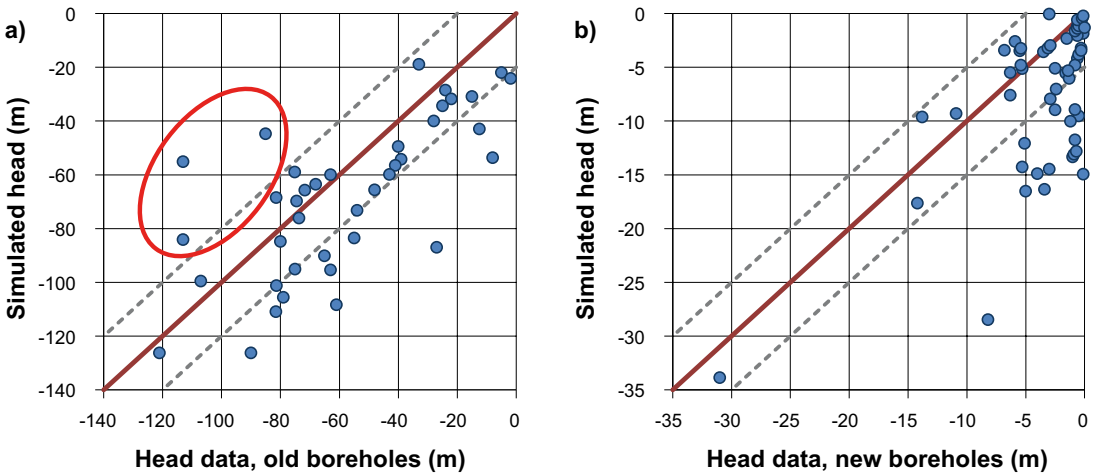

Figure 5-3. *Simulated versus measured head in exercise M0; a) old boreholes and b) recent boreholes. The simulated head decrease is generally too large (except in KFR7A, marked by red oval). Dashed lines indicate a ± 20 m uncertainty interval for old boreholes, and a ± 5 m uncertainty interval for recently installed boreholes.*

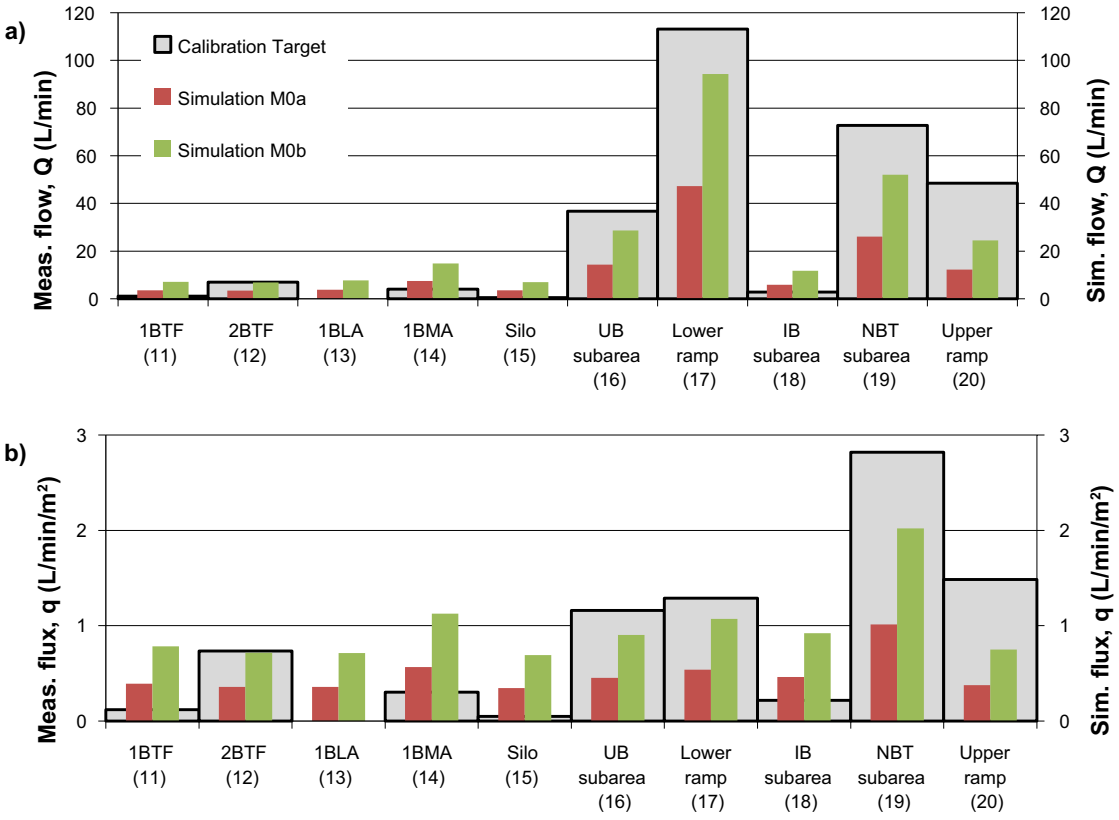

Figure 5-4. *Flow simulation results in exercise M0; a) inflow, Q, and b) average flux, q (i.e. area-normalised inflow).*

5.2 M1: HRD anisotropy (no HCD or skin)

Data analysis indicates that the flowing fracture network in the shallow bedrock hosting the SFR facility is highly anisotropic, as the most transmissive PFL-f data are horizontal to gently dipping (Öhman et al. 2012). The purpose of Model Exercise M1 is to explore how three cases of anisotropy (M1a–c), affect the spatial pattern in simulated head decrease. The notion on strong hydraulic anisotropy in the shallow bedrock at SFR is reinforced if cases M1b and M1c sequentially improve the agreement between simulated and measured head decrease.

M1a is used as a starting point. In M1a, the hydraulic conductivity $K_{HRD} = 6.5 \cdot 10^{-9}$ m/s is first assigned to all model cells within the entire SFR Regional domain. In cases M1b and M1c, anisotropy is implemented by increasing the horizontal component by the factor *a*, simultaneously as the vertical component is reduced by the same factor, Equation 3-5. The purpose of this procedure is to minimize the net effect on tunnel inflow, and thereby making the three cases more comparable.

The tested anisotropy cases (see Figure C-6) are:

M1a: $a = 1$ (isotropic, $K_H = K_Z = 6.5 \cdot 10^{-9}$ m/s),
M1b: $a = 3$ (ratio $K_H/K_Z = 9$), and
M1c: $a = 10$ (ratio $K_H/K_Z = 100$).

The HSD is implemented as defined in SR-Site Forsmark (i.e. not subject to anisotropy elaboration). Thus, the effect of including HSD can be evaluated by comparing M1a to M0a. HCD and skin are not implemented at this stage (see equivalent anisotropy elaboration for HCD in Model Exercise M2).

The expectations are that the simulated inflow will still be underestimated, as HCDs are not included in this model setup (i.e. similar to the M0 results. Increasing anisotropy ratios are expected to spread the head decrease laterally, but to have a minor net effect on tunnel inflow.

5.2.1 Observations

Along with expectations, the total tunnel inflow is more or less preserved for the three cases of anisotropy (very similar to M0a). However, anisotropy does re-distribute the locations of tunnel inflow towards the outer, vertically exposed walls of SFR (for example, the simulated inflow to the Silo is increased in M1c, whereas inflow to the centrally located 2BTF and BLA decreases; Figure C-9). The inflow measurements do not support horizontal anisotropy. For instance, simulated inflow for a high anisotropy is inconsistent with the notably low measured inflow for the Silo.

As intended, increasing levels of horizontal anisotropy enhance the head decrease laterally (Figure C-7). Evaluation with head data does not support horizontal anisotropy, at least not in absence of HCD (Figure C-8).

5.3 M2: Anisotropy with HCD (no skin)

Both anisotropy and HCD control the lateral spread of head decrease. Therefore, this matter is elaborated further in Model Exercise M2. In this model setup, the HCD is introduced and the anisotropy test from M1are repeated. In this exercise, the anisotropy is applied equally to all three hydraulic units of the SFR Regional domain, i.e. HRD, HSD, and HCD. The starting point is referred to as M2a, in which K_{HRD} is set to $6.5 \cdot 10^{-9}$ m/s, K_{HSD} is taken directly from SR-Site Forsmark (Table 3-1), and the HCD are defined by the ground-surface transmissivity, $T_{eff}(0)$ and depth trend, Equation 3-3. This is referred to as the initial deformation-zone parameterisation (Table A-1; note that $T_{eff}(0)$ reported in Table 3-2 are the final values). It should be noted that at this stage, the HCDs are not conditioned by borehole intercepts and no tunnel skin is implemented (Figure 5-5a). In analogy to M1, three anisotropy cases, as defined by the factor *a* in Equation 3-5, are compared:

M2a: $a = 1$ (isotropic starting point, equivalent to including HCD to M1a),

M2b: $a = 3$ (ratio $K_H/K_Z = 9$ relative to M2a applied to HRD, HSD, and HCD), and

M2c: $a = 10$ (ratio $K_H/K_Z = 100$ relative to M2a applied to HRD, HSD, and HCD).

The conductivity parameterisations are presented in Figure C-10. Note that the only difference between M1a and M2a is the introduction of HCD.

The expectations are the following: 1) The simulated inflow will be too high, as tunnel skin is not implemented, and 2) the spatial pattern of head decrease will primarily be controlled by HCD.

5.3.1 Observations

Similar to the observations in Model Exercise M1, horizontal anisotropy distributes the head decrease laterally. However, the head decrease is also controlled by the structural HCD geometry, disrupting the homogeneous pattern observed in Model Exercises M0 and M1. The most significant effect of HCDs is extending head decrease to greater depths (Figure C-11). The HCD improve the agreement to head data (particularly for the new data set) and also dampens the impact of anisotropy (Figure C-12).

However, in this model setup simulated inflows exceed the measured data by a factor of c 25. Note that the simulated inflow was realistic prior to the introduction of HCDs (i.e. M1). The excessive simulated inflow from HCDs signifies a necessity to revise the HCD parameterisation and to introduce tunnel skin (see Model Exercise M3 below).

5.4 M3: Conditioning HCD and introducing skin

In line with expectations, the inclusion of HCD without tunnel skin in the previous Model Exercise, M2, proves to have a dramatic impact on simulated total inflow. Therefore two possible approaches to constrain the simulated inflow are explored in this exercise:

M3a: revised HCD parameterisation (Table A-1) combined with local borehole-intercept conditioning (Table A-3).

M3b: introducing tunnel-wall skin, set to $K_{skin} = 6.5 \cdot 10^{-9}$ m/s (Figure 2-2).

The revised HCD parameterisation in M3a is visualised relative to M2a in Figure 5-5a and Figure 5-5b. M3a was preceded by a complete re-evaluation of the underlying data for HCD, specifically concerning deformation zone intercepts. The excessive HCD inflow in M2 partly relates to factors discussed in Section 2.4, but is also due to biased data interpretation related to model and data uncertainties (summarised Appendix A). As a result of this data re-assessment, some data were rejected and some were re-interpreted (primarily Northern and Southern boundary belts, as well as ZFM871). Moreover, tunnel intercepts without notable tunnel inflow in Christiansson and Bolvede (1987) are taken as observation points of "standard rock-mass conductivity" (pink circles in Figure 5-5b). In other words, the intercepts of ZFMENE3118, ZFMWNW3259, ZFMWNW0813, ZFMNW0805B are taken as conditional points with $T = 6.5 \cdot 10^{-9}$ m/s * zone thickness. It should be noted that the modelled deformation zone geometry in RVS covers an envelope that exceeds the width of the interpreted structure (Curtis et al. 2011). Hence, the modelled tunnel intercept of ZFMNW0805B is a model artefact, which is not supported by geology or inflow observations. The re-interpretation of borehole intercepts (reported in Table A-3) form the basis for the revised HCD transmissivity, $T_{eff}(0)$ (reported in Table A-1). All HCDs are parameterised according to Table A-1 and conditioned by borehole intercepts within a radius of 50 m (Table A-3).

The expectation of M3a was that some of the excessive inflow will be reduced by HCD conditioning at tunnel intercepts that lack notable flow (pink circles in Figure 5-5b) and that borehole-intercept conditioning may improve the simulated head in surrounding boreholes. However, as may be expected, the updated parameterisation and local conditioning of HCD in M3a is not sufficient to constrain the simulated total inflow to realistic levels. This suggests that the HCDs have a less pronounced effective, large-scale role in tunnel inflow, compared to what has been inferred from small-scale borehole data. M0b indicated that, taken as an average, tunnel inflow is subject to a resistance corresponding to an conductivity on the order of 10^{-8} m/s. Thus, current inflow data suggest that a resistance, on the order of 10^{-8} m/s, acts also on the HCDs. Three alternative hypotheses are considered:

1) The resistance occurs close to the tunnel wall. It is a so-called local skin effect (Section 2.5), caused by the underground construction itself. Consequently, tunnel inflow simulations are not very representative of HCD hydraulic properties during natural state (re-saturated tunnel conditions).
2) The resistance is located within HCDs and is a scaling effect of heterogeneity, or related to the particular flow regime for the open SFR facility. The discrepancy between hydraulic borehole data and effective, large-scale flow is possible if HCDs are heterogeneous, discontinuous, or

highly anisotropic. This makes it difficult to clearly state if borehole hydraulic data or tunnel inflow data are most the representative of the hydraulic properties of HCDs (Section 2.4).

3) The resistance is located in the overlying sediments, or at the contact between sediments and HCDs. The sediment coverage is particularly thick above the Southern boundary belt, containing patches of glacial and postglacial clay (parameterized as $K = 2 \cdot 10^{-8}$ m/s; Table 3-1). This would also imply that tunnel inflow is not very characteristic for hydraulic properties of HCDs, but instead to the occurrence of clay. Possibly, apertures are locally sediment-filled at the HSD/HCD contact, which could explain in a shallow, local resistance for tunnel inflow.

The impact of introducing tunnel-wall skin is explored in M3b. At this stage, tunnel-wall skin is set to $K_{skin} = 6.5 \cdot 10^{-9}$ m/s for all tunnel walls of the existing SFR facility (Figure 5-5c). This skin value was taken from the calibrated average rock-mass conductivity in Holmén and Stigsson (2001), which is considered to be relevant as a starting point. The principle of skin implementation to tunnel-wall cells is demonstrated in Figure 2-2. In general, the skin value is lower than values used in earlier SFR models (Holmén and Stigsson 2001). The reason for this is that recent inflow data (measurements per 2010) is lower than the calibration data used in previous models which refer to measurements made 1997).

The skin implemented in M3b is expected to provide a crude estimate of the resistance required to constrain simulated excess inflow, at least given the current inflow target and model setup. The impact of skin on simulated head is expected to indicate if the constraining resistance in inflow is located at the tunnel wall, or at a greater distance away from the underground facility.

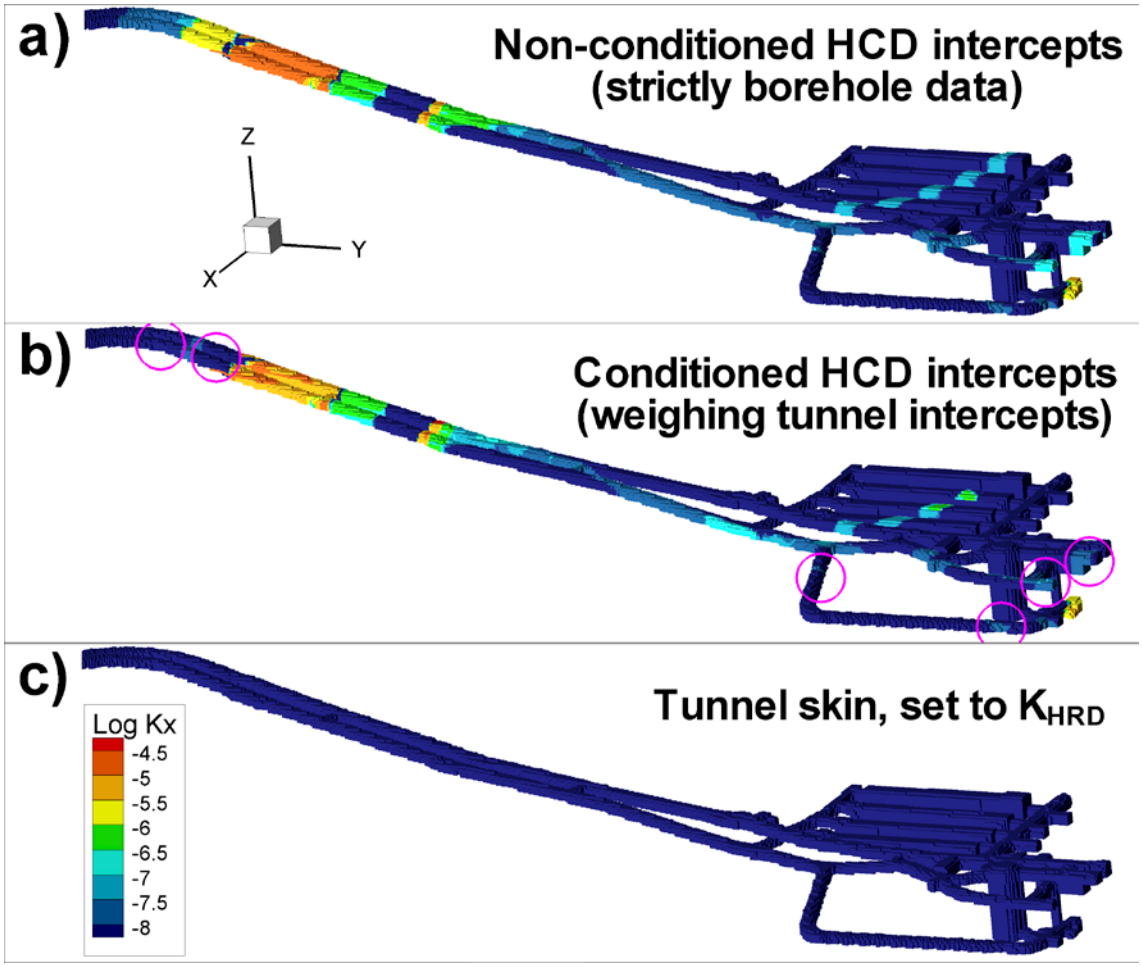

Figure 5-5. *Conductivity adjustments in M3 shown as tunnel intercepts: a) non-conditioned HCDs (i.e. used in M2), b) HCDs conditioned to borehole data, as well as low-transmissive, non-grouted tunnel intercepts used in M3a (pink circles; low-transmissive tunnel intercepts were also used to adjust $T_{eff}(0)$, and c) tunnel skin set to default value of $6.5 \cdot 10^{-9}$ m/s , applied in M3b.*

5.5 M4: Significance of SBAs for existing SFR

In addition to the geological deformation zones, eight so-called deterministic SBA-structures have been defined in Öhman et al. (2012) (Section 3.4.3). SBA1 to SBA6 are modelled in the recently investigated area southeast of the existing SFR facility. These are expected to be significant for the SFR extension, but to have a minor role in inflow to the existing SFR. SBA7 is located above the existing SFR. Its role for the current inflow is difficult to evaluate directly by simulations, as it neither intersects the existing facility, nor any of the monitored boreholes. The spatial extension of SBA8 is highly uncertain. Its role in current tunnel inflow is expected to be insignificant due to intensive grouting during construction. SBA8 is therefore not included in simulations.

a) SBA without HCD (i.e. introducing SBA to M1a).

b) SBAs with HCD (i.e. introducing SBA to M3b).

In both cases, K_{HRD} is set to $6.5 \cdot 10^{-9}$ m/s and K_{HSD} is taken directly from SR-Site Forsmark (Table 3-1).

5.5.1 Observations

As expected, the introduction of SBA-structures has a small impact on tunnel inflow simulations. Insignificant improvements can be noted in head evaluation of the recent data set (surface boreholes). This demonstrates the limitations of using tunnel inflow simulations for calibrating structures that are not in direct contact to the existing SFR, but nevertheless are potentially significant for the SFR extension.

5.6 M5: Various modifications of M4b

As described above, the M4b model setup has a significant level of complexity in which several degrees of freedom for improving the simulation results can be identified. As stated earlier, limitations in available data are simplifications in the model setup, as well as targeting structures that are not necessarily directly involved in tunnel inflow and thereby hinders "parameter optimisation" by flow modelling. Instead, the purpose of Model Exercise M5 is to address the impact of four identified conceptual issues (see Öhman et al. 2012 and Appendix A). These issues are evaluated separately, and implemented as modifications of the previous model setup, M4b:

a) Reducing the hydraulic connection between ZFM871 and ZFMNW0805B. Specifically, along this deformation-zone junction the hydraulic conductivity is reduced to $6.5 \cdot 10^{-9}$ m/s).

b) Introducing a hydraulic conductivity depth trend in HRD, according to Equation 3-6. This equation renders $K_{HRD} = 6.5 \cdot 10^{-9}$ m/s at the typical depth of the present SFR disposal facilities (z = –70 m elevation).

c) Imposing global anisotropy to HRD, HSD, and HCD, $a = 3$ in Equation 3-5.

d) Reducing vertical conductivity of HSD by a factor of 10.

Simulation results, M5a to M5d, are used to evaluate the credibility in the notions raised in the conceptual modelling. Substantial improvement is taken as support for the concepts.

5.6.1 Observations

Contradictory to expectations, none of the simulation cases provide substantial model improvement. The anisotropy in M5c provides a poorer fit to head data. The other exercises, M5a, -b, and -d, have negligible impact on the outcome of simulations, and thus provide little guidance for improving the hydrogeological flow model. Again, results demonstrate the following: 1) Model insensitivity to parameterisation, and 2) the limitations of using tunnel-inflow simulations for model calibration.

5.7 M6: Optimisation of main flow paths

The pursuit of model adjustments to improve simulation results is continued in Model Exercise M6. In spite of the lack of model improvement in M5, all its variants are considered realistic. Hence, the combined modifications M5a to M5d were implemented to form the starting point of M6. The strategy in M6 is to identify the key discrepancies in the flow model, and to sequentially test alternative parameterisations and hypotheses that improve model performance. This is done by trial-and-error; successful adjustments are retained, while unsuccessful adjustments are rejected (not described in detail). Thus, the goal of M6 is to test how far the model setup can be "optimised" at the expense of additional detail in parameterisation. The level of achievement in relation to effort in refinement demonstrates the constraining power of data (or lack thereof).

The limitations in this optimisation must be recognised. Firstly, the heterogeneity of the hydrogeological system can never be deterministically modelled in full detail. Secondly, some limitations in the constraining power of data are known beforehand, e.g. geometric inconsistency in head evaluation and uncertainties in measured tunnel inflow, as described in Chapter 2 and Section 4.4. Just as for the other Model Exercises the goal of M6 is *not* to establish a perfect fit to data at each data point. Instead, the goal is to address the most obvious discrepancies in simulated head, yet keeping the simulated inflow within realistic bounds. Head data were divided into subgroups representing different hydraulic units (for example, "Southern boundary belt"; Table D-2). The model performance is then evaluated as the discrepancy in simulated average head in these hydraulic units.

The poorest matches in simulated head in M5 are identified as underestimated head decrease in vicinity of the two dominant flow paths of the system: the Southern boundary belt and ZFM871 (see red values in Table 5-2). Hence both these locations are addressed in detail. Both locations are notable sink terms to the system and both were intensively grouted during tunnel constructions. Based on the conclusions of Model Exercise M3, three primary explanations are considered:

1) The representation of skin is inadequate (more precisely, numerically implemented as a local resistance occurring over a 2 m wide tunnel-wall cell; Figure 2-2). This narrow skin zone localizes most of the pressure drop to occur in the immediate vicinity of the tunnel, which may be an unrealistic representation in perspective of the variety of its potential underlying physical phenomena (discussed in Sections 2.5 and 2.8). Note also that the model files of tunnel section NDB1, which is an important sink of ZFM871, was unavailable during M5 (cf. Figure 5-6 and Figure 5-7).
2) HCD parameterisation based on historic borehole data potentially overestimates the effective transmissivity of zones (Section 2.4). A transmissivity reduction in HCD, combined with a lowered tunnel-wall resistance, is expected to extend the head decrease further away from the tunnel wall.
3) Upstream hydraulic contact to the sea (i.e. a positive hydraulic flow boundary) is subject to potential hydraulic chokes, either occurring in overlying sediments, or at junctions to hydraulically significant upstream structures. Any reduction in hydraulic contact to the sea is expected to increase simulated head decrease around SFR.

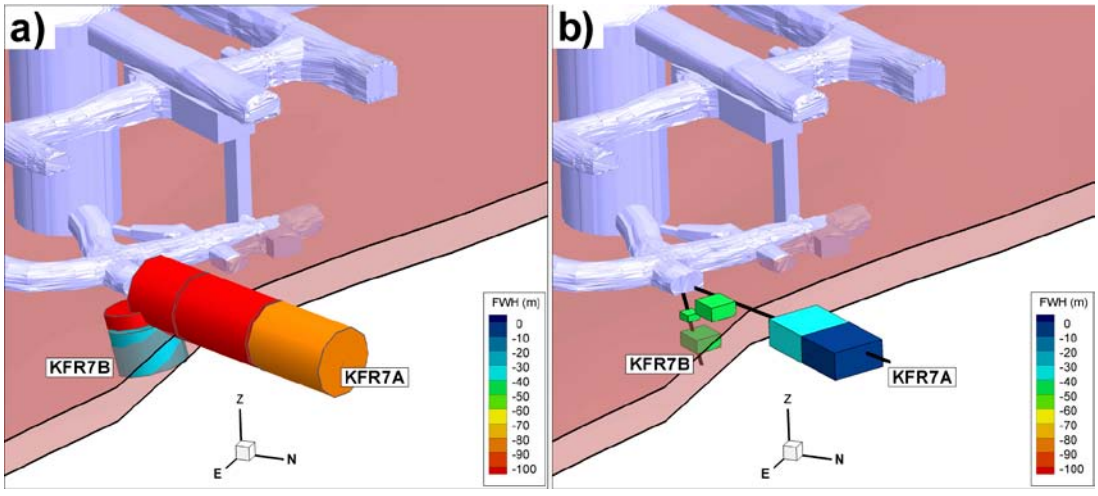

Figure 5-6. *Underestimated head decrease (m) at the ZFM871 intersection; a) measured data and b) simulation in Exercise M5. Large head decrease indicates strong hydraulic connection to the SFR tunnel, relative to the connection to the sea. Note that tunnel section NDB1 was unavailable during M0 to M5 (cf. Figure 5-7).*

Actions to improve the simulations in the vicinity of ZFM871 are the following:

- **Inclusion of tunnel section NDB1**: NDB1 is an important contact between the SFR facility and ZFM871 (i.e. an important sink of the tunnel inflow setup; Figure 5-7).
- **Geometric extension of ZFM871**: In the geological model, ZFM871 is terminated against ZFMNW0805B. Head decrease data in KFR7A suggests strong horizontal hydraulic, dead-end connection to SFR with poor vertical connection to the sea (see Öhman et al. 2012). In order to simulate the large head decrease in KFR7A, ZFM871 is at least expected to cover the midpoint of its lowest section, KFR07A_1. This is achieved by expanding ZFM871 by 15% in all directions from its geometric midpoint (cf. Figure 5-6 and Figure 5-7).
- **Maintaining reduced hydraulic contact between ZFM871 and ZFMNW0805A/B:** The junction between ZFM871 and ZFMNW0805A/B appears poorly connected to the sea, as indicated by the large head decrease and Littorina content found in KFR7A (Nilsson et al. 2010), which is clearly different from KFR08. This is numerically implemented by reducing the vertical hydraulic conductivity along the deformation-zone junction to that of the average rock mass ($K_{HRD} = 6.5 \cdot 10^{-9}$ m/s. This value is the same as that used in model setup M5a, but here it is also applied to ZFMNW0805A.
- **Grouted volume of ZFM871:** The large, widespread head decrease observed in ZFM871 cannot be attained by the simplified numerical representation of skin/grout (Figure 2-2). As an alternative, the NDB/ZFM871 intercept was modelled as a large volume of poorly grouted rock. The volume of injected grouting (67 m^3) can be related to the rock-mass volume inside a cylinder with a height of 11 m (i.e. the ZFM871 thickness) and a radius of 14 m, assuming a porosity of 1%. However, a wider influence area is motivated by the general fact that grout is known to spread unevenly (i.e. asymmetrically) and was also performed over several tunnel sections (i.e. not originating from a single point). The best match was found for "poor grouting over a wide area" ($K_{skin} = 1.3 \cdot 10^{-7}$ m/s, penetration radius = 55 m, x´= 6,505, y´= 10,292; see yellow area in Figure 5-7).
- **Adjusting the parameterisation of ZFM871**: Deformation zones close to SFR are parameterised by hydraulic data from the old data set. The old data set contain short-term measurements, which implies that the effective, large-scale transmissivity of zones may be overestimated due to inclusion of compartmentalized fracture networks. In the current model, ZFM871 has a considerably higher transmissivity than that used in previous models, e.g. Holmén and Stigsson (2001) (cf. black and dashed lines in Figure 3-4). Therefore, the transmissivity was reduced by a factor of 5, which may be more representative of its effective hydraulic property (brown line in Figure 3-4).

Actions to improve the simulation results in the vicinity of the Southern boundary belt are the following:

- **Adjusting the transmissivity parameterisation:** Based on the same argument as above, the effective transmissivity of ZFMWNW0001 and ZFMWNW1035 was reduced by a factor of 10, which also is more in line with previous modelling (see Table 3-2).
- **Sediment contact to the Southern boundary belt:** Modelling exercises M0 to M5 cannot reproduce the large head decrease in the Southern boundary belt without causing excessive simulated tunnel inflow (Table 5-2). A potential reason is that its hydraulic contact to the sea is constrained by overlying sediments (clay). The uppermost part of the Southern boundary belt zones are assigned a conductivity that corresponds to overlying glacial clay. Unfortunately, this "sediment choking" is rather crudely implemented owing to coarse meshing of these zones (triangles of side length c 50 m; Figure 3-5). It should be noted that the SFR access tunnels penetrate the Southern boundary belt at c –40 to –50 m elevation and that, in reality, the sediment choking is not expected to reach this depth.
- **Revision of Forsmark sheet joints:** Analysis of an interference test performed in HFM33, subsequent to the development of sheet joints, motivates truncating the sheet joints inside the SFR Regional domain (Figure 3-10). The reduced hydraulic contact between the Forsmark sheet joints and the Southern boundary belt improves the simulated head decrease somewhat for borehole sections in the Southern boundary belt**.**

Further actions taken are the following:

- **Spatial differentiation of tunnel-wall skin:** The tunnel-wall skin is allowed to vary between different deformation-zone intercepts (Table 5-3). The Silo is assigned particularly low skin conductivity. Values are varied to improve the relation to head and inflow data.
- **Grid refinement in the shallow bedrock:** Above –200 m elevation, the computational grid inside the SFR Regional domain is refined to a minimum cell side length of 8 m (Table 4-1).

5.7.1 Outcome

Key changes are transmissivity reductions of ZFMWNW0001, ZFMWNW1035 and ZFM871, leading to the final HCD parameterisation (Table 3-2). A shallow resistance, related to HSD conductivity, is implemented in the shallow parts of Singö, ZFMWNW1035, and ZFMWNW3259. In summary, a significant level of sophistication has been implemented at this model stage, including:

- HCD: Final parameterisation (Table 3-2), conditioned intercepts (Table A-3), differentiated tunnel-wall skin (Table 5-3), as well as local adjustment at important junctions (ZFM871/ Northern boundary belt and Southern boundary belt/Sheet joints).
- HRD: Anisotropy (a = 3 in Equation 3-5) and depth trend defined by Equation 3-6.
- HSD: Parameterised as in SR-Site Forsmark, but K_z reduced by a factor of 10.
- SBA: Implemented as deterministic structures SBA1 to SBA7.
- Refined discretisation (maximum cell size is 8 m in the upper part of the bedrock).

Some improvement is accomplished in the evaluation with constraining data (Figure 5-2). Minor achievements are accomplished in simulated inflow (Figure C-36 and Table C-6). Differentiated skin at deformation-zone intercepts (Table 5-3) renders realistic levels of simulated HCD inflow (Table C-6). Grid refinement in the upper 200 m of the bedrock (side length of cells 8 m) renders a *poorer fit to head data*, which demonstrates dependence of grid resolution in the evaluation of model performance (see Section 4.4). Grid refinement was nevertheless retained in Model Exercise M7, in order to enhance the ECPM translation of stochastic features.

The level of achievement compared to the Initial Case (M0) is found to be small (e.g. Figure C-34 and Figure C-36), in relation to the additional level sophistication in the model setup. Again, results demonstrate 1) model insensitivity to parameterisation, and 2) limitations in using tunnel-inflow simulations for model calibration.

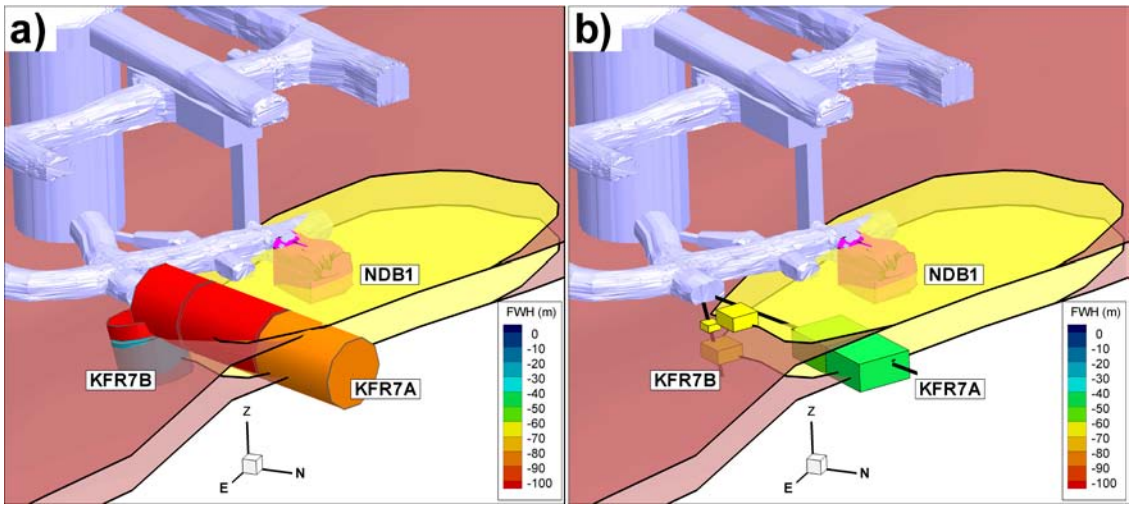

Figure 5-7. *Simulating head decrease at the ZFM871 intersection; a) measured data and b) simulation in Exercise M6. ZFM871 is extended to include KFR7A, the NDB1 geometry is included as a sink (pink shade), grouting is implemented as a low resistance within a radius of 55 m (yellow) and the transmissivity of ZFMNW0805A and B is reduced locally along their intersections with ZFM871.*

5.8 M7: Stochastic SBA-structures in areas outside borehole coverage

Model Exercises M4 to M6 include deterministic SBA-structures, SBA1 to SBA7. None of them are in direct contact with SFR, and owing to their location, their impact in current inflow simulations is negligible. However, their spatial extension, as well as potentially additional SBA-structures outside borehole coverage, is of key relevance for the planned SFR extension. As an example, simulation of the interference test using HFR101 as pumping borehole (Chapter 6) suggest the existence of additional horizontal hydraulic connections.

Model Exercise M7 was set up to explore the impact of additional SBA-type structures. The deterministic SBA-structures (SBA1 to SBA7) were complemented by a simplified stochastic representation of SBA-type structures beyond borehole coverage. Details of this setup are provided in Appendices B and C.8. The purpose of this exercise is to explore if the current tunnel-inflow setup provides additional indications on the existence (or absence) of SBA-structures near the existing SFR.

Due to several circumstances it is difficult to draw conclusions:

1) Only two realisations were addressed.
2) The grid resolution is clearly insufficient to resolve the anisotropy of SBA-type structures during ECPM translation.
3) Stochastic features in direct contact with the SFR facility are removed. This decision is motivated by the fact that all significantly flowing structures (if existing) are expected to have been grouted during tunnel construction. The decision is reasonable, but significantly reduces the role of these structures in the model setup.

The only notable impact of the stochastic SBA-type structures is a poorer fit in simulated head near the Silo (the KFR7A/B outliers marked by red oval in Figure C-37). This may reinforce earlier interpretations of particularly low-conductive rock mass around the Silo where so-called SBA-type structures are *absent*.

5.9 Simulating initial tunnel inflow

Earlier Model Exercises (M2 and M3) have demonstrated the need to implement skin resistance in order to avoid excessive simulated tunnel inflow from HCDs, at least if HCDs are parameterised from borehole data. The simulated inflow without skin, in setups M2a–c and M3a, exceeds the current inflow data by a factor of c 25, but also the estimated "undisturbed inflow" (estimated by "theoretical initial tunnel inflow at time $t = t_0$) by a factor of c 7 (Section 2.8.1). Additional potential resistances have been included in subsequent exercises M3b to M6, in terms of an effective HCD transmissivity, along structure junctions, as well as contact between HCD and HSD.

Limitations in constraining data and the model setup obscure inference on the exact location of these potential resistances. Realistic simulated inflow was accomplished by the introduction of skin (Model Exercise M3b). However, the skin also tends to mask the role of additional resistances. Therefore, it is of interest to simulate cases where the skin-resistance is reduced to only reflect grouting. This final test was performed for cases M7a and M7b.

Tunnel-wall conductivity at deformation-zone intersections were assigned $K_{skin} = 10^{-6}$ m/s for standard cement in the upper part of the facility, and $K_{skin} = 10^{-7}$ m/s for the finer grouting material in the NBT tunnel (Section 2.5). The simulated inflows are 1,100 to 1,050 L/min, which compares well to the estimated initial tunnel inflow at time t_0 (Section 2.8.1). This improvement, relative to M2 and M3a, has primarily been accomplished by 1) lowering the effective transmissivity of ZFMWNW0001, ZFMWNW1035 and ZFM871, and 2) implementing "HSD-choking" in upper part of the three zones of the Southern boundary belt. These results reinforce the previous notions that the tunnel-wall resistance is not confined to the bedrock immediate to the tunnel wall.

Table 5-3. Applied skin factors.

Deformation zone intercept	K_{skin} (m/s)	Factor[1]
Southern boundary belt	$1.04 \cdot 10^{-8}$	1.6
ZFMWNW1035	$4.55 \cdot 10^{-9}$	0.7
ZFMNNE0869	$4.55 \cdot 10^{-9}$	0.7
ZFMNE0870	$4.55 \cdot 10^{-9}$	0.7
ZFM871[2]	$1.3 \cdot 10^{-7}$	20
ZFMNE3118	$4.55 \cdot 10^{-9}$	0.7
ZFNNW1209	$4.55 \cdot 10^{-9}$	0.7
Silo	10^{-10}	1/65
HRD	$6.5 \cdot 10^{-10}$	1/10
Artificial intercepts[3]	$3.25 \cdot 10^{-9}$	0.5

1 Expressed as a multiple of the reference value $6.5 \cdot 10^{-9}$ m/s.

2 Not applied over single tunnel-wall grid cell, as shown in Figure 2-2. Conceptual illustration of inflow calculation. Grid cells completely inside the tunnel are removed (i.e. red cross, cell C). Grid cells intersected by the tunnel wall are prescribed an atmospheric pressure (i.e. cell B is assigned atmospheric pressure, H0 = z m). The cell wall between an intersected cell and its adjacent cell in the rock mass (i.e. illustrated by the blue line between cells A and B) are identified as an inflow surface. Such cell walls are classified by inflow area (Table 4-3) and assigned skin values., but over a 55 m radius.

3 Necessary to reduce model artifacts. Applied at ZFMNW0805B (the intercept a model artifact) and to HSD at the tunnel entrance (contact between tunnel and HSD is only a model artifact).

6 Interference tests

6.1 Context and objectives

Interference tests are useful for identifying and characterising large-scale, hydraulically significant structures. The experience from the SDM-Site Forsmark is that hydraulic interferences can provide key evidence for the characterisation of the superficial bedrock (i.e. existence and character of sheet joints). Therefore, hydraulic interferences have been evaluated during the SFR extension investigations. It should be noted that the response pattern in fractured rock does not only depend on hydraulic properties and connectivity between fractures, but also on the connectivity to hydraulic boundaries. These interferences occur below the Baltic Sea, close to an open underground facility, which is an unusual situation for this type of analysis.

The observed hydraulic responses during the SFR extension investigation have been evaluated by Walger et al. (2010). Most of these responses have been interpreted from various drilling activities. Such interpretations are useful for conceptual modelling, i.e. for definition of the so-called SBA-structures, see Appendix B in Öhman et al. (2012). Unfortunately, drilling responses are difficult to model numerically, as the hydraulic conditions are rarely known in detail and/or are difficult to represent numerically. However, in addition to the interpreted drilling responses, three controlled interference tests have also been performed. As described in Section 6.2, only two of these are meaningful to simulate. It was decided to simulate the interferences in a simplistic model setup of deterministic structures (details given in Section 6.3). The limitations of the tests are the following:

1) They have a relatively short duration, which necessitates transient simulations (introducing the highly uncertain parameter storativity, S, Equation 6-2).
2) Their location in the Central block is of high relevance to the SFR extension, but provides little confirmatory evidence in the sub-domain identified as most critical (Northern boundary belt and ZFMNNW1034).

The objective of this study is therefore *not* to establish a fine-tuned parameterisation, but to study the system in context of the conceptual hydrogeological model to gain further insight and confidence in the model.

The approach can be summarised as follows:

1) The level of detail in the model setup is kept to a minimum, focussing on the deterministically modelled structures that are assumed to be the key components of the hydrogeological system, i.e. relevant deformation zones and SBA-structures but excluding stochastic components of the DFN model and Unresolved PDZs.
2) The *in situ* head-field around the existing SFR facility is first simulated by a steady-state solution for the simplified model setup, where the overlying sea and the SFR tunnel are set as prescribed-head boundary conditions. The hydraulic contact to these boundaries is hampered by fitting tunnel-wall skin and sediment resistance that match inflow and head data.
3) Using the steady-state solution as starting point, the two interference tests are simulated transiently, including the pumping phase and the recovery phase.
4) The transient response is monitored in simulated borehole sections and compared with the data interpretations of Walger et al. (2010).
5) The model setup is modified in order to explore the general agreement versus data observations.

The data analysis presented in Öhman et al. (2012) suggests that at shallow depths the hydrogeological properties of deterministically modelled geological structures (HCD and SBA) are not very different from the hydraulic properties of the less fractured rock between zones (HRD). In particular, sub-horizontal fractures appear to be highly transmissive and not necessarily confined to deterministic deformation zones. On the other hand, the HRD is represented by a Hydro-DFN model, which introduces a stochastic component to simulations. In turn, this would cause the additional complexity and uncertainty in addressing multiple realizations. It was therefore decided only to include deterministic structures (HCD); the sub-horizontal component is partly represented by deterministic SBA-structures.

6.1.1 Hydraulic response measures

Hydraulic communication is quantified in terms of *strength* (related to monitored head decrease magnitude) and *speed* (pressure pulse propagation rate). It should be emphasised that these two characteristics are not necessary related, but depend on geometric configuration and on the hydraulic properties of flow paths, as well as the presence of hydraulic boundaries. The measured entities are head decrease, s (m), and response time, dt_L (s). The response time is defined as the time taken for the monitored head decrease to exceed a specified criterion, d_p (m). The head decrease criterion is here set to $d_p = 0.01$ m (Follin 2008). However, due to noise caused by sea-level fluctuations (Figure 6-5), it was decided to use a higher head decrease criterion in the interpretations at SFR, $d_p = 0.1$ m (Walger et al. 2010). This implies that low-head decrease responses, i.e. less than 0.1 m, are potentially disqualified as noise; even a low-magnitude head decrease can be rapid and relate to hydraulic significant features. It also implies that the quantified response times, dt_L (s), are larger as compared to e.g. SDM-Site Forsmark (i.e. as the head decrease (s) passes 0.01 m before reaching 0.1 m). The underlying data are presented in detail in Section 6.2.

Hydraulic diffusivity is a measure of the rate of hydraulic communication between a disturbance and an observation point. A highly transmissive, well-connected fracture system has a high hydraulic diffusivity, whereas a highly compartmentalised fracture system composed of poorly connected dead-end clusters has a lower diffusivity. Streltsova (1988) defined the *apparent hydraulic diffusivity*, α, for radial flow in a confined porous medium as:

$$\alpha = \frac{T}{S} = \frac{r_s^2}{4dt_L\left(1+{dt_L}/{t_p}\right)\ln\left(1+{t_p}/{dt_L}\right)} \qquad (6\text{-}1)$$

where T is transmissivity (m^2/s), S is storativity (–), r_s is the 3D radial distance between the disturbance and the monitored borehole section (m), t_p is the duration of the disturbance (s), and dt_L is the measured response time (s). Storativity is considerably more difficult to measure compared to transmissivity. It is therefore considered to be a highly uncertain parameter. Rhén et al. (1997) suggest an empirical relationship to estimate storativity from transmissivity:

$$S = 0.0007\ \sqrt{T} \qquad (6\text{-}2)$$

The *apparent storativity* has been evaluated for 27 responses to the HFR101 and KFR105 interference tests (Walger et al. 2010). These apparent values were obtained by type-curve matching of transient responses, and thus reflect effective values of an equivalent homogeneous medium. The obtained vales of the *apparent storativity* range from c $2\cdot10^{-5}$ to $2\cdot10^{-3}$, which exceeds the values estimated from the standard relationship Equation 6-2 by an average factor of 70. The values inferred by Walger et al. (2010) suggest a good hydraulic communication between the HCDs and HRDs, which implies a slow propagation rate of the pressure responses. The simulations reported here in Section 6.4 use effective storativity values based on the standard relationship, Equation 6-2, that is scaled by a factor to represent compartmentalisation. This scaling factor is found by trial and error.

Finally, since the apparent diffusivity in Equation 6-1 is based on an analogy to cylindrical flow in porous media, an alternative, more straight-forward measure of pressure propagation is used in parallel, the so-called *response index 1* (Walger et al. 2010). This index has the same units as hydraulic diffusivity, but avoids the analogy to cylindrical flow in porous media:

$$\textit{response index}\ 1 = \frac{r_s^2}{dt_L}, \qquad (6\text{-}3)$$

6.2 Presentation of data

Three interference tests have been performed and evaluated during the SFR extension investigation (Table 6-1). HFR101 is an open, percussion-drilled borehole with a groundwater level at c –30 m elevation. Thus, to cover anomalies above –30 m, the HTHB logging was performed as a short injection test (May 23, 2008), which only caused a response in the uppermost section of KFR02. However, on April 6, 2009 HFR101 was also pumped for three days, which caused considerably

stronger and more widespread responses. KFR105 is an underground borehole, drilled from the NBT tunnel of the existing SFR facility. The interference test in KFR105 was performed by releasing the shut-in pressure for one day. It should be noted that during the drilling of KFR105, groundwater from the borehole drained into the SFR tunnel. This caused similar, although gradual, disturbances that spread over a longer period of time. Out of the three controlled interference tests, only the pumping test of HFR101 and KFR105 are analysed further in this chapter (presented in Sections 6.2.2 and 6.2.3).

HFR101 and KFR105 have similar total transmissivity and the applied flow rates are also of similar magnitude. The main difference between the two tests, in terms of sinks/sources to the system, is therefore the test duration (three days and one day, respectively).

6.2.1 Initial state

The *in situ* head field at SFR is subject to head decrease from the existing facility (Figure 6-1), which in itself can be regarded as an on-going interference test. On the time scale of interference tests, this *in situ* head field is taken as the initial state. A steady-state solution that approximates this initial state is used as the starting point in the forthcoming transient simulation of interference tests. The monitored head data depend on the distance from SFR, as well as the strength in hydraulic connections to the hydraulic boundaries (i.e. the SFR facility and the overlying sea, respectively). The monitored section in HFR101 has a point-water head of c –31 m (8.04 to 209.3 m borehole length). This indicates an indirect connection to SFR, possibly via ZFMNE0870 or ZFMNE3118 (or the Unresolved PDZ, HFR101_DZ2), but also a comparatively poor connection to the sea, in spite of its shallow casing (at –4.65 m elevation); potentially indicating constrain by low-permeable sediments.

Thus, the head data provide local information on the *relative strength* between connections to the hydraulic boundaries that is useful for conditioning the steady state simulations. For example, the deepest sections of KFR104 and KFR105 are located at similar distance from SFR and intersect the same zone (ZFMWNW3267; Figure 6-1a), but indicate higher head decrease at depth (Figure 6-1b). This suggests that the hydraulic connection to SFR is relatively stronger in KFR104, while the relative connection to the sea is stronger in KFR105, and that the vertical connection between the two monitored sections is comparatively weak albeit they intersect the same zone.

The HCD transmissivity has been parameterised with respect to both borehole data and tunnel inflow (a calibration in which the HRD component was included, see Chapter 5). The objective of this study is therefore *not* to fine-tune this parameterisation. As the relative strength in connections to the hydraulic boundaries controls the head decrease pattern around SFR, two resistance parameters are calibrated to match head data, namely tunnel skin and the HCD/HSD contact (more precisely, K_{skin} and K_{HSD}; see Section 6.3).

6.2.2 The HFR101 interference test

HFR101 was pumped for 3 days with a flow rate that varied in the beginning but stabilised at c 10 L/min by the end of the flow period. The pressure in HFR101 was monitored during the pumping and recovery phases (Figure 6-2).

Table 6-1. Interference tests performed the SFR extension investigation.

Borehole	Length interval	Date (YYYY-MM-DD)	Duration (hrs)	Flow (L/min)	s_{max} (m)	Q/s_{max} (m^2/s)	Type
HFR101	8.04–209.3 m	2008-05-23	6.1	–22.4	–22.7	$1.6 \cdot 10^{-5}$	Injection
HFR101	8.04–209.3 m[1)]	2009-04-06	73.2	10.0	15.6	10^{-5}	Pumping
KFR105	0–306.81 m	2010-03-03	23.6	11.4	~100	$2 \cdot 10^{-6}$	Flushing

1) Owing to initial head decrease, the effective test interval is c 33 to 209.3 m.

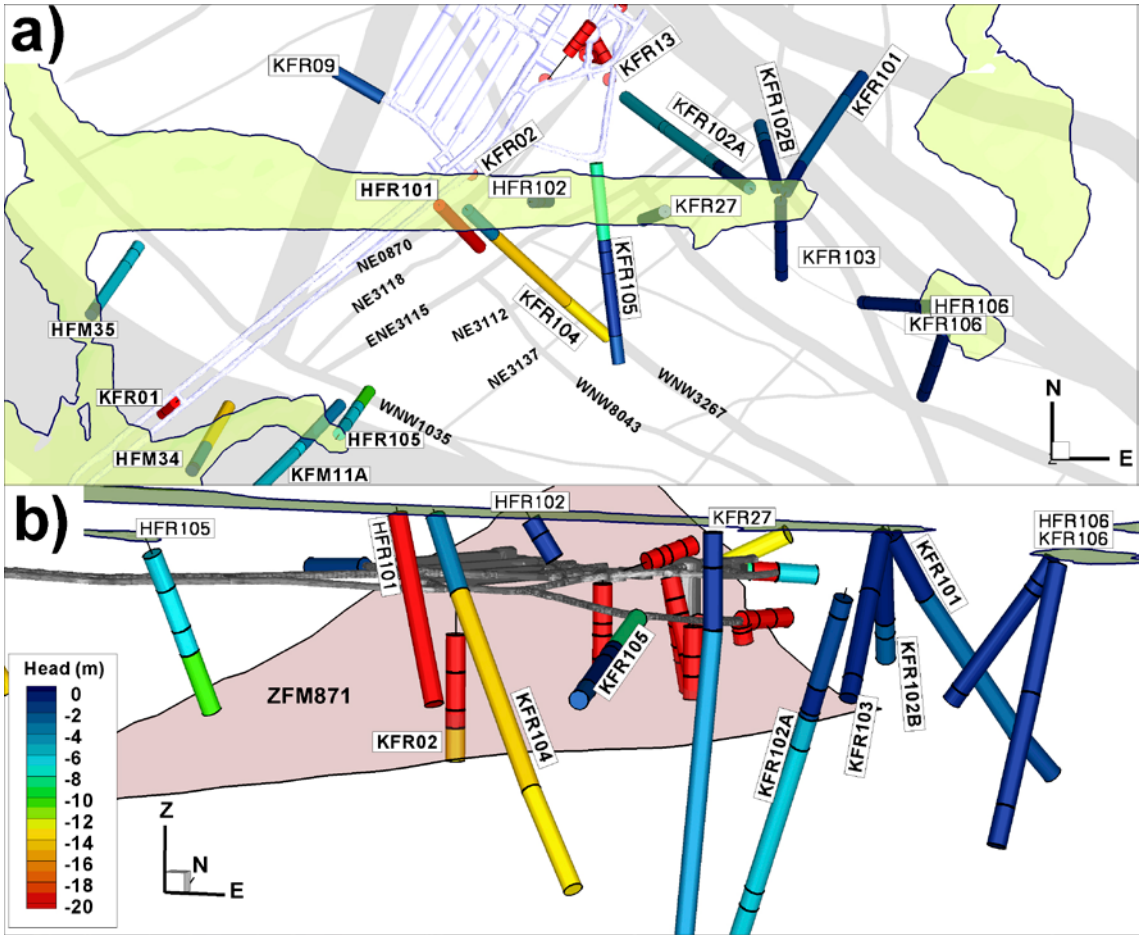

Figure 6-1. *Heads (m elevation) in monitored sections (PWH in surface boreholes and FWH in underground boreholes). Note that very low heads close to SFR (below –100 m) are not covered by the colour scale. The head in the deepest section in HFM34 cannot be measured but is below –14 m.*

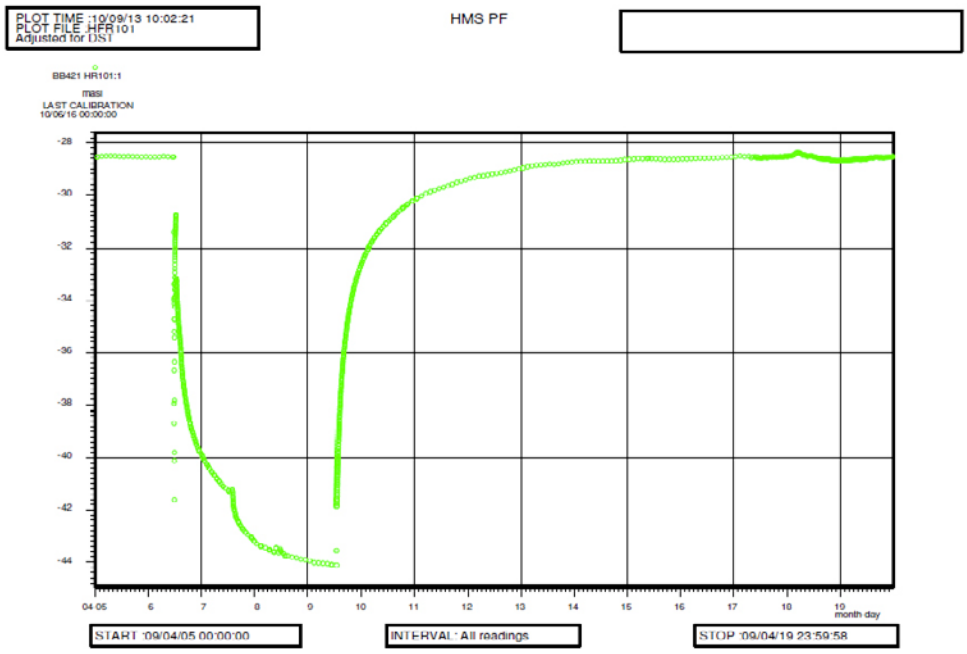

Figure 6-2. *Monitored head in HFR101 during pumping and recovery phase.*

Interferences are observed in KFR02, HFR105, and KFR104 (Figure 6-3); a common trait of these boreholes – including HFR101 – is that they all exhibit large head decrease in the initial state (Figure 6-1). Thus, the hydraulic connections observed in the interference test support the suspicions based on in situ head decrease data, alone. It should be noted that KFR105, KFR106, and HFR106 had not yet been drilled at the time of the test (their final positions are indicated by black lines in Figure 6-3). Responses are not expected to reach the remotely located KFR106 and HFR106, but it needs to be emphasised that potential responses in KFR105 could not be measured in the HFR101 test. The response in the mid-section of KFR104 is both the strongest (Figure 6-3) and, by far, the most rapid (Figure 6-4 and Figure 6-5); this indicates an unusual strong sub-horizontal hydraulic connection. This notion has bearings on the discussion on the spatial extension of ZFM871. In the geological model, ZFM871 is terminated against ZFMENE3115, based on lack of geological evidence (Curtis et al. 2011). On the other hand, a hydraulic connection does not necessarily provide evidence on the spatial extension of a geological structure; it may equally well relate to the type of highly transmissive sub-horizontal flowing fractures that has been interpreted to exist as a fringe around the Southern and Northern boundary belts (Öhman et al. 2012). For the purposes of this study, a deterministic, sub-horizontal structure has been included in the simplified model setup (Section 6.3).

The responses in monitored sections are shown as "relative head since pump start", t_0 (Figure 6-5). The air pressure was favourably stable during both the pumping and recovery phases (unlike the KFR105 test, Section 6.2.3). The responding sections (as interpreted by Walger et al. 2010) exhibit clear head decrease and recovery phases, while the non-responding sections follow the sea level fluctuation (Figure 6-5). The responses in HFR105 and KFR02_1 are very late, and are small in magnitude. The response criterion dilemma, discussed in Section 6.1.1, is evident in these data as the sea-level fluctuation itself exceeds 0.1 m (as indicated by blue and red lines in Figure 6-5b). It can be noted that the PWH in HFR102_2 is rather uncorrelated to sea-level fluctuations. The responses as interpreted by Walger et al. (2010) are summarised in Table 6-2.

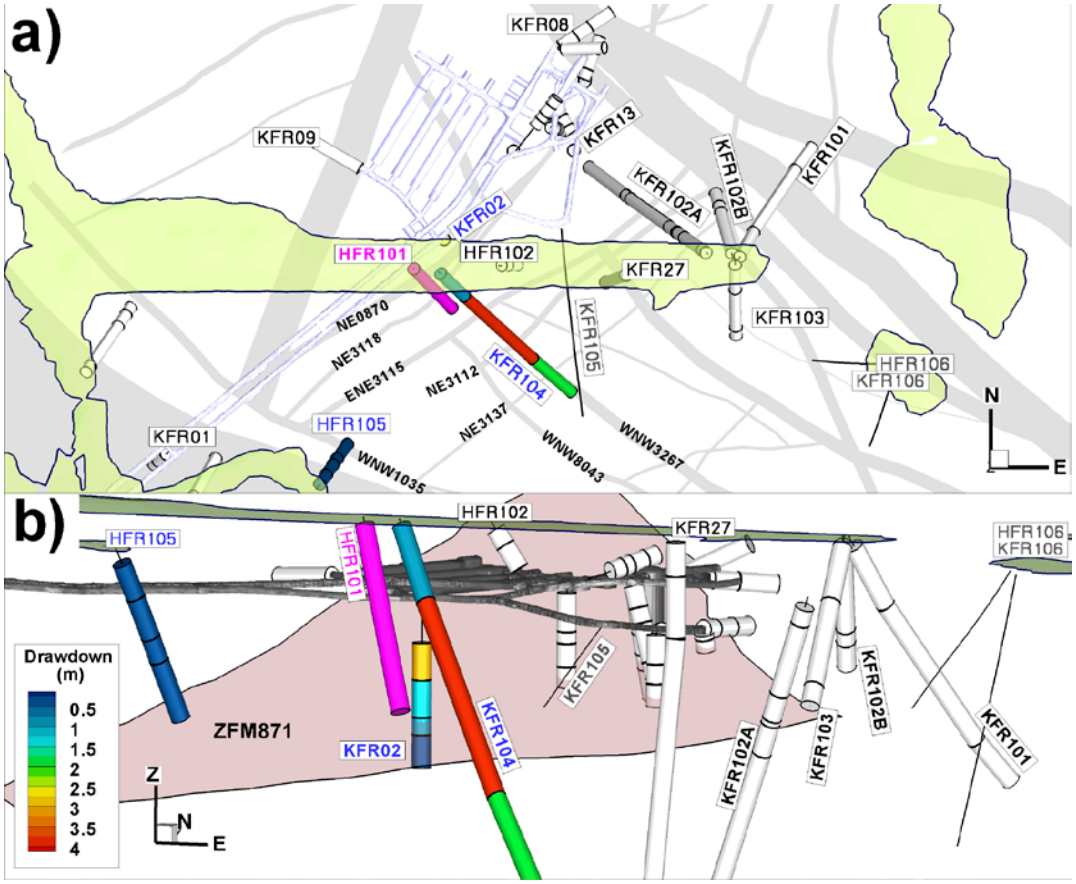

Figure 6-3. *Observed head decrease (m) from the three-day long pumping test in HFR101 (pink); a) top view and b) side-view from the South. The head decrease exceeds the response criterion, d_p, in KFR02, KFR104, and HFR105 (Figure 1-2). The largest observed radius of influence (spherical distance) was c 360 m. Deformation zones are shown as surface traces. The head decrease in HFR101 was c 16 m.*

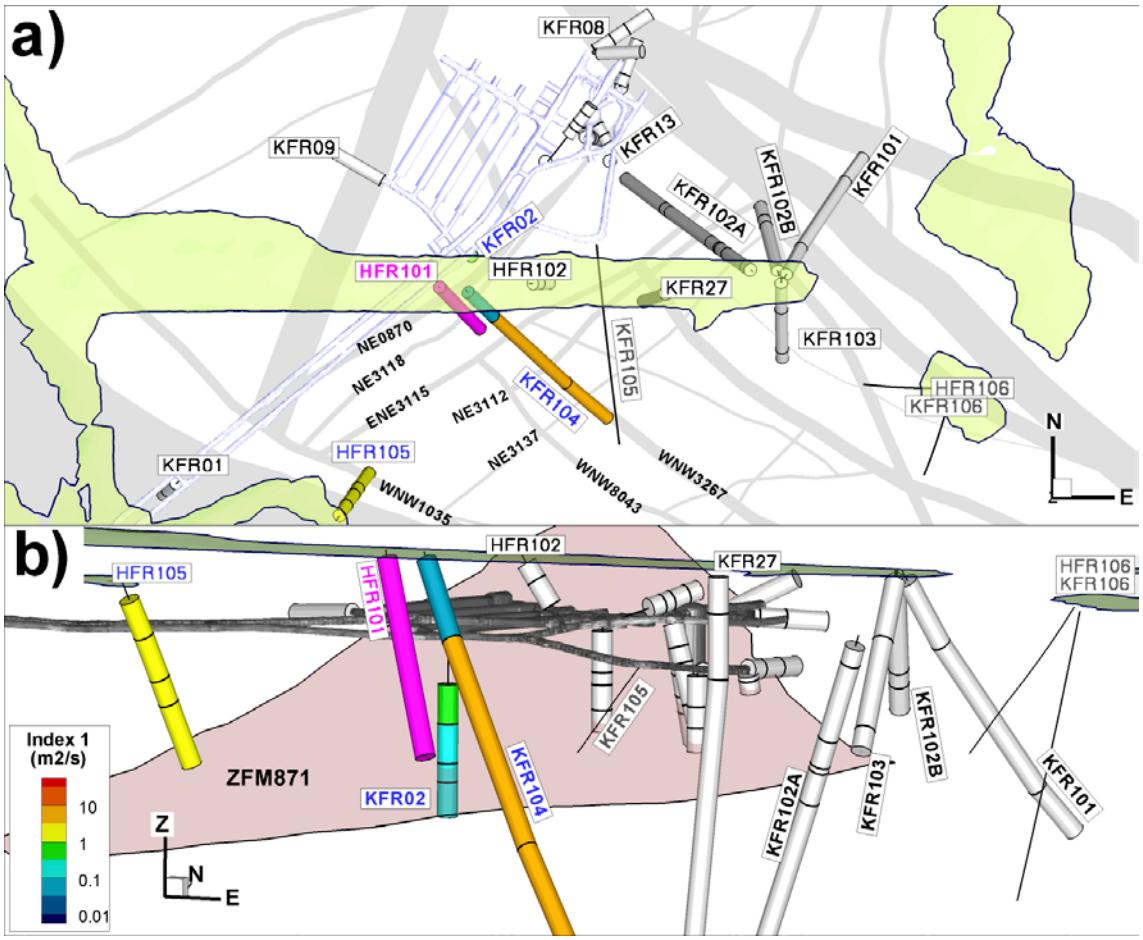

Figure 6-4. *Propagation rate in responses to the interference test in HFR101 (pink); a) top view and b) side-view from the South. The fastest propagation, as quantified by the "response index 1", is observed in KFR104 (Figure 1-2). Deformation zones are shown as surface traces.*

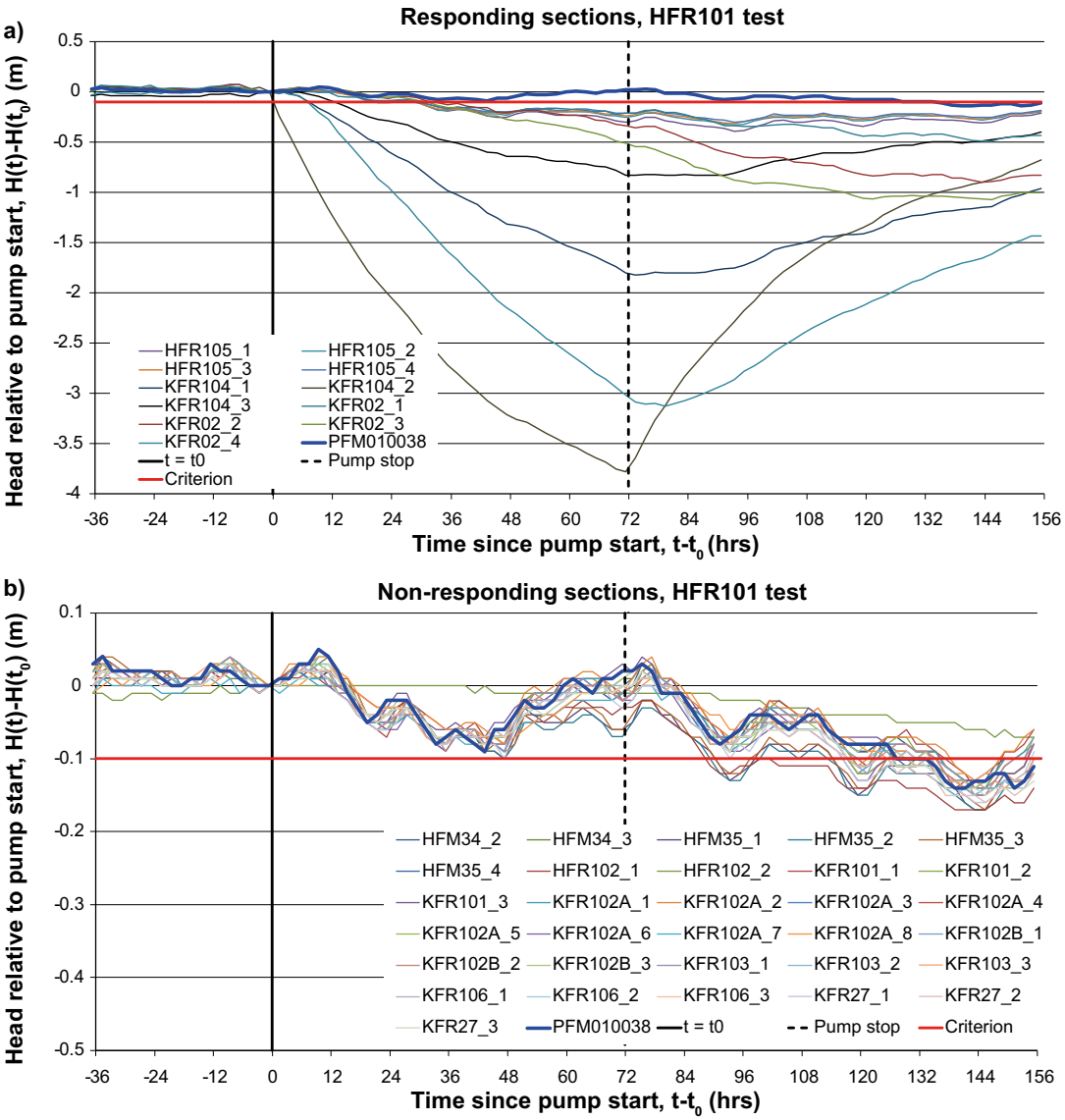

Figure 6-5. *Monitored head (m elevation) relative to pump start in the HFR101 interference test; a) Responding sections, and b) non-responding sections. Sea level is indicated by the blue line (PFM010038).*

6.2.3 The KFR105 interference test

KFR105 is an underground, sub-horizontal borehole drilled south from the NBT tunnel of the existing SFR (pink cylinder in Figure 6-7). The interference was caused by releasing the shut-in pressure for c 24 hrs from an outlet located at c –107 m elevation. The total flow rate from all sections was c 11.4 L/min by the end of the flow period. The monitored head indicates rapid head decrease (equivalent to atmospheric pressure at the outlet level, except for sections 2 and 4; Figure 6-6), as well as rapid recovery. Perhaps the tubing resistance for sections 2 and 4 is large relative to the inflow at these sections. The deepest section KFR105_1 has a notably slower recovery, which can be related to its poor hydraulic communication with the deep section of KFR104 (See 6.2.1). At the time of the KFR105 interference test, all boreholes were installed and monitored. Unfortunately, there was a leakage between sections 3 and 8 in KFR102A, and therefore, responses in these sections cannot be differentiated.

The strongest response is found in KFR27_2 (Figure 6-7). No extremely fast responses are observed, although the response in KFR104 stand out as slow (Figure 6-8). This reinforces the notions on poor communication between KFR104 and KFR105 (Section 6.2.1). It is noteworthy that even the deepest section of KFR102A responds (–400 to –537 m elevation). It should also be noted that interpretation of drilling activities for KFR105 render additional slow-responding sections (Figure 6-9). On the contrary, no responses were observed in the two deepest sections of KFR102A.

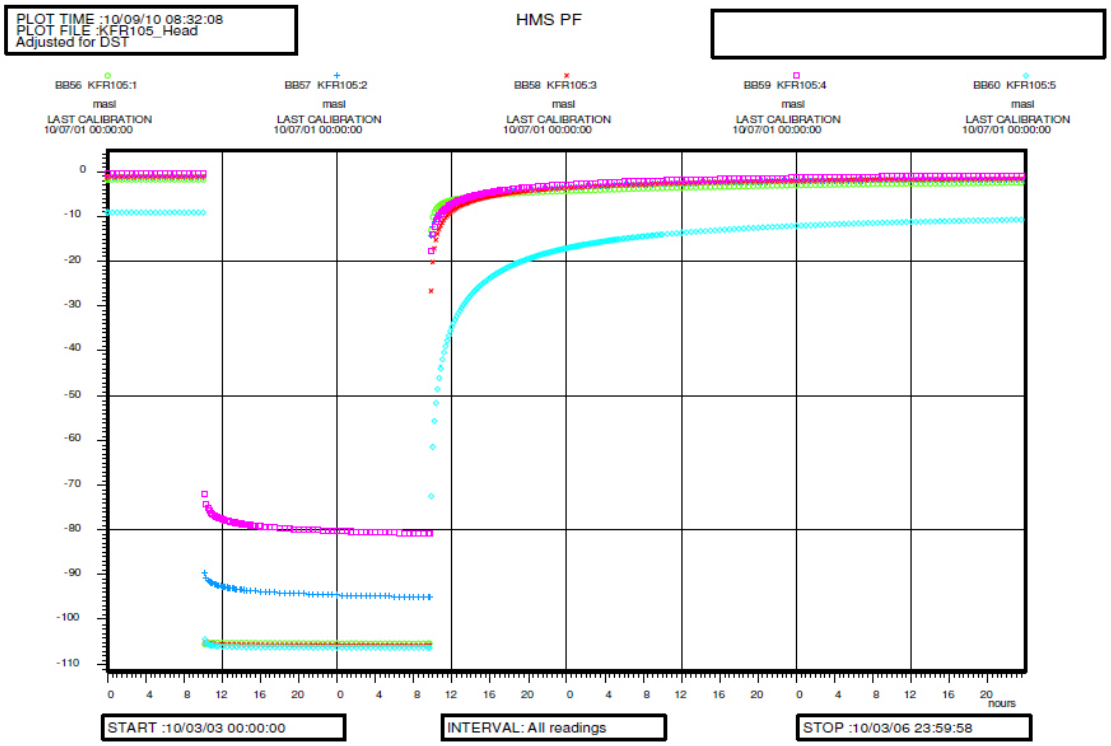

Figure 6-6. *Monitored head in KFR105 during release of shut-in pressure and recovery phase (reproduced from Walger et al. 2010). Atmospheric pressure at the outlet corresponds to a head of –107 m.*

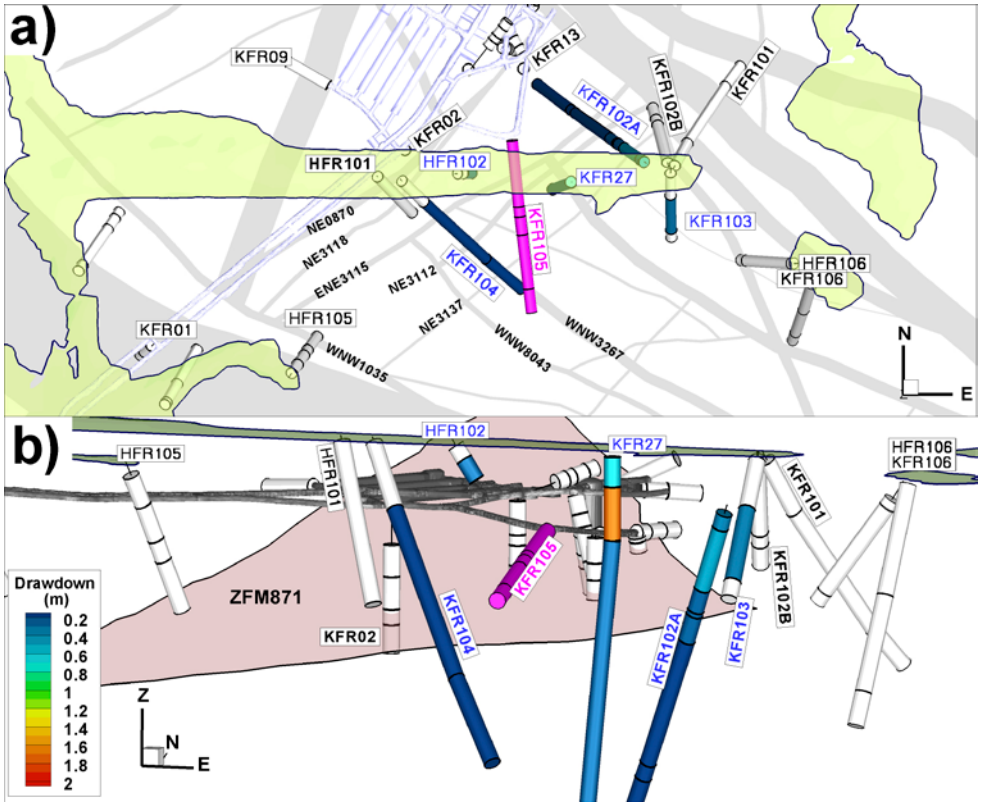

Figure 6-7. *Observed head decrease (m) from the interference test in KFR105 (pink); a) top view and b) side-view from the south. Head decrease exceeds response criterion, d_p, in HFR102, KFR102A, KFR103, KFR104, and KFR27 (Figure 1-2). The largest observed radius of influence (spherical distance) was c 400 m. Deformation zones are shown as surface traces. The interference was performed by releasing the shut-in pressure during c 24 hrs.*

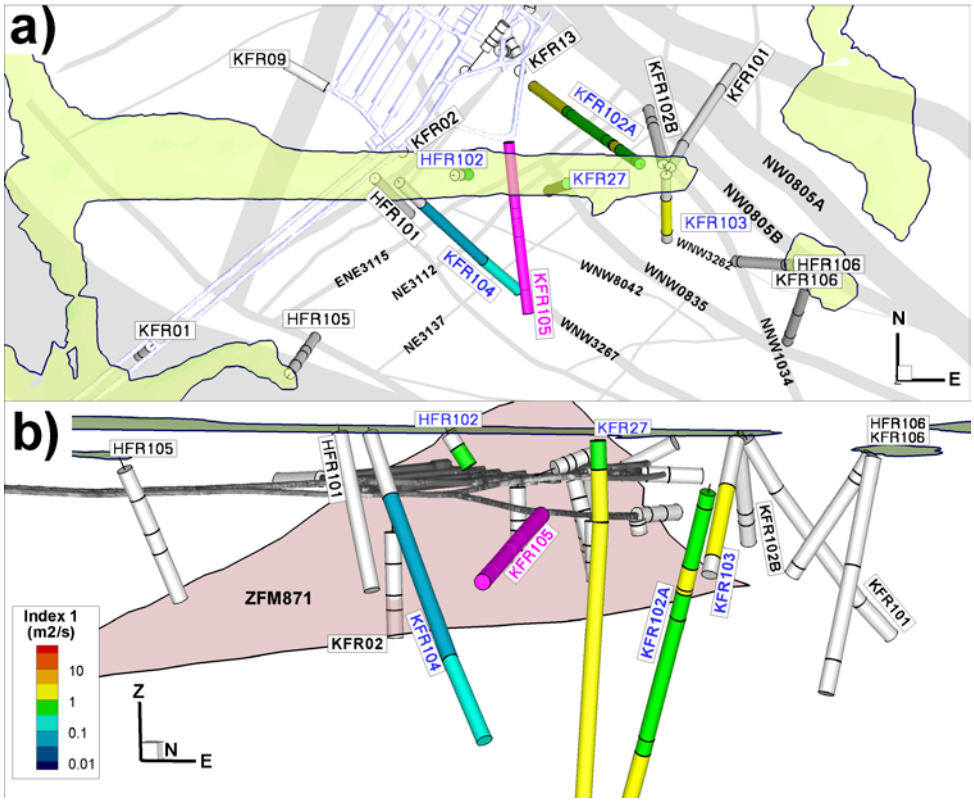

Figure 6-8. *Propagation rate in responses to the interference test in KFR105 (pink); a) top view and b) side-view from the south. Deformation zones are shown as surface traces.*

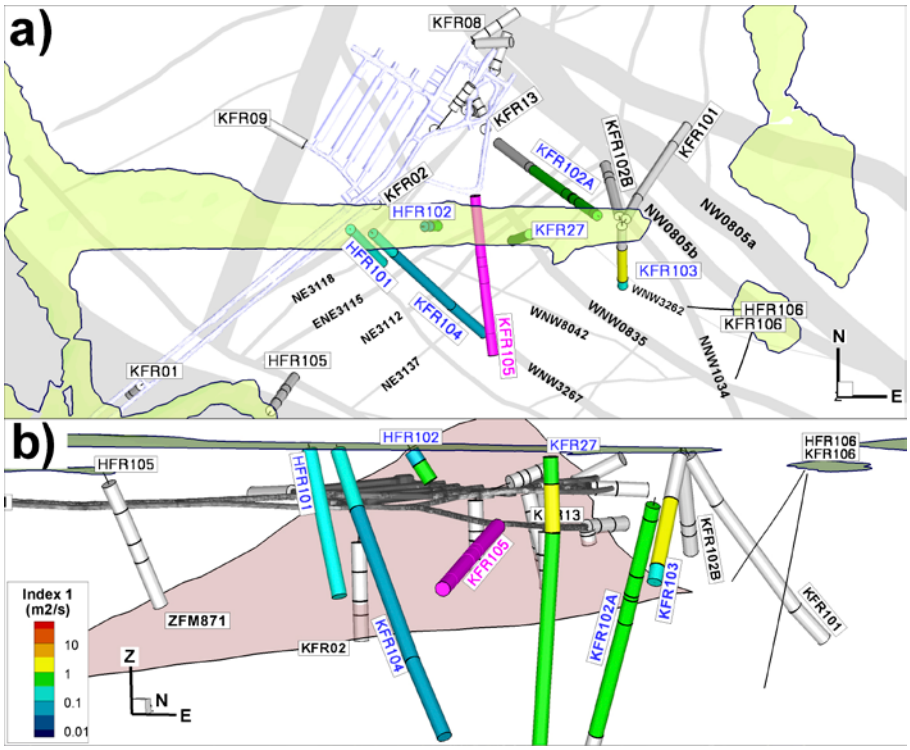

Figure 6-9. *Hydraulic responses to the drilling of KFR105 (pink) in April–June 2009; a) top view and b) side-view from the south. In addition to observations during the controlled interference test (March 3, 2010; Figure 6-8), slow responses are also observed in HFR101, the uppermost sections of HFR102 and KFR104, and the deepest section of KFR103.*

Similar to HFR101 test, the "responding" sections (as interpreted by Walger et al. 2010) exhibit clear head decrease and recovery phases, while the "non-responding" sections follow the sea level fluctuation Figure 6-10. However, a couple of differences can be noted. The head decrease in the uppermost sections of KFR102A (Chapters 7 and 8) appears to start 12 hrs after initiation of the test, and the maximum head decrease is reached c 24 hrs after the test has ended (i.e. during recovery). It cannot be ruled out that the initial head *increase* in KFR27_2 (red arrow Figure 6-10) is caused by field preparations related to initiation of the test (Walger et al. 2010). During the recovery phase, there is a gradually increasing offset from the sea level among the non-responding sections. These could potentially be late responses (i.e. similar to KFR102A). However, during this test there a significant change of air pressure occurred. Therefore, an effort was made to filter out the effect of air pressure change (Section 6.2.4).

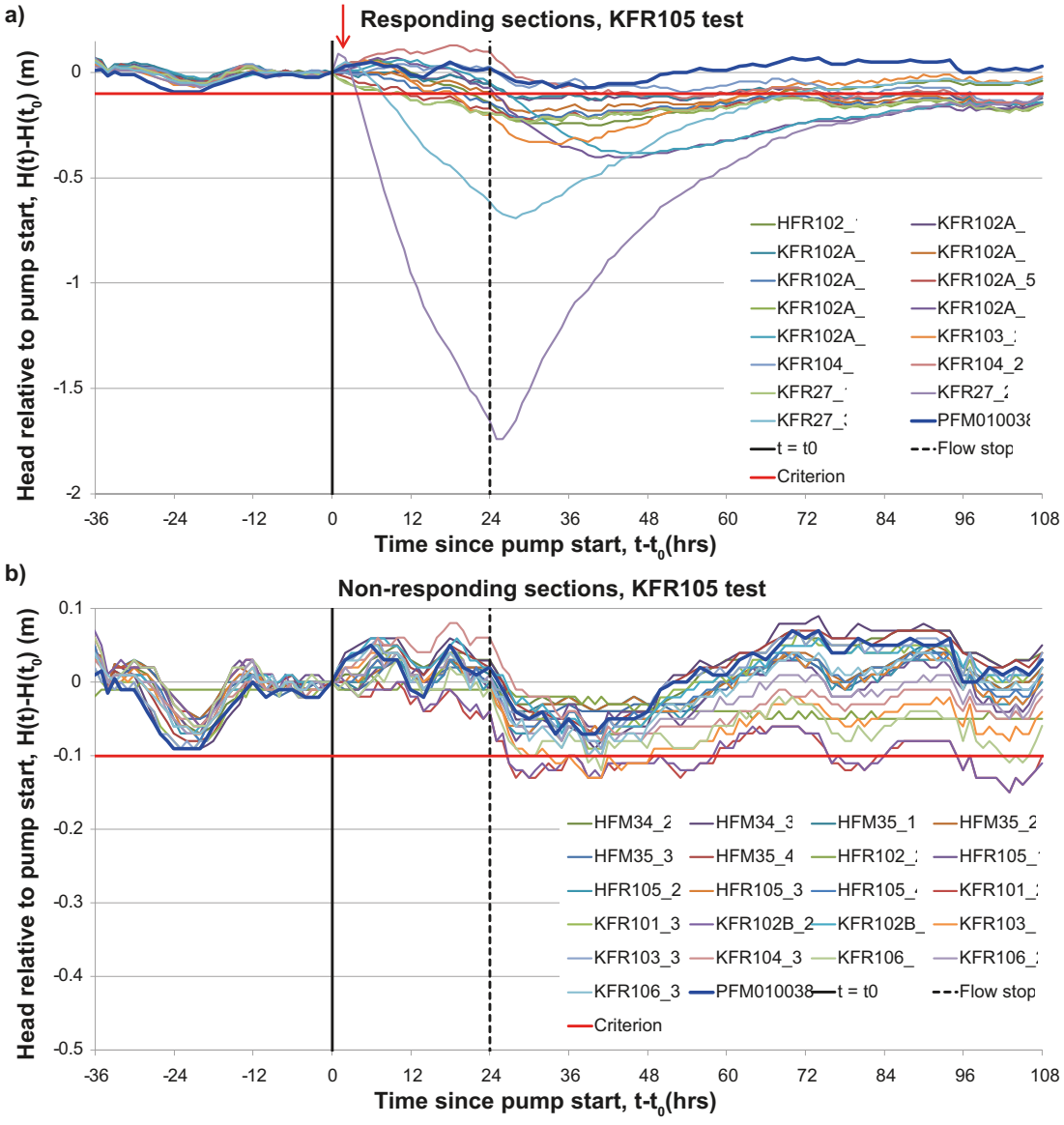

Figure 6-10. *Monitored head relative to pump start in the HFR101 interference test; a) Responding sections, and b) non-responding sections. Sea level indicated by blue line (PFM010038). A suspicious initial head increase is indicated in KFR27_2 (red arrow).*

6.2.4 Data noise filtering

An air pressure change occurred during the KFR105 test (Figure 6-11). In comparison, the air pressure was more stable during the HFR101 test. An attempt was made to reduce the noise level in data by means of multiple regression. A time period was analysed, September 3–12, 2009, during which a similar air pressure event took place, but where monitored head data are not disturbed by interference tests (red line in Figure 6-11). The undisturbed relationship of head was estimated as functions of sea level fluctuation and air pressure (i.e. $H(t) = x_1 * \text{sea level}(t) + x_2 * \text{air pressure}(t)$). The obtained coefficients vary somewhat among borehole sections, but the typical values are 0.7 for sea level and –0.2 for air pressure (if air pressure is expressed in head units). HFR102_2 is relatively unaffected by sea level and air pressure, its coefficients were only 0.03 and 0.09, respectively. An interesting finding in this analysis is that the uppermost sections are consistently more affected by the sea (high coefficients), while the deepest sections are more consistently affected by air pressure (increasingly negative coefficients).

In a second step, the obtained coefficients are subtracted from the monitored head data during the KFR105 test, in order to reduce the noise level (Figure 6-12). Reducing the air-pressure and sea level components is helpful for enhancing the contrasting pattern between "responding" and "non-responding" sections, as defined by Walger et al. (2010). Although a substantial noise component still remains in the "non-responding" data, the remaining pattern seems unrelated to the KFR105 test. The early rise in head of "responding" sections, just after test initiation, seems to occur in several sections. Perhaps, the field preparations for the KFR105 test accidentally caused a temporary source term.

6.2.5 Structural inference

HFR101 intersects three structures: ZFMNE0870 (Zone 9), an Unresolved PDZ (HFR101_DZ2), and ZFMNE3118. HFR101 is a percussion borehole and has therefore been investigated by the HTHB method. The transmissivity in its upper intercept, ZFMNE0870, is below detection limit (on the order 10^{-7} m^2/s). Its deep intercept ZFMNE3118 has a transmissivity of $2.5 \cdot 10^{-7}$ m^2/s. The largest transmissivity, $2.8 \cdot 10^{-6}$ m^2/s, is found between the two deterministically modelled deformation zones, inside HFR101_DZ2. Based on orientation estimates of this Unresolved PDZ, it has been interpreted as a splay to either of the ambient deterministic deformation zones (ZFMNE0870 or ZFMNE3118). Unresolved PDZs are not included in simulations, and therefore the transmissivity of HFR101_DZ2 is instead added to the ZFMNE3118 intercept. The reason for not choosing the ZFMNE0870 intercept is that the pumped groundwater level is below this intercept, and therefore it is unclear if the pumping influences ZFMNE0870. Furthermore, it is suspected that the strong hydraulic connection between HFR101 and KFR104 relates to a horizontal component that is not included in the deterministic modelling, possibly an extension of ZFM871, an Unresolved PDZ, or a sub-horizontal high-transmissive structure of SBA-type. Therefore the inclusion of such a structure is tested (Section 6.3).

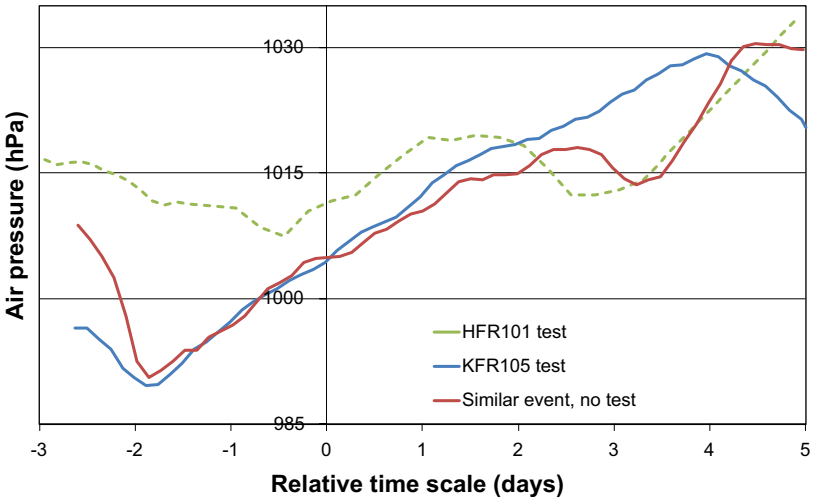

Figure 6-11. *Monitored air pressure during the HFR101 and KFR105 tests, as well as an undisturbed period with similar pressure change.*

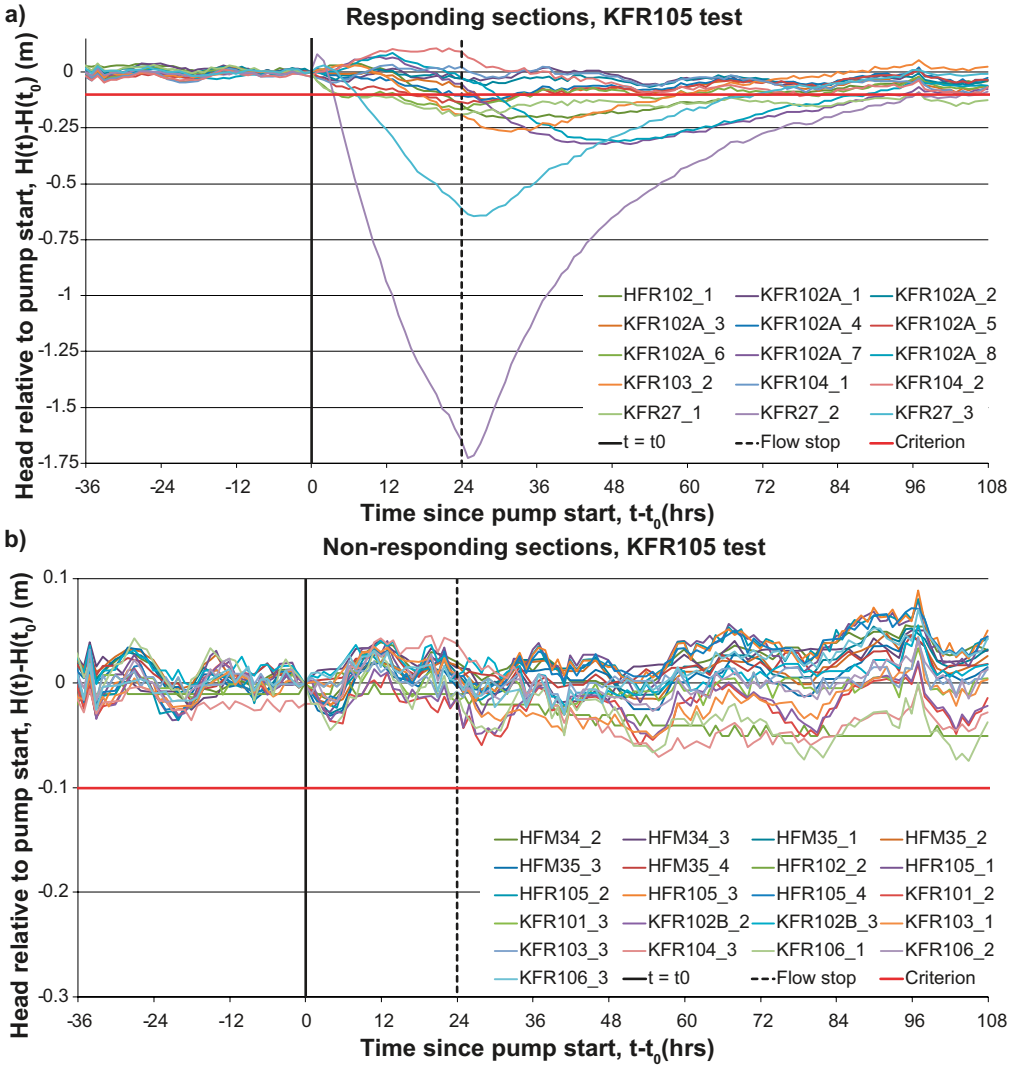

Figure 6-12. *Head during the KFR105 test where disturbance from sea level fluctuations and changing air pressure has been reduced by multiple regression.*

KFR105 intersects 6 structures: ZFMENE3115, ZFMNE3112, ZFMWNW8042, ZFMNE3137, ZFMWNW3267, KFR105_DZ5. Out of these intercepts ZFMWNW8042 has the highest transmissivity, $2.7 \cdot 10^{-7}$ m^2/s, while the others are considerably less transmissive, $2.3 \cdot 10^{-9}$ m^2/s to $4.1 \cdot 10^{-8}$ m^2/s. The drilling of KFR105 caused interferences that were related to reaching 133 m borehole length (KFR105_4). This borehole length coincides with the single most transmissive PFL-f, $6.5 \cdot 10^{-7}$ m^2/s, and it is located in HRD and steeply dipping. Shallow responses from the KFR105 test are suspected to involve SBA1, whereas deep responses are suspected to involve SBA6. None of these SBA-structures intersect KFR105, but they may be indirectly involved in responses.

Structural intercepts for responding sections are provided in Table 6-2. These serve as simulation targets in the forthcoming simulations (Section 6.5). Most sections have at least one structural intercept. A few responding sections lack intercepts: KFR02_1, KFR02_4, KFR102A_4, KFR102A_5, and KFR27_3; these are handled separately (Section 6.3.4). Prior speculations on the different roles of structures in these responses are presented in Table 6-3.

Table 6-2. Structural intercepts in responding sections.

Test borehole	Response	Response time (hrs)	H_i (m)	H_{final} (m)	ΔH (m)	Responding structure
HFR101	KFR02_4	7.7	–40.65	–43.79	3.14	None, close to NE0870
	KFR02_3	31.7	–28.36	–29.44	1.08	ZFM871 (HFR101_DZ2)
	KFR02_2	33.3	–24.94	–25.84	0.90	ZFM871
	KFR02_1	25.0	–16.09	–16.58	0.49	None
	HFR105_4	29.2	–6.02	–6.32	0.30	WNW0001
	HFR105_3	29.2	–6.38	–6.69	0.31	WNW0001
	HFR105_2	29.2	–6.38	–6.70	0.32	WNW1035
	HFR105_1	28.3	–10.96	–11.34	0.38	WNW1035
	KFR104_3	25.0	–3.39	–4.21	0.82	NE3118
	KFR104_2	1.2	–13.69	–17.51	3.82	ENE3115,NE3112
	KFR104_1	8.0	–13.44	–15.26	1.82	NE3137,WNW3267
KFR105	HFR102_1	20.8	–1.23	–1.48	0.25	SBA1
	KFR102A_8	27.5	–1.10	–1.48	0.38	SBA2
	KFR102A_7	24.7	–1.23	–1.64	0.41	NE3137
	KFR102A_6	10.0	–3.63	–3.86	0.23	SBA6
	KFR102A_5	11.8	–3.70	–3.93	0.23	None
	KFR102A_4	18.3	–3.98	–4.21	0.23	None
	KFR102A_3	24.2	–5.02	–5.21	0.19	NE3112
	KFR102A_2	31.7	–5.39	–5.52	0.13	ENE3115
	KFR102A_1	31.7	–5.17	–5.30	0.13	ENE3115
	KFR103_2	16.7	–0.52	–0.87	0.35	SBA2,SBA3 (close to WNW3262)
	KFR104_2	45.0	–15.13	–15.26	0.13	ENE3115,NE3112
	KFR104_1	90.0	–14.28	–14.43	0.15	NE3137,WNW3267
	KFR27_3	11.0	–0.57	–1.09	0.52	None (close to SBA1, WNW0835)
	KFR27_2	3.8	–0.74	–2.48	1.74	SBA1, SBA2, WNW0835
	KFR27_1	10.0	–3.60	–3.83	0.23	SBA6, WNW0835

Table 6-3. Speculated role of structures in responses.

Structure	Test	Responding section	Response time (hrs)	ΔH (m)	Suspected route
Gently dipping structures					
ZFM871	HFR101	KFR02_2	33.3	0.90	NE0870
		KFR02_3	31.7	1.08	
		KFR104_2	1.2	3.82	Extension of ZFM871?
		KFR104_1	8.0	1.82	
SBA6	KFR105	(KFR102A_4)	18.3	0.23	Indirect, via steeply dipping ZFMs or fracture
		(KFR102A_5)	11.8	0.23	
		KFR102A_6	10.0	0.23	
		KFR27_1	10.0	0.23	(WNW0835)
SBA1/SBA2	KFR105	HFR102_1	20.8	0.25	Indirect via KFR27_2 (involving ENE3115, WNW0835)
		KFR103_2	16.7	0.35	
		(KFR27_3)	11.0	0.52	
		KFR102A_8	27.5	0.38	
ENE to NNE set					
NE0870	HFR101	KFR02_4	7.7	3.14	Direct (via HRD)
ENE3115/NE3112	HFR101	KFR104_2	1.2	3.82	Via NE3118, ZFM871
	KFR105		45	0.13	Direct
ENE3115	KFR105	KFR102A_1	31.7	0.13	Direct
		KFR102A_2	31.7	0.13	Direct
NE3112	KFR105	KFR102A_3	24.2	0.19	Direct
NE3118	HFR101	KFR104_3	25.0	0.82	Direct
NE3137	KFR105	KFR102_7	24.7	0.41	Direct
NE3137/WNW3267	HFR101	KFR104_1	8.0	1.82	Possibly ZFM871?
	KFR105		90.0	0.15	Direct
WNW to NW set					
WNW0001	HFR101	HFR105_3, HFR105_4	29.2	0.30	NE0870, NE3118, ZFM871
WNW1035	HFR101	HFR105_1, HFR105_2	28.3	0.38	NE0870, NE3118, ZFM871
			29.2	0.32	
WNW0835	KFR105	KFR27_2	3.8	1.74	ENE3115/NE3112

6.3 Model setup in FracMan

As stated earlier, the data at hand are considered insufficient for fine-tuning the parameterisation of the hydrogeological model. Instead, the analysis is intended to test if the model can reproduce the hydraulic responses *reasonably well*, and if required modifications are in accordance with the conceptual model. For this purpose, it is judged sufficient to apply a simplistic model setup, where only deterministic structures are included. The decision *not* to include stochastic features (HRD and Unresolved PDZs) was taken to circumvent the additional complexity in addressing multiple realizations. The expected effect of neglecting HRD and Unresolved PDZs is that horizontal channelling is underrepresented. Furthermore, the homogeneous hydraulic parameterisation of modelled structures (with exception of imposed depth trends and local borehole conditioning) potentially exaggerates the hydraulic continuity within and between structures.

6.3.1 Modelled structures

Deformation zones

The deformation zones are parameterised according to Table 3-2 (i.e. same as Model Exercise M6). Out of the 40 deterministically modelled deformation zones in the SFR Regional domain, only 20 were considered relevant for simulating the interference tests (Figure 6-13). The remaining 20 structures (shown as grey planes in Figure 6-13) were excluded to reduce computational demand, and to shift the focus towards the near-field around the performed interference tests. The Southern and Northern boundary belts, as well as ZFMNNE0869 and ZFMNNW1034, have been interpreted to act as positive (constant head) hydraulic boundaries around the Central block (Öhman et al. 2012). Hence, deformation zones located outside these structures are not included. In addition, four deformation zones located inside the Central block are also excluded (ZFMNNE3130, ZFMWNW3268, ZFMENE3135, ZFMNE3134). The hydraulic characteristics of these four structures are highly uncertain, as they lack borehole intercepts. However, it is assumed that they are low-transmissive (Table 3-2).

SBA-structures

SBA-structures SBA1 to SBA7 are included in the model setup (Section 3.4.3; Figure 6-14). Similarly to Model Exercise M6, SBA8 is not included. There are two reasons for excluding SBA8: 1) Due to grouting, it is not expected to have an active role in current tunnel inflow, and 2) its modelled geometry is of low confidence. Specifically, its geometry is not based on hydraulic interference data, but on tunnel trace mapping, grouting records and anomalous transmissivity without oriented fracture data, see Öhman et al. (2012). The SBA-structures have primarily been modelled based on observed responses from drilling activities. Unfortunately, drilling disturbances cannot be modelled (discussed in Section 6.1). Hence, the simulations in this chapter are not expected to provide conclusive evidence regarding the existence and character of SBA-structures.

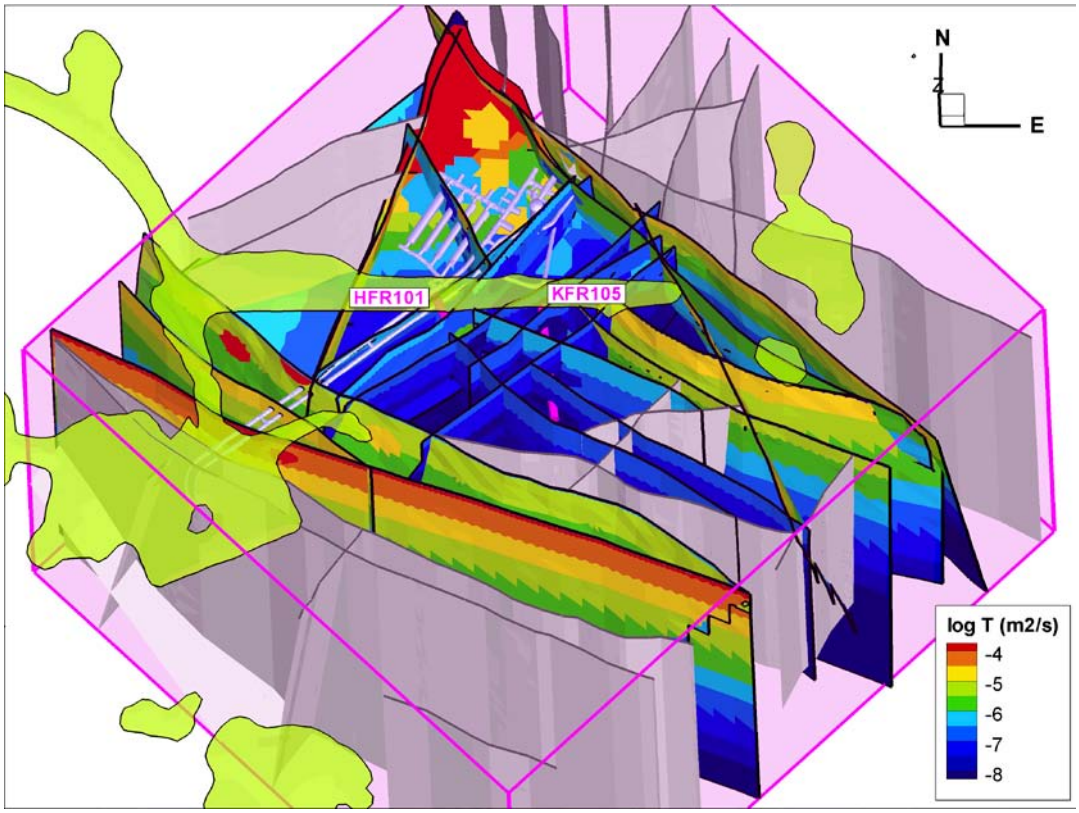

Figure 6-13. *Deformation zones included in the model setup coloured by transmissivity parameterisation (Table 3-2). Excluded deformation zones are shown grey-shaded. Boreholes where interference tests were performed are shown as pink cylinders. Ground surface is shown as transparent green shade.*

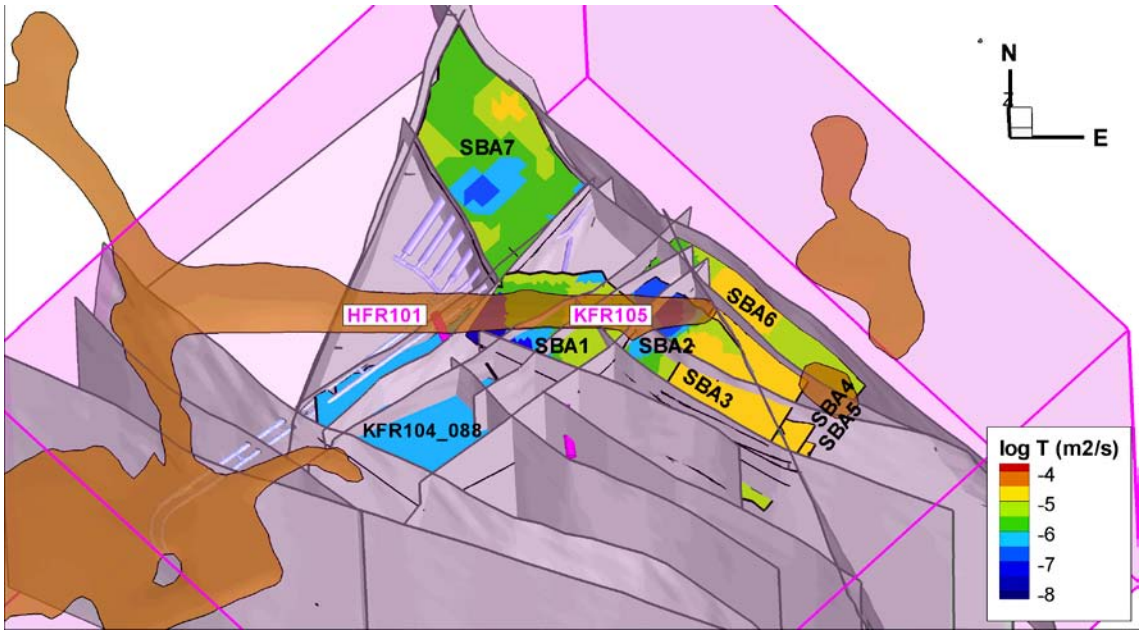

Figure 6-14. *Sub-horizontal structures (SBA1-SBA7) included in the model setup coloured by transmissivity parameterisation. A single PFL-f record (KFR104, no. 88) is also included as a deterministic structure. Deformation zones are shown grey-shaded. Boreholes where interference tests were performed are shown as pink cylinders. Ground surface is shown as transparent brown shade.*

However, SBA1, SBA2 and SBA6 are potentially also involved in the hydraulic tests that are addressed in this study (Table 6-3).

An exceptional horizontal hydraulic connection is indicated in the vicinity of KFR104, both by the *in situ* head decrease (Section 6.2.1) and by the rapid response to the HFR101 test (Section 6.2.2). This hydraulic connection has been speculated to be 1) a potential extension of ZFM871, 2) an Unresolved PDZ, or 3) a sub-horizontal high-transmissive structure of SBA-type. Irrespective of which, it must be explicitly represented as a deterministic structure in the simulations. It is noteworthy that SBA8, which is not included in simulations, is defined in the vicinity of this hydraulic connection.

A rudimentary geometry was defined for this feature. It was decided to extrapolate a large plane from a selected PFL-f in KFR104. The criteria for the candidate PFL-f were: exceptional transmissivity, horizontal to gently dipping orientation, and indication of large head decrease (Table 6-4). Different extrapolations were tested and it was finally decided to select KFR104_088 (light-blue structure in Figure 6-14) as its extrapolated plane does not intersect HFR101 (located below HFR101). The extrapolated plane terminates against steeply dipping deformation zones: ZFMNE0870, ZFMWNW1035, and ZFMNE3137, and also against zone ZFM871.

Moreover, borehole sections intersecting more than one structure potentially short-circuit the pressure propagation between structures. Hence, such borehole intersections are represented in the numerical grid as artificial channels of high transmissivity and low storativity (10^{-4} m^2/s and 10^{-7}, respectively).

Table 6-4. Candidate PFL-f for deterministically modelled plane.

PFL-f_No.	Borehole length (m)	Strike (º)	Dip (º)	Elevation (m)	T (m^2/s)	FWH (m)
KFR104_052	109.2	334	13	–85.93	$1.6 \cdot 10^{-7}$	–11.3
KFR104_080	209.0	113	10	–164.99	$3.3 \cdot 10^{-7}$	–15.9
KFR104_088	293.5	356	24	–230.44	$3.0 \cdot 10^{-7}$	NA

6.3.2 Boundary conditions and parameterisation

The purpose of these initial-state simulations is to obtain a realistic starting point for the transient simulations. As the primary purpose is *not* to address tunnel inflow in detail, the model setup is simplified somewhat compared to the preceding DarcyTools Model Exercises (Chapter 5). A constant density system is assumed (i.e. neglecting density effects related to salinity or temperature). Constant head boundary conditions are prescribed at two locations: at the top of the model (i.e. the seafloor) and at tunnel-wall intersections (i.e. sink terms). No boundary conditions are prescribed to the vertical sides or to the bottom of the SFR Regional model domain, which is equivalent of imposed no-flow conditions. The tunnel intersection of ZFMWNW001 is taken as an example of the numerical setup (Figure 6-16).

The top boundary is a prescribed constant head, which corresponds to steady state with the sea if the salinity difference between the groundwater and the overlying Baltic Sea is negligible (i.e. H = 0 m at z = 0 m). The hydraulic contact to the sea is regulated by adjusting the transmissivity in the uppermost 10 m of modelled structures (Figure 6-16). This adjustment is intended to reflect the potential resistance between the HSD and HCD, and it is treated as a fitting parameter in order to match the *in situ* head (Figure 6-1). The HSD resistivity is implemented on the form $T = K_{HSD} \cdot b$, where K_{HSD} is the effective conductivity of sediments and b is the width of the zone. The expanded model geometry of ZFM871 is used (see Section 5.7), which causes an unintentional outcropping in the North. To effectively eliminate the unintentional direct seafloor contact, the transmissivity of ZFM871 is therefore locally reduced to 10^{-10} m^2/s in the northern corner (dark blue in Figure 6-13).

Tunnel-wall intersections are prescribed atmospheric pressure (i.e. H = z, assigned to nodes located inside and along the perimeter of the tunnel wall; Figure 6-16). Minor tunnel inflows are neglected in this setup (i.e. tunnel intersections with ZFMNE3118 and ZFMNNW1209). The main tunnel inflows are represented by long line sinks along the access tunnels, BT and DT, as well as a sink in the deep NDB tunnel. The access tunnel inflows occur at intercepts with deformation zones ZFMWNW0001, ZFMNW0002, ZFMWNW1035, ZFMNNE0869, and ZFMNE0870. The NDB tunnel inflow comes from its intersection with ZFM871. Elements completely inside tunnels are deleted (i.e. elements where all nodes have prescribed fixed head). Elements along the tunnel-wall perimeter (or more precisely, to all elements where one or two nodes have prescribed fixed head) are assigned a local skin resistance, $T = K_{skin} \cdot b$ (see Section 2.5).

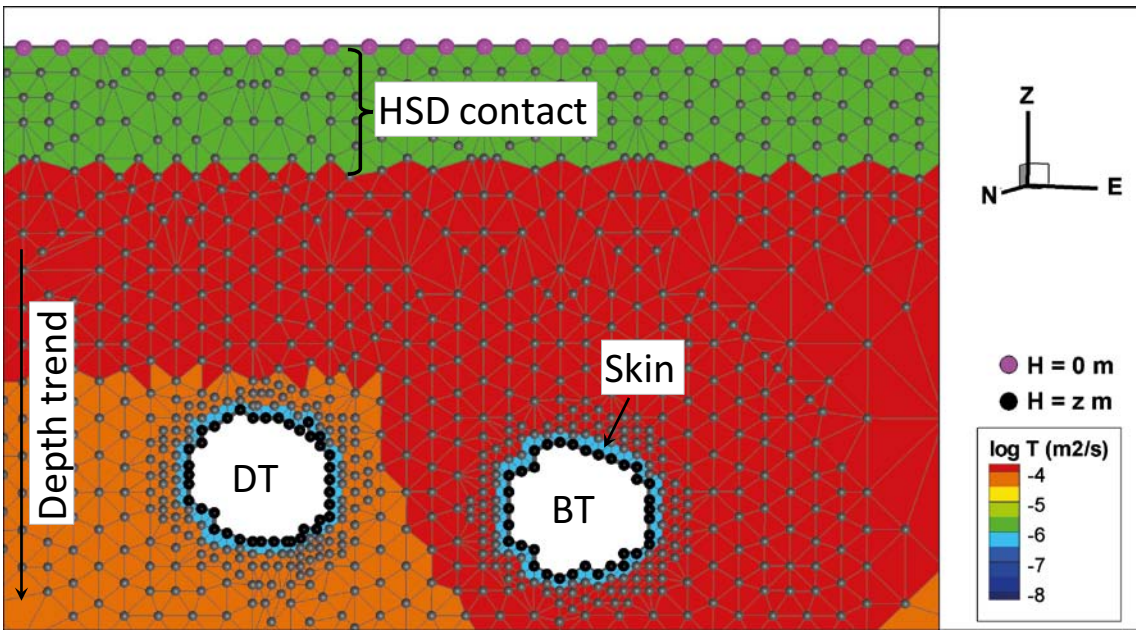

Figure 6-15. *Example of a numerical setup: Tunnel intersections of ZFMWNW0001. Prescribed head at seafloor (pink dots) and tunnel-wall intersection (black dots). Skin is applied along the perimeter of the tunnel wall (light-blue). Transmissivity is adjusted in the uppermost 10 m (green) to represent a potentially constrained contact between HSD and HCD.*

There are several reasons for expressing both HSD resistivity and skin in terms of conductivity: 1) This approach honours the relatively uniformly distributed pattern in tunnel inflow (i.e. where the area-normalised specific inflow is relatively constant; see Table 4-3), 2) it compensates for highly variable model widths of intersecting zones (Table 3-2), and 3) it facilitates comparison to the previous Model Exercises (Chapter 5, Table 5-3). Owing to the formulation based on conductivity a wide zone, such as the 108 m wide ZFMWNW0001, is assigned comparatively higher transmissivity at tunnel intersections and along its seafloor contact.

Apart from the HSD contact and the tunnel skin, the HCD parameterisation is taken directly from the final values established in previous Model Exercise 6 (Table 3-2). The purpose is that this simplified model setup should perform as similarly as possible to the previously described DarcyTools simulations. However, the simplified representation of tunnel inflow and HSD necessitates minor adjustments. The negligence of the HRD component requires a few additional rudimentary modifications to improve the simulation results (Section 6.3.3). These modifications are of speculative nature, and are rather crudely implemented in context of the simplified model setup. Hence, they are not intended as final modifications in the hydrogeological model.

The storativity value used in simulations is based on the standard relationship, Equation 6-2, but scaled by a factor to represent compartmentalisation. A few trial-and-error cases are tested to elaborate the significance of this scaling factor. In the standard setup, a scaling factor of 8 is used for deformation zones, and a factor of 1/8 is used for the SBA-structures.

6.3.3 Modifications to structure parameterisation

During the course of simulations, a few adjustments were explored on trial-and-error basis, in order to improve the general pattern of simulated responses. These modifications can be summarised as follows:

1) Introduction of a feature to enhance the sub-horizontal hydraulic connection in the vicinity of HFR101 (referred to as KFR104_088; details given in Section 6.3.1).
2) Implementation of a low-transmissive horizontal band at depth to reduce vertical hydraulic connection in the Central block.
3) Reduction of the hydraulic connection of SBA1.

The structure called “KFR104_088” is found to be important for propagating the head decrease to the two deepest sections of KFR104. Note that this structure is not one of the deterministic SBA-structures defined in Öhman et al. (2012). However, in order to simultaneously uphold the strong vertical gradient between KFR104_1 and KFR105_1 (Figure 6-17), a horizontal low-transmissive band is also implemented in four structures of the Central block (ZFMNE3137, ZFMWNW8042, ZFMNE3112, and ZFMWNW3267). This band was implemented by reducing the transmissivity an order of magnitude for elements located at –180 m elevation (± 35 m), and west of the coordinate EASTING =1,633,160 (between KFR105 and KFR27).

Moreover, simulations demonstrate that the hydraulic contact between SBA1 and the steeply dipping deformation zones ZFMWNW8042 and ZFMNE3118 must be reduced. SBA1 was defined based on responses in HFR102 and KFR27 during the KFR105 test, but its spatial extension is highly uncertain (Öhman et al. 2012). In lack of contradictory evidence, SBA1 was extrapolated to terminate against ZFMNE3118, to the west, and against ZFMWNW8042, to the south. Reducing the transmissivity of SBA1, *west* of HFR102, as well as *south* of HFR102, by an order of magnitude is found to improve the simulation of interferences.

Finally, the effective transmissivity, $T_{eff}(0)$, (as defined at zero elevation) were reduced in two zones; by a factor of 2 in ZFMNE3137 and by a factor of 5 in ZFMENE3115. These adjustments improved the transient simulation of KFR105 somewhat. However, the improvement is judged to be insignificant, due to the simplified model setup, uncertainty in interference data, and in the light of non-unique solutions.

These three modifications (introducing KFR104_088, the low-transmissive band in the Central block, and reducing the hydraulic contact of SBA1) are found to improve both simulated initial-state head decreases and pressure propagation in transient simulations.

6.3.4 Simulated transient head decrease

At any given point, the transient simulations allow monitoring the simulated head decrease as a function of time. Thus, simulated response curves can be extracted from intersections between borehole sections and modelled structures to enable a direct comparison to data observations (Section 6.2). However, as described below, the simplified model setup causes a few technical difficulties.

As stated earlier, only deterministically modelled structures (deformation zones and SBA-structures) are included in the simplified model setup. Most borehole sections intersect at least one deterministically modelled structure, in which simulated head decrease can be studied. However, head responses outside deterministically modelled structures are not represented in the numerical model, and hence, head decrease is not simulated in the borehole sections that lack structural intercepts (Table 6-5).

Moreover, deformation zones have defined thicknesses (see Table 3-2, in Chapter 3.2). This thickness is not geometrically represented in simulations. Instead, the modelled structures are reduced to zero-width, central planes. A borehole section may intercept a deformation zone *partially*, without fully penetrating the centre of the zone (i.e. does not intersect its central plane). A consequence of this simplified numerical representation is that head decrease is not monitored in borehole sections with *partial* deformation intercepts. This artefact occurs in three borehole sections, which are related to the large thickness of ZFMWNW0001 (HFR105_3, HFR105_4, and HFM35_3; Table 6-5).

A common trait of borehole sections KFR02_1, KFR02_4, and KFR27_3 is that they have significant interpreted responses and are located rather close and sub-parallel to deformation zones (ZFMNE0870 and ZFMWNW0835, respectively). The observed responses in these sections are potentially related to indirect flow paths via the ambient structures. To facilitate comparison to data, the simulated head decrease in these sections was therefore taken as half of the head decrease in the adjacent zone.

Sections 3 and 4 in HFR105 cover partial intercepts of ZFMWNW0001 and are interpreted as responding to the HFR101 test. Their interpreted responses are very similar to sections 1 and 2, which cover ZFMWNW1035 (Table 6-2). However, the subsequent simulations suggest that the responses in HFR105 do not primarily relate to the Southern boundary belt structures, but rather to the speculated sub-horizontal connectivity (modelled as KFR104_088). These monitoring points are therefore discussed separately.

Sections 4 and 5 of KFR102A have no structural intersection, but nevertheless have responses to the KFR105 test. Their responses are very similar to ambient sections of KFR102A (Table 6-2). These sections are comparatively short (34 and 5 m, respectively), and hence the responses could reflect local hydraulic connection to the ambient sections. These sections are *not* included in the simulated interference tests.

Table 6-5. Borehole sections lacking central plane intercepts.

Section	Description	Response from
KFR02_1	No structural intercept, near ZFMNE0870	HFR101
KFR02_4	No structural intercept, near ZFMNE0870	HFR101
KFR27_3	No defined intercept, very near ZFMWNW0835	KFR105
HFR105_3	Partial intercept of ZFMWNW0001	HFR101
HFR105_4	Partial intercept of ZFMWNW0001	HFR101
KFR102A_4	No structural intercept	KFR105
KFR102A_5	No structural intercept	KFR105
KFR102B_2	No structural intercept	None
KFR103_3	Unresolved PDZ, no deterministic intercept	None
KFR105_4	No structural intercept, but high-transmissive PFL-f related to drilling response (Figure 6-9)	NA
HFM34_3	No structural intercept, located south of ZFMWNW0001	None
HFM35_3	Partial intercepts of ZFMWNW0001 and ZFMWNW1035	None
HFR102_2	No structural intercept	None

No responses have been interpreted in the remaining borehole sections listed in Table 6-5. Therefore it is considered sufficient to evaluate these sections by visual inspection (i.e. to visually confirm the lack of response).

6.4 Simulations

6.4.1 Initial state

The initial head field is obtained from a steady-state solution with the existing SFR as the only sink term. Tunnel skin, K_{Skin}, is calibrated in order to reproduce the measured total inflow (286 L/min; see Table 4-3). The access tunnels, BT and DT, were assigned $K_{Skin} = 7 \cdot 10^{-9}$ m/s, which is very similar to that previously used in Model Exercise M3b in the DarcyTools simulations (Section 5.4). The NDB intercept was assigned the considerably higher value, $K_{Skin} = 4 \cdot 10^{-7}$ m/s, which is also very similar to M6 of the DarcyTools simulations (cf. Table 5-3). The resulting inflow is 219 L/min for the access tunnels and 67 L/min for the NDB tunnel (with a total of 286 L/min; cf. Table 4-3).

Once tunnel skin has been calibrated to reproduce tunnel inflow, the HSD resistivity is adjusted in the uppermost 10 m of modelled structures. The K_{HSD} values are simply fitted by trial-and-error, without undertaking any rigorous optimization procedure. The fitted values are considered to be of minor interest, as the purpose is only to provide a realistic initial state in the simplified model setup for the forthcoming transient simulations. The highest K_{HSD} values are assigned to ZFMNNE0869 and ZFMWNW8042 ($1 \cdot 10^{-7}$ and $3 \cdot 10^{-7}$ m/s, respectively). Somewhat lower K_{HSD} are fitted to the remaining structures (ranging from $7 \cdot 10^{-9}$ m/s to $7 \cdot 10^{-8}$ m/s), where the highest values are associated to the Southern and Northern boundary belt, as well as ZFMNNW1034.

Fitting the two resistivity parameters, K_{skin} and K_{HSD}, provides a resulting steady-state solution with reasonable agreement to measured data (Figure 6-16 and Figure 6-17). Visual inspection suggests that the agreement is also satisfactory among the old borehole sections in the vicinity of the Silo. However, the focus is here on the vicinity of the performed interference tests (i.e. the target area for the SFR extension, southeast of the existing SFR facility). Hence, the evaluation includes only the more recently installed borehole sections (i.e. KFM11A, HFM34, HFM35, KFR101 to KFR106, HFR101, HFR102, HFR105, and HFR106). KFR02 is also included in the evaluation, as it is located close to HFR101 and responds to the HFR101 test.

A tentatively modelled sub-horizontal feature (KFR104_088; Section 6.3.1) must be implemented in order to propagate head decrease to the deepest sections of KFR104 (Figure 6-16).

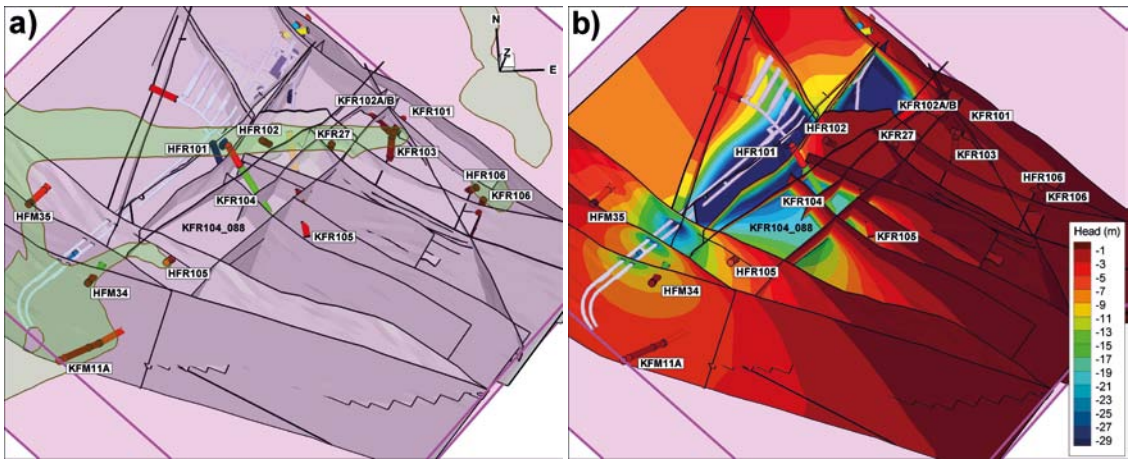

Figure 6-16. *Simulated initial-state head decrease (m); a) monitored borehole sections and b) simulated head in modelled structures. Head decreases exceeding 30 m are shown as dark blue (unresolved by the colour scale). Ground surface is shown as transparent green shade.*

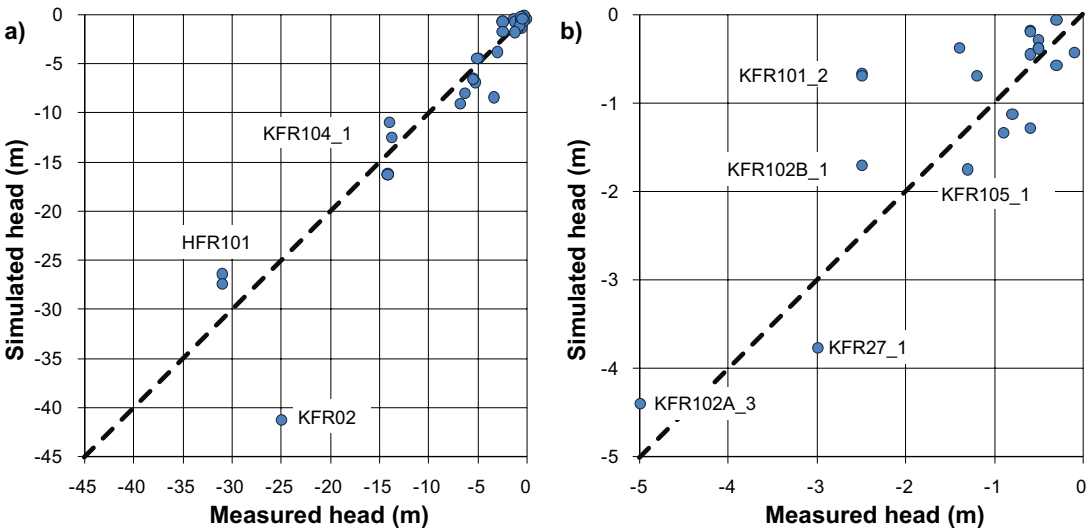

Figure 6-17. *Cross plot between in situ measurements and initial-state simulations; a) all recently installed monitored borehole sections (and KFR02) and b) close up for monitored sections with low head decrease.*

6.4.2 The HFR101 test

The pumping in HFR101 was simulated by imposing a constant, linear sink term along the geometry of HFR101 for 72 hrs, followed by a recovery period of 82 hrs. The total, constant flow rate was 4 L/min, which is 40% of the flow rate measured at the end of the pump test. Nevertheless, the maximum simulated head decrease in HFR101, c 24 m, exceeds the maximum measured head decrease (c 16 m; Figure 6-3). This is considered to be a realistic representation of the HFR101 pump test, as a substantial amount of the pumped water can be expected to come from the HRD (which is not included in the model setup; cf. parameterisation described in Section 6.2.5 and Table 6-1).

The HFR101 test supports the actual existence of the tentatively modelled sub-horizontal feature, KFR104_088 (Sections 6.3.1 and 6.4.1). In the original model setup, where KFR104_088 is not implemented, the simulated head decrease does not reach HFR105 and KFR104 (Figure 6-19). Implementation of the sub-horizontal feature KFR104_088 allows the head decrease to expand towards HFR105 and KFR104 (Figure 6-20).

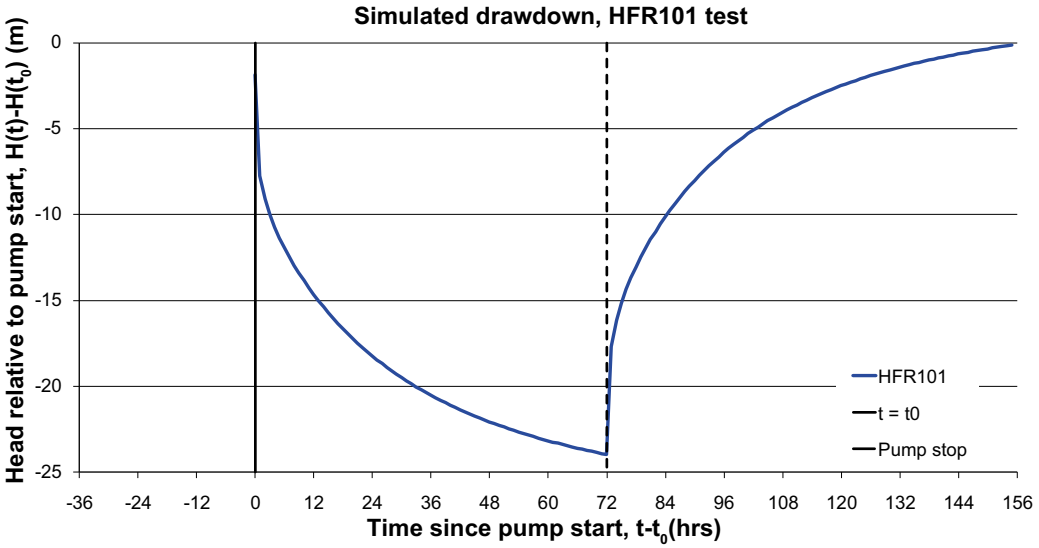

Figure 6-18. *Simulated head change in HFR101 during the transient simulation.*

Furthermore, in the original model setup, a large head decrease is simulated for HFR102_1 (Figure 6-19). However, this section is classified as non-responding (Section 6.2.2). Hence, simulations indicate that the hydraulic connection of SBA1 is overrepresented towards connected structures in the southeast (i.e. ZFMNE3118 and ZFMWNW8042). Reducing the transmissivity locally, east of HFR102 and south of HFR102, effectively hampers the head decrease propagation towards HFR102 (Figure 6-20).

Note that KFR105 had not yet been drilled at the time of this test, and that monitored borehole sections classified as non-responding are shown as white cylinders. It should also be noted that the maximum head decrease can be reached after 72 hrs of pumping.

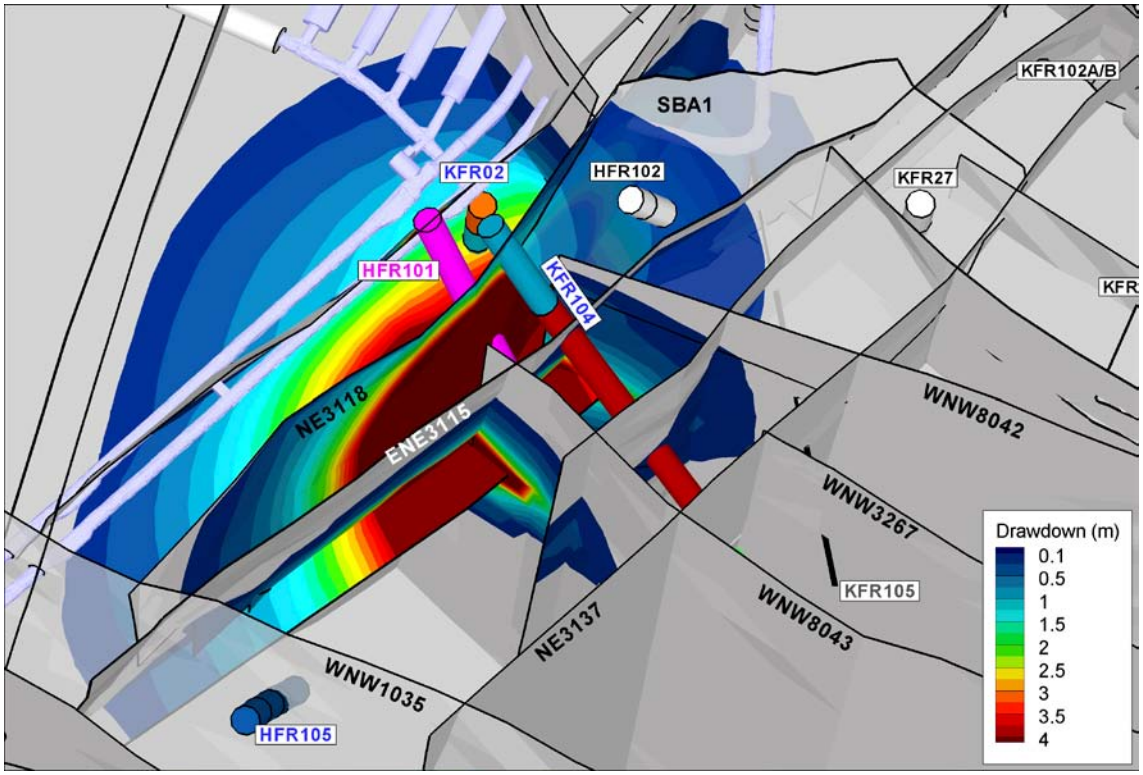

Figure 6-19. *Simulated head decrease (m) after 72 hrs of pumping in HFR101 with the original model setup. Responses in KFR104 and HFR105 are not reproduced. Only head decrease exceeding the response criterion d_p = 0.1 m is shown.*

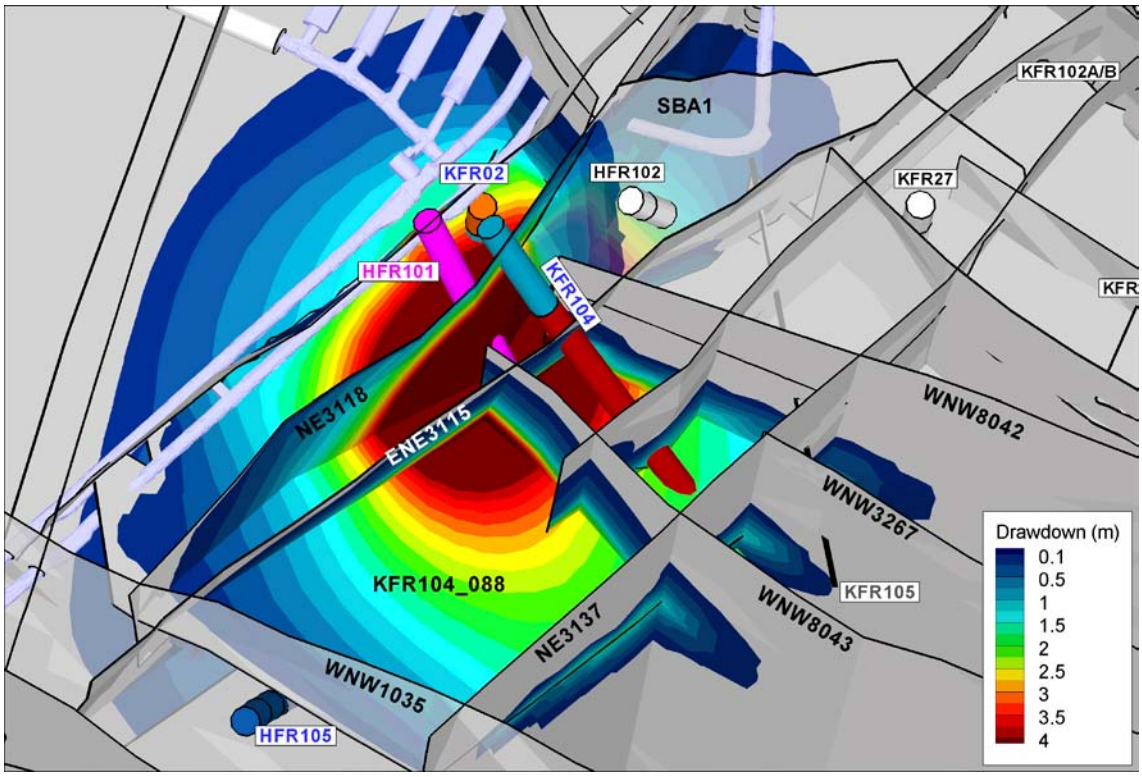

Figure 6-20. *Simulated head decrease (m) after 72 hrs of pumping in HFR101 for the modified model setup, with responses in KFR02, KFR104, and HFR105. Only head decrease exceeding the response criterion d_p = 0.1 m is shown. The maximum head decrease may occur after 72 hrs.*

6.4.3 The KFR105 test

The KFR105 test is simulated by 24 hrs of pumping followed by 82 hrs of recovery after pump stop. Section KFR105_4 is not simulated, as it lacks structural intercept (Table 6-5). A fixed head condition is prescribed along the borehole trajectory during the pumping phase. The fixed head corresponds to atmospheric pressure of the KFR105 outlet (H = –107 m, also for Section 2; Figure 6-6). At the end of the pump phase, the total simulated outflow from KFR105 is 4.0 L/min, which is about 35% of the measured outflow (Table 1-2). This is in line with expectations, since 77% of the measured PFL-f transmissivity belongs to HRD, which is neglected in these simulations.

The simulated recovery is notably slower than monitored data (cf. Figure 6-6 and Figure 6-21), which indicates that the assigned hydraulic diffusivity (T/S) is too low. Perhaps this too is an artefact of excluding the HRD in the model setup. It may also indicate that the parameterised HSD resistance is too large. However, it is noteworthy that the slowest recovery is found in KFR105_5, both in monitored data and in simulations (cf. Figure 6-6 and Figure 6-21).

The KFR105 test confirms an overrepresentation of vertical transmissivity/connectivity in the original model setup. During the initial-state simulations it was found necessary to reduce the vertical hydraulic contact locally to uphold the vertical gradient between the deepest sections of KFR104 and KFR105. This reduction was coarsely implemented as a horizontal low-transmissive band, at c –180 m elevation in four steeply dipping deformation zones inside the Central block (Section 6.3.3). The implementation of the horizontal low-transmissive band reduces the responses in sections 1 and 2 of KFR104 (cf. Figure 6-22 and Figure 6-23).

The overrepresented hydraulic contact of SBA1 is evident also in the simulated KFR105 test (i.e. similar to conclusions from the HFR101 simulations; Section 6.4.2). This causes excessively simulated responses in KFR104_3 and HFR102_1 (Figure 6-22). On the other hand, SBA1 has an important role for propagating head decrease towards KFR27_2 (cf. Figure 6-7 and Figure 6-22).

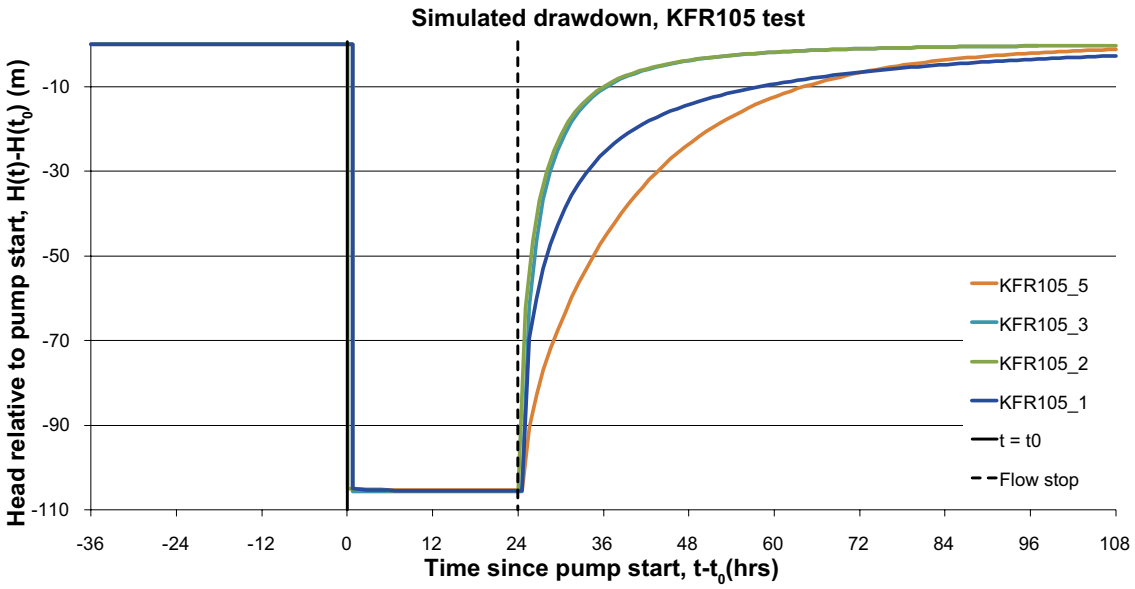

Figure 6-21. Simulated head change in KFR105 during the transient simulation.

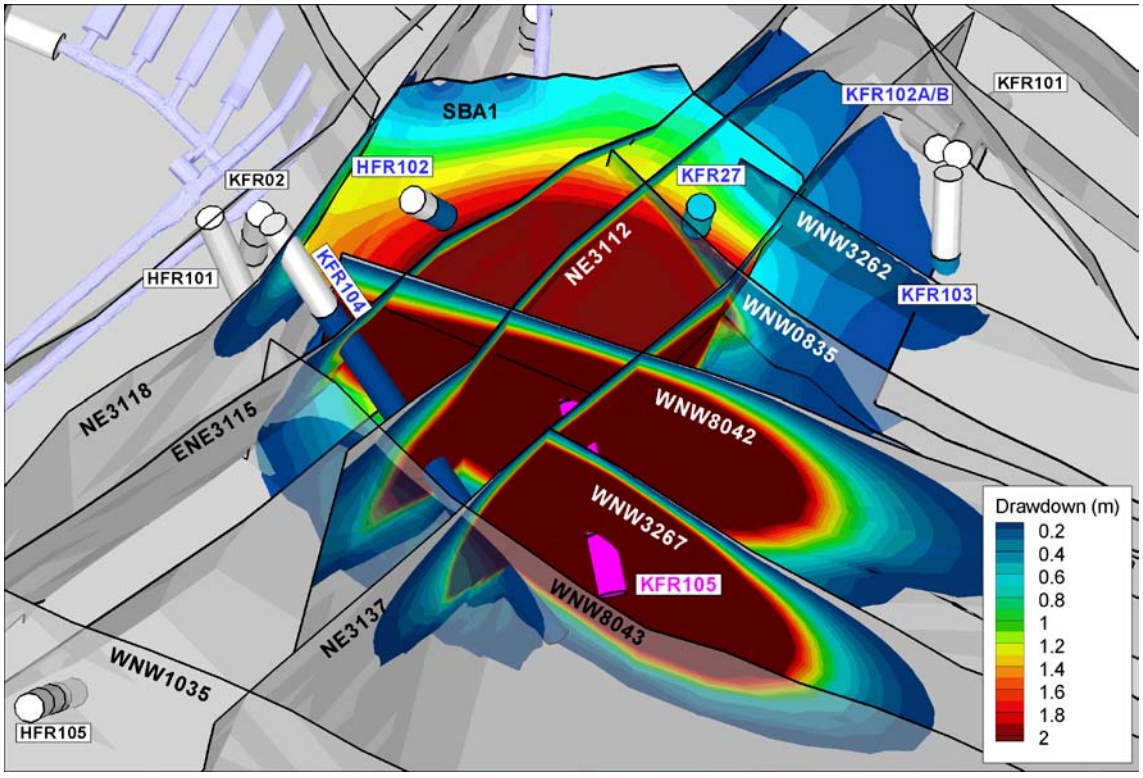

Figure 6-22. Simulated head decrease (m) after 24 hrs of pressure release in KFR105 for the original model setup. The responses in KFR104 and HFR102 are too large. Only head decrease exceeding the response criterion d_p = 0.1 m is shown.

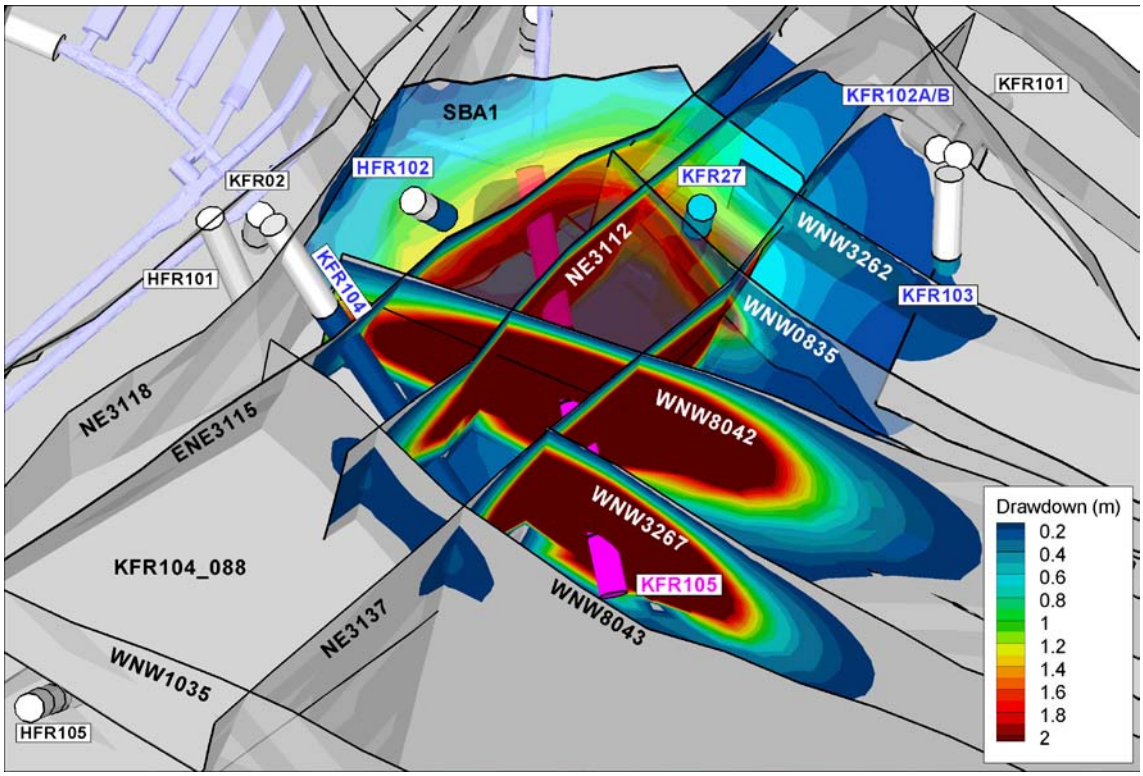

Figure 6-23. *Simulated head decrease (m) after 24 hrs of pressure release in KFR105 for the modified model setup, with responses in KFR102A, KFR103, KFR104, KFR27, and HFR102. Head decrease below the response criterion d_p = 0.1 m is not shown. Note that the maximum head decrease may occur later than 24 hrs after pump start.*

The implemented transmissivity reduction east and south of HFR102 eliminates head decrease in KFR104_3, reduces the head decrease in HFR102_1, but preserves the head decrease for KFR27_2 (Figure 6-23). Thus, although this coarse modification of SBA1 does not provide a perfect match, it indicates that the spatial extent or hydraulic continuity of SBA1, as defined in Öhman et al. (2012), is overrepresented.

6.5 Results

The transient simulations are compared to monitored head decrease as a function of time. Note that KFR02_1, KFR02_4, KFR102A_4, KFR102A_5, and KFR27_3 are classified as "responding", although they lack structural intercepts. These responses must be conducted via fractures outside deterministic deformation zones (i.e. HRD fractures which are not included in the model setup). Relevant responses are interpolated from the nearest structure (Section 6.3.4); the head decrease of KFR02_1 and KFR02_4 was taken as half of the value at the nearest point in ZFMNE0870 and KFR27_3 is estimated similarly from ZFMWNW0835. Sections 4 and 5 of KFR102A and sections 3 and 4 of HFR105 do not provide additional information and are therefore not evaluated numerically.

The simulation targets are: 1) to simulate responses exceeding the criterion d_p = 0.1 m in borehole sections identified as "responding" by Walger et al. (2010), 2) to simulate the *absence* of response in sections identified as "non-responding". Simulated responses exceeding d_p = 0.1 without data support are referred to as *undue* responses. In the light of the simplified model setup, the simulated response patterns have reasonable resemblance to field data. In general, the simulated undue responses are few, while most responses exceeding the criterion d_p = 0.1 m are simulated in "responding" sections.

However, at the more detailed level, discrepancies are evident in terms of both response times and magnitudes (Table 6-6). A few undue responses are also simulated (Figure 6-24b and Figure 6-25b). The discrepancies are expected to relate to local heterogeneity at the level of detail not addressed in the model setup, such as hydraulic responses outside modelled structures (i.e. in the HRD). Discrepancies in response times are expected to relate to uncertainties in the storativity. The results of the HFR101 and KFR105 tests are discussed in more detail in Sections 6.5.1 and 6.5.2, respectively.

It is noteworthy that delayed responses, continuing after the end of the interference test is observed both in data and simulations (although not for the same sections). This phenomenon is interpreted as a combined effect of geometry and heterogeneous hydraulic properties that may, for example, occur in compartmentalised dead-end structures.

6.5.1 The HFR101 test

The primary targets of the HFR101 simulations were KFR104 and HFR105, and to avoid an undue response in HFR102_1. Implementation of the tentatively modelled structure "KFR104_088" successfully replicates a rapid, large response in KFR104_2, and slow, small responses in sections 1 and 2 of HFR105 (Figure 6-24a). However, KFR104_088 is terminated against ZFMWNW1035, and hence, no responses reach ZFMWNW0001 (i.e. sections 3 and 4 of HFR105; not shown). The more detailed simulations demonstrate that the SBA1 modifications were insufficient. Specifically, an undue response exceeding d_p is simulated in HFR102_1 (Figure 6-24b). To some extent, the response in SBA1 is exaggerated by the exclusion of HRD responses; connectivity to the sea (hydraulic boundary) is expected to hamper pressure propagation at shallow depths. Nevertheless, SBA1 serves as an example to confirm earlier hypotheses that the continuous, extrapolated planes with uncertain spatial extension, as modelled in Öhman et al. (2012), exaggerate the hydraulic continuity in SBA-structures.

Table 6-6. Comparison between observations and simulations.

Interference	Response	Observation		Simulation	
		d_{tL} (hrs)	ΔH (m)	d_{tL} (hrs)	ΔH (m)
HFR101	KFR02_4[1)]	7.7	3.14	9.5	0.61
	KFR02_3	31.7	1.08	0.3	6.75
	KFR02_2	33.3	0.90	0.7	6.33
	KFR02_1[1)]	25.0	0.49	1.7	3.17
	HFR105_4[2)]	29.2	0.30	NA	0
	HFR105_3[2)]	29.2	0.31	NA	0
	HFR105_2	29.2	0.32	59	0.13
	HFR105_1	28.3	0.38	59	0.13
	KFR104_3	25.0	0.82	3.4	4.6
	KFR104_2	1.2	3.82	6.5	4.95
	KFR104_1	8.0	1.82	25.9	1.63
KFR105	HFR102_1	20.8	0.25	1.3	1.25
	KFR102A_8	27.5	0.38	12.9	0.19
	KFR102A_7	24.7	0.41	22.0	0.20
	KFR102A_6	10.0	0.23	13.7	0.21
	KFR102A_5[3)]	11.8	0.23	NA	NA
	KFR102A_4[3)]	18.3	0.23	NA	NA
	KFR102A_3	24.2	0.19	NA[4)]	0.05
	KFR102A_2	31.7	0.13	NA[4)]	0.05
	KFR102A_1	31.7	0.13	NA[4)]	0.05
	KFR103_2	16.7	0.35	20.6	0.12
	KFR104_2	45.0	0.13	30.4	0.97
	KFR104_1	90.0	0.15	44.9	0.91
	KFR27_3[1)]	11.0	0.52	1.1	1.03
	KFR27_2	3.8	1.74	0.6	2.02
	KFR27_1	10.0	0.23	NA[4)]	0.07

1) Section lacks structural intercept. Head decrease interpolated as half the value in the nearest zone.
2) Partial intercept of ZFMWNW0001, without intersecting the modelled central plane. Inspected visually.
3) Section lacks structural intercept. Not evaluated numerically.
4) Response time, d_{tL}, is undefined, if the maximum head decrease, ΔH, does not exceed the criterion dp = 0.1 m.

In particular, the responses in KFR02 are too rapid and too large in magnitude (Figure 6-24; note that KFR02_1 and KFR02_4 are interpolated from the nearby ZFMNE0870). A few conclusions can be drawn concerning the structures involved in these responses, specifically concerning ZFMENE3118, ZFM871, and KFR104_088. Firstly, the groundwater level during the pumping of HFR101 is below the ZFMNE0870 intercept, and hence does not directly affect the pressure in ZFMNE0870 (i.e. interpolated as KFR02_4). Secondly, the large observed head decrease in KFR02_4 suggests the existence of a sub-horizontal connection (above KFR104_088). Thirdly, the rudimentary modelled geometry of KFR104_088 should have been terminated against ZFMENE3118, to avoid contact with ZFMNE0870. Finally, the parameterised transmissivity, or hydraulic connection, of the flow path along ZFMENE3118 and ZFM871 is too high.

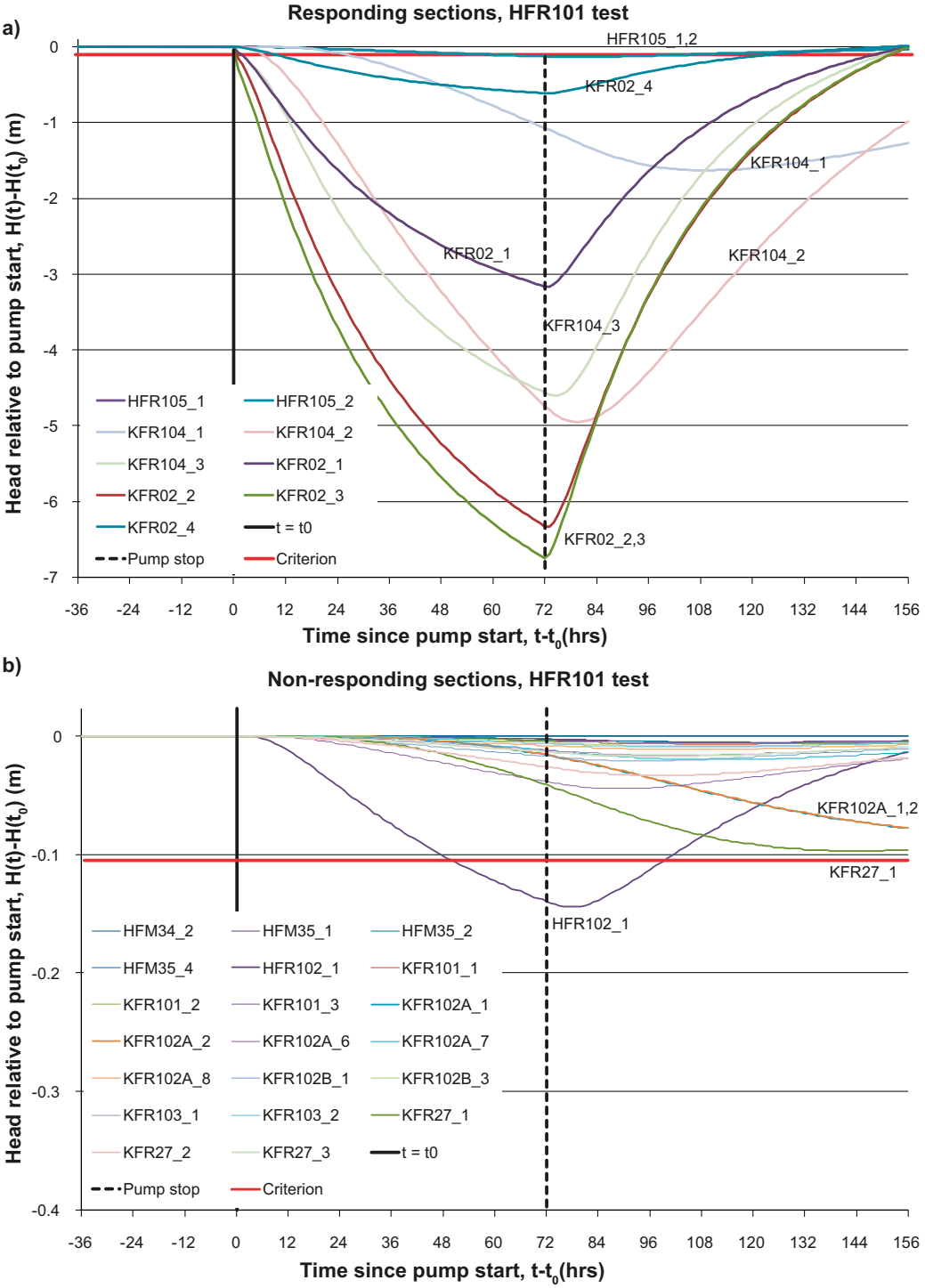

Figure 6-24. *Simulated head responses to the HFR101 test in borehole sections classified as; a) "responding" and b) "non-responding".*

The late response phenomenon is simulated in deep borehole sections KFR104_1, KFR27_1, KFR102A_1, and KFR102A_2 (not supported by data). This is interpreted as a combined effect of: 1) decreasing hydraulic diffusivity with depth due to the corresponding transmissivity depth trend (cf. Eqs. (6-1) and (6-2)), 2) they are located far from source/sink terms, and 3) the no-flow boundary imposed at the bottom of the model domain.

6.5.2 The KFR105 test

The primary targets of the KFR105 simulations were the large, rapid response in KFR27_2, the remote section KFR103_2, and to constrain the responses in HFR102_1 and KFR104. Some of these targets were accomplished while others were not. The best agreement, in terms of both response time and magnitude, is found in the uppermost sections of KFR102A (sections 6 to 8), KFR27_2, and KFR103_2 (Figure 6-25). The late response times in KFR104_1 and KFR104_2 are also well-reproduced in the model, although the simulated magnitude is too large. At greater depth, sections 1 to 3 in KFR102A and KFR27_1, the simulated responses fall below the criterion d_p (and hence no response time d_{tL} can be defined). The main hydraulic connection between KFR105 and the deep sections of KFR102A is ZFMENE3115. It should be noted that responses in the deep sections *can* be simulated. For example, is can be accomplished by slightly reducing the storativity S, and doubling the conditioned transmissivity T around the KFR105/ZFMENE3115 intercept. However, these modifications can only be done at the expense of more and larger and thereby undue responses in ambient sections.

There are three simulated undue responses: KFR102B_1, KFR102B_3, and KFR103_1 (Figure 6-25b). These are referred to as undue, as they were interpreted as "non-responding" by Walger et al. (2010). The structural intercepts of these sections are ZFMNE3112, ZFMNE3137, and ZFMWNW3262, respectively. The hydraulic framework in the model setup consists of structures modelled as continuous planes with homogeneous hydraulic properties (except for the imposed transmissivity depth trend and locally conditioned transmissivity around borehole intercepts (Table A-3, in Appendix A). Without including local heterogeneity to this hydraulic framework, it is not possible to attain the targets in nearby sections of KFR102A and KFR103_2 (Table 6-6), without causing these undue responses. For example, the response in KFR103_2 must pass ZFMWNW3262, which has highly transmissive sub-horizontal PFL-f ($T>10^{-6}$ m^2/s); thus, unless the structure is poorly connected vertically it will transmit an undue response in KFR103_1. Such internal horizontal channelling inside steep zones were speculated in Öhman et al. (2012).

The KFR105 simulations confirm earlier conclusions from HFR101, i.e. that the modifications of the SBA1 structure are insufficient for reproducing the slow, small head decrease observed in HFR102_1. The simulated response in KFR27_2 is also too rapid, suggesting that the parameterised hydraulic connection of SBA1 is also exaggerated in its eastern part.

An artificial numerical oscillation is observed in KFR104_2 (Figure 6-25a). The probable reason for this is that this section short-circuits two structures of different transmissivity: ZFMNE3112 ($T = 1.15\cdot10^{-7}$ m^2/s) and ZFMENE3115 ($T = 8.6\cdot10^{-9}$ m^2/s; see Table A-3, in Appendix A). The connecting borehole is numerically represented by a fine-meshed channel with the assigned values $T = 10^{-4}$ m^2/s and $S = 10^{-7}$. The oscillation is expected to be the combined result of meshing, widely contrasting hydraulic properties, and convergence criteria. This matter was not fully resolved within the present study, and hence, the simulated response time should be interpreted cautiously.

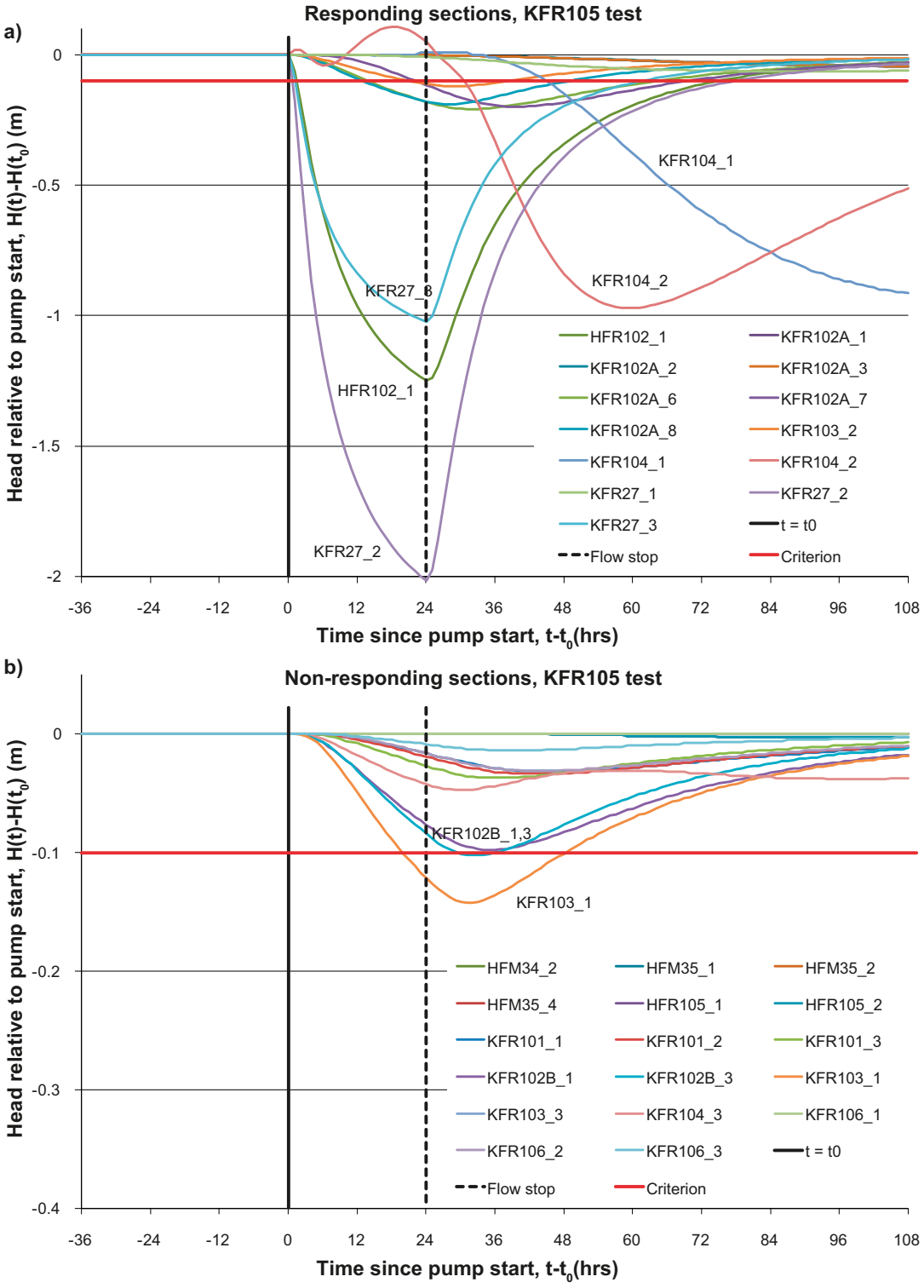

Figure 6-25. *Simulated head responses to the KFR105 test, in borehole sections classified as; a) "responding" and b) "non-responding".*

7 Flow for two different flow regimes

This chapter analyses simulated steady-state flow fields for two different flow regimes:

a) Inflow to the existing SFR facility ("radial flow" conditions to an open repository).

b) Topographically driven flow through a closed existing SFR facility to the current sea level ("uniform flow" conditions through a saturated repository).

The simulations are visualised in terms of flow paths and recharge/discharge areas for groundwater flow that passes the existing SFR facility. The visualised flow paths are selected based on flux magnitude across the tunnel wall (i.e. only flow paths exceeding a certain tunnel-inflow threshold are visualised; Table 7-1). The flow paths are simulated by a so-called cell-jump particle tracking, in which trajectories are discretised by traversing adjacent cell centres in the computational grid. The cell-to-cell traversal procedure is routed by the Darcy velocity field and entails a stochastic component. In case a given cell has outward-directed flux into several downstream cells, the probability of navigating into any downstream cell is proportional to the outward-directed Darcy velocity in that direction. This is equivalent of assuming complete mixing of particles/flow paths at the interface between each cell centre, and can therefore be argued to provide a conservative estimate of transversal dispersion (or geometric spreading of flow paths). A drawback of the method is that an unfavourable orientation of the grid versus the direction of the dominating (regional) groundwater flow forces flow-path trajectories into an unrealistic zigzag pattern and exaggerates transversal dispersion.

The tunnel wall is taken as the starting point of simulated flow paths (where specified flux thresholds are used to identify flow path starting points; Table 7-1). The method used in this study to represent groundwater recharge and discharge implies that recharge/discharge areas only can exist at prescribed head boundaries (i.e. cells representing the top surface. Recharge areas are identified by back-tracking the groundwater flow to the tunnel wall, until reaching a constant-head location in the hydrogeological model. The cell-jump method implies that the probability of navigating into an upstream cell is proportional to the inward-directed Darcy velocities). Likewise, discharge areas are simulated by forward-tracking the groundwater flow from the tunnel wall, until reaching a constant-head cell in the hydrogeological model.

A couple of aspects should be noted for the defined particle tracking cases (Table 7-1):

1) For the open tunnel flow regime, the model only identifies recharge areas, identified by back-tracking. The reason is that the inflow represents a sink, from which particles cannot be tracked further downstream. On the other hand, the re-saturated tunnel flow regime has both recharge and discharge areas, identified via backward and forward particle tracking.

2) In order to provide a similar number of trajectories for visualisation, the flux criteria for the disposal facilities (BTF1, BTF2, BLA, BMA and the Silo) are orders of magnitude lower than the criteria applied to the SFR tunnel.

3) Under re-saturated conditions, the hydraulic gradients are very low compared to the open tunnel regime. This causes low tunnel flux in spite of the tunnel skin removal; again, the flux criteria are selected in order to provide a similar number of trajectories for visualisation.

Table 7-1. Definition of particle tracking cases.

Scenario	Target[1]	Flow path type	No. particles	Flux criterion (m^3/s)
Open tunnel	Tunnel	Recharge	3,570	$Q > 0.25$
	Facilities	Recharge	4,415	$Q > 0.001$
Re-saturated	Tunnel[2]	Re-/discharge	3,767	$\lvert Q \rvert > 0.001$
	Facilities	Re-/discharge	2,784	$\lvert Q \rvert > 0.00001$

1 "Facilities" refer to BTF1, BTF2, BLA, BMA and the Silo, whereas "Tunnel" refers to tunnel sections that are not used for waste disposal.

2 The cross-flow in the first c 150 m of the access tunnels (Singö passage) is very high and therefore not included. Criterion for exclusion: Recharge/discharge areas $y' < 9300$, where y' refers to the rotated local coordinate system (Section 4.3).

7.1 Model setup

The fundamentals of the model set up are described in Chapters 3 and 4. Notable changes specifically introduced for the flow-field analysis are:

1) The general grid cells in the shallow bedrock ($z > -200$ m elevation) have a maximum side length of 8 m. Note that the HSD and the surroundings of the SFR tunnel have finer discretisations.
2) The HRD is parameterised by means of a Hydro-DFN realisation (Figure 3-7 and Figure 3-9), which introduces heterogeneity, correlation, and anisotropy consistent with hydrogeological borehole data.
3) Two flow regimes are simulated and compared:

a) "Radial flow" to an open repository (current situation).

b) "Uniform flow" through a saturated repository (future situation).

The current state is numerically implemented as prescribed atmospheric pressure at the tunnel wall in combination with tunnel-wall resistance, parameterised as K_{skin}, as described in Section 4.1 and Table 5-3, respectively.

The re-saturated state is numerically implemented by removing the prescribed-head condition and skin are removed from tunnel-wall cells. Instead the tunnel is assigned a conductivity value of 10^{-5} m/s (cf. Holmén and Stigsson 2001, Odén 2009).

The different conditions of the SFR tunnels are visualised in Figure 7-1. Note that *inflow*, as well as *gradient*, are defined as directed towards the tunnel (i.e. positive vector components are directed towards SFR, whereas negative vector components are directed outward from SFR). Note also the difference in scales between the two cases. The high gradients and inflow across the tunnel wall in Figure 7-1c and Figure 7-1e are the result of prescribed atmospheric pressure and skin factors, while the comparatively low values in Figure 7-1d and Figure 7-1f reflect topography-driven flow without skin.

7.2 Unsaturated conditions

Unsaturated conditions (atmospheric pressure inside tunnels) impose strong hydraulic gradients, where tunnel inflow is largely determined by deformation zone intercepts and the parameterised tunnel-wall skin (Figure 7-1). Under these conditions, the topographically driven gradients clearly are of subordinate significance. Consequently, the recharge locations primarily relate to ground-surface intercepts of deformation zones (Figure 7-2). The recharge locations for the largest inflows of the general SFR tunnel (access tunnels and NDB; Figure 7-1c) are concentrated to ground-surface intercepts of the Southern and Northern boundary belts (Figure 7-2a), while the primary recharge locations for the disposal facilities are intercepts of ZFMNNE0869 and ZFMNNW1209 (Figure 7-2b). The recharge locations for the disposal facilities are more or less confined between the Southern and Northern boundary belts.

To some extent, the recharge locations on land are concentrated to topographical heights (e.g. the SFR pier, the Aspöhällan harbour pier, and the Forsmark inland) that are not directly related to deformation-zone intercepts. The reason for this is that the flow paths between the ground surface and the bedrock are controlled by HSD layering (i.e. the deformation-zone geometry terminates at the HSD/bedrock interface; Figure 3-1). The glacial clay above the Southern boundary belt (Figure 3-2b) clearly impedes recharge through sediments on the sea bottom (Figure 7-2a). However, in comparison saturated-state simulations, the correlation between recharge areas and topography is small (cf. Figure 7-7). The recharge areas located in the Forsmark inland contribute to tunnel inflow at the Singö passage, and south of Singö.

The locations of recharge areas that contribute to groundwater inflow to the five disposal facilities depend on ambient zones (Figure 7-3). The inflow to the Silo is mainly vertical and is associated to groundwater recharge at the junction between ZFMNW0805A/B and ZFMNE0870, whereas deeper, longer flow paths traverse ZFM871 and SBA6 (Figure 7-3b and Figure 7-4).

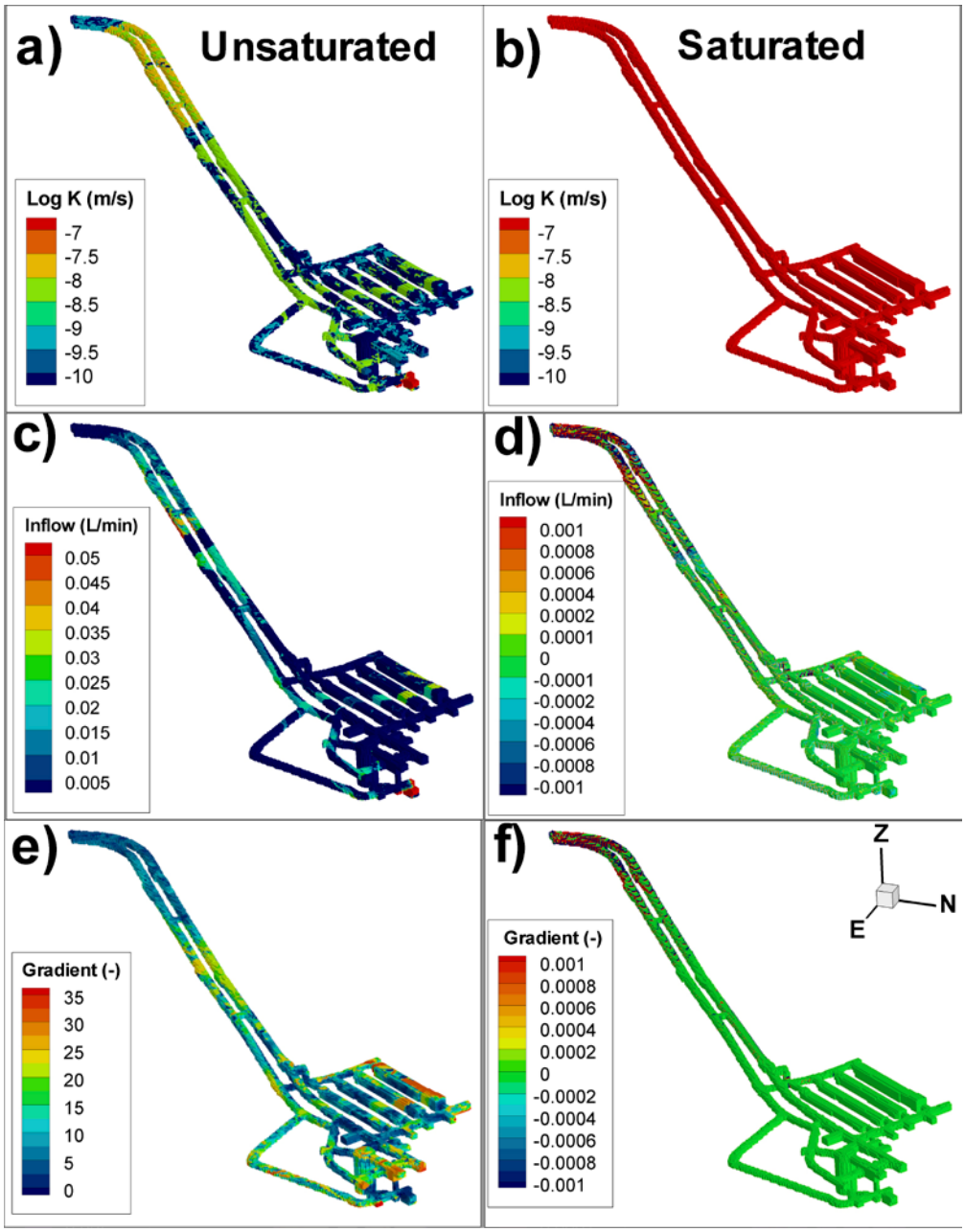

Figure 7-1. *Role of the SFR tunnel in the two simulation setups; unsaturated conditions (left) and saturated conditions (right).*

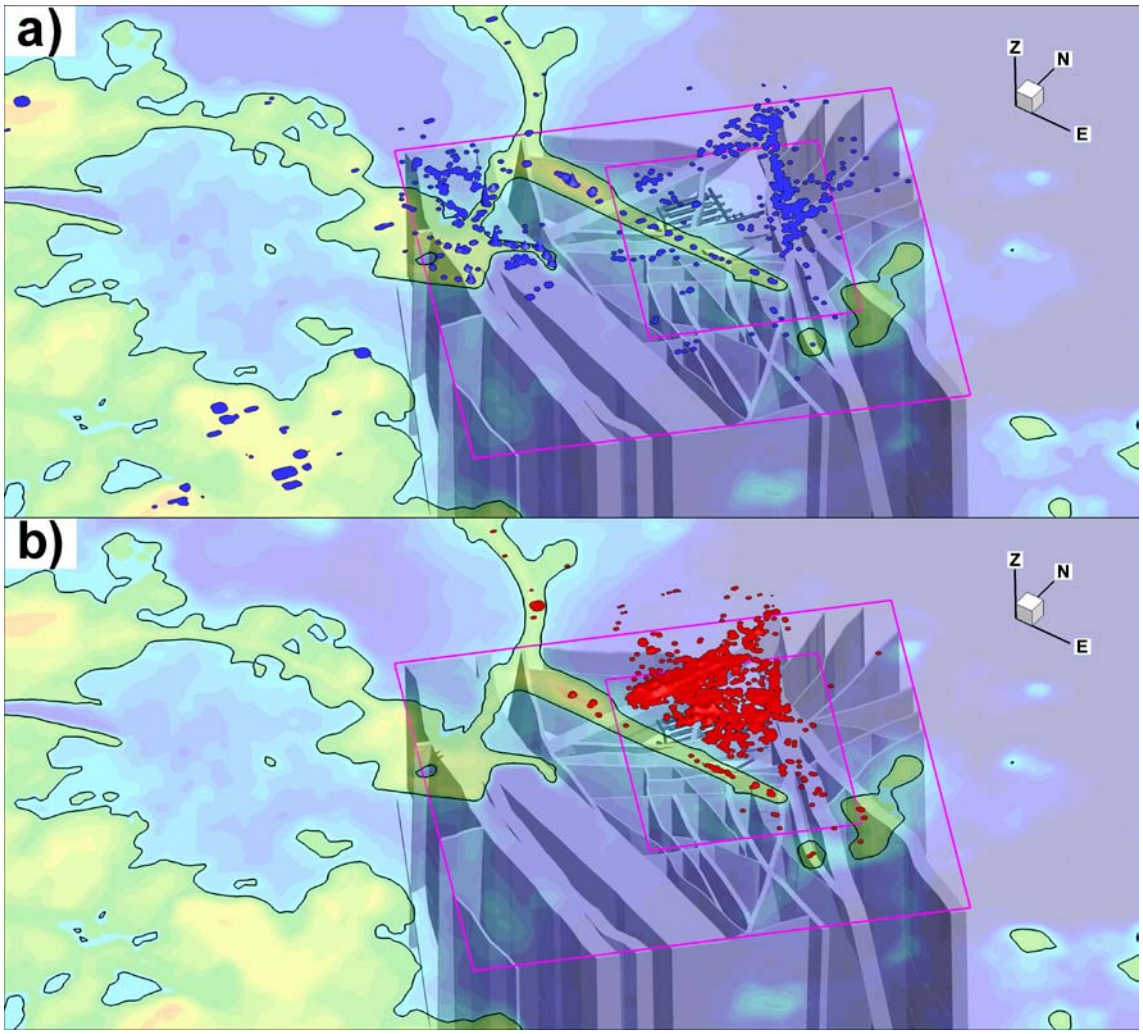

Figure 7-2. *Simulated recharge areas to the open SFR facility, shown as hill-shaded histograms; a) general tunnel sections (blue) and b) storage facilities, specifically (red).*

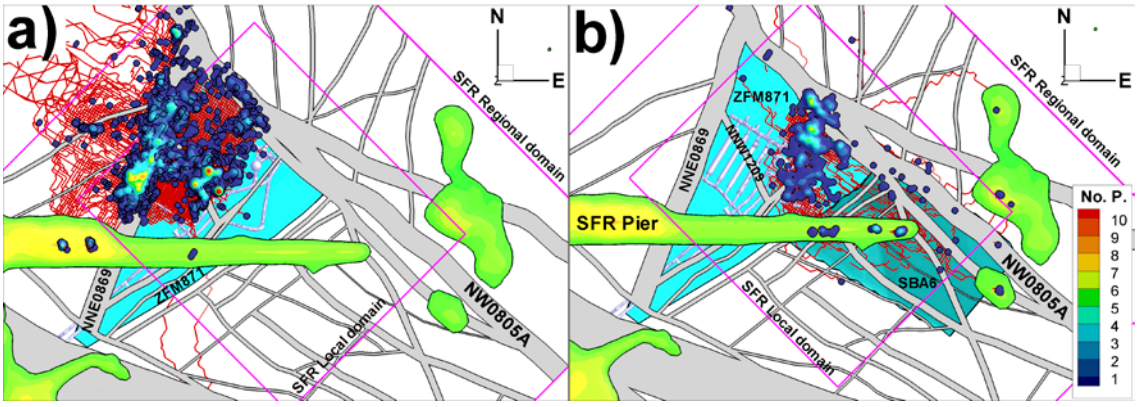

Figure 7-3. *Top-view of simulated recharge areas for the open, drained SFR waste-storage facilities; a) the four rock caverns (1BTF, 2BTF, BLA, and BMA) and b) the Silo.*

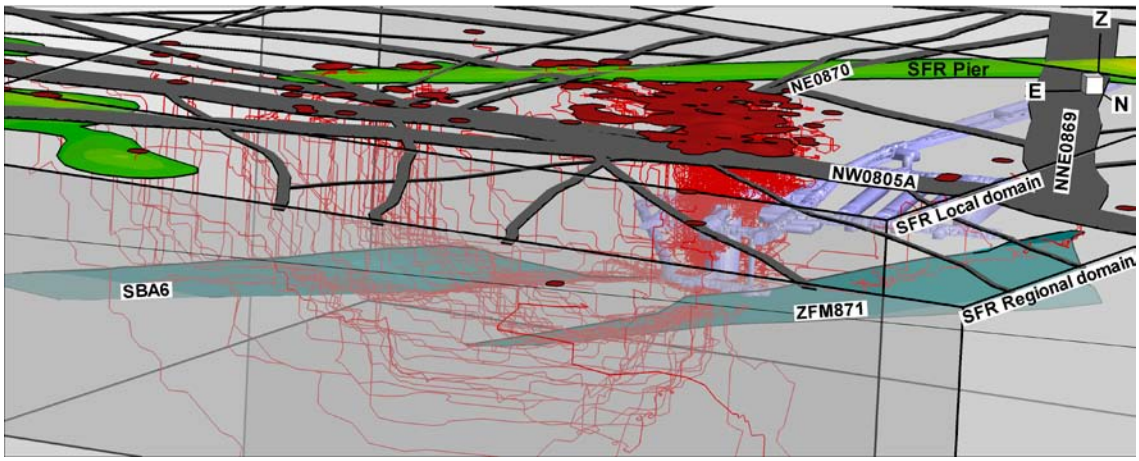

Figure 7-4. *Simulated inflow trajectories to the Silo for unsaturated conditions. The flow paths are mainly vertical and associated to groundwater recharge at the junction between ZFMNE0870 and ZFMNW0805A/B. Deeper and longer flow paths traverse ZFM871 and SBA6.*

Groundwater recharge that contribute to the groundwater inflow to the four rock caverns has two main pathways: 1) Directly via ZFMNNW1209 or 2) indirectly via ZFMNNE0869 and its junction with ZFM871. This active role of ZFM871 in tunnel inflow is not supported by inference from hydrochemical data (Nilsson et al. 2010), according to which ZFM871 is interpreted *not* to have an active role in current tunnel inflow based on its proportions of remnant groundwater of Littorina type. The two rock caverns located furthest to the east, 1BTF and 2BTF, primarily have vertical inflow via ZFMNNW1209, whereas the caverns located further to the west, BLA and BMA, primarily have inflow via ZFMNNE0869 (Figure 7-5 and Figure 7-6). It can be noted that the two middle caverns, 2BTF and BLA, also have some inflow via ZFMNW0805A/B.

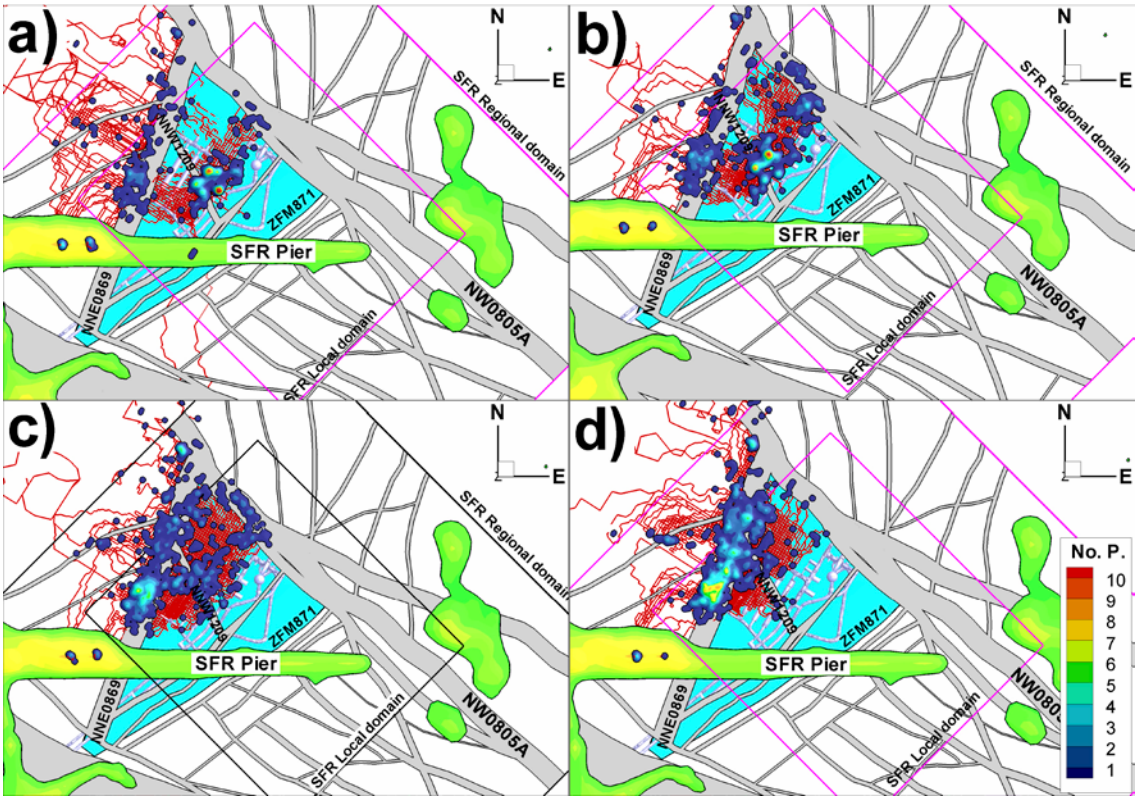

Figure 7-5. *Top-view of simulated inflow to the unsaturated SFR waste-storage facilities; a) 1BTF, b) 2BTF, c) BLA, and d) BMA. The main flow paths for 1BTF and 2BTF follow ZFMNNW1209, whereas the inflow to BLA and BMA is primarily related to ZFMNNE0869 (via ZFM871).*

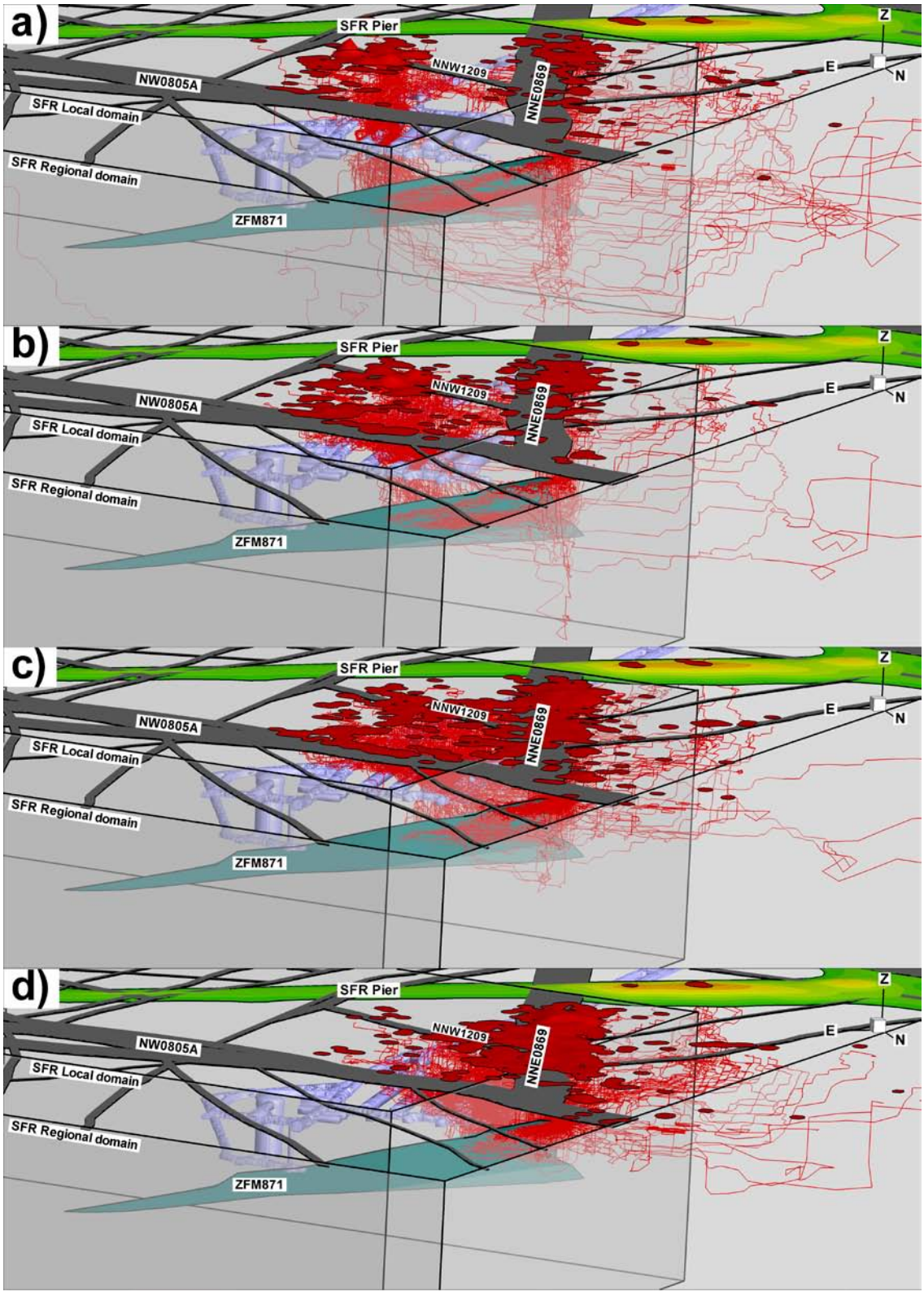

Figure 7-6. *Side view of simulated recharge areas that contribute to the groundwater inflow to the unsaturated SFR waste-storage facilities; a) 1BTF, b) 2BTF, c) BLA, and d) BMA. The main flow paths are vertical: ZFMNNW1209 and ZFMNNE0869 (via ZFM871).*

7.3 Saturated conditions

As stated in Section 4.1, the top of the model domain is prescribed a fixed-head boundary condition. Consequently, the topographically driven groundwater flow confines the simulated recharge locations to local topographical heights (the SFR Pier and Stora Asphällan; Figure 7-7). Compared to the open tunnel simulations (Figure 7-2), recharge areas for saturated conditions are considerably less correlated to deformation zone intercepts (cf. Figure 7-7). The dominant recharge pathways are identified as: 1) from the SFR Pier via ZFMNNE0869 and 2) from Stora Asphällan via the Southern boundary belt.

It should be noted that, although the simulated hydraulic gradients are small, they are substantially exaggerated by the prescribed head at ground surface; the SFR Pier is constructed from coarse fill (consisting of boulders and gravel), which is not expected to hold groundwater table much above sea level. Thus, in reality, the recharge is expected to be more evenly distributed, as well as potentially involving deep, regional flow paths from the Forsmark inland.

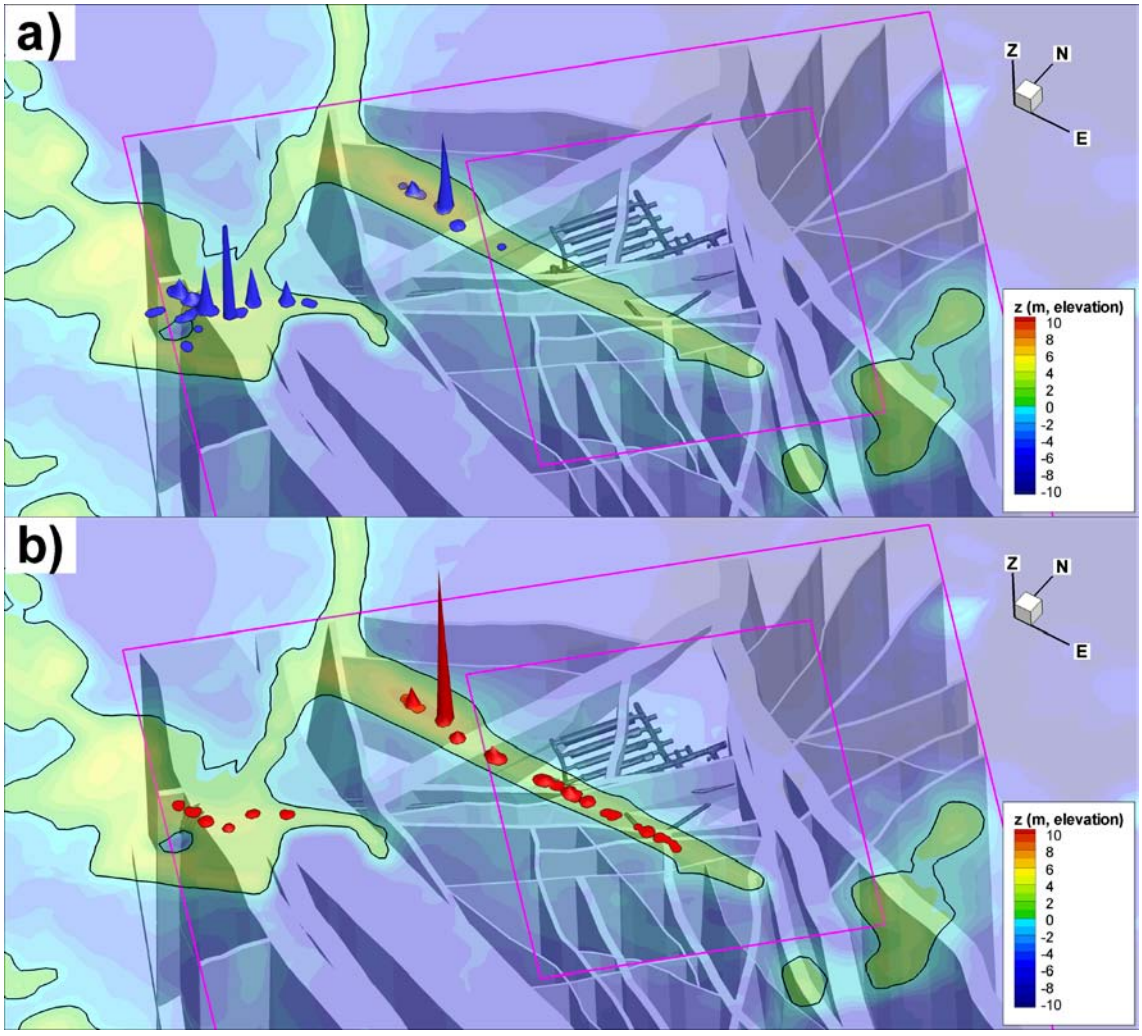

Figure 7-7. *Simulated recharge locations under saturated conditions; a) for flow paths crossing the SFR tunnel (blue) and b) for flow paths crossing the SFR storage facilities (red).*

The discharge areas for groundwater that has passed the SFR bedrock volume are located to the sea-floor south of the SFR pier, and along ground-surface intercepts of the Northern boundary belt and ZFMNNE0869, north of the Pier (Figure 7-8). Specifically, the discharge areas for flow paths from the waste-disposal facilities are exclusively located north of the SFR pier (Figure 7-8b). In other words, the Pier acts as a local groundwater divide in these simulations, an effect that is exaggerated by its unrealistically prescribed groundwater table. Under topography-driven gradients, the HSD layering has a relatively more significant role in determining locations of recharge/discharge areas. For example, no recharge or discharge occur in the glacial-clay covered areas above the Southern boundary belt (cf. Figure 3-2b). Inspection of particle-tracking trajectories demonstrate that the unrealistically high conductivity parameterisation of the SFR tunnel ($K = 10^{-5}$ m/s), causes the tunnel to act as a conductor for the flow field (Figure 7-9a). This causes the NBD intersection of ZFM871 to be the major exit point for flow from the SFR tunnel, particularly from its disposal facilities (Figure 7-9b).

In summary, results and uncertainties are both in line with expectations and rather similar to earlier modelling results of Holmén and Stigsson (2001), Odén (2009), and Öhman (2010).

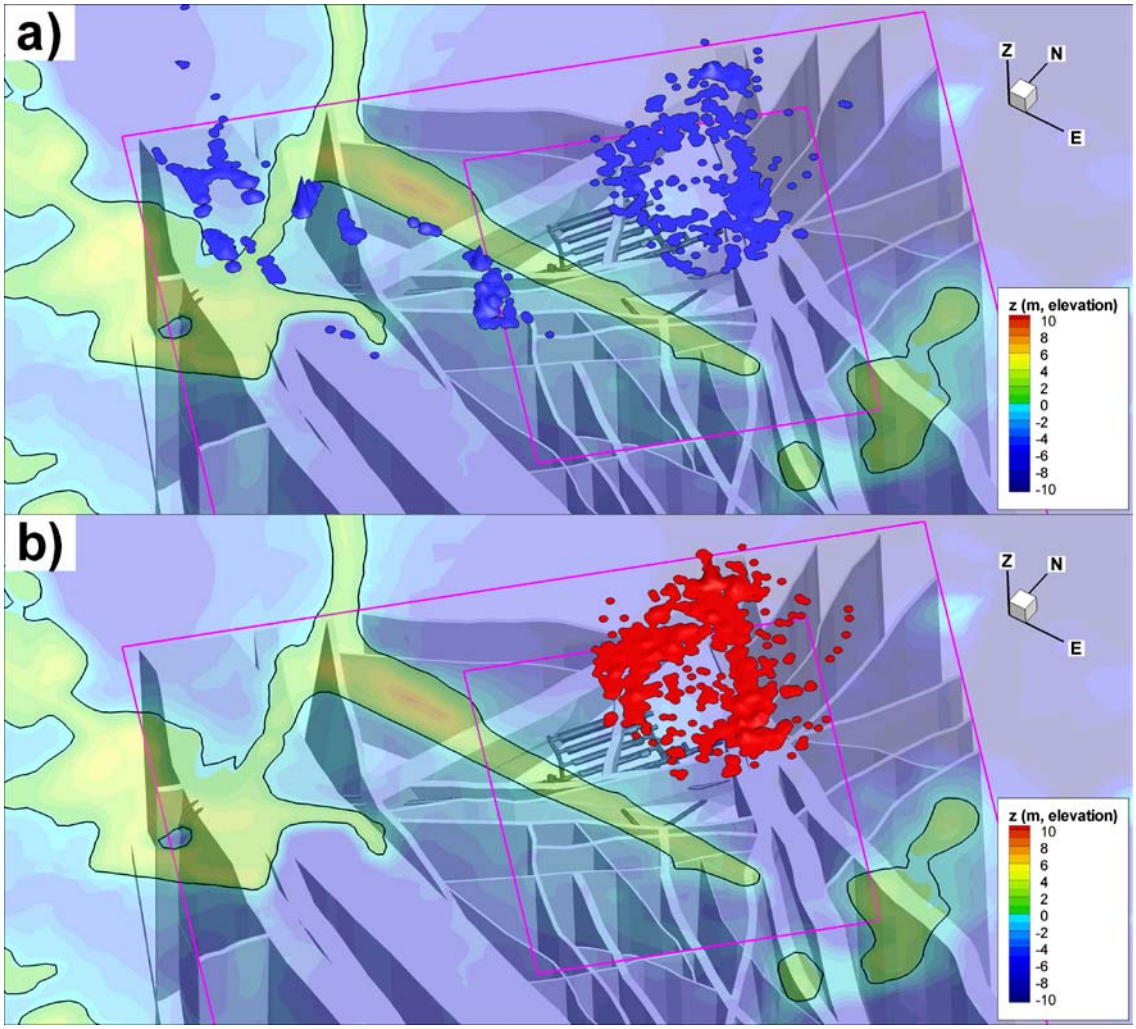

Figure 7-8. *Simulated groundwater discharge areas under saturated conditions; a) flow paths crossing the general tunnel (blue) and b) flow paths crossing SFR waste-storage facilities (red).*

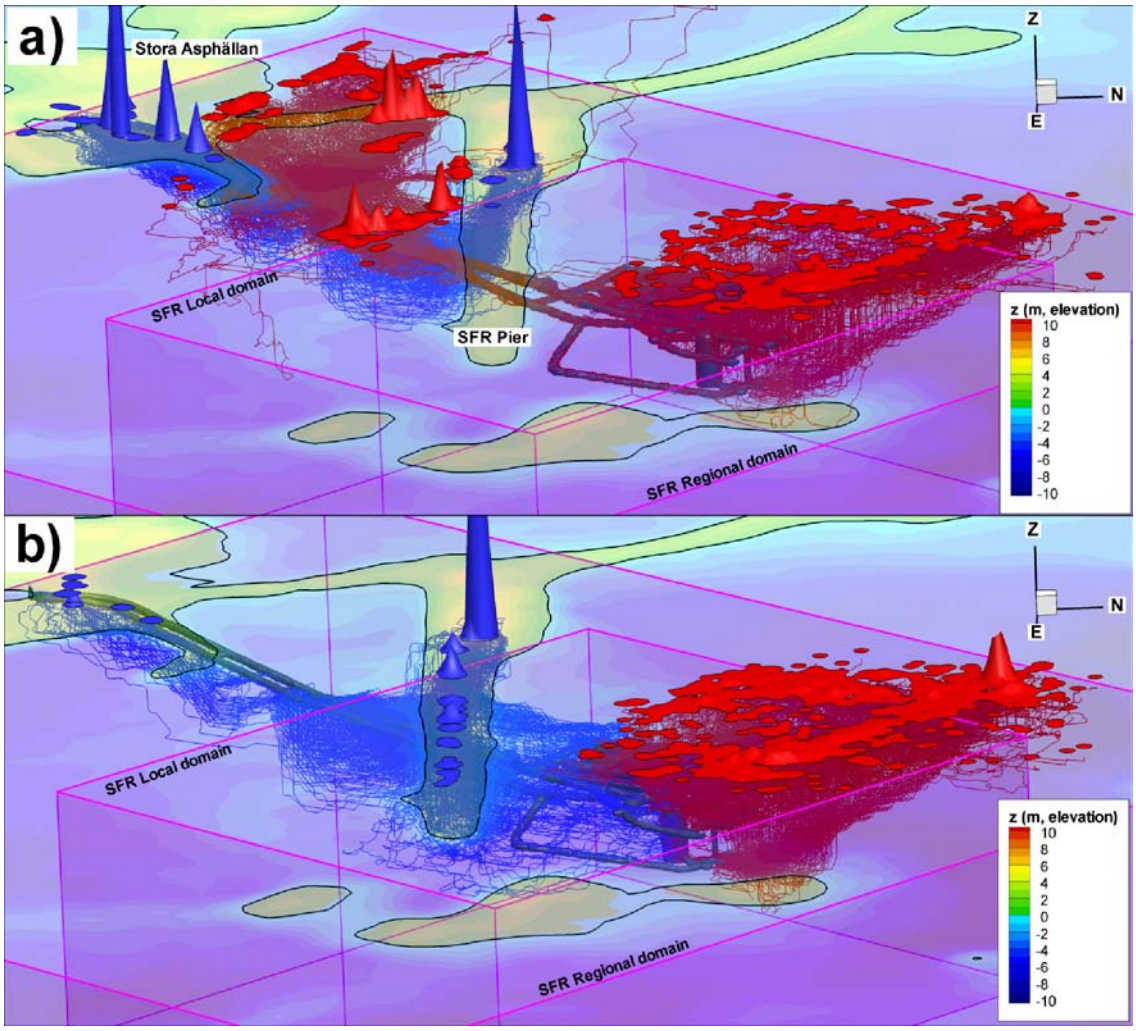

Figure 7-9. *Simulated trajectories for saturated conditions; a) the largest fluxes across the general SFR tunnel and b) the largest fluxes through SFR waste-storage facilities. Groundwater recharge areas and backward trajectories are shown as blue, whereas discharge areas forward trajectories are red.*

8 Summary and conclusions

This study presents the numerical implementation of the hydrogeological model for SFR v. 1.0, which has been previously parameterised based on single-hole transmissivity data interpretations (Öhman et al. 2012). Model-performance evaluation by comparing simulation results with available measurements is a necessary step in order to build confidence in the conceptual model

Owing to several circumstances, the outcome of tests performed in this study is not very conclusive for model-calibration purposes. One of the key uncertainties relates to the interpretation of the on-going, declining tunnel inflow, which raises concerns regarding the *representativeness* of current inflow data for describing the undisturbed (future, re-saturated) hydrogeological system. Another limitation to the prospect of tunnel-inflow calibration is that the constraining power in data weakens beyond the controlling flow resistance. Specifically, local physical/chemical alterations near the tunnel wall (so-called skin effects) obscure the determination of hydraulic properties in the bedrock outside the affected area if the analysis is based on tunnel-inflow data. In other words, the constraining power of tunnel inflow is small for structures in the target area for the planned SFR extension. This difficulty is further accentuated by necessary simplifications in the numerical implementations, which make simulation results inconclusive for model calibration if current tunnel inflow is used as calibration data.

As opposed to a formal flow model calibration, a perturbation analysis is employed where the performance of each simulation (perturbation) of the flow model is checked by comparing model results with available data. The purpose is to build confidence in the parameterisation of the hydrogeological model by investigation whether available motivate any substantial changes. The simulations are divided into three parts, addressing the following:

1. Constraining power in data versus model complexity (Model Exercises M0 to M7; Chapter 5).
2. Interference tests and deterministic structures (Chapter 6).
3. Recharge and discharge under open (current state) and re-saturated (initial or future state) flow regimes, respectively (Chapter 7).

8.1 Model Exercises M0 to M7

In the first part of the model simulations, the sensitivity of the model parameterisation to the complexity of the model is tested by exposing the model to a series of "perturbations" (sequentially added hydrogeological complexity). The sensitivity is evaluated by the impact on performance measures in terms of simulated tunnel inflow and head in monitored borehole sections. The simplest, homogeneous model setup (denoted M0), agrees surprisingly well with inflow and head data. The tunnel inflow simulations do not support the strong horizontal/vertical anisotropy in hydraulic conductivity, which has been interpreted from borehole data (M1). The introduction of deformation zones (M2), as parameterised from borehole data, causes excessive simulated tunnel inflow (c 25 times the measured inflow). Thus, the hydraulic role of the predominantly vertical deformation zones in *current* tunnel inflow is less significant than one would expect based on single-hole transmissivity data alone. Or, put in other words, tunnel inflow due to intercepts with steeply dipping deformation-zone inflow is reduced by some resistance that is not apparent in local-scale borehole transmissivity data.

Three types of flow resistances, or hydraulic bottlenecks, of the system are considered in the subsequent exercises M3, M5, and M6. These exercises explore if the available data are sufficient for determining which resistance type (1, 2, or 3) is dominating:

1) The flow resistance can be due to a scaling effect related to large-scale discontinuity and/or within-plane heterogeneity within zones. However, reassessing the hydraulic parameterisation from a less conservative standpoint and introducing local conditioning (Appendix A) provides only minor improvements (M3a).

2) The flow resistance can reflect local physical/chemical/mechanical alterations of the disturbed hydrogeological system (tunnel-wall skin, grouting, and natural processes discussed in Sections 2.5 and 2.8). Introducing tunnel-wall skin reduces the simulated inflow, but at the expense of poor agreement to measured head (M3b).
3) Wide-spread head decrease patterns can indicate that the flow resistance is located closer to the contact to the overlying Baltic Sea and/or poor fracture connective in the vertical direction. The hydraulic contact in significant flow paths is addressed in M5 and M6 (i.e. Singö/SDM-Site Forsmark sheet joints and ZFM871/ZFMNW0805B).

The introduction of SBA-structures (M4) has negligible impact on performance measures (head and inflow). None of these structures have direct contact to the existing SFR, and clearly, their role in simulated tunnel inflow is minor. This demonstrates the limitations of using tunnel inflow simulations for calibrating structures that are not in direct contact to the existing SFR, but nevertheless are of potential significance for the SFR extension.

Different parameterisation alternatives are tested in Model Exercise M5. However, contradictory to expectations none of the cases have substantial effects on performance measures (inflow and head), and thus provide little guidance for reducing uncertainty or improving the parameterisation. The insensitivity to model parameterisation further emphasises the limitations of using the tunnel inflow setup for model calibration.

The simulated head decrease due to the ongoing drainage of SFR is underestimated near both the dominant sink terms of the system, namely the Southern boundary belt and zone ZFM871 (both were intensively grouted during the SFR construction). Therefore, the upstream flow paths for these two inflow locations are addressed in detail in Model Exercise M6. In this exercise, the model setup has a significant level of model sophistication, including the following:

- HCD: Final parameterisation (Table 3-2), conditioned intercepts (Table A-3), differentiated tunnel-wall skin (Table 5-3), as well as local adjustments to the ZFM871/ZFMNW0805 junction and the Singö/sheet-joint junction (Section 3.4.1).
- HRD: Increased anisotropy in the hydraulic conductivity (a = 3 in Equation 3-5) and depth trend defined by Equation 3-6.
- HSD: Implemented according to SR-Site Forsmark, but with a vertical hydraulic conductivity (K_z) that is reduced by a factor of 10.
- SBAs: Implemented as deterministic structures SBA1 to SBA7.
- Refined discretisation (maximum cell size is 8 m in the upper bedrock).

Some improvement in simulated head is noted among the recently drilled boreholes at greater distance from the existing SFR). The introduction of spatially variable tunnel skin (Table 5-3) reduces the inflow to the existing SFR to a more realistic magnitude (Table C-6). Still, the current deformation-zone flow must be subject to some type of flow resistance, which is not captured by local-scale hydraulic borehole data.

In conclusion, some improvement was accomplished in exercise M6, but in perspective of the level of additional model complexity compared to the performance of the most simplistic case set-up, M0, the improvement is small. Thus, the available performance measures, measured inflow and borehole heads, after c 25 years of operation of the existing SFR, cannot be used to distinguish a clear "best set-up" among the studied models M0–M6.

In exercise M7, several resistances are added sequentially to reduce the high tunnel inflow that was simulated in exercise M2. The implemented resistances reflect: a) a skin effect, b) grouting, c) effective HCD transmissivity, d) structural junctions, and e) HSD isolation. All these resistances have some impact on the simulation results but their relative importance cannot be deduced.

Therefore, the tunnel-skin resistance was reduced to reflect only grouting and the simulated inflow is compared with the estimated initial tunnel inflow at time $t = t_0$, i.e. at time of start of operation of SFR some 25 years ago (Section 2.8.1). This calculated inflow is found to be realistic compared to historic data, which tends to support the most significant adjustments subsequent to the M3b exercise: 1) Reducing the effective transmissivities of ZFMWNW0001, ZFMWNW1035 and ZFM871, and 2) increasing the sea-bottom sediment resistance in the upper parts of ZFMNW0002, ZFMWNW0001, and ZFMWNW1035 (cf. Figure 3-2b).

8.2 Interference-test simulations

Two actual interference tests were simulated to study the performance of the hydrogeological model. The performance measures in this study do not only include observed hydraulic responses in responding borehole sections, but also the *absence* of response in non-responding borehole sections. Owing to necessary simplifications in the model setup, the objective is *not* to establish a fine-tuned model calibration, but instead to elaborate with the setup to gain more insight into model performance.

The short duration of the tests (one and three days, respectively) necessitates a transient onset, which introduces the highly uncertain parameter storativity. Owing to this circumstance, it was decided to apply a simplistic model setup, where only deterministic structures are included (selected deformation zones and SBA-structures). The exclusion of stochastic components (DFN fractures and Unresolved PDZs) is expected to substantially under represent the sub-horizontal hydraulic connectivity. Nonetheless, the simplification was considered to be necessary in order to avoid the time-consuming complexity of addressing multiple realizations. The FracMan software was used for this purpose, as it allows more feasible handling of transient simulations and borehole discretisation. Apart from this simplification, the parameterisation is kept as consistent as possible to the previous DarcyTools exercises.

In principle, the starting point of transient simulations is a steady-state solution for current conditions (open, drained SFR), where the overlying sea and the SFR tunnel are represented as constant-head conditions. The hydraulic contact to these boundaries is dampened by fitting tunnel-wall skin and sediment resistance that match inflow and head data. With this steady-state solution as starting point, the pumping and recovery phases are simulated transiently for the two separate tests, and simulated head decrease at borehole intercepts is compared with observed data.

The model setup and the parameterisation are elaborated to study the impact on model performance. These three adjustments were found to improve simulations:

1) The sub-horizontal hydraulic connectivity must be *increased* around HFR101 in order to reproduce steady-state head decrease and responses in KFR104. A deterministic structure is introduced to compensate the neglected component of DFN fractures and Unresolved PDZs.
2) The vertical hydraulic connectivity of deformation zones must be *reduced* inside the Central block in order to locally dampen vertical responses and to uphold the observed head difference between KFR104 and KFR105. Heterogeneity and discontinuity of steeply dipping deformation zones is mimicked by a low-transmissive band across zones inside the Central block.
3) The hydraulic connectivity of SBA1 is *reduced* to dampen the response in HFR102. This may indicate a) that the modelled geometry and properties of SBA1 is too conservative, or b) an artefact of the neglected DFN fracture-component (i.e. as shallow fractures are expected to provide hydraulic contact to the sea and dampen the pressure propagation).

In result, most responses could be reproduced and the number of undue simulated responses is reduced. Undue simulated responses indicate that deterministic structures are overly connected At the more detailed level, there are evident discrepancies in both simulated response times and magnitudes. Such discrepancies are expected to reflect heterogeneity beyond the level of detail addressed in this study. Discrepancies in response time probably relate to parameterised storativity, which is a highly uncertain parameter that has not been given much attention in this study. (It is noted that storativity is not needed for safety assessment flow calculations since the analyses are made with the assumption of steady-state conditions.)

The three adjustments specified above are associated to shortcomings in the simplified model set-up and uncertainty in storativity. Hence, *none* of the findings from the interference-test simulations are used to adjust the flow model parameterisation.

8.3 Recharge and discharge areas for two different flow regimes

Particle tracking was used to identify recharge and discharge areas for the following two flow regimes:

a) Inflow to the existing SFR facility (“radial flow” conditions to an open repository).
b) Topographically driven flow through a closed existing SFR facility to the current sea level (“uniform flow” conditions through a saturated repository).

The two flow regimes are widely different.

- In the open-tunnel case, the topography-driven gradients are clearly subordinate to the gradients imposed by the tunnel inflow. Under these conditions all gradients close to SFR are directed towards the underground facility. The most conductive components dominate the recharge areas to SFR (primarily deformation zones, and to a lesser extent also HSD layers, large stochastic fractures, and SBA-structures).
- Under topography-driven gradients, the topography above sea level in combination with stratigraphy and hydraulic properties of regolith layers determine the locations of recharge and discharge areas and the involved conductive structures. For example, the simulated tunnel inflow involves zone ZFM871 for unsaturated conditions, but not for saturated conditions. This active role of ZFM871 in current tunnel inflow is not supported by measured hydrochemical data, which indicates that the model is overly connected. The glacial-clay covered area south of the SFR pier is an example of how HSD locally controls recharge/discharge above the Southern boundary belt.

  The main flow paths from the rock caverns 1BTF, 2BTF, BLA and BMA to the downstream discharge areas pass ZFMNNW1209 and ZFMNNE0869. The main flow path from the Silo passes the NDB intercept in ZFM871, via ZFMNW0805A/B and ZFMNE0870. In summary, results are in line with expectations and rather similar to earlier modelling results of Holmén and Stigsson (2001), Odén (2009), and Öhman (2010). Large, transmissive stochastic fractures (primarily horizontal to gently dipping) cause a somewhat larger spreading of the discharge areas.

8.4 Concluding remarks

The tests of model performance in this study cannot substantially reduce the uncertainty in model parameterisation. There are several reasons for this: Limited constraining power in performance measures and associated data, uncertainty in data interpretation, and necessary simplifications in model setups. However, the overall impression is that the applied implementation (i.e. homogeneous hydraulic parameterisation of deformation zones and SBA-structures) leads to overrepresented hydraulic connectivity of deterministically modelled structures. Several actions taken to reduce large-scale hydraulic connectivity have improved, or at least not weakened, model performance. This is in line with the data-based conceptualisation in Öhman et al. (2012), according to which the fracture network is interpreted as locally highly transmissive (particularly near the geological boundary belts), but compartmentalised at the larger scale.

Tunnel-inflow simulations demonstrate that effective deformation-zone properties are constrained by some type of resistance that is not apparent in local-scale borehole data. Such resistances can reflect a) hydraulic disturbances from the SFR underground facility, b) scale effects related to heterogeneity within and discontinuity of large-scale structures, as well as limited contact at junctions between structures), and c) overlying sediments limiting the contact between groundwater in bedrock and the Baltic Sea.

The interference-test simulations demonstrate the presence of a significant sub-horizontal connectivity near the Southern boundary belt, which supports speculations on the existence of such structures (i.e. with characteristics of SBA or Unresolved PDZ) in that area (Öhman et al. 2012). If the occurrence of such structures is wide-spread along the Southern boundary belt, the volume of poorly connected bedrock mass in the Central block may be smaller than expected, which raises uncertainties about the hydraulics of in the southern, less charted part of the SFR Regional domain (see e.g. Figure 3-12).

This study suggests that the available data (head and inflow) for flow model calibration do not motivate a substantial adjustment of the parameterisation of the initial structural-hydraulic model of the charted part of the SFR Regional model domain, which is based on single-hole transmissivity data. It is unclear whether the model and its parameterisation would change substantially if additional interference test data were available. Therefore, it is suggested that uncertainties in the conceptual structural-hydraulic model and its parameterisation are studied in the safety assessment by means of multiple stochastic realisations. These should include the less charted parts of the SFR Regional model domain.

References

SKB's (Svensk Kärnbränslehantering AB) publications can be found at www.skb.se/publications.

Axelsson C-L, Mærsk Hansen L, 1997. Update of structural models at SFR nuclear waste repository, Forsmark, Sweden. SKB R-98-05, Svensk Kärnbränslehantering AB.

Axelsson C-L, Ekstav A, Lindblad Påsse A, 2002. SFR – Utvärdering av hydrogeologi. SKB R-02-14, Svensk Kärnbränslehantering AB. (In Swedish.)

Bosson E, Gustafsson, L-G, Sassner M, 2008. Numerical modelling of surface hydrology and near-surface hydrogeology at Forsmark. Site descriptive modelling, SDM-Site Forsmark. SKB R-08-09, Svensk Kärnbränslehantering AB.

Bosson E, Sassner M, Sabel U, Gustafsson, L-G, 2010. Modelling of present and future hydrology and solute transport at Forsmark. SR-Site Biosphere. SKB R-10-02, Svensk Kärnbränslehantering AB.

Carlsson A, Chritiansson R, 2007. Construction experiences from underground works at Forsmark. Compilation report. SKB R-07-10, Svensk Kärnbränslehantering AB.

Carlsson L, Carlsten S, Sigurdsson T, Winberg A, 1985. Hydraulic modelling of the final repository for reactor waste (SFR). Compilation and conceptualization of available geological and hydrogeological data. Edition 1. SKB SFR 85-06, Svensk Kärnbränslehantering AB.

Carlsson L, Winberg A, Arnefors J, 1986. Hydraulic modelling of the final repository for reactor waste (SFR). Compilation and conceptualization of available geological and hydrogeological data. SKB SFR 86-03, Svensk Kärnbränslehantering AB.

Carlsson L, Winberg A, Grundfelt B, 1987. Hydraulic modelling of the final repository for reactor waste (SFR). Evaluation of the groundwater flow situation at SFR. SKB SFR 86-07, Svensk Kärnbränslehantering AB.

Christiansson R, Bolvede P, 1987. Byggnadsgeologisk uppföljning. Slutrapport. SKB SFR 87-03, Svensk Kärnbränslehantering AB. (In Swedish.)

Curtis P, Markström I, Petersson J, Triumf C-A, Isaksson H, Mattsson H, 2011. Site investigation SFR. Bedrock geology. SKB R-10-49, Svensk Kärnbränslehantering AB.

Dershowitz W, Lee G, Geier J, Foxford T, La Pointe P, Thomas A, 1998. FracMan, Interactive discrete feature data analysis, geometric modelling and exploration simulation. User documentation, version 2.6. Redmond, WA: Golder Associates, Inc.

Follin S, 2008. Bedrock hydrogeology Forsmark. Site descriptive modelling, SDM-Site Forsmark. SKB R-08-95, Svensk Kärnbränslehantering AB.

Follin S, Stigsson M, Svensson U, 2005. Regional hydrogeological simulations for Forsmark – numerical modelling using DarcyTools. Preliminary site description. Forsmark area – version 1.2. SKB R-05-60, Svensk Kärnbränslehantering AB.

Follin S, Johansson P-O, Levén J, Hartley L, Holton D, McCarthy R, Roberts D, 2007a. Updated strategy and test of new concepts for groundwater flow modelling in Forsmark in preparation of site descriptive modelling stage 2.2. SKB R-07-20, Svensk Kärnbränslehantering AB.

Follin S, Levén J, Hartley L, Jackson P, Joyce S, Roberts D, Swift B, 2007b. Hydrogeological characterisation and modelling of deformation zones and fracture domains, Forsmark modelling stage 2.2. SKB R-07-48, Svensk Kärnbränslehantering AB.

Follin S, Johansson P-O, Hartley L, Jackson P, Roberts D, Marsic N, 2007c. Hydrogeological conceptual model development and numerical modelling using ConnectFlow, Forsmark modelling stage 2.2. SKB R-07-49, Svensk Kärnbränslehantering AB.

Gokall-Norman K, Ludvigson J-E, 2008. Hydraulic interference test with borehole HFM33 used as pumping borehole, November of 2007. SKB P-07-229, Svensk Kärnbränslehantering AB.

Gustafson G, 2009. Hydrogeologi för bergbyggare. Stockholm: Formas. (In Swedish.)

Hedenström A, Sohlenius G, 2008. Description of the regolith at Forsmark. Site descriptive modelling, SDM-Site Forsmark. SKB R-08-04, Svensk Kärnbränslehantering AB.

Hedenström A, Sohlenius G, Strömgren M, Brydsten L, Nyman H, 2008. Depth and stratigraphy of regolith at Forsmark. Site descriptive modelling, SDM-Site Forsmark. SKB R-08-07, Svensk Kärnbränslehantering AB.

Holmén J G, 2005. SFR-1. Inverse modelling of inflow to tunnels and propagation of estimated uncertainties to predictive stages. SKB R-05-74, Svensk Kärnbränslehantering AB.

Holmén J G, Stigsson M, 2001. Modelling of future hydrogeological conditions at SFR. SKB R-01-02, Svensk Kärnbränslehantering AB.

Jarsjö J, Destouni G, 2000. Degassing of deep groundwater in fractured rock around boreholes and drifts. Water Resources Research 36, 2477–2492.

Laaksoharju M, Gimeno M, Auqué L F, Gómez J B, Acero P, Pedersen K, 2009. Hydrogeochemical and microbiological effects on fractures in the Excavation Damaged Zone (EDZ). SKB R-09-05, Svensk Kärnbränslehantering AB.

Munier R, Stenberg L, Stanfors R, Milnes A G, Hermanson J, Triumf C-A, 2003. Geological Site Descriptive Model. A strategy for the model development during site investigations. SKB R-03-07, Svensk Kärnbränslehantering AB.

Nilsson A-C, Tullborg E-L, Smellie J, 2010. Preliminary hydrogeochemical site description SFR (version 0.2). SKB R-10-38, Svensk Kärnbränslehantering AB.

Odén M, 2009. Site investigation SFR. Hydrogeological modelling at SFR using DarcyTools. Site description SFR version 0.0. SKB P-08-94, Svensk Kärnbränslehantering AB.

Rhén I (ed), Gustafson G, Stanfors R, Wikberg P, 1997. Äspö HRL – Geoscientific evaluation 1997/5. Models based on site characterization 1986–1995. SKB TR 97-06, Svensk Kärnbränslehantering AB.

Rhén I, Follin S, Hermanson J, 2003. Hydrogeological Site Descriptive Model – a strategy for its development during Site Investigations. SKB R-03-08, Svensk Kärnbränslehantering AB.

SKB, 2008. Geovetenskapligt undersökningsprogram för utbyggnad av SFR. SKB R-08-67, Svensk Kärnbränslehantering AB. (In Swedish.)

Streltsova T D, 1988. Well testing in heterogeneous formations. New York: Wiley.

Svensson U, 2010. DarcyTools version 3.4. Verification, validation and demonstration. SKB R-10-71, Svensk Kärnbränslehantering AB.

Svensson U, Ferry M, Kuylenstierna H-O, 2010. DarcyTools version 3.4 – Concepts, methods and equations. SKB R-07-34, Svensk Kärnbränslehantering AB.

Walger E, Ludvigson J-E, Gentzschein B, 2010. SFR site investigation. Evaluation of selected interference tests and pressure responses during drilling at SFR. SKB P-10-43, Svensk Kärnbränslehantering AB.

Öhman J, 2010. Site investigation SFR. Hydrogeological modelling of SFR v 0.1. Influence of the ridge on the flow fields for different target volumes. SKB R-09-43, Svensk Kärnbränslehantering AB.

Öhman J, Follin S, 2010a. Site investigation SFR. Hydrogeological modelling of SFR. Data review and parameterisation of model version 0.1. SKB P-09-49, Svensk Kärnbränslehantering AB.

Öhman J, Follin S, 2010b. Site investigation SFR. Hydrogeological modelling of SFR. Model version 0.2. SKB R-10-03, Svensk Kärnbränslehantering AB.

Öhman J, Bockgård N, Follin S, 2012. Site investigation SFR. Bedrock hydrogeology. SKB R-11-03, Svensk Kärnbränslehantering AB.

Appendix A

Revised transmissivity evaluation of HCD intercepts

Deformation zones inside the SFR Regional domain are parameterised based on borehole hydraulic data, where intercepts are available. Deformation zones lacking support from hydraulic data at borehole intercepts are either taken from pooled statistics within the same deformation zone set, or taken directly from SDM-Site Forsmark. The measured transmissivity at a deformation-zone intercept, T(z), is depth-adjusted to calculate mean ground-surface level transmissivity, T_0, as defined in (3-4). Most deformation-zone intercepts are straightforward to evaluate. However, in some cases data the calculation of ground-surface transmissivity, T_0, requires a preceding step of manual interpretation and judgment (Öhman et al. 2012). A few complications in data interpretations are given below.

Deformation-zone junctions: At junctions between several HCDs, assumptions must be made to which HCD is the dominant and which are subordinate. Following SDM-Site Forsmark, gently dipping zones are considered to be the most dominant (i.e. ZFM871). Second in rank, the Northern boundary belt, ZFMNW0805A and B, is assumed to be dominant over general HCDs. Similarly, ZFMWNW0001 is assumed to dominate over ZFMWNW0002 and ZFMWNW1035 (i.e. Singö dominates over parallel splays). Finally, ZFMNNE0869 is assumed to dominate hydraulically over ZFMENE0870 (i.e. Zone 3 dominates over Zone 9).

Incomplete data support: Decisions must also be made if incomplete intercepts should be rejected or retained (i.e. borehole intercepts that *geometrically* only cover part of the full deformation zone width, as well as, borehole intercepts that only partially cover the intercept with *hydraulic data*). The details on geometric and hydraulic coverage are given in Öhman et al. (2012). It was decided not to use a strict rule for rejection of incomplete intercepts (such as presented in Öhman and Follin 2010a), but instead to evaluate each intercept manually in context of the general understanding of deformation zones. For example poor hydraulic coverage of ZFMNE3118 intercepts in KFR13, KFR54, and KFR55 all suggest that the deformation zone is low-transmissive (i.e. c 10^{-7} m^2/s). This would support the general understanding, as also tunnel intercepts exist without reported inflow. Therefore, the three intercepts are combined into *one* retained intercept (the other two are rejected), in order to provide a more balanced calculation of the mean $T_{eff}(0)$ for the zone.

Tunnel intercepts: Fracture inflow during the tunnel constructions and tunnel sections with grouting requirements are reported in Christiansson and Bolvede (1987). It is difficult to directly translate such information into realistic deformation-zone transmissivity values. Nevertheless, it does provide supplementary guidance, particularly in cases where borehole data are uncertain and scarce. Tunnel intercepts without notable inflow are assigned an intercept transmissivity that corresponds to the average rock mass outside deformation zones (more precisely, $T = K_{HRD} \cdot b$, where $K_{HRD} = 6.5 \cdot 10^{-9}$ m/s after Holmén and Stigsson (2001), and b is the hydraulic width of the zone).

Model Exercise M2 (Chapter 5), which was based on the initial deformation-zone parameterisation, result in excessive simulated tunnel inflow. The parameterisation of deformation zones in the vicinity of SFR are based on the historic data set, which is associated to poorer quality and larger uncertainties in interpretations. Therefore, as part of Model Exercise M3, it was decided to revise the supporting data for deformation-zone parameterisation, with guidance from the simulation results of M2. Particular emphasis was paid to the complex junction in the Southern boundary belt, as well as, a possible extension of ZFM871 beyond steeply dipping deformation zones. This appendix presents a few details on the analysis and assumptions made. Revised T_0-values for borehole intercepts in are listed in Table A-3. These intercepts were used to calculate the effective depth-adjusted ground-surface transmissivity $T_{eff}(0)$ for the 40 HCDs inside the SFR Regional domain (Table A-1).

Table A-1. Initial and revised deformation-zone parameterisation inside the SFR Regional model domain.

Deformation zone	Initial[1]		Revised interpretation[2]			Final[3]	Determination of final $T_{eff}(0)$
	log $T_{eff}(0)$ (m^2/s)	No. intcps[4]	log $T_{eff}(0)$ (m^2/s)	No. intcps[4]	Cond. points[5]	log $T_{eff}(0)$ (m^2/s)	
ZFM871	–4.8	14	log T(z) = z/30	19 (4)	15	log T(z) = z/30 – 0.7	A special depth-trend relations for transmissivity is fitted based on all 19 intercepts (5 of these are not included in the geological model). Difference between "Revised" and "Final" shown in Figure 3-4.
ZFMA1	–4.8	None			None		Taken from SDM-Site Forsmark
ZFMB10	–4.8	None			None		Assumed similar to ZFMA1
ZFMENE3115	–6.5	3			3		Taken as average from all 3 intercepts.
ZFMENE3135	–6.7	None			None		Taken as pooled average of the NNE to ENE set (only new data)
ZFMENE3151	–6.7	None			None		Taken as pooled average of the NNE to ENE set (only new data)
ZFMENE8031	–6.7	None			None		Taken as pooled average of the NNE to ENE set (only new data)
ZFMENE8034	–6.7	None			None		Taken as pooled average of the NNE to ENE set (only new data)
ZFMNE0870	–6.2	7	–6.3	8 (5)	7		Taken as average from 8 intercepts. Evaluated transmissivity at intercepts are exaggerated by unfavourable borehole orientations, causing long intercepts.
ZFMNE3112	–6.6	4			4		Taken as average from all 4 intercepts.
ZFMNE3118	–6.2	2	–6.6	3 (2)	3 (+1)		Taken as average of all 3 intercepts, weighted by low-transmissive tunnel intercept[3].
ZFMNE3134	–6.7	None			None		Pooled average of the NNE to ENE set (only based on new data)
ZFMNE3137	–7.3	4			4		Taken as average from all 4 intercepts.
ZFMNNE0725	–4.0	None			None		Taken from SDM-Site Forsmark
ZFMNNE0869	–4.6	4			4		Taken as average from all 4 intercepts
ZFMNNE2308	–6.1	None			None		Taken from SDM-Site Forsmark
ZFMNNE3130	–6.7	None			None		Taken as pooled average of the NNE to ENE set (only based on new data)
ZFMNNE3264	–6.7	None			None		Taken as pooled average of the NNE to ENE set (only based on new data)
ZFMNNE3265	–6.7	None			None		Taken as pooled average of the NNE to ENE set (only based on new data)
ZFMNNE3266	–6.7	None			None		Taken as pooled average of the NNE to ENE set (only based on new data)
ZFMNNW0999	–7.8	rejected			None		Rejected overlapping intercept. Value taken from pooled average of NNW group in SDM-Site Forsmark
ZFMNNW1034	–4.4	3			3		Taken as average from all 3 intercepts.
ZFMNNW1209	–5.9	2			2 (+4)		Taken as average from both 2 intercepts. The zone is interpreted as highly heterogeneous, and therefore the zone is conditioned at its intersections with the four disposal facilities.
ZFMNNW3113	–7.8	None			None		Taken from SDM-Site Forsmark, pooled average of NNW group
ZFMNS3154	–4.4	None			None		Assumed similar to ZFMNNW1034, based on location and orientation.
ZFMNW0002	–3.6	1	–4.6	1 (2)	1		Rejected intercept. Value taken from SDM-Site Forsmark

Deformation zone	Initial[1]		Revised interpretation[2]			Final[3]	Determination of final $T_{eff}(0)$
	log $T_{eff}(0)$ (m^2/s)	No. intcps[4]	log $T_{eff}(0)$ (m^2/s)	No. intcps[4]	Cond. points[5]	log $T_{eff}(0)$ (m^2/s)	
ZFMNW0805A	–4.3	7	–4.7	6 (2)	6		Taken as average of all 6 intercepts.
ZFMNW0805B	–4.7	7	–5.5	7 (1)	7 (+2)		Taken as average of 7 intercepts and 2 low-transmissive tunnel intercepts[3].
ZFMWNW0001	–3.8	9	–2.9	3 (9)	3	–3.9	Taken as average from 3 intercepts: KFR71, HFM34, and KFM11A render $T_{eff}(0) = 1.3\times10^{-3}$ m^2/s or log $T_{eff}(0) = –2.9$. The value was lowered one order of magnitude as a result of flow simulations.
ZFMWNW0813	–5.7	1	–5.9	1	1 (+1)		KFM11A, weighted by low-transmissive tunnel intercept[3]
ZFMWNW0835	–5.2	2			2		Taken as average of the 2 intercepts in KFR27
ZFMWNW0836	–7.1	rejected	–7.1	0 (2)	None		Two rejected intercepts. Value taken from SDM-Site Forsmark
ZFMWNW1035	–4.0	4	–4.0	2 (2)	4	–5.0	Only two intercepts used: HFM35, HFR105. This renders $T_{eff}(0) = 1.1\times10^{-4}$ m^2/s or log $T_{eff}(0) = –4.0$. The value was lowered one order of magnitude as a result of flow simulations.
ZFMWNW1056	–7.1	None			None		Taken from SDM-Site Forsmark
ZFMWNW3259	–4.2	1	–5.3	1	1 (+1)		KFM11A, weighted by low-transmissive tunnel intercept[3]
ZFMWNW3262	–4.6	2			2		Average of both intercepts
ZFMWNW3267	–6.7	2			2		Average of both intercepts.
ZFMWNW3268	–5.8	None			None		Taken as pooled average of the WNW to NW set (only new data).
ZFMWNW8042	–6.0	1			1		Single intercept used. Well-supported by sub-parallel PFL-f data.
ZFMWNW8043	–6.5	None			None		Taken as pooled average of the WNW to NW set (only new data).

1) Initial deformation-zone parameterisation used in M2a. Taken from Öhman et al. (2012, Table 6-1).

2) Revised deformation-zone parameterisation used in M3a. Determination of ground-surface transmissivity, Teff(0), is described in the comment field. Complete list of underlying data presented in Table A-3. In principle, Teff(0) is calculated as the geometric mean of T0 for available intercepts. Pooled deformation zone-set statistics, or values from SDM-Site Forsmark, are applied to zones without intercepts.

3) Final adjustments resulting from M6. Teff(0) is reduced for ZFMWNW1035, ZFMWNW0001, and ZFM871 to increase simulated head decrease.

4) Number of intercepts with hydraulic data that are judged representative for the HCD. The number in brackets indicate that additional intercepts exist, but that hydraulic data are unavailable, or judged to be misleading due to junction with other deformation zones that may dominate.

5) Number of conditional points for the particular HCD. The number in brackets indicates additional tunnel intercepts that have no record of inflow. Low-transmissive tunnel intercepts were set equal to the background conductivity used in Holmén and Stigsson (2001) (i.e. set to $T = 6.5 \times 10^{-9}$ m/s multiplied by the hydraulic width).

Southern boundary belt evaluation

There exist alternative interpretations of hydraulic data for the Southern boundary belt intercepts. The Southern boundary belt is a complex junction of several deformation zones. The experience from SDM-Site Forsmark is that the highest transmissivity data does not necessarily occur inside the geologically interpreted deformation-zone intercepts, but often close to the rim or just outside the interpreted intercepts. This causes particular uncertainty to hydraulic-data inference in the complex Sothern Belt junction.

Furthermore, prior experience from SDM-Site Forsmark indicates on the presence of high-transmissive SBA-structures or sheet-joint features in the shallow bedrock, close to the Southern boundary belt. Even though such structures are not understood to have formed from tectonic processes, their spatial distribution may be indirectly related to the Southern boundary belt area.

Table A-2. Interpretation of hydraulic properties of the Southern boundary belt.

WNW0001	log T_0	Comment
KFR71	–3	Data quality? Possible influence by SBA presence? Applied value.
KFM11A	–3	Geometrically complete, long intercept (498–824 m borehole length), subject to uncertainty in depth-adjustment. (The total measured transmissivity – without depth-adjustment – is only on the order 10^{-6} m^2/s) Applied value.
HFM34	–3 (or –4)	Geometrically complete. High-transmissive HTHB data **above** the interpreted intercept **included** (on the order 10^{-3} m^2/s). If these are interpreted as SBA-structures, the HCD intercept transmissivity is only on the order 10^{-4} m^2/s. Applied value.
HFR105	(–4.6)	Geometrically incomplete intercept. Excluded.
KFR61-67	(–3 to –5)	Geometrically incomplete intercepts. Possible influenced by SBA presence? All intercepts excluded.
SFR tunnel	(Grouted)	Grouted from ground surface, as well as, during tunnel construction. Still considered a major source of SFR inflow. Grouting and inflow data indicates high transmissivity, at least in the core.
NW0002		
KFM11A	(–3.5)	Only RVS intercept available. The intercept is assumed subordinate to ZFMWNW0001. Excluded. Parameterisation taken from Forsmark SDM.
WNW3259		
KFM11A	–4.2	Geometrically complete. Subject to uncertainty in depth-adjustment. Applied value.
SFR tunnel	(low)	No indication of grouting requirements, or excessive tunnel inflow. Tunnel intercept interpreted as “average rock”
WNW0813		
KFM11A	–5.7	Geometrically complete. Subject to uncertainty in depth-adjustment. Applied value.
SFR tunnel	(low)	No indication of grouting requirements, or excessive tunnel inflow. Tunnel intercept interpreted as “average rock”
WNW1035		
HFM35	–3.4	Geometrically complete. Applied value.
HFR105	–4.5	Geometrically complete. Applied value.
KFM11A	(–5.4)	Only RVS intercept available. The intercept is assumed to be dominated by ZFM-WNW0001. Excluded.
KFR68	(–2.8)	Geometrically incomplete. High-transmissive data **below** the interpreted intercept included (on the order 10^{-3} m^2/s). If these are interpreted as SBA-structures, the HCD intercept has no hydraulic coverage. Excluded.
SFR tunnel	(Grouted)	Intensively grouted, close to junction of ZFMNNE0869 and ZFMNE0870. Grouting data interpreted as indication of a high-transmissive HCD.

ZFM871 evaluation

Previous structural models of SFR have, to a large extent, included interpretations and considerations to hydraulic data. The current geological model SFR v. 1.0 is based on geological data and data interpretations, according to SKB’s established modelling methods. As a result, several unresolved issues are identified in the recent hydrogeological model v. 1.0, which are comparatively more difficult to assimilate in the conceptual understanding.

In the geological model SFR v. 1.0, the gently dipping ZFM871 is terminated at ZFMNW0805B and ZFMNNE0869. The uncertainties of these terminations are discussed in Curtis et al. (2011, Appendix 11). Hydraulic interpretations suggest that ZFM871 extends through these zones. One difficulty in data interpretation is that many borehole intercepts of ZFMNW0805A,B occur at their junction with ZFM871. In the earlier structural model of Axelsson and Maersk Hansen (1997), ZFM871 was modelled to outcrop to the seafloor. However, its Littorina character suggests that it has minor contact to the sea.

Hydrochemistry: According to the structural model, sections of KFR7A and KFR10 belong to steep zones (ZFMNW0805B and ZFMNNE0869). These sections are located within the same elevation interval as the intersection of an extended ZFM871 and also have Littorina water type (which is a characteristic for ZFM871). Other sections inside the steep zones (above the ZFM871 intersection) have Baltic water type, which is more in line with expectations.

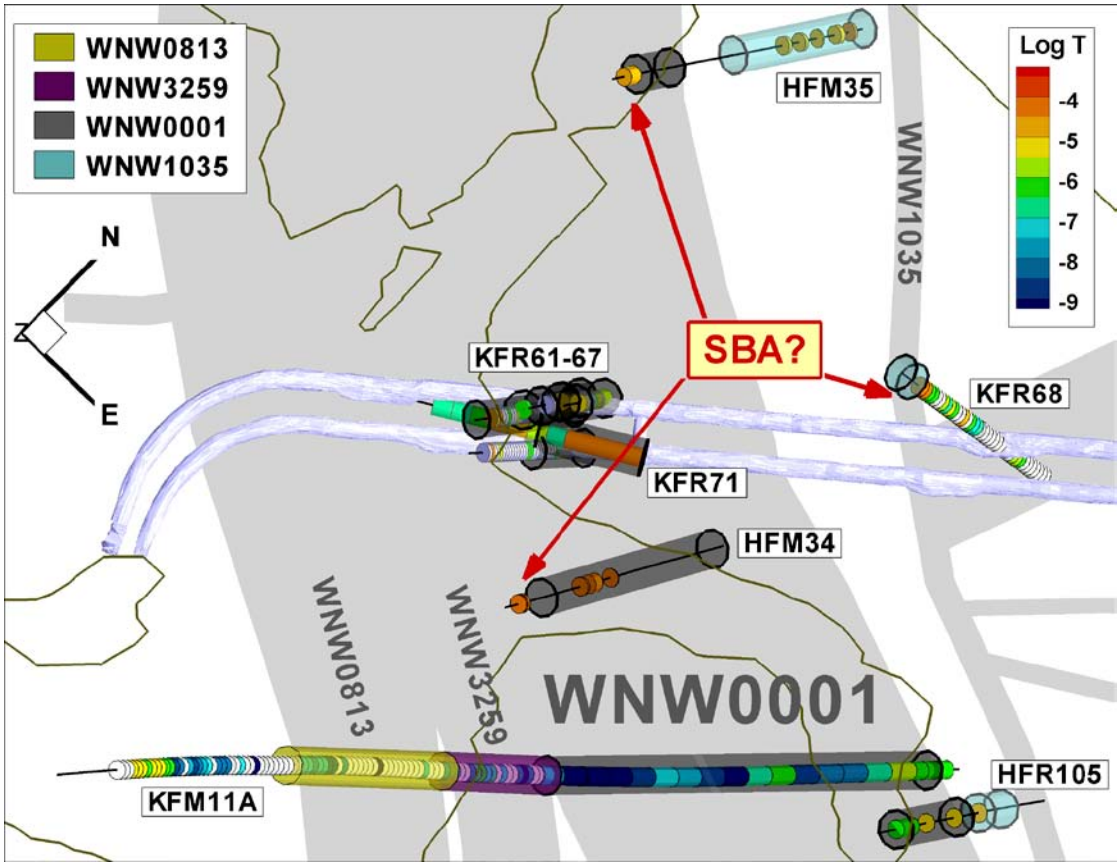

Figure A-1. *HCD intercept interpretation of the Southern boundary belt. HCD intercepts are shown as large transparent cylinders (coloured by HCD). Hydraulic data are shown with smaller cylinders (coloured by log T scale). The complexity of the Southern boundary belt causes uncertainty whether high transmissivities outside intercepts (red arrows) should be interpreted as 1) belonging to the nearest zone, or 2) independent SBA/sheet-joint structures.*

Virgin excess head: Although early reported data are *highly uncertain*, virgin excess head values have only been found for ZFM871 and KFR25. In KFR25, there are only early data available for the elevation interval that coincides with an extension of ZFM871. Excess head are only possible in a confined structure, i.e. possibly ZFM871, but not in a structure with good contact to the sea.

SFR head decrease: KFR7A has a large head decrease, which has increased over time and hence indicates poor contact with other sections inside ZFMNW0805B (boreholes KFR08 and KFR56)

Historic interference-test data: Direct responses from interference tests were observed between ZFM871 and ZFMNW0805A, while responses tend to be indirect for ZFMNW0805B (although the opposite would be expected from their relative locations). Based on this finding, Axelsson and Maersk Hansen (1997) interpreted "zone 8" to be of lesser hydraulic significance.

Peak transmissivity data: In four boreholes (KFR24, KFR25, KFR38, and KFR7A) transmissivity peaks occur at the same elevation interval as the expected extension of ZFM871. These transmissivity values are "more in line" with expectations of ZFM871 (as also modelled in previous models).

ZFMNW0805A,B compartmentalization: ZFMNW0805A,B have signs of compartmentalisation. It is modelled to actually intersect the SFR tunnel (i.e. according to RVS geometry, not tunnel mapping). No grouting or high tunnel inflows are reported at this modelled intersection, suggesting that the zone is discontinuous or low-transmissive in the vicinity of the Silo. This is also indicated in KFR56. In KFR101 (i.e. further away from SFR), there is evidence of Glacial Brackish water (i.e. isolated water).

The final interpreted HCD transmissivity intercepts are summarised in Table A-3. Intercepts where the log T_0 value is missing or placed within brackets have been rejected. Rejections are made if the hydraulic data coverage is poor, incomplete geometric coverage, or assumed subordination to another deformation zone.

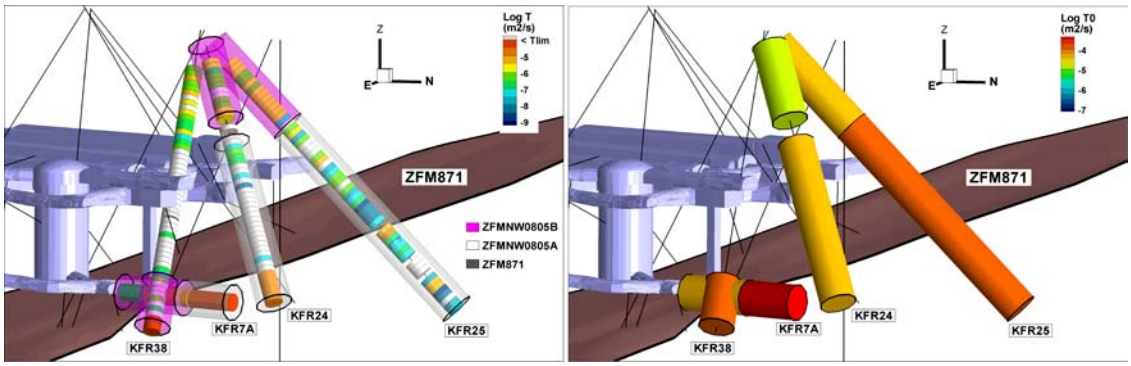

Figure A-2. *Hydraulic data and deformation zone intercepts in the geological model belonging to ZFMNW0805A,B (shown as large cylinders). The corresponding HCD T_0 are shown to the right.*

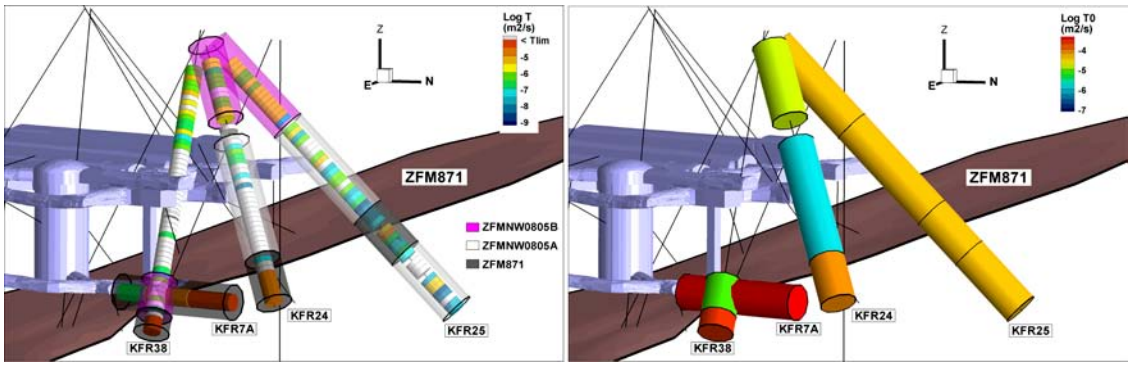

Figure A-3. *Alternative intercepts of an extended ZFM871 (as shown by black, large cylinders). The corresponding HCD T_0 are shown to the right.*

Table A-3. Compilation of total transmissivity measured inside HCD intercepts.

HCD	IDCODE	Intercept type	T (m^2/s)[1)]	Log T_0[2)]	Comment
ZFM871	KFR02	TARGET	$1.95 \cdot 10^{-7}$	NA	Supported by two transient injection tests from 106 to 126 m BHL.
ZFM871	KFR03	TARGET	$2.20 \cdot 10^{-8}$	NA	Notably low transmissivity in single pressure-build-up test 81 to 101.6 m BHL.
ZFM871	KFR04	TARGET	$5.00 \cdot 10^{-7}$	NA	Supported by single pressure-build-up test 84 to 100.5 m BHL.
ZFM871	KFR05	TARGET			No data available.
ZFM871	KFR10		$3.2 \cdot 10^{-5}$	NA	Interpreted as a possible extension of ZFM871 beyond ZFMNNE0869 (from 95.65 m to 107.28 m BHL)
ZFM871	KFR12	TARGET	$2.60 \cdot 10^{-6}$	NA	Supported by single pressure-build-up test 20 to 33 m BHL.
ZFM871	KFR13	TARGET	$3.00 \cdot 10^{-6}$	NA	Supported by two transient injection tests from 54 to 74 m BHL.
ZFM871	KFR21	RVS	$1.21 \cdot 10^{-5}$	NA	Well-supported by peaking transmissivity in the intercept. Hydraulic data in the interval 115 to 121 m used.
ZFM871	KFR22	RVS	$3.34 \cdot 10^{-6}$	NA	
ZFM871	KFR23	RVS	$6.31 \cdot 10^{-5}$	NA	Well-supported by peaking transmissivity in the intercept. Hydraulic data in the interval 71 to 107 m used.
ZFM871	KFR24		$1.93 \cdot 10^{-5}$	NA	Interpreted as a possible extension of ZFM871 beyond ZFM-NW0805B (132 to 158 m BHL)
ZFM871	KFR25		$2.02 \cdot 10^{-5}$	NA	Interpreted as a possible extension of ZFM871 beyond ZFM-NW0805B (124 m to 154 m BHL)
ZFM871	KFR31	TARGET	$1.81 \cdot 10^{-6}$	NA	Poor resolution in hydraulic data. Hydraulic data in the interval 200 to 242.1 m used.
ZFM871	KFR32	TARGET	$1.20 \cdot 10^{-4}$	NA	Single packer data from 157 to 209 m BHL used.
ZFM871	KFR33	RVS	$3.90 \cdot 10^{-6}$	NA	Supported by single packer data from 156 to 159 m BHL.
ZFM871	KFR37	TARGET	$5.42 \cdot 10^{-5}$	NA	Supported by high-transmissive data in the interval 183 to 209 m used.
ZFM871	KFR38		$4.2 \cdot 10^{-5}$	NA	Interpreted as a possible extension of ZFM871 beyond ZFM-NW0805B (175 m to 185.4 m BHL)
ZFM871	KFR57	TARGET			No data
ZFM871	KFR7A	RVS	$1.05 \cdot 10^{-4}$	NA	Interpreted as a possible extension of ZFM871 beyond ZFM-NW0805B (2 m to 74.7 m BHL)
ZFM871	KFR7B	TARGET	$2.60 \cdot 10^{-5}$	NA	Supported by single pressure build up test 7 to 21 m BHL.
ZFM871	KFR7C	TARGET	$6.72 \cdot 10^{-7}$	NA	Supported by single pressure build up test 6 to 34 m BHL.
ZFM871	KFR80	RVS			No data
ZFM871	KFR83	RVS			No data
ZFMENE3115	KFR102A	TARGET	$1.73 \cdot 10^{-6}$	–4.1	Exceptionally high-transmissive, gently dipping PFL-f for an ENE deformation zone at great depth (z < –400 m elevation). No PFL-f found over a 100 m borehole interval above the intercept. Subject to uncertainty in depth-adjustment. Possibly locally affected by the Northern boundary belt.
ZFMENE3115	KFR104	TARGET	$8.60 \cdot 10^{-9}$	–7.6	No PFL-f found inside the interval. The detection limit is taken as an upper estimate of the interval transmissivity. Considered typical of Central block characteristics.
ZFMENE3115	KFR105	TARGET	$6.10 \cdot 10^{-9}$	–7.7	Little hydraulic support by two PFL-f, which are sub-parallel to the deformation zone.
ZFMNE0870	HFR101	TARGET	$1.00 \cdot 10^{-7}$	–6.9	Below HTHB detection limit. Assumed value, as an upper estimate.
ZFMNE0870	KFR02	TARGET	$1.08 \cdot 10^{-6}$	–5.4	
ZFMNE0870	KFR03	TARGET	$3.55 \cdot 10^{-7}$	–5.8	
ZFMNE0870	KFR04	TARGET	$1.40 \cdot 10^{-7}$	–6.4	Long intercept due to sub-parallel borehole orientation, interpreted to exaggerate transmissivity. Only packer interval 28 to 43 m BHL used.
ZFMNE0870	KFR104	RVS			Intercept inside borehole casing. Not used.
ZFMNE0870	KFR31	TARGET			Assumed subordinate to ZFM871. Not used.
ZFMNE0870	KFR53	RVS	$2.35 \cdot 10^{-8}$	–7.2	Intercept covered by two long, low-transmissive packer data from 17 to 40.6 m.
ZFMNE0870	KFR54	TARGET	$\approx 10^{-7}$	–7[3)]	Possible erroneous data indicating 10^{-7} m^2/s. The value has been included to represent similar low-transmissive data partly inside, or close to other rejected intercepts of ZFMNE0870.
ZFMNE0870	KFR55	TARGET	$1.70 \cdot 10^{-7}$	–6.2	Covered by single pressure-build up interval from 22 to 39 m BHL.
ZFMNE0870	KFR68	TARGET			Subordinate to ZFMNNW0869. Not used.
ZFMNE0870	KFR70	RVS	$2.49 \cdot 10^{-6}$	–5.4	
ZFMNE0870	KFR7B	RVS			Poor data
ZFMNE0870	KFR7C	TARGET			Subordinate to ZFM871. Not used.

HCD	IDCODE	Intercept type	T (m^2/s)[1]	Log T_0[2]	Comment
ZFMNE3112	KFR102A	TARGET	$1.90 \cdot 10^{-8}$	–6.5	Little hydraulic support by single PFL-f, which is sub-parallel to the deformation zone.
ZFMNE3112	KFR102B	TARGET	$5.90 \cdot 10^{-7}$	–5.6	Supported by two moderately transmissive, horizontal and gently dipping PFL-f.
ZFMNE3112	KFR104	TARGET	$1.15 \cdot 10^{-7}$	–6	
ZFMNE3112	KFR105	TARGET	$2.25 \cdot 10^{-9}$	–8.1	Three low-transmissive PFL-f with scattered orientation. Considered typical pattern of Central block characteristics (inside as well as outside zones).
ZFMNE3118	HFR101	TARGET	$2.50 \cdot 10^{-7}$	–5.8	Moderate HTHB transmissivity. Estimated HTHB orientation sub-parallel to the zone.
ZFMNE3118	KFR104	TARGET	$1.78 \cdot 10^{-7}$	–6.6	
ZFMNE3118	KFR13	TARGET	$\approx 10^{-7}$	–7[3]	Poor data resolution. One of the hydraulic tests ($1.4 \cdot 10^{-6}$ m^2/s) partly covers the adjacent ZFM871 intercept. The interval is partly covered by an adjacent packer interval ($3.5 \cdot 10^{-8}$ m^2/s). The value 10^{-7} is been included to represent similar observations of low-transmissive data partly covering, or found close to ZFMNE3118 intercepts.
ZFMNE3118	KFR54	TARGET			No data ($T<10^{-7}$ m^2/s in surrounding rock)
ZFMNE3118	KFR55	TARGET			No data ($T<10^{-7}$ m^2/s in surrounding rock)
ZFMNE3137	KFR102A	TARGET	$9.50 \cdot 10^{-9}$	–7.4	Little hydraulic support. Only two low-transmissive, horizontal PFL-f. Typical pattern of NNE to ENE set.
ZFMNE3137	KFR102B	TARGET	$1.41 \cdot 10^{-7}$	–6.5	Little hydraulic support. Five moderately transmissive, sub-horizontal PFL-f. Typical pattern of NNE to ENE set.
ZFMNE3137	KFR104	TARGET	$1.70 \cdot 10^{-9}$	–7.5	No PFL-f found inside the interval. The detection limit is taken as an upper estimate of the interval transmissivity. Considered typical of Central block characteristics.
ZFMNE3137	KFR105	TARGET	$5.36 \cdot 10^{-9}$	–7.7	Several low-transmissive PFL-f with scattered orientation. Considered typical pattern of Central block characteristics (inside as well as outside zones).
ZFMNNE0869	KFR09	TARGET	$4.28 \cdot 10^{-5}$	–4	Highest transmissivity found at the end of the intercept.
ZFMNNE0869	KFR10	RVS	$3.00 \cdot 10^{-6}$	–4.9	Available hydraulic data in the interval 0 to 86 m BHL used.
ZFMNNE0869	KFR36	TARGET	$4.09 \cdot 10^{-5}$	–4.2	
ZFMNNE0869	KFR68	TARGET	$4.08 \cdot 10^{-6}$	–5.2	Only three packer data above detection limit (98 to 107 m BHL). Assumed to dominate over ZFMNE0870.
ZFMNNW0999	KFR08	RVS			Subordinate to ZFMNW0805A. Not used
ZFMNNW1034	HFR106	TARGET	$2.10 \cdot 10^{-5}$	–4.1	Distinct, high-transmissive HTHB with an estimated orientation parallel to the zone. Taken as key evidence for the Northern boundary belt characteristics. Estimation of HTHB orientation is highly uncertain.
ZFMNNW1034	KFR101	TARGET	$4.97 \cdot 10^{-6}$	–5.2	Several sub-horizontal to gently dipping PFL-f, which is typical of the shallow rock.
ZFMNNW1034	KFR106	TARGET	$7.60 \cdot 10^{-6}$	–4.1	Single, distinct, high-transmissive PFL-f parallel to the zone. Taken as key evidence for the Northern boundary belt characteristics.
ZFMNNW1209	KFR33	RVS	$6.00 \cdot 10^{-8}$	–7	The only data above detection limit in the interval are assigned to the possible stress-release structure SBA7. Remaining data below detection limit (6.00E-08 m2/s).
ZFMNNW1209	KFR35	TARGET	$1.09 \cdot 10^{-5}$	–4.8	Supported by 3 packer data above detection limit, 54 to 63 m BHL. The interval is also intersected by the possible stress-release structure SBA7.
ZFMNW0002	HFM34	TARGET			Subordinate to WNW0001. Not used
ZFMNW0002	HFM35	TARGET			Subordinate to WNW0001. Not used
ZFMNW0002	KFM11A	RVS	$8.72 \cdot 10^{-7}$	–3.5	The intercept is overlapped by the WNW0001. The peak transmissivity coinciding with the RVS intercept is associated to ZFMNW0002.
ZFMNW0805A	KFR08	TARGET	$1.93 \cdot 10^{-5}$	–4.3	
ZFMNW0805A	KFR101	TARGET	$6.14 \cdot 10^{-6}$	–4.2	Well-supported by several PFL-f; the most transmissive at c 300 m BHL are parallel to the deformation zone. Taken as key evidence for the Northern boundary belt characteristics.
ZFMNW0805A	KFR11	TARGET	$5.76 \cdot 10^{-5}$	–3.8	
ZFMNW0805A	KFR23	RVS			No data
ZFMNW0805A	KFR24	RVS	$7.50 \cdot 10^{-7}$	–5.8	Part of the intercept (above 132 m BHL) interpreted as possible extension of ZFM871. Hydraulic data in the interval 60 to 132 m used.
ZFMNW0805A	KFR25	RVS	$2.20 \cdot 10^{-5}$	–4.3	Hydraulic data in the interval 61 to 195.09 m used, except a midsection of the intercept interpreted as possible extension of ZFM871 (124 m to 154 m BHL).

HCD	IDCODE	Intercept type	T (m^2/s)[1)]	Log T_0[2)]	Comment
ZFMNW0805A	KFR56	RVS	$5.49 \cdot 10^{-7}$	–6	Covered by several low-transmissive, pressure-build up data with 3-m spacing.
ZFMNW0805A	KFR7A	TARGET			Re-interpreted as possible extension of ZFM871. Not used for ZFMNW0805A.
ZFMNW0805B	KFR08	TARGET	$6.10 \cdot 10^{-7}$	–5.8	
ZFMNW0805B	KFR101	TARGET	$8.30 \cdot 10^{-6}$	–4.7	Single, distinct, high-transmissive PFL-f parallel to the zone. Taken as key evidence for the Northern boundary belt characteristics.
ZFMNW0805B	KFR11	RVS	$9.20 \cdot 10^{-6}$	–4.7	Single packer interval 7 to 24 m BHL.
ZFMNW0805B	KFR24	RVS	$1.02 \cdot 10^{-5}$	–4.9	Hydraulic data in the interval 0 to 46 m used.
ZFMNW0805B	KFR25	RVS	$2.68 \cdot 10^{-5}$	–4.5	Hydraulic data in the interval 0 to 61 m used.
ZFMNW0805B	KFR38	TARGET	$1.54 \cdot 10^{-6}$	–5.2	Part of the intercept (175 m to 185.4 m BHL) interpreted as possible extension of ZFM871. Hydraulic data in the interval 153 to 175 m used.
ZFMNW0805B	KFR56	RVS	$2.00 \cdot 10^{-7}$	–6.4	Covered by single, low-transmissive, pressure-build up interval from 10 to 81.7 m BHL (i.e. covering also ZFMNW0805A).
ZFMNW0805B	KFR7A	TARGET			Re-interpreted as possible extension of ZFM871. Not used for ZFMNW0805A.
ZFMWNW0001	HFM34	TARGET	$1.10 \cdot 10^{-3}$	–2.6	Important intercept for determining the transmissivity in the upper part of ZFMWNW0001.
ZFMWNW0001	HFM35	TARGET			Incomplete coverage. No HTHB data inside the interval. High-transmissive interval near the intercept.
ZFMWNW0001	HFR105	TARGET	$(1.25 \cdot 10^{-5})$	(–4.6)	Incomplete coverage
ZFMWNW0001	KFM11A	TARGET	$3.41 \cdot 10^{-6}$	–3.1	Long, deep, complex intercept. Subject to uncertainty in depth-trend adjustment.
ZFMWNW0001	KFR01	TARGET			Poor coverage. Not used
ZFMWNW0001	KFR61	TARGET	$(4.31 \cdot 10^{-4})$	(–3.3)	Several data with 2 m packer spacing provides insight into local heterogeneity. However, due to incomplete coverage of the zone it is not used.
ZFMWNW0001	KFR62	TARGET	$(2.35 \cdot 10^{-4})$	(–3.4)	Several data with 2 m packer spacing provides insight into local heterogeneity. However, due to incomplete coverage of the zone it is not used.
ZFMWNW0001	KFR64	TARGET	$(3.25 \cdot 10^{-5})$	(–4.5)	Several data with 2 m packer spacing provides insight into local heterogeneity. However, due to incomplete coverage of the zone it is not used.
ZFMWNW0001	KFR65	TARGET	$(1.65 \cdot 10^{-5})$	(–4.8)	Several data with 2 m packer spacing provides insight into local heterogeneity. However, due to incomplete coverage of the zone it is not used.
ZFMWNW0001	KFR66	TARGET	$(4.67 \cdot 10^{-5})$	(–4.3)	Several data with 2 m packer spacing provides insight into local heterogeneity. However, due to incomplete coverage of the zone it is not used.
ZFMWNW0001	KFR67	TARGET	$(1.48 \cdot 10^{-5})$	(–4.8)	Several data with 2 m packer spacing provides insight into local heterogeneity. However, due to incomplete coverage of the zone it is not used.
ZFMWNW0001	KFR71	TARGET	$7.80 \cdot 10^{-4}$	–3	Important, perpendicular intercept for determining the transmissivity in the upper part of ZFMWNW0001.
ZFMWNW0813	KFM11A	TARGET	$1.41 \cdot 10^{-7}$	–5.7	Peak transmissivity above 300 m BHL resolved in this part of the long intercept KFM11A_PDZ1.
ZFMWNW0835	KFR27	TARGET	$8.1 \cdot 10^{-8}$ and $3.2 \cdot 10^{-6}$	–6.6 and –3.8	The upper intercept (108 to 120 m BHL) provides little hydraulic support, $T = 8.1 \cdot 10^{-8}$ m^2/s. In contrast, the considerably longer, deep intercept (323 to 469 m BHL) provides strong support from high frequency of PFL-f data, with a total transmissivity of $3.2 \cdot 10^{-6}$ m^2/s. The total value is dominated by 3 steeply dipping PFL-f at c 424 m BHL that are sub-parallel to the zone. The borehole has a strong head decrease peak at c 250 m BHL, which coincides with a potential extension of ZFM871 beyond its modeled termination against ZFMENE3115.
ZFMWNW0836	KFR08	RVS			Assumed subordinate to ZFMNW0805A. Not used
ZFMWNW0836	KFR25	RVS			Assumed subordinate to ZFMNW0805A. Not used
ZFMWNW1035	HFM35	TARGET	$1.20 \cdot 10^{-4}$	–3.4	Five highly transmissive HTHB data; three estimated to be sub-horizontal and two estimated to be parallel to the zone. Estimation of HTHB orientation is highly uncertain.
ZFMWNW1035	HFR105	TARGET	$1.10 \cdot 10^{-5}$	–4.5	Single high-transmissive HTHB data; estimated to be gently dipping. HTHB orientation is highly uncertain.
ZFMWNW1035	KFM11A	RVS	$(8.86 \cdot 10^{-9})$	(–5.4)	Subordinate to WNW0001. Not used
ZFMWNW1035	KFR68	RVS	$(1.38 \cdot 10^{-3})$	(–2.8)	High T outside intercept. Not used

HCD	IDCODE	Intercept type	T (m^2/s)[1]	Log T_0[2]	Comment
ZFMWNW3259	KFM11A	TARGET	$1.43 \cdot 10^{-6}$	–4.2	Peak transmissivity resolved in this part of the long intercept KFM11A_PDZ1.
ZFMWNW3262	KFR103	TARGET	$5.08 \cdot 10^{-6}$	–4.7	Three sub-horizontal to gently dipping, high-transmissive PFL-f. Alternatively modelled as SBA3,4,5.
ZFMWNW3262	KFR106	TARGET	$1.96 \cdot 10^{-5}$	–4.4	Four sub-horizontal to gently dipping, high-transmissive PFL-f. Alternatively modelled as SBA3,4,5.
ZFMWNW3267	KFR104	TARGET	$1.10 \cdot 10^{-8}$	–6.6	Little hydraulic support by single PFL-f, which is sub-parallel to the deformation zone. Considered typical pattern of Central block characteristics.
ZFMWNW3267	KFR105	TARGET	$4.10 \cdot 10^{-8}$	–6.7	Several low-transmissive PFL-f with scattered orientation (considered typical of Central block characteristics).
ZFMWNW8042	KFR105	TARGET	$2.74 \cdot 10^{-7}$	–6	Five moderately transmissive PFL-f that are sub-parallel to the zone.
ZFMNW0805B	IB	Tunnel	Estimated	–6.5[4]	Low-transmissive tunnel intercept. T set equal to $6.5 \cdot 10^{-9}$ m/s * b.
ZFMNW0805B	BT (end)	Tunnel	Estimated	–6.5[4]	Low-transmissive tunnel intercept. T set equal to $6.5 \cdot 10^{-9}$ m/s * b.
ZFMNE3118	NBT	Tunnel	Estimated	–7.0[4]	Low-transmissive tunnel intercept. T set equal to $6.5 \cdot 10^{-9}$ m/s * b.
ZFMWNW0813	BT, DT	Tunnel	Estimated	–6.2[4]	Low-transmissive tunnel intercept. T set equal to $6.5 \cdot 10^{-9}$ m/s * b.
ZFMWNW3259	BT, DT	Tunnel	Estimated	–6.4[4]	Low-transmissive tunnel intercept. T set equal to $6.5 \cdot 10^{-9}$ m/s * b.
ZFMNNW1209	1BTF	Tunnel	Estimated	–7.1[4]	Estimated based on low measured inflow (Table 4-3) and discrete inflow observations by Christiansson and Bolvede (1987). The local transmissivity is estimated as an order of magnitude lower than its average value (i.e. 0.1 · the value calculated from $T_{eff}(z)$ using Equation 3-3.
ZFMNNW1209	2BTF	Tunnel	Estimated	–6.1[4]	With consideration to measured inflow, the observed tunnel inflow (Christiansson and Bolvede 1987) is judged to be typical of this zone. Hence this conditional point is calculated from $T_{eff}(z)$ using Equation 3-3. Somewhat lower than the value log T = –5.7 used in Holmén and Stigsson (2001).
ZFMNNW1209	1BLA	Tunnel	Estimated	–5.1[4]	The 5 tonnes of grouting during construction indicates a particularly transmissive intercept. Prior to grouting, the local transmissivity is estimated as an order of magnitude higher than its average value (i.e. 10·the value calculated from $T_{eff}(z)$ using Equation 3-3. This is similar to the assigned transmissivity of SBA8, which was also grouted by 5 tonnes of cement. No flow in recent measurements (Table 4-3), suggests a value on the order log T ≈ –8 , after grouting.
ZFMNNW1209	1BMA	Tunnel	Estimated	–6.1[4]	With consideration to measured inflow, the observed tunnel inflow (Christiansson and Bolvede 1987) is judged to be typical of this zone. Hence this conditional point is calculated from $T_{eff}(z)$ using Equation 3-3.

1) Summed transmissivity inside the deformation zone intercept. Blank cells indicate rejection due to lack of hydraulic data. Values in parentheses indicate rejection due to incomplete geometric coverage of the zone.

2) Log T_0 is the logarithmic value of the depth-compensated intercept transmissivity that is used to define the effective transmissivity of the zone, $T_{eff}(0)$ (i.e. taken as the geometric mean of all available T_0 intercepts). ZFM871 is assigned a special relation in transmissivity depth trend, hence T_0 is inapplicable.

3) Uncertain value based on available data partly inside the intercept. These are assigned interpreted representative values that are considered necessary to provide a balanced, interpretation of the zone (only applied to ZFMNE0870 and ZFMNE3118).

4) Available hydraulic information from tunnel intersection of deformation zones, e.g. reported grouting or specific fracture inflow (Christiansson and Bolvede 1987), are also considered to provide a more balanced interpretation of the hydraulic characteristics of deformation zones. It is not straightforward information how such information should be used. It was decided to assume that *low-transmissive* tunnel intercepts (i.e. without record of grouting of specific fracture inflow) are equally weighted to a single borehole intercept, where the conductivity was assumed equal to the background conductivity used in Holmén and Stigsson (2001) (i.e. the intercept was set to $T = 6.5 \cdot 10^{-9}$ m/s multiplied by the hydraulic width).

Appendix B

Stochastic representation of SBA-structures

Introduction

The spatial extension of the deterministically modelled SBA-structures and their hydraulic continuity are highly uncertain, particularly in areas outside borehole coverage. This appendix describes a stochastic representation of the SBA-structures outside the deterministic modelled planes described in Öhman et al. (2012). It should be emphasised that although Öhman et al. (2012) represented the SBA-structures geometrically as large uniform planes, these structures are intended to represent interconnected clustered networks of composed of smaller, horizontal to gently dipping fractures. The SBA-structures are envisaged to depend intimately on connectivity to the Southern and Northern boundary belts and ZFMNNW1034, which are perceived as important vertical connectors to the overlying sea (Figure B-1).

The spatial extension and existence of SBA-structures outside borehole coverage is plausible, but also highly uncertain. It was therefore decided to complement the deterministic structures SBA1 to SBA7 by a stochastic representation, and to examine the impact in tunnel inflow simulations (Figure B-1). This analysis is referred to as Model Exercise M7 (see Section 5.8). The objective of this Model Exercise is to demonstrate a numerical implementation of the current conceptual understanding of the model domain. The simplified, informal approach taken for this purpose does *not* strictly follow the established SKB methodology for hydro-DFN modelling (e.g. Munier et al. 2003).

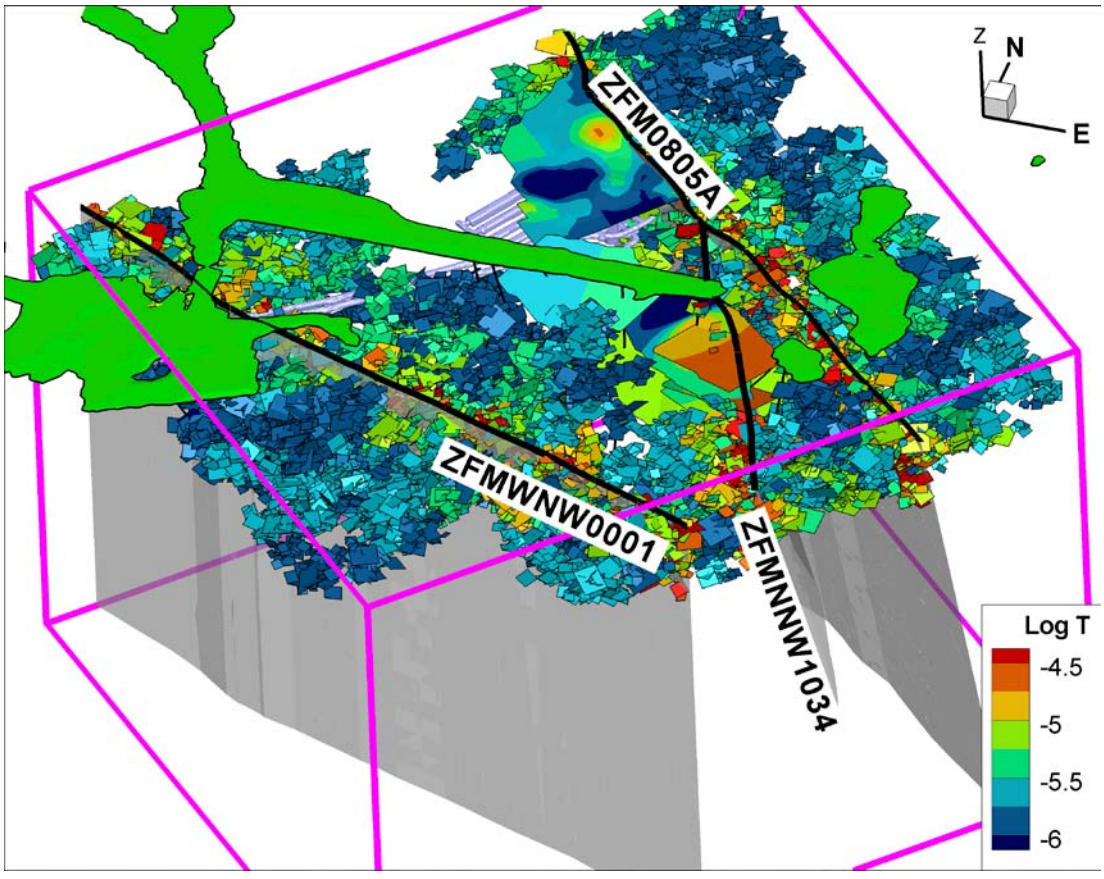

Figure B-1. *Deterministic SBA-structures (SBA1 to SBA7) complemented by stochastic representation in areas of poor borehole coverage. The three deformation zones ZFMWNW0001, ZFMNW0805A, ZFMNNW1034 are envisaged as hydraulic boundaries for the sub-horizontal stochastic network.*

Data used

Only the most transmissive PFL-f data ($T \geq 10^{-6}$ m^2/s) outside deterministic deformation zones are used as the basis to generate stochastic SBA-structures. Data inside Unresolved PDZs are included. In addition, two HTHB data (in HFR106 and HFR101; $T \geq 10^{-6}$ m^2/s) are included; their orientation estimates are highly uncertain. Four HTHB data (from boreholes HFM34 and HFM35) located close to the Southern boundary belt were *not* included. The reason is that the separation between HRD and HCD is less distinctive in the vicinity of the Southern boundary belt (i.e. it is not fully clear if they should be interpreted as SBA or belonging to deformation zones, see Appendix A; Figure B-1). For the same reason, these boreholes are excluded in the subsequent simulated exploration. In total, there are 34 records with transmissivity exceeding 10^{-6} m^2/s; all data are above –200 m elevation (Table B-1).

Orientation and set representation

Out of the 34 studied features, 31 are horizontal to gently dipping (dip ≤ 40º; referred to as set Hz/Gd) and three are steeply dipping (dip ≥ 70º; Figure B-2). Fracture sets are implemented as Fisher distributions, defined by a mean pole and an orientation distribution, defined by the Fisher concentration, κ. The mean pole of the Hz/Gd set has a trend of 33º and a plunge of 86º and with a Fisher concentration of κ = 21.1. Among the steeply dipping features, two are steep NE-striking and one steep EW-striking (Figure B-3). Only these three records are available for the steeply dipping sets (EW and NE striking sets) and hence, no orientation parameterisation can be estimated. Instead the parameterisation of the EW and NE sets is taken from the preliminary hydro-DFN for SFR v. 0.2 (Öhman and Follin 2010b), see Table B-2.

Table B-1. Transmissivity data used as basis for stochastic SBA representation.

Borehole PFL-f	Borehole length [m]	Strike [º]	Dip [º]	Elevation [m, elevation]	Set	Class	Log T
KFR101_026	180.95	124	18	–143.6	Hz	PDZ	–4.9
KFR102A_034	188.3	109	9	–169	Hz	HRD	–5.6
KFR102A_042	200.81	147	20	–180.4	Hz	HRD	–5.7
KFR102A_048	205.89	166	16	–185	Hz	HRD	–5.5
KFR102B_031	48.62	132	12	–37	Hz	HRD	–5.9
KFR102B_072	130.24	359	5	–102.9	Hz	HRD	–5.6
KFR102B_079	149.81	160	4	–118.6	Hz	PDZ	–5.3
KFR103_002	14.05	224	22	–9	Gd	HRD	–4.6
KFR103_005	20.38	288	19	–14.2	Hz	HRD	–5.3
KFR103_028	64	99	4	–49.5	Hz	HRD	–5.8
KFR103_031	84.58	357	15	–66.1	Gd	PDZ	–5.9
KFR103_032	85.67	223	2	–67	Hz	PDZ	–5.0
KFR103_033	86.61	157	9	–67.7	Hz	PDZ	–5.3
KFR104_027	64.52	157	22	–49.8	Gd	HRD	–5.6
KFR27_013	192.51	63	23	–189.6	Gd	HRD	–5.2
KFR106_004	37.51	30	23	–34.2	Gd	PDZ	–5.8
KFR106_023	85.31	125	7	–79	Hz	PDZ	–4.8
KFR106_029	100.7	344.6	16.1	–93.5	Hz	PDZ	–4.8
KFR106_035	113.16	302	36	–105.1	Gd	HRD	–5.6
KFR106_047	154.36	98	38	–143.7	Gd	PDZ	–5.6
KFR106_048	154.58	100	32	–143.9	Gd	PDZ	–5.4
KFR106_049	156.08	116	7	–145.3	Hz	PDZ	–4.7
KFR106_061	188.02	34	23	–175.1	Gd	HRD	–5.6
HFR106_001	39	232.6	7.1	–31.9	Hz	PDZ	–4.5
HFR101_001	107.65	9.2	86.	–97.1	NE	PDZ	–5.6
KFM11A_005	77.385	201.9	69.3	–65.4	NE	HRD	–5.5
KFM11A_006	79.307	228.1	14.4	–67.1	Hz	HRD	–6.0
KFM11A_007	80.205	191.3	22.8	–67.9	Gd	HRD	–5.3
KFM11A_013	94.967	282.8	9.6	–81	Hz	HRD	–6.0
KFM11A_014	95.587	300.6	13.1	–81.6	Hz	HRD	–6.0
KFM11A_016	97.296	281.5	17.6	–83.1	Hz	HRD	–6.0
KFM11A_018	100.25	298.7	7.3	–85.7	Hz	HRD	–5.3
KFM11A_023	108.38	81.9	2.8	–92.9	Hz	HRD	–5.5
KFM11A_048	88.8	108.3	81.8	–75.6	EW	HRD	–5.0

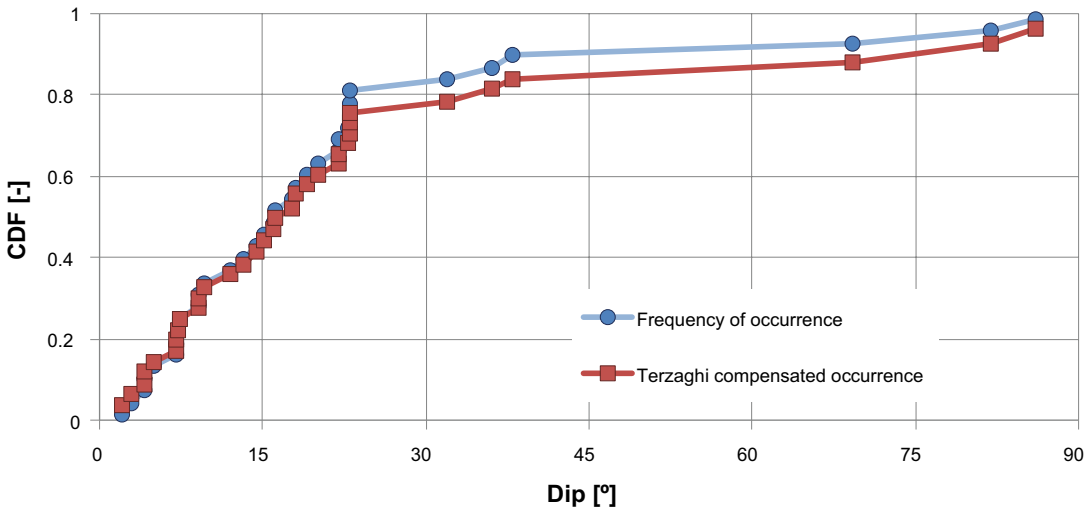

Figure B-2. *Hydraulic data used in stochastic SBA modelling, only transmissivity exceeding 10^{-6} m^2/s outside deterministic deformation zones are included (i.e. also data inside Unresolved PDZs are included). Approximately 80% dip less than 30°.*

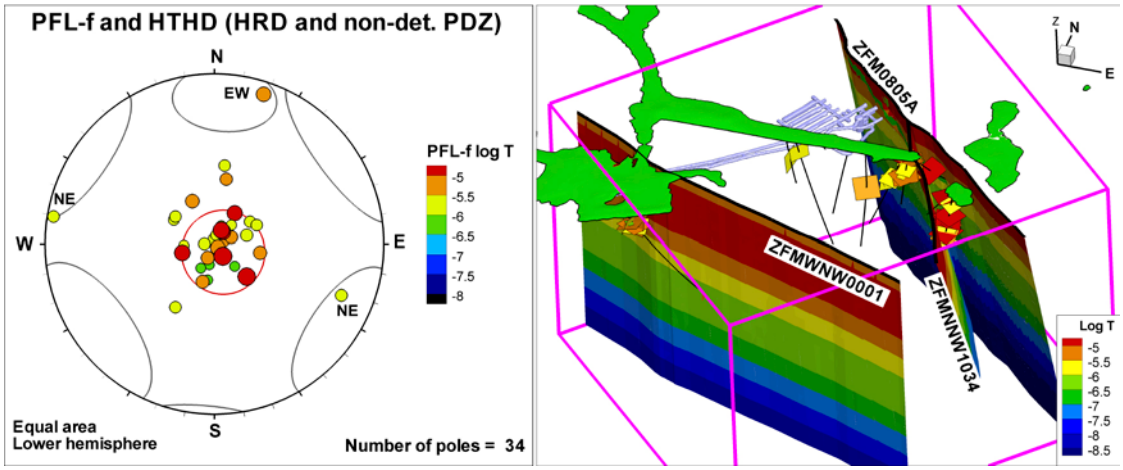

Figure B-3. *Hydraulic data used in stochastic SBA modelling, only transmissivity exceeding 10^{-6} m^2/s outside deterministic deformation zones are included; a) orientation distribution and b) spatial location of hydraulic data in relation to the hydraulic boundaries used.*

Size scaling

Little information on size distribution can be inferred from data. However, the SBA-structures are not envisaged as large uniform planes, but instead as clustered networks of smaller interconnected features (Öhman et al. 2012). On the other hand, based on their high transmissivity, SBA-structures are considered to belong to a fraction of larger fractures (i.e. considerably larger than the smallest flowing fracture considered in Öhman and Follin (2010b); $r_0 = 0.038$ m). From a practical aspect of the numerical upscaling procedure in DarcyTools, anisotropy is not resolved for stochastic features smaller than the resolution of the computational grid (GEHYCO; Svensson et al. 2010). The key trait of SBA-structures is envisaged as a strong horizontal anisotropy. Thus, in order to resolve this numerically in the flow model, the minimum size must at least exceed the cell size of the computational grid. Smaller fractures are expected to result in larger heterogeneity between realisations, and thus reflect a higher degree of model uncertainty.

Guidance was taken from the largest estimated sizes in Öhman and Follin (2010b) (c 50 m), the distance between transmissive non-deterministic PDZs and nearest deformation zones of the Northern boundary belt calculated in Öhman et al. (2012) (≤ 75 m), as well as, the expected resolution of the numerical model (cell size 16 m). Based on this, the SBA-structures were generated as square planes with side lengths in the range 16 to 64 m.

The size distribution of stochastic fractures is often assumed to follow a power-law scaling that is defined by the size-scaling exponent, k_r. The size-scaling exponent controls the proportion of short fractures in relation to large fractures. A high value of k_r implies that large fractures are relatively rare, whereas a low value implies that the size distribution tends to be more uniform. Typical model values range between 2 and 3, where the horizontal set has been associated to somewhat lower values (e.g. Follin et al. 2007b, Öhman and Follin 2010b). Without inference from data, it was decided to assume a value of 2.1 for all sets (Table B-2).

Intensity with depth

All the 34 records are located above –200 m elevation (Table B-1). Most SBA-structures are found within the elevation interval –50 to –110 m elevation (Figure B-4). It can be noted that the three steeply dipping features are also found in this interval. Below –100 m elevation, the frequency drops, in spite of high borehole coverage. Steeply dipping features are important for connectivity, and therefore possibly enhances the intensity of horizontal features in the interval (–50 to –110 m) elevation.

It was decided to generate Hz/Gd features with constant intensity over the entire interval (0 to –200 m elevation). With consideration to borehole coverage and data uncertainty, it is quite possible that steeply dipping features also exist over that same interval (i.e. 0 to –200 m elevation). However, the current understanding of the hydrogeological system at SFR is the Northern and Southern boundary belts control the connectivity to the sea. Therefore, to avoid excessive connectivity to the sea, i.e. with consideration to their vertical extent, steeply dipping features are only generated in the interval (–50 to –110 m) elevation (supported by data). Fractures are generated using the Poisson distribution (i.e. fracture centres uniformly distributed in space).

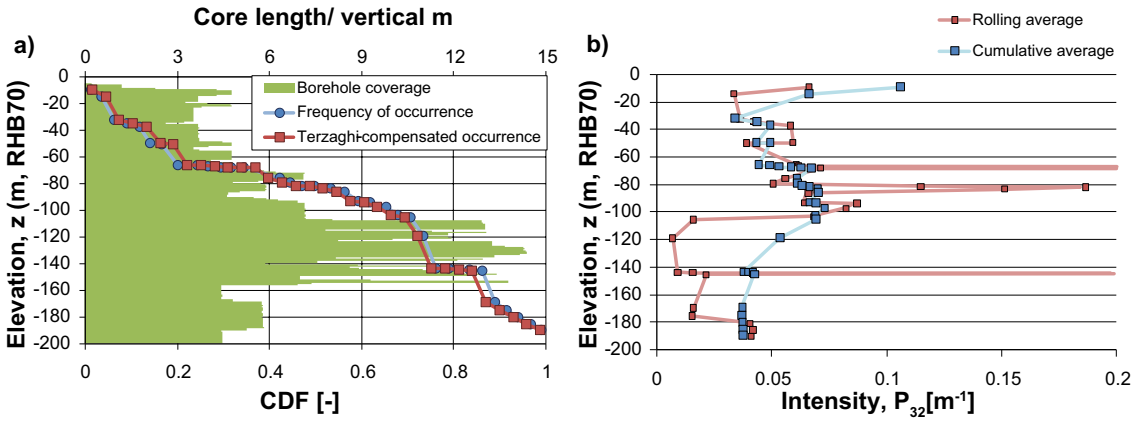

Figure B-4. Intensity of SBA-type structures with depth (all transmissivity exceeding 10^{-6} m^2/s outside deterministic zones are included); a) cumulative frequency of occurrence in relation to borehole coverage and b) calculated intensity.

Table B-2. Parameterisation of the stochastic SBA representation.

Set	Intensity $P_{32,Tot}$ (m^{-1})	Size distribution r_{min} (m)	k_r	Orientation Trend [º]	Plunge[º]	Fisher k	Depth interval, z (m elevation) From	To
EW	0.0054	16	2.1	4	14	9.05	–50	–110
NE	0.015	16	2.1	124	3	11.98	–50	–110
Hz/Gd	0.048	16	2.1	33	86	21.1	+10	–200

The resulting parameterisation used to generate "stochastic features of SBA-type" is summarised in Table B-2. Note that the intensity of PFL-f data (Figure B-4) reflects the *connected* subset of the fracture network, which is different from the *total* intensity, $P_{32,Tot}$. The total fracture intensity includes both connected and isolated fractures, and must therefore, depending on the connectivity of the fracture network, be higher than the intensity of PFL-f data (see details in Öhman and Follin 2010b). Therefore, the model input intensity was fitted by trial-and-error until the intensity of connected fractures in simulated borehole exploration was in reasonable agreement with PFL-f data (i.e. the only confirmative entity as the total intensity is unknown). The connectivity analysis and the simulated borehole exploration are explained below.

Connectivity analysis

The purpose of the connectivity analysis is to remove isolated fractures (i.e. not part of the flowing fracture network) and to reproduce the pattern of gradually decreasing transmissivity with distance from the hydraulic boundaries. This is performed in accordance with the conceptual interpretation of the role of PFL-f data in context of hydraulic chokes, discussed in Öhman and Follin (2010b). All stochastic features are assigned an initial transmissivity value (i.e. the "true fracture transmissivity"). To mimic the effect of hydraulic chokes, fractures are also assigned an *apparent transmissivity* (intended to reflect the largest measurable specific capacity in PFL-f logging). A fracture in direct contact with the hydraulic boundary does not depend on upstream transmissivity, and hence its apparent transmissivity is equal to its true fracture transmissivity. The apparent transmissivity is dependent on hydraulic choking along the upstream flow path. Note that the hydraulic-choking component caused by limited geometric contact between fracture planes is not addressed here.

The apparent transmissivity of indirectly connected fractures depends on its upstream hydraulic path. It cannot exceed the lowest apparent transmissivity along its upstream path to the hydraulic boundary. However, in the presence of several upstream paths, the calculation is based on the most transmissive alternative path. In other words, the apparent transmissivity of a daughter feature cannot exceed the maximum value of its connecting parent features (nor can it exceed its "true fracture transmissivity"). The purpose of this numerical calculation scheme is to gradually reduce the transmissivity and the intensity of the stochastic fracture network with distance from its hydraulic boundary, similarly to data observations (Figure B-5). High-transmissive paths are more likely to propagate further away from the hydraulic boundaries in the presence of many alternative routes (i.e. locally high connectivity).

Two main cases are explored: 1) A complete stochastic SBA representation (i.e. replacing the deterministic planes SBA1 to SBA7, presented in Öhman et al. 2012), and 2) complementary stochastic SBA representation (i.e. only covering the model volume outside the deterministic planes SBA1 to SBA7). The approach taken to generate realizations can be summarised as follows:

1) Stochastic realisations are generated inside a theoretical volume that encloses the SFR model domain, according to Table B-2. The fracture generation domain is bounded by $x'_{min} = 5{,}900$, $x'_{max} = 8{,}200$, $y'_{min} = 8{,}400$, $y'_{max} = 10{,}800$ in the rotated local coordinate system (described in Section 4.3).
2) Fractures located completely outside the SFR Regional domain, as well as fractures intersecting the tunnel wall of SFR (Figure B-5), are removed. It is beyond the scope to include fractures outside the SFR Regional domain. Furthermore, the model domain southeast of SFR is also covered by sheet joints as defined in Site-SDM Forsmark (see Section 3.4.1). Excluding the SBA-structures that intersect the SFR tunnel is motivated by conditional information from the tunnel; either they are known to be insignificant for tunnel inflow, or they have been identified as transmissive structures and have therefore been grouted (Öhman et al. 2012).
3) Three deformation zones are envisaged as hydraulic boundaries in the connectivity analysis: ZFMWNW0001, ZFMNW0805A, and ZFMNNW1034. Fractures in *direct contact* with the three hydraulic boundaries are assigned a lognormal-distributed transmissivity, according to Equation B-1 with $\mu = -5.0$ and $\sigma = 0.25$. Fractures *indirectly connected* to the hydraulic boundaries are assigned a larger heterogeneity, $\mu = -5.0$ and $\sigma = 0.5$ in Equation B-1. Fractures lacking hydraulic connectivity, neither direct nor indirect, are removed (Figure B-5).

4) Apparent transmissivity is calculated for indirectly connected fractures, which depends on the apparent transmissivity of its upstream hydraulic path.

5) Stochastic realisations are evaluated with simulated borehole exploration (e.g. Figure B-9). Fracture set intensity is modified by trial-and-error for 10 realisations until reasonable accordance with data is found.

6) For the complementary simulations, all stochastic fractures within 10 m from the deterministic planes are removed (Figure B-6).

7) The stochastic fracture network is merged with deterministic structures and upscaled into equivalent continuum grid-cell properties using the DarcyTools module GEHYCO (e.g. Figure B-7), after which tunnel inflow is simulated. The GEHYCO algorithm is based on *geometric upscaling*, which is a simplified method to translate fracture network properties into equivalent continuum properties. *Flow-based upscaling* is an alternative upscaling method that is more complex, but preserves the flowing characteristics of the "true" underlying fracture network during the upscaling process (i.e. taking phenomena as connectivity and hydraulic choking into account). Thus, for the standard cell-size discretisation applied in regional-scale modelling, GEHYCO does not preserve the connectivity of the underlying fracture network very well (or more specifically, gaps in connectivity that are smaller than the cell size), nor does it take the hydraulic choking phenomenon into account. In order to at least account for hydraulic choking, it was decided to use the *apparent transmissivity* in the GEHYCO upscaling (although it should be noted that the geometric connectivity is still overrepresented).

Fracture transmissivity is randomly assigned from a log-normal distribution:

$$T = 10^{N(\mu,\sigma)} \qquad \text{(B-1)}$$

where μ is the logarithmic mean (set to –5.0) and σ is the standard deviation in logarithmic transmissivity (set to 0.25 for fractures in direct contact with hydraulic boundaries, and 0.5 for other fractures). The apparent transmissivity for a fracture is calculated as the maximum apparent transmissivity among its upstream paths to the hydraulic boundary. The apparent transmissivity of an upstream path is taken as the minimum fracture transmissivity along the connected fracture sequence.

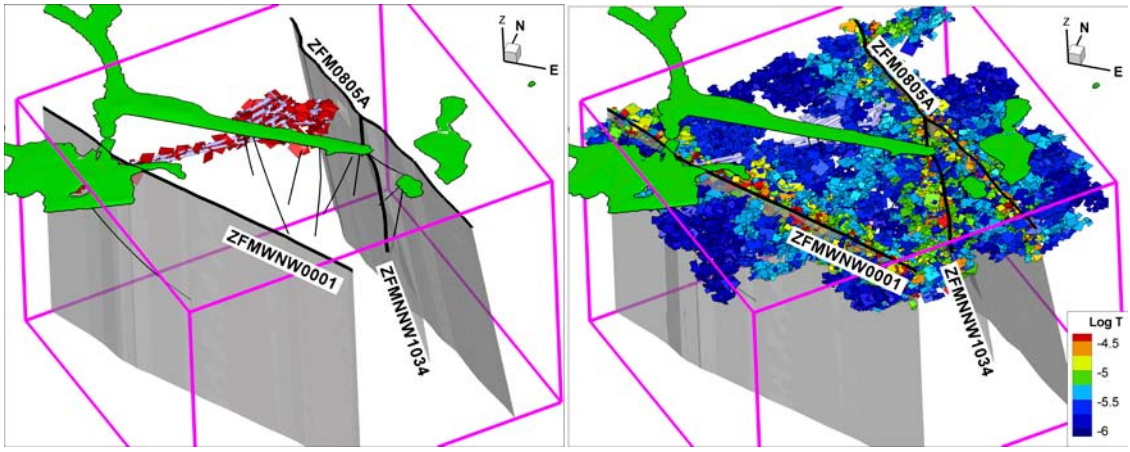

Figure B-5. *Stochastic features intersecting the SFR tunnel removed prior to connectivity analysis (left). Stochastic realization of SBA-structures connected to any of the three hydraulic boundaries (right).*

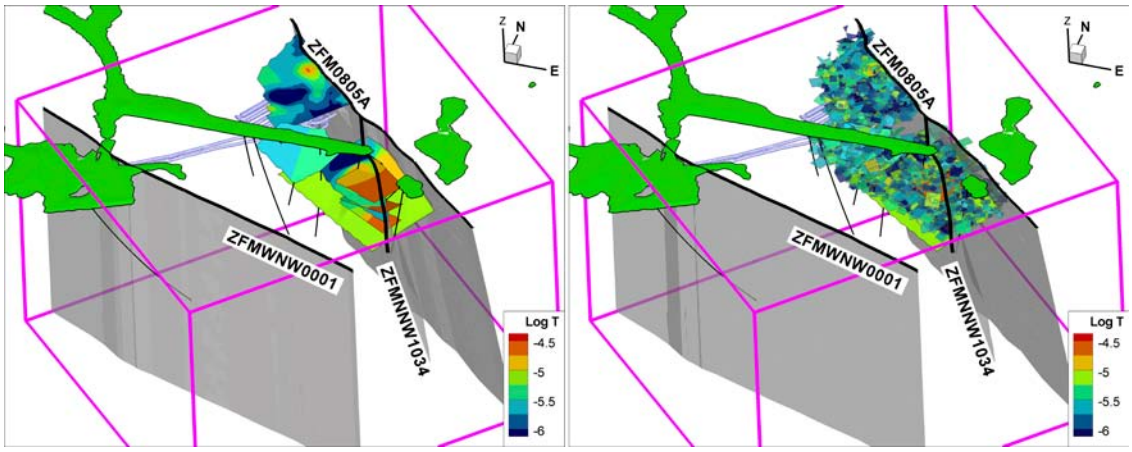

Figure B-6. *Deterministic planes representing SBA-structures in areas of borehole coverage (SBA1 to SBA7; left). In the "complementary simulations" the model volume with less borehole coverage are complemented by stochastic. Hence, all stochastic fractures closer than 10 m from the deterministic planes (right) are removed.*

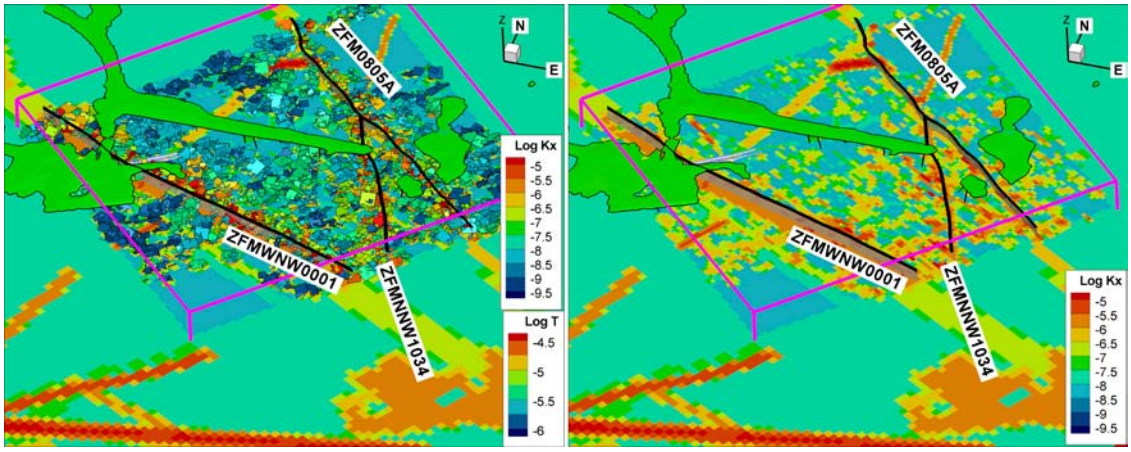

Figure B-7. *Translating stochastic SBA-structures into an "equivalent" porous medium conductivity field using the DarcyTools geometric upscaling module GEHYCO (horizontal cross-section at z = –60 m elevation; cf. Figure B-8).*

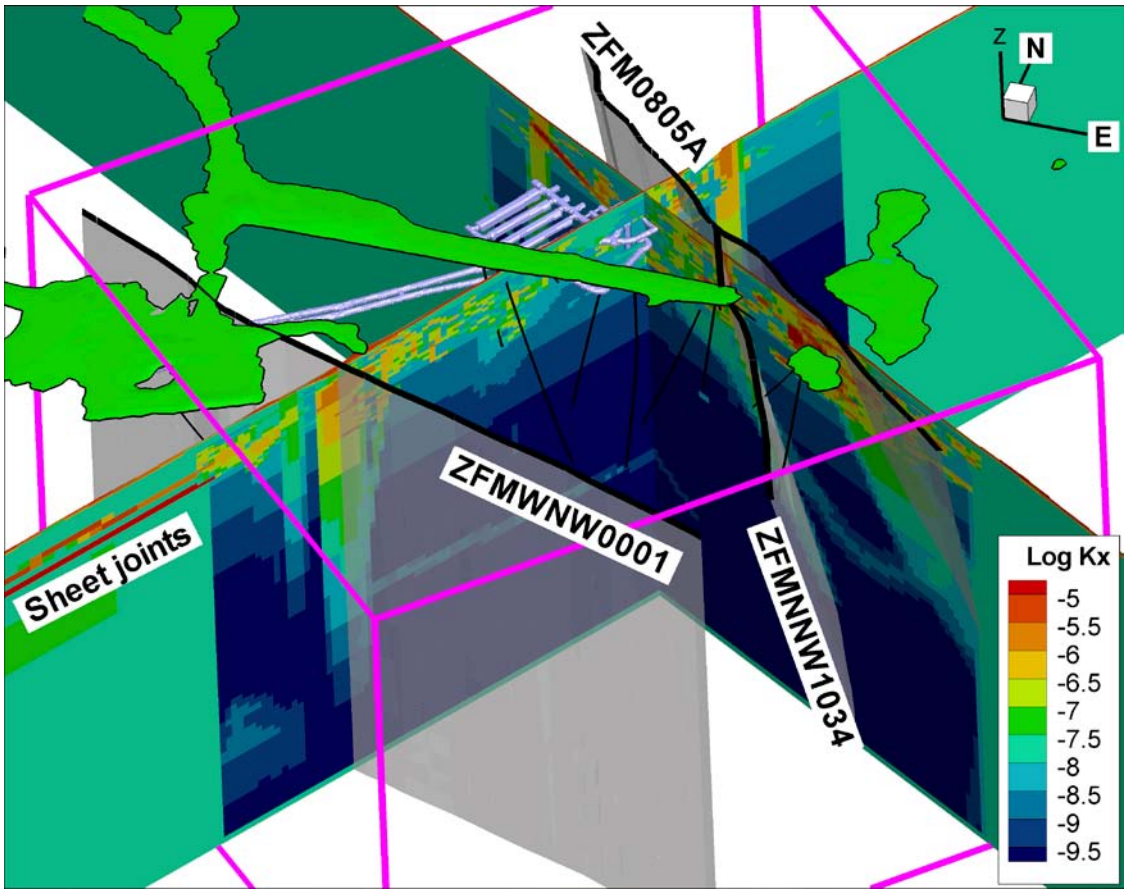

Figure B-8. *Translating stochastic SBA-structures into an "equivalent" porous medium conductivity field using the DarcyTools geometric upscaling module GEHYCO (vertical cross-sections; cf. Figure B-7).*

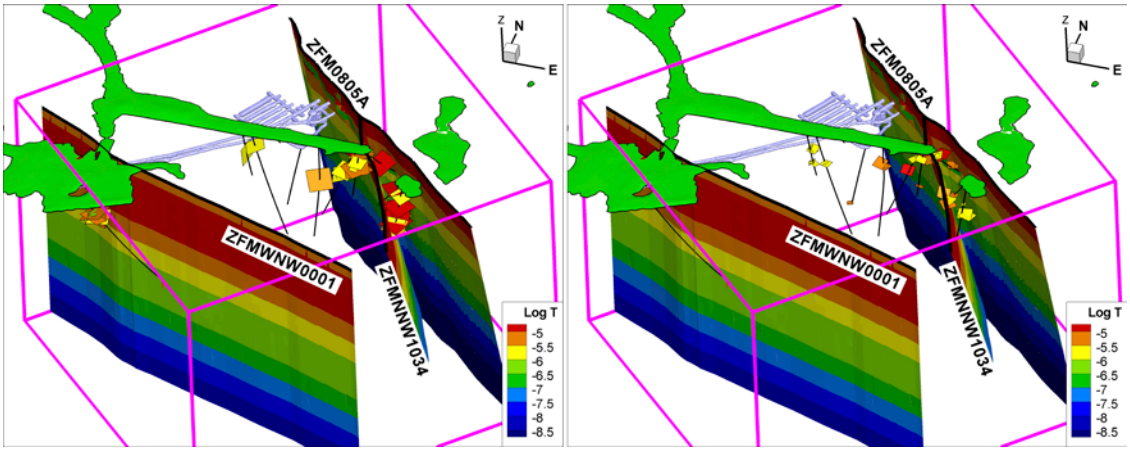

Figure B-9. *Based on location of high-transmissive SBA-structures ($T \geq 10^{-6}$ m^2/s) three deformation zones are defined as hydraulic boundaries: ZFMWNW0001, ZFMNW0805A and ZFMNNW1034. SBA-structures intersected by boreholes; PFL-f data (left) and single realization of stochastic SBA-structures connected to the hydraulic boundaries (right).*

Simulated borehole exploration and intensity calibration

The intensity of PFL-f data (Figure B-4) only reflects the *connected* subset of the fracture network. The model input in Table B-2 must reflect *total* intensity, $P_{32,Tot}$ (i.e. including both connected and isolated fractures). In this aspect, the total fracture intensity is unknown and must therefore, depending on the connectivity of the fracture network, be calibrated by means of simulated borehole exploration (see details in Öhman and Follin 2010b). Note that the theoretical upper intensity bound, defined by the intensity of open fractures/crush zones, is of little practical value, as the high transmissive SBA-structures constitute a very small fraction of the Open fractures/crush zones. Therefore, the model input intensity, $P_{32,Tot}$ in Table B-2, was fitted by trial-and-error until a reasonable agreement with PFL-f data is established.

After the removal of isolated fractures, the remaining network of connected fractures is no longer Poissonian (fracture centres uniformly distributed in space), but instead clustered or referred to as *Poissonian clusters*. Clustered fracture networks are known to exhibit a considerably larger variability between realizations (i.e. heterogeneity) in simulated borehole exploration. Therefore, simulated exploration must normally be performed for a large number of realisations (on the order of 100), in order to establish a robust, well-underpinned model calibration. However, as explained earlier, the objective is not to develop a fully calibrated DFN model, but to test the potential impact of stochastic features on tunnel inflow. Furthermore, one purpose of this study is to demonstrate a simplified implementation of the conceptual model, i.e. a model subject to both conceptual uncertainties and lack of data support for several assumed model parameters (e.g. fracture size). Therefore it was decided to use the following simplified calibration criteria: 1) Only *10 realisations* are evaluated, and 2) the simulated borehole exploration is only required to be in *reasonable agreement* with PFL-f data.

Boreholes (see Figure B-9 and Table B-3) are implemented as scan lines (i.e. neglecting borehole radius). The scan line is defined as a straight line between two points, namely the upper and the lower borehole coordinates. A few rules are implemented to improve the consistency in the comparison to data:

1) Any part of the scan-line not representing a *PFL-f logged section* of the borehole (e.g. casing), or being located below –200 m elevation is excluded from sampling connected fractures.
2) Similarly, any part of the scan line intersecting a deterministic deformation zone (i.e. a ZFM structure) is also excluded from the sampling, as calibration is only made to data outside deterministic deformation zones.
3) The scan line is discretised into 0.1 m segments. Fracture intersection is evaluated separately for each segment. If more than one stochastic fracture should intersect the same segment, it is counted as a *single* record with a detected apparent transmissivity equal to the *sum* of all intersecting features. This is analogous to the fact that there may exist more than one alternative Best Choice for a single PFL-f record, see Öhman and Follin (2010b).
4) Locally variable detection limit along the borehole length is also accounted for. However, it has no practical effect as no detection limits exceed 10^{-6} m^2/s.

A few iterations on trial-and-error basis were run until *reasonable* consistency to PFL-f data was established (Table B-3 and Figure B-10). Firstly, it can be noted that the connected fracture network is highly clustered, which renders large variability between the realizations. The high variability is an outcome of the selected DFN parameterisation setup. For example, an alternative setup with larger and more uniformly distributed fracture sizes would result in lower variability. The DFN parameterisation was intentionally chosen as such to reflect the uncertainty in the concept of stochastic SBA modelling.

Secondly, it can be noted that the low expected apparent transmissivity and intensity values in boreholes associated to the Central block (KFR27, KFR105, HFR102 and KFR104) are fairly well reproduced, as compared to the higher expected values closer to the Northern boundary belt (KFR106, KFR103, KFR102A, KFR102B, and HFR106). Most notably, KFM11A is consistently underestimated in terms of intensity. This is because KFM11A is located close to fracture removal areas, i.e. both close to the border of the SFR Regional domain and close to the entry of the SFR tunnel.

Table B-3. Simulated borehole intercepts of connected SBA-structures (10 realisations).

Per set	Simulated average	Number of PFL-f data
EW	0.8	1
Hz	34.9	31
NE	2.3	2
Total	**38.0**	**34**

Simulated borehole SBA intercepts on borehole basis

Borehole	PFL-f data	Simulated average	Realisation number 1	2	3	4	5	6	7	8	9	10
HFR101[1)]	1	3.5	3	3		12		4		1	6	6
HFR102[1)]	1	0.2		1	1							
HFR106[1)]	1	2.7	2	1	2	2	2	1	7	5		5
KFM11A	9	2					2	2	3	7	6	
KFR101	1	4.8	5	5	2	8	5	5	2	4	7	5
KFR102A	3	3.6	2	1	1	9	8	2	4	1	6	2
KFR102B	3	6.8	2	11	7	4	10	7	5	7	7	8
KFR103	6	5.1	3	5	10	2	2	2	5	8	11	3
KFR104	1	3.5	1	8		2		3		15	4	2
KFR105	0	0.6	1				1		1	2		1
KFR106	8	4.5	13	5	2		3		7	6	6	3
KFR27	1	0.7				2			1		1	3
Grand Total	**34**	**38**	**32**	**40**	**25**	**41**	**33**	**26**	**35**	**56**	**54**	**38**

1) HFR101 and HFR106 have HTHB data, while HFR102 have a single interval pumping test with T> 10–6 m2/s

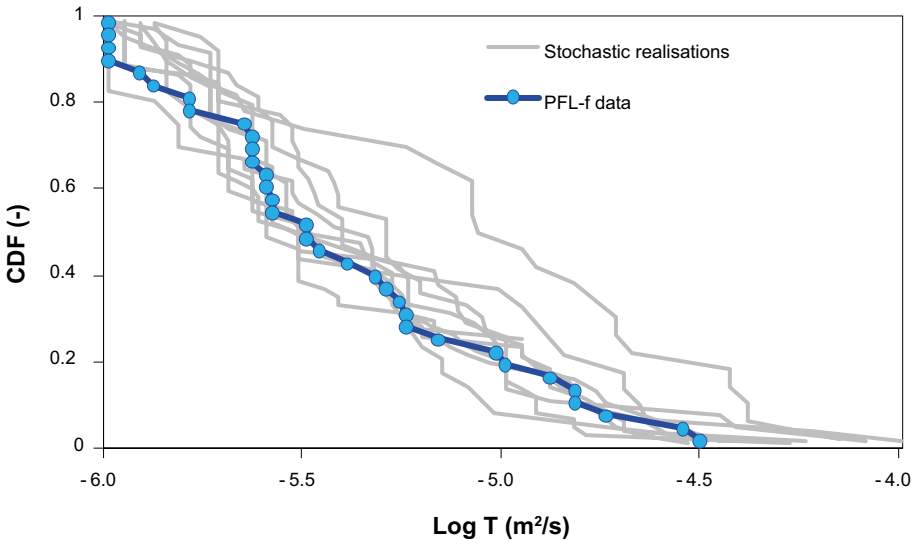

Figure B-10. *Distribution of so-called apparent transmissivity for 10 stochastic realisations of connected fracture networks compared with PFL-f data.*

Appendix C

Presentation of Model Exercise results, M0 to M7

Introduction

The performance of the groundwater flow model is explored by means of a perturbation analysis in context of constraining head and inflow data. Starting from a simplistic Initial Case, increasing level of complexity is sequentially included in the model. The Model Exercises, M0 through M7, are described in Chapter 5, along with a summary of the outcome of the various tests. This appendix provides a more detailed presentation of the modelling sequence and the results obtained.

C.1 Model Exercise M0: Initial Case

Model Exercise M0 is referred to as the Initial Case. It is parameterised by an isotropic, average conductivity K_{CPM}, where no differentiation between hydraulic domains (HRD, HCD, and HSD) is made. The bedrock mass conductivity, $K_{CPM} = 6.5 \cdot 10^{-9}$ m/s, obtained by inverse flow modelling by Holmén and Stigsson (2001), was taken as the starting point. It should be noted that this value was established by tunnel-inflow modelling in an earlier model setup for SFR and hence it is not valid in the current setup. For example, this value was calibrated for measured inflow data in 1997 in the presence of deformation zones. Nevertheless, it was considered to be useful as a starting point.

Two cases are compared: M0a with $K_{CPM} = 6.5 \cdot 10^{-9}$ m/s and M0b with $K_{CPM} = 1.3 \cdot 10^{-8}$ m/s.

In this simplistic model setup, the simulated head decrease has a very smooth appearance that is clearly related to the geometry of the SFR facility and its location below sea (Figure C-1). The potential field is asymmetric in the vertical direction, with clearly stronger hydraulic gradients above the facility than it is below. Large head decrease (exceeding 40 m) does not extend further away from the underground facility than c 100 m (Figure C-2). Comparison with data demonstrates that the simulated head decrease tends to be overestimated, particularly for the more remote new data set (Figure C-2b and Figure C-3b).

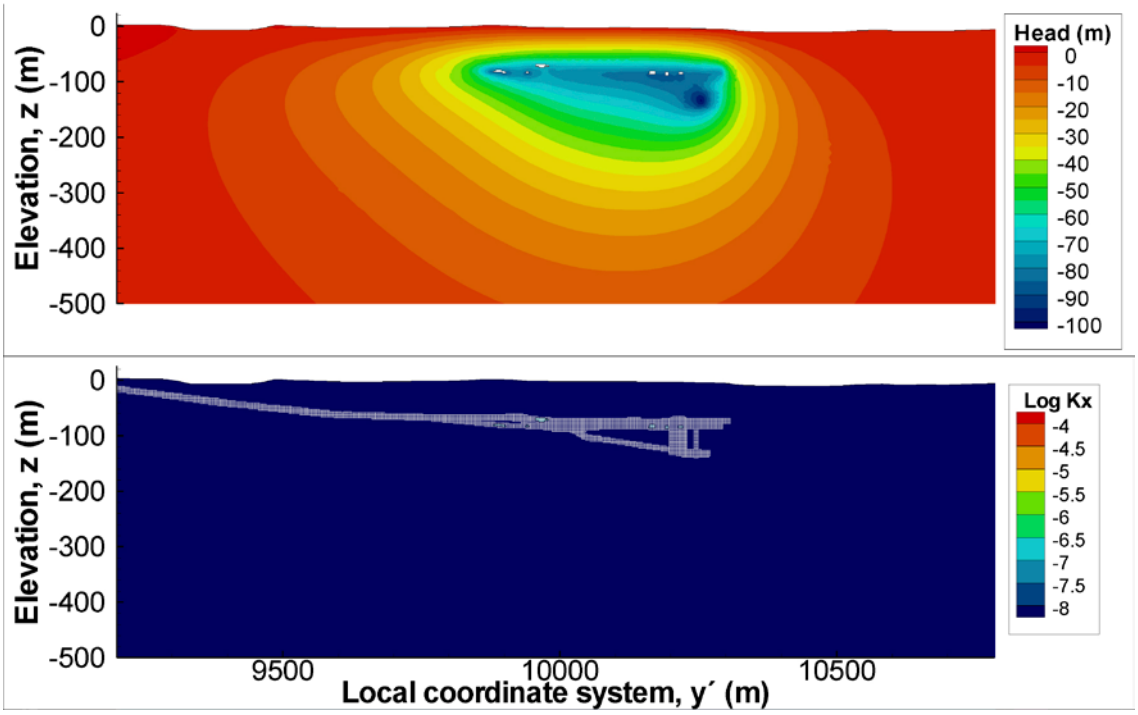

Figure C-1. *Exercise M0a: a) simulated head and b) conductivity field. Hydraulic conductivity is isotropic, $K_{CPM} = 6.5 \cdot 10^{-9}$ m/s (taken from Holmén and Stigsson 2001).*

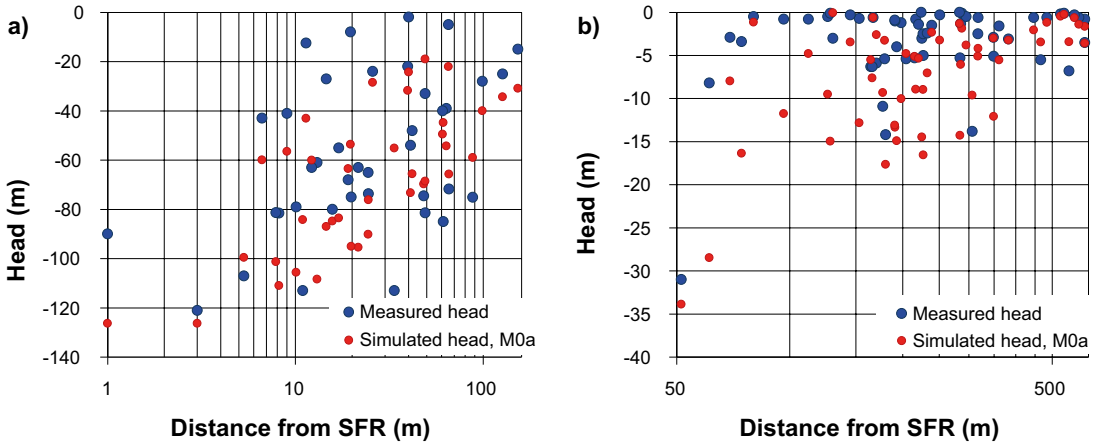

Figure C-2. *Exercise M0a: simulated and measured head as function of the distance from the tunnel wall; a) old boreholes and b) recently installed boreholes.*

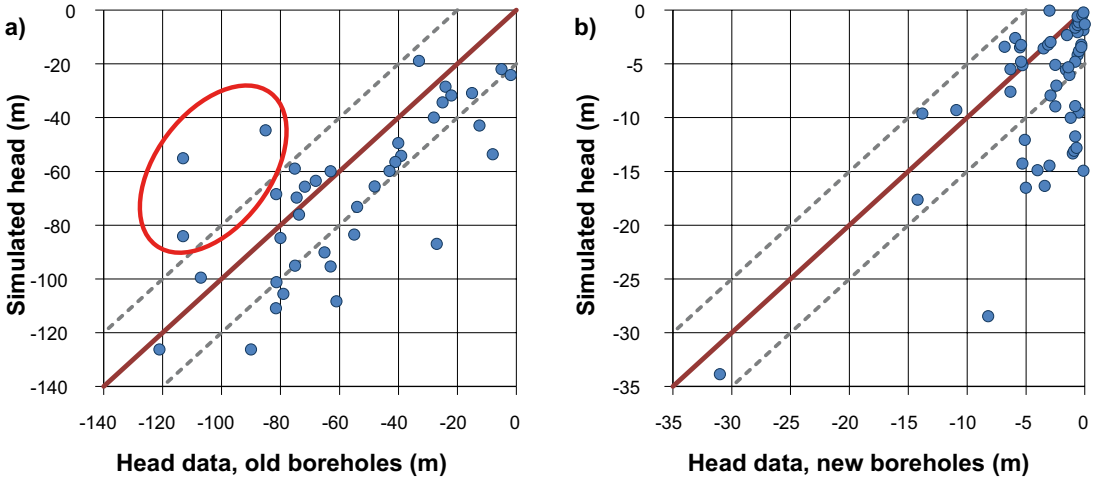

Figure C-3. *Simulated versus measured head (m) in exercise M0; a) old boreholes and b) new (recent) boreholes. The simulated head decrease is generally too large (notable exception in KFR7A, marked by red oval). Dashed lines show a ± 20 m interval for old boreholes, and a ± 5 m interval for recently installed boreholes.*

This suggests that steeply dipping deformation zones (which are not included in this setup) may have a significant role in controlling the lateral propagation of head decrease. If the NE to ENE striking zones, ZFMNE3118 and ZFMENE3115, which are located between SFR and the recently investigated area, are well-connected to the sea, they may dampen the propagation of head decrease into the now recently investigated area. The only difference between cases M0a and M0b is a constant rescaling of effective conductivity, and they are hence expected to render identical head solutions. The observed discrepancy is negligible, but provides a demonstration of the precision of simulations (Figure C-4).

The simulated total inflow in M0a is less than *half* of the current measurements (Table C-1). Rescaling the average conductivity by a factor 2.0 in case M0b increases the simulated inflow by a factor of about 2. Again, this demonstrates the linearity of the system in context of numerical accuracy limitations. The largest simulated inflow occurs in the lower part of the ramp (area 17; in line with measurements) of the simulated inflow comes from the Thomson weir (marker 17). Excessive inflow is simulated in the IB subarea (area 18; Figure 5-1), as well as all waste-storage facilities (except 1BMA; Figure C-5).

In spite of the simplicity in this basic model setup, the simulated inflow in M0b (Figure C-5a) is surprisingly proportional to measurements, i.e. with consideration to the fact that HCDs are not included here. This demonstrates that the geometry of the inflow areas (relative location and exposed tunnel-wall area; see Table 4-3) largely determines tunnel inflow. Thus, geometric aspects are of key significance

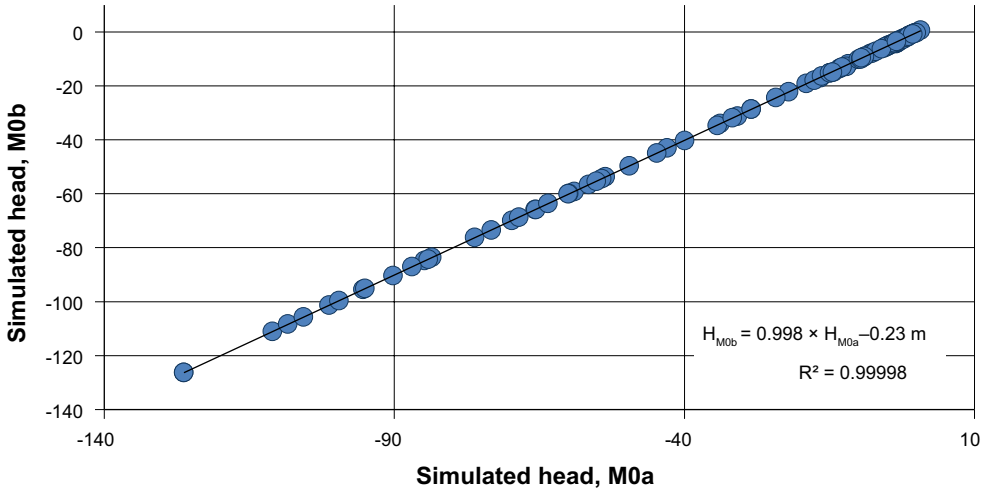

Figure C-4. *Cross-plot between simulated head in M0a and M0b. The discrepancy between simulations is suspected to reflect accuracy limitations in flow simulations. Constant rescaling of hydraulic conductivity is not expected to influence simulated head decrease.*

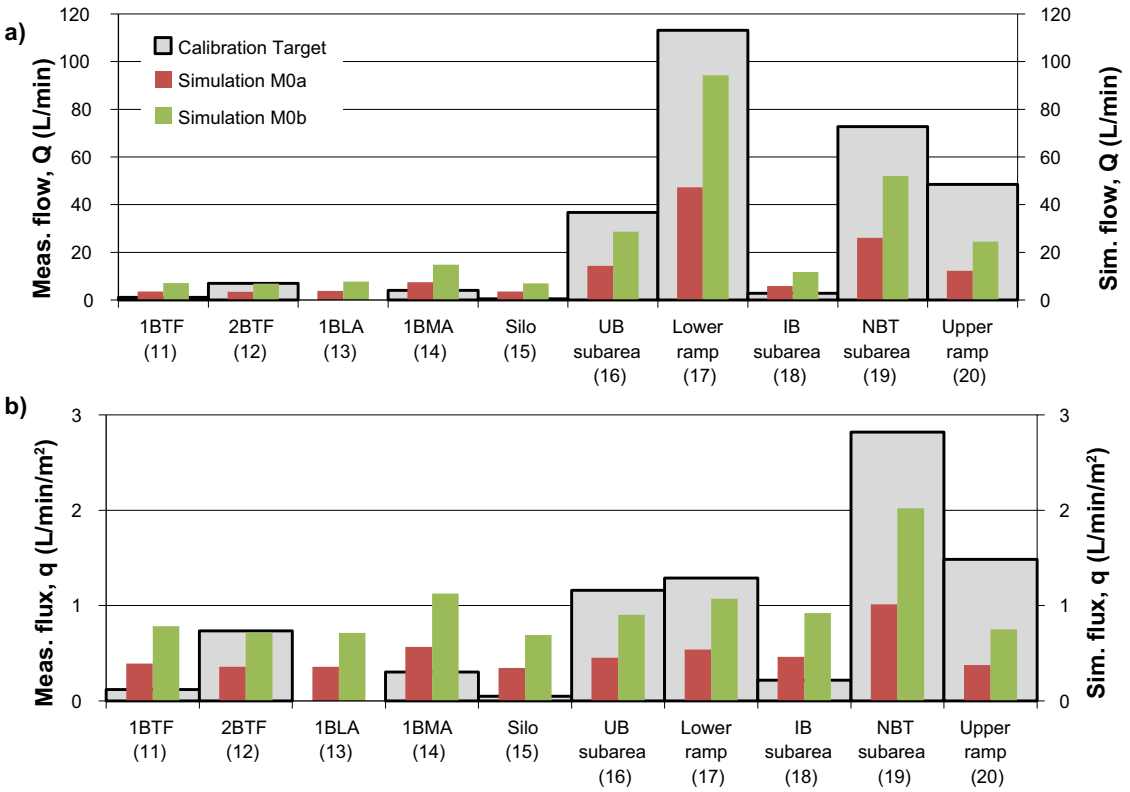

Figure C-5. *Simulated inflows compared to measured inflows for Initial Cases M0a and b: a) tunnel inflow, Q, and b) average flux, q (normalised inflow per cross-sectional area). As K_{CPM} is doubled in M0b, the total simulated inflow increases by a factor 1.996 (i.e. almost proportional to the conductivity increase).*

in relation to geological structures (which are not included at this stage). The significance of cross-sectional area is demonstrated by the poorer correlation in terms of average flux, q (area-normalised inflow; Figure C-5b). Notably, the experience from tunnel construction was, quite contradictory, that tunnel inflow was strongly correlated to deformation zone intercepts (Christiansson and Bolvede 1987). Thus, with consideration to the on-going decline in tunnel inflow, it is possible that the role of HCDs has diminished (i.e. perhaps the decline in tunnel inflow is mainly due to dewatering of HCDs). This also suggests that the differentiated flow areas, 11 to 20 in Table 4-3, provide little constraining power for hydraulic calibration of zones (at least for structures located far away from the SFR facility).

Table C-1. Simulated tunnel inflow in case M0.

Area code (Figure 5-1)	Reference name	Measured (L/min)	Simulation M0a (L/min)	Simulation M0b (L/min)
11	1BTF	1.1	3.6	7.1
12	2BTF	7.0	3.4	6.8
13	1BLA	1.0	3.8	7.7
14	1BMA	4.0	7.4	14.9
15	Silo	0.5	3.5	7.0
16	UB subarea	36.7	14.3	28.6
17	Lower ramp	113.1	47.2	94.3
18	IB subarea	2.8	5.9	11.8
19	NBT subarea	72.7	26.1	52.1
20	Upper ramp	48.5	12.3	24.5
21	Rock cavern connections	NA	1.2	2.5
	TOTAL	**286.4**	**128.9**	**257.2**

C.2 Model Exercise M1: HRD anisotropy

The purpose of Model Exercise M1 is to test HRD anisotropy (Section 5.2). In this exercise HCD are not included. HSD is parameterised according to the SR-Site Forsmark model (Table 3-1); anisotropy is not implemented in HSD.

The starting point is referred to as case M1a. It has isotropic, constant hydraulic conductivity, $K_{HRD} = 6.5 \cdot 10^{-9}$ m/s, assigned inside the SFR Regional domain. HRD anisotropy is then tested in cases M1b and M1c, by varying the factor a in Equation 3-5. Vertical conductivity, K_Z, is reduced by the factor a, simultaneously as the horizontal conductivity, K_H, is increased by the same factor. The purpose of this procedure is to minimize the net effect on tunnel inflow, and thereby making the three cases more comparable.

The tested anisotropy cases (see Figure C-6) are:

M1a: $a = 1$ (isotropic, $K_H = K_Z = 6.5 \cdot 10^{-9}$ m/s),

M1b: $a = 3$ (ratio $K_H/K_Z = 9$), and

M1c: $a = 10$ (ratio $K_H/K_Z = 100$).

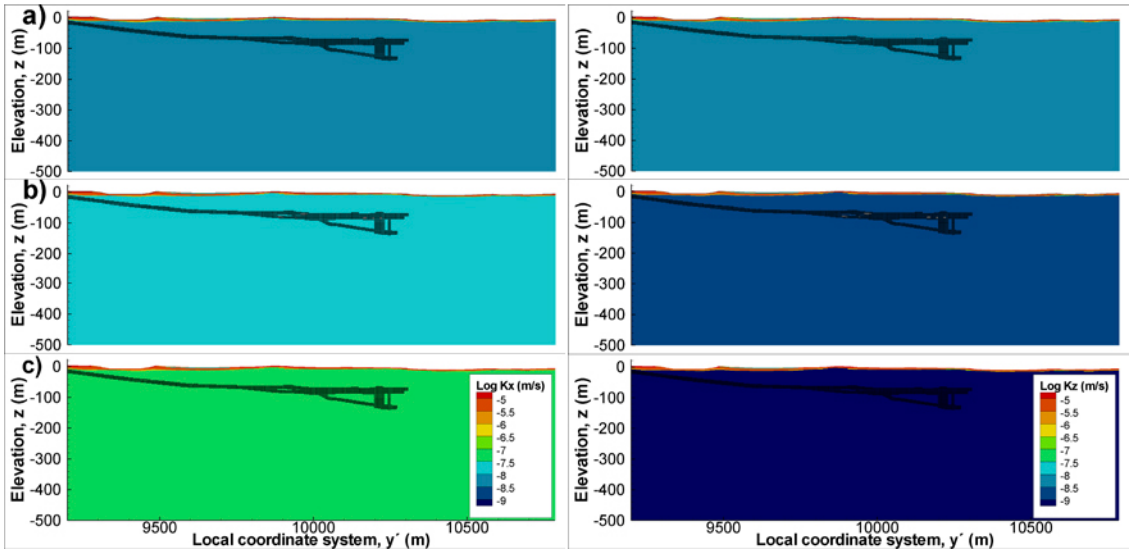

Figure C-6. *Exercise M1: Assigned horizontal conductivity (left) and vertical conductivity (right); a) M1a, isotropic hydraulic conductivity, $K_H/K_z = 1$, b) M1b, intermediate anisotropy, $K_H/K_z = 9$, and c) M1c, strong anisotropy, $K_H/K_z = 100$. HSD is included, but not subject to variation.*

The effect of including HSD can be evaluated by comparing cases M1a and M0a. The impact on the simulated head-field is small, although the high conductivity of HSD somewhat reduces the head decrease at shallow depths (cf. Figure C-7a and Figure C-1a).

As expected, increasing levels of anisotropy enhance the lateral extent of head decrease dramatically (Figure C-7a to c). The previous exercise M0 demonstrated excessive simulated head decrease in remotely located boreholes of the recent data set, even for isotropic conductivity (Figure C-3). Hence, the additional lateral propagation head decrease caused by simulated horizontal anisotropy in M1b and M1c does not improve the agreement to data (Figure C-8). Thus, in absence of HCD, simulation results do not support the notion on large-scale horizontal anisotropy in hydraulic conductivity.

As intended, the total tunnel inflow is more or less preserved for the three cases of anisotropy. The total simulated inflow is still about *half* of the current measurements (i.e. very similar to M0a). Thus, the total inflow is rather independent on anisotropy. However, anisotropy does re-distribute the locations of tunnel inflow towards the outer, vertically exposed walls of SFR. For example, the simulated inflow to the Silo increases in case M1c, whereas inflow to the centrally located 2BTF and BLA decreases (Table C-2 and Figure C-9). The inflow measurements do not support horizontal anisotropy (e.g. inconsistent with the notably low measured inflow for the Silo).

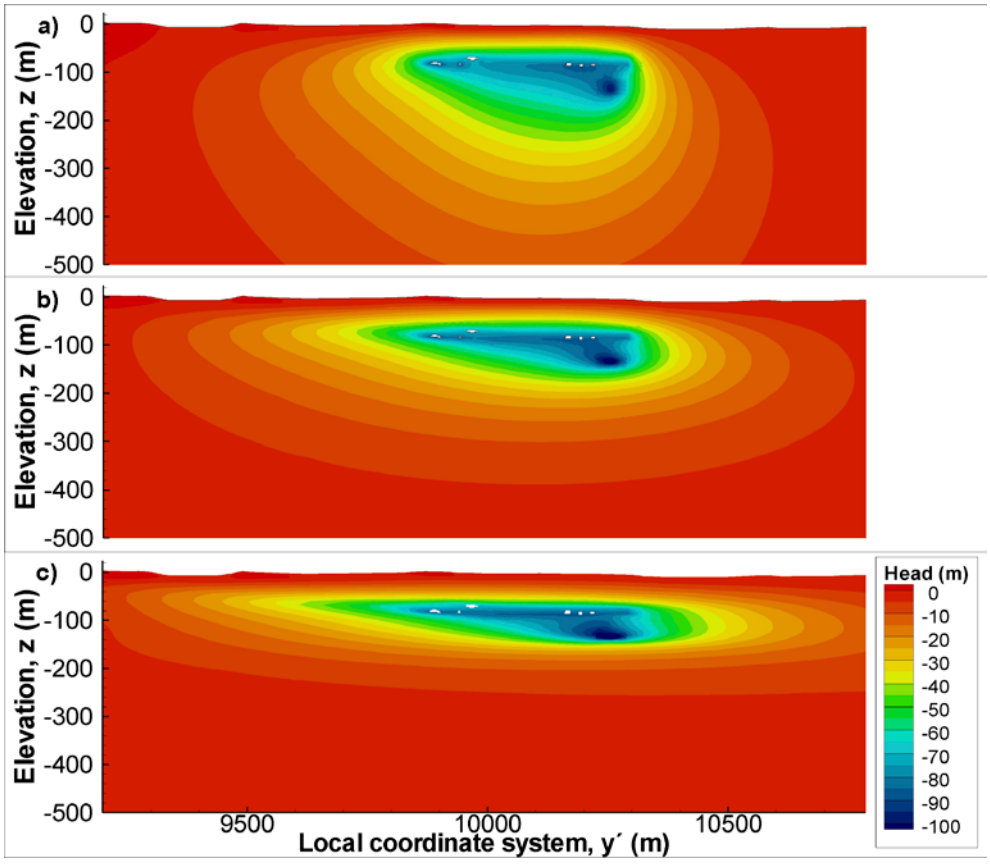

Figure C-7. *Exercise M1a-c head-field: Isotropic case (M1a; top), intermediate anisotropy (M1b; middle), and large anisotropy (M1c; bottom). Increasing anisotropic ratio (K_H/K_Z) spreads the head decrease horizontally, but reduces its vertical propagation.*

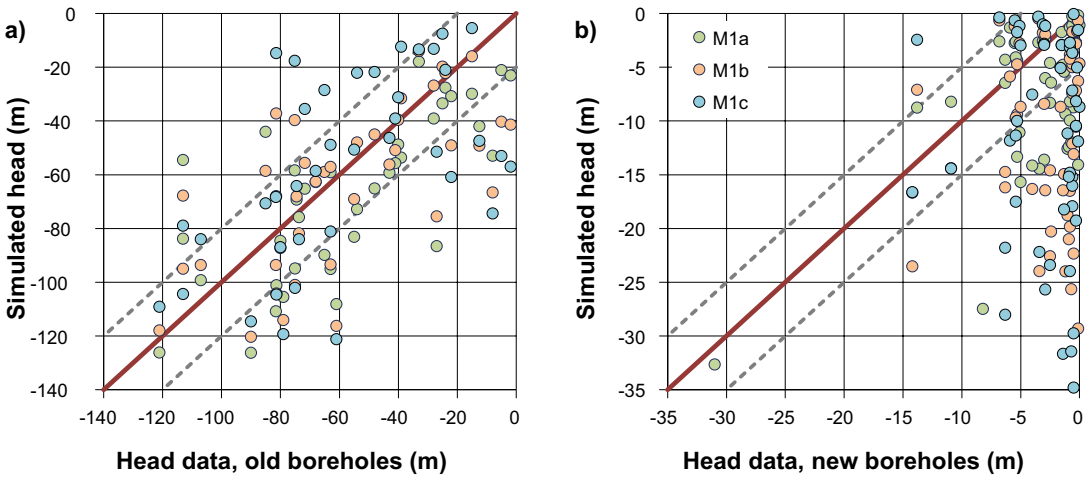

Figure C-8. *Exercise M1a-c: Simulated head versus measured head: a) old boreholes and b) recently installed boreholes. The agreement deteriorates for increasing levels of horizontal anisotropy primarily for distant boreholes of the recent data set. Some outliers with low measured head (KFR7A; head = –80 to –120 m) show a better fit with anisotropy.*

Table C-2. Simulated tunnel inflow in case M1.

Area code (Figure 5-1)	Reference name	Measured (L/min)	M1a (L/min)	M1b (L/min)	M1c (L/min)
11	1BTF	1.1	3.8	1.8	0.9
12	2BTF	7.0	3.6	1.8	1.0
13	1BLA	1.0	4.0	2.3	1.6
14	1BMA	4.0	7.7	6.5	8.1
15	Silo	0.5	3.6	5.7	15.0
16	UB subarea	36.7	14.9	10.1	10.0
17	Lower ramp	113.1	50.4	36.8	38.9
18	IB subarea	2.8	6.2	5.9	8.2
19	NBT subarea	72.7	26.4	27.5	44.9
20	Upper ramp	48.5	14.8	11.6	15.8
21	Rock cavern connections	NA	1.3	0.6	0.3
	TOTAL	**286.4**	**135.4**	**110.0**	**144.4**

C.3 Model Exercise M2: anisotropy in presence of HCDs

Decrease in head is controlled by both anisotropy and large-scale structures (HCD). Therefore, the synergy between anisotropy and HCD is pursued in Model Exercise M2. In essence, the previous case studies, M1, are repeated in the presence of HCD (described in Section 5.3).

The HCD are parameterised by the ground-surface transmissivity, $T_{eff}(0)$ and the assumed depth trend, Equation 3-3. In this exercise, the HCD parameterisation employs $T_{eff}(0)$ values taken directly from Öhman et al. (2012). This is referred to as the "initial" parameterisation, reported in Table A-1. It should be noted that tunnel skin is not implemented in this exercise. The three anisotropy cases are defined by the factor *a* in Equation 3-5:

M2a: $a = 1$ (isotropic starting point, equivalent to including HCD to M1a),

M2b: $a = 3$ (ratio $K_H/K_Z = 9$ relative to M2a applied to HRD, HSD, and HCD), and

M2c: $a = 10$ (ratio $K_H/K_Z = 100$ relative to M2a applied to HRD, HSD, and HCD).

The conductivity parameterisations are presented in Figure C-10. Note that the only difference between M1 and M2 is the introduction of HCD.

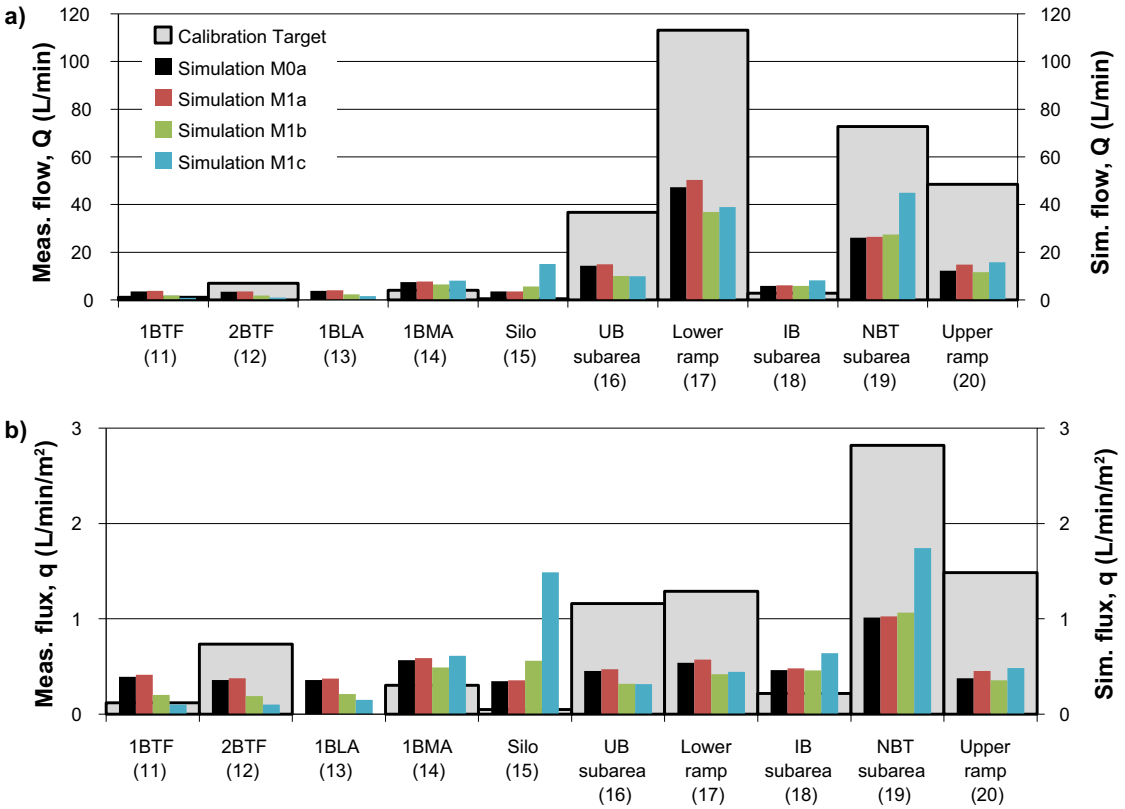

Figure C-9. *Exercise M1a-c simulated inflow compared to measurements and Initial Case M0a: a) tunnel inflow, Q, and b) average influx, q (inflow divided by the cross-sectional area).*

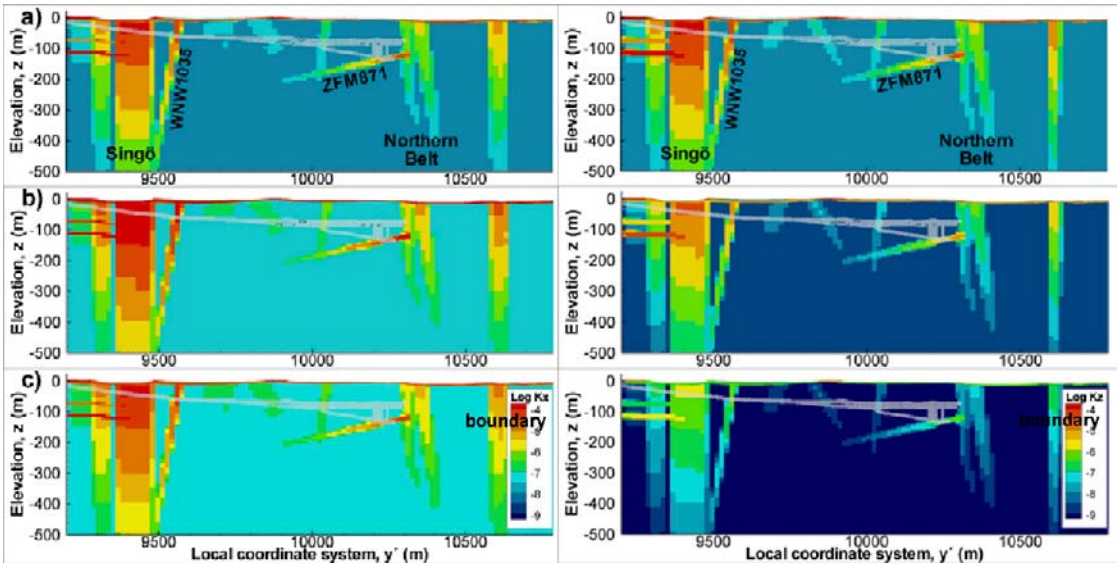

Figure C-10. *Exercise M2a-c: assigned horizontal conductivity (left) and vertical conductivity (right); a) M2a, isotropic hydraulic conductivity, K_H/K_z = 1, b) M2b, intermediate anisotropy, K_H/K_z = 9, and c) M2c, strong anisotropy, K_H/K_z = 100. Anisotropy is applied to all three units, HRD, HCD, and HSD. No tunnel skin is applied. ZFM871 located at the bottom of the Silo.*

Similar to the previous M1 observations, horizontal anisotropy spreads the head decrease laterally. However, in comparison to previous M0 and M1 observations (Figure C-1 and Figure C-7), the homogeneous appearance in head decrease is clearly disrupted by structural geometry (Figure C-11).

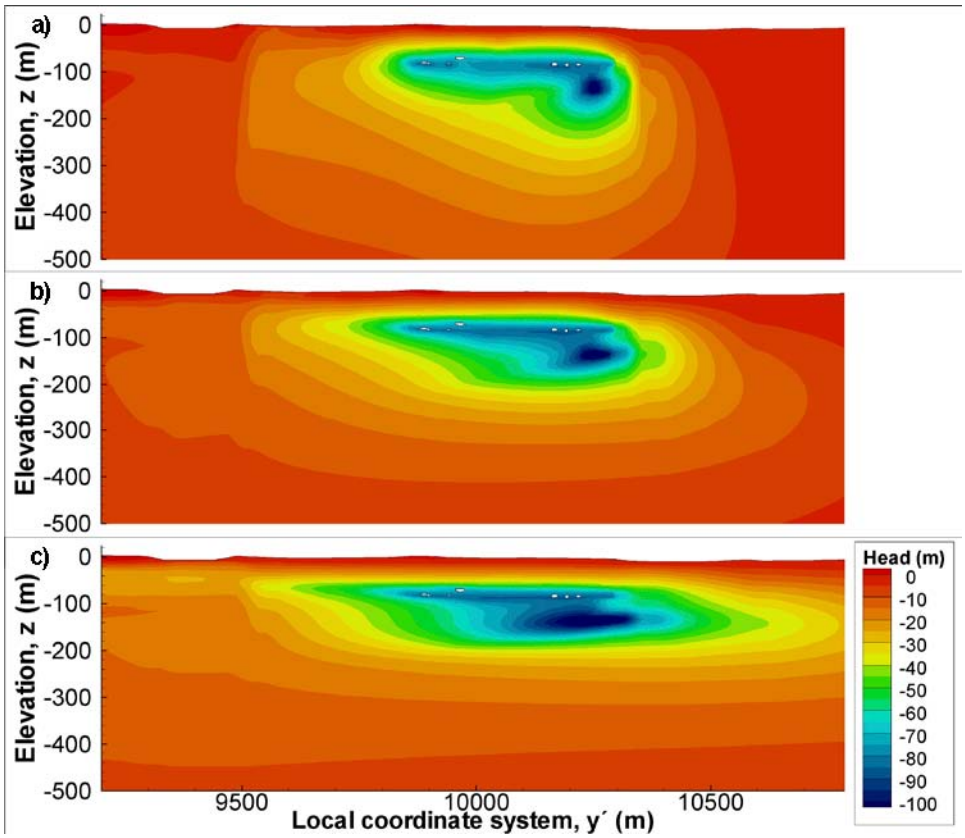

Figure C-11. *Exercise M2a–c: simulated head in presence of anisotropy and HCD; a) isotropic case, b) intermediate anisotropy, K_H/K_z = 9, and c) strong anisotropy, K_H/K_z = 100. No tunnel skin applied. Deformation zone locations visible in Figure C-10. HCDs cause head decrease at larger depths in the bedrock (cf. exercise M1).*

The most significant effect of HCDs is that the head decrease is extended downwards to greater depths. Also similar to earlier observations, high horizontal anisotropy causes excessive simulated head decrease for remotely located boreholes (Figure C-12). However, the inclusion of HCD is found to improve the agreement to data somewhat and also to dampen the effects of anisotropy.

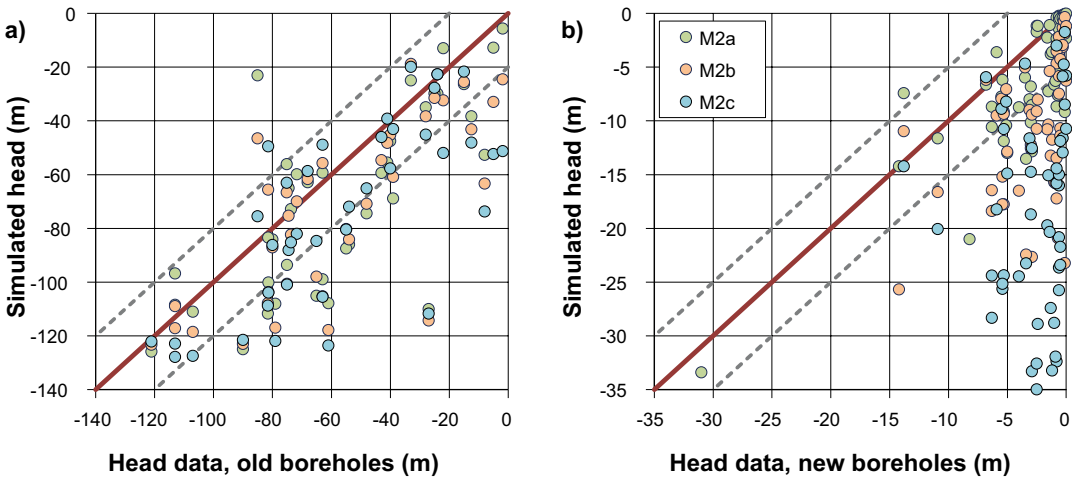

Figure C-12. *Exercise M2a–c: Simulated head versus measured head: a) old boreholes and b) recently installed boreholes. The agreement for high anisotropy is still poor, particularly for recent boreholes. However, inclusion of HCDs improves the agreement to data (cf. M1a–c).*

Inclusion of HCDs without tunnel-wall skin cause simulated inflow to exceed measurements by a factor of c 25 (Table C-3). The simulated inflows even exceed the estimated theoretical initial tunnel inflow by a factor of c 7 (Section 2.8.1). Note that the simulated inflow in the previous simulations without HCDs (exercises M0 and M1) render the correct order of magnitude of the inflow. The largest excessive inflow is simulated in the upper ramp (area 20), which intersects the Southern boundary belt (Figure 5-1). Other notable excessive inflows are simulated in the NBT subarea (area 19), which intersects ZFM871, and in the lower ramp (area 17), which intersects ZFMWNW1035 and ZFMNE0869. Notable excessive inflow is also simulated in the IB subarea, which is caused by an artificial tunnel intercept of ZFMNW0805B (i.e. a model artefact). These unrealistic simulated inflows signify the necessity of revising this "initial" HCD parameterisation and to introduce tunnel skin (see Model Exercise M3).

Conclusions

The initial HCD parameterisation, taken from Öhman et al. (2012), renders unrealistic simulated tunnel inflow. Thus, the current hydraulic role of HCDs is not as important to tunnel inflow as inferred from borehole data. This implies that parameterisation based on borehole data (local-scale point observations) overestimates the large-scale hydraulic properties of HCDs. This conclusion is at least valid for the historic data set and for their role in the current tunnel inflow situation. In turn, this conclusion implies that the current inflow via HCDs is somehow constrained by a resistance that is not evident in local-scale borehole data, and therefore not yet implemented in the model. Three types of plausible flow resistances, or hydraulic bottlenecks of the system, are considered here:

4) Large-scale discontinuity and/or within-plane heterogeneity of zones is a plausible explanation for a discrepancy between short-term, local-scale borehole data and long-term, large-scale flow. However, as discussed in Sections 2.4 and 2.8, the effective large-scale hydraulic properties are governed by the flow regime, and inflow calibration is not necessarily more representative to the natural state than estimation from borehole data. On the other hand, parameterisation based on historic data involves other shortcomings and uncertainties. The first option was to reassess borehole data from a less conservative standpoint and to introduce local conditioning of HCDs in exercise M3a.
5) Tunnel-wall skin related to grouting and natural processes is discussed in Sections 2.5 and 2.8. This type of resistance is expected to occur near the tunnel wall (i.e. a couple of meters into the rock mass). If this resistance is large, it will cause a strong hydraulic gradient across the affected skin zone, which in turn reduces the head decrease in the bedrock mass outside the skin zone. The effect of introducing skin is tested in exercise M3b.
6) Limited contact to a positive flow boundary (i.e. the overlying Baltic Sea, representing an unlimited water source) may be caused by a) overlying sediments, b) sediment filling in fracture apertures, and/or c) poor contact to hydraulically significant upstream structures (i.e. the Singö/SDM-Site Forsmark sheet joint contact, or the ZFM871/ZFMNW0805B contact). This is pursued in exercises M5 and M6.

Hydraulic bottlenecks (or locations of large flow resistances) cause large pressure drops which are potentially recognisable in the spatial pattern of head data. A prospect in subsequent exercises (M3, M5, and M6) is to examine if the available data are sufficient to identify the dominant bottleneck type (1–3 above), while constraining simulated inflow within reasonable bounds.

Table C-3. Simulated tunnel inflow in exercise M2.

Area code (Figure 5-1)	Reference name	Measured (L/min)	M2a (L/min)	M2b (L/min)	M2c (L/min)
11	1BTF	1.1	8.2	3.2	1.2
12	2BTF	7.0	7.8	3.1	1.3
13	1BLA	0.0	9.9	4.3	2.3
14	1BMA	4.0	20.4	15.0	15.2
15	Silo	0.5	4.0	6.5	18.9
16	UB subarea	36.7	25.4	18.0	18.9
17	Lower ramp	113.1	1,288	1,352	1,307
18	IB subarea	2.8	53.8	56.7	66.1
19	NBT subarea	72.7	596	999	1,040
20	Upper ramp	48.5	5,650	5,491	5,021
21	Rock cavern connections	NA	2.0	0.8	0.4
	TOTAL	**286.4**	**7,666**	**7,950**	**7,492**

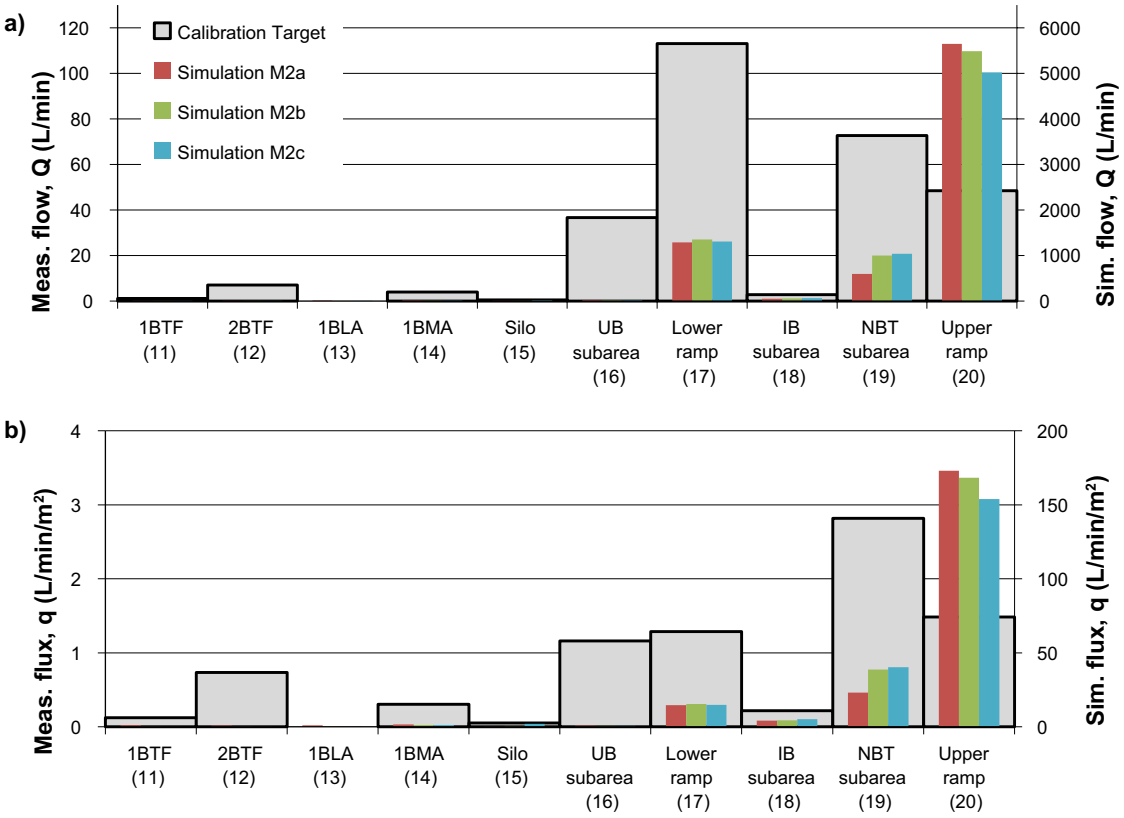

Figure C-13. *Exercise M2a–c simulated inflows compared to measured inflows: a) tunnel inflow, Q, and b) average flux, q (normalised inflow per cross-sectional area). The simulated total inflow exceeds the recent measurements by a factor c 25 (note the difference of scales and that no tunnel-skin is applied). Inflow is rather independent of anisotropy.*

C.4 Model Exercise M3: HCD conditioning and tunnel skin

The unrealistic inflows simulated in the previous M2 Model Exercise signify the necessity of revising the HCD parameterisation and to introduce tunnel-wall skin. The excessive inflow via HCD was therefore constrained in two steps (Section 5.4):

M3a: Revised HCD parameterisation, based on borehole data, and introducing local conditioning.

M3b: Implementing tunnel-wall skin, set to $K_{skin} = 6.5 \cdot 10^{-9}$ m/s (Figure 2-2).

The excessive HCD inflow in exercise M2 partly relates to factors discussed in Section 2.4, but also due to several data uncertainties in the HCD parameterisation, primarily in the historic data set near complex deformation-zone junctions in the Southern boundary belt and ZFM871/ ZFMNW0805B. Therefore, the underlying HCD data (i.e. data inside deformation zone intercepts) were re-evaluated in context of the outcome of exercise M2 as well as experiences from earlier SFR modelling (Holmén and Stigsson 2001).

Tunnel intercepts lacking reported inflow in Christiansson and Bolvede (1987) are taken as observation points of "standard rock-mass conductivity" (pink circles in Figure 5-5b). These observations are not included in the initial HCD parameterisation of Öhman et al. (2012). In the revised parameterisation, tunnel intercepts of ZFMENE3118, ZFMWNW3259, ZFMWNW0813, ZFMNW0805B are taken as conditional points with $T = 6.5 \cdot 10^{-9}$ m/s * zone thickness. Particular emphasis is paid to artificial tunnel intercepts of ZFMNW0805B (model artefact related to the resolution of the geological model). The data re-assessment is summarised in Appendix A. Re-interpreted borehole intercepts (reported in Table A-3) form the basis for defining "revised" effective HCD transmissivity, $T_{eff}(0)$ (Table A-1). Tunnel intercepts were also included in the revised HCD parameterisation. All HCDs are conditioned by borehole intercepts within a radius of 50 m (Table A-3). The revised HCD parameterisation for M3a is demonstrated in Figure 5-5a and Figure 5-5b.

M3b has the same model setup as M3a (i.e. the revised HCD parameterisation), but it also includes tunnel-wall skin. The calibrated average rock-mass conductivity of Holmén and Stigsson (2001) was taken as a reasonable value for skin, $K_{skin} = 6.5 \cdot 10^{-9}$ m/s, and was applied to all tunnel walls of the existing SFR facility (Figure 5-5c). The principle of skin implementation to tunnel-wall cells is demonstrated in Figure 2-2. Note that this value in general is lower than used in earlier SFR modelling (Holmén and Stigsson 2001). The implemented skin is expected to provide a crude estimate of necessary level of modification necessary to constrain the simulated inflow. Its impact on the simulated flow-field also indicates if the constraining resistance is located in the immediate tunnel wall, or further away from the facility.

The data-based revision and local conditioning of the HCD parameterisation in M3a has a relative small effect on simulations. The revised parameterisation only causes a minor reduction in total simulated inflow (from 8,347 L/min to 6,883 L/min; cf. M2a and M3a in Table C-4). This corresponds to an excess factor of c 24. The largest excessive simulated inflows occur in the same tunnel sections as in M2a (Figure C-18). Conditioning the artificial intercept between IB and ZFMWN0805B as "normal rock mass" (white circle in Figure C-14) reduces the simulated inflow to subarea IB (area 18) by a factor of 3.6 (Table C-4), which is still too high. The resistance imposed at the artificial IB/ZFMWN0805B intercept causes a strong hydraulic gradient (white circle in Figure C-14), which demonstrates the effect that imposed hydraulic bottlenecks have on propagation of head decrease. Only minor achievements are accomplished in the overall evaluation with head data (Figure C-15 and Figure C-16a). In summary, local conditioning of HCDs and the detailed data revision of the underlying HCD parameterisation in M3a does not provide any significant model improvement.

In contrast, the introduction of tunnel-wall skin in M3b has drastic impacts on modelling results. The skin reduces the excessive simulated total inflow to 499 L/min (Table C-4), which exceeds measurements by a factor 1.7 only. In fact the simulated inflow is rather similar to the Initial Case M0 (Figure C-19). This reinforces that $K = 6.5 \cdot 10^{-9}$ m/s is on the right order of magnitude for the average conductivity of the current flow regime. However, imposing a strong resistance at the tunnel wall dampens the head decrease in the bedrock mass outside the skin zone (cf. Figure C-14a and b). Therefore, the reduction in simulated inflow is achieved at the expense of a poor agreement to measured head (Figure C-16b and Figure C-17). The mismatch is particularly large for boreholes with large monitored head decrease KFR7A/B close to NDB (red oval in Figure C-16b). (Note that the detailed geometry of tunnel section NDB was unavailable prior to Model Exercise M6.)

Conclusions

Introduction of tunnel-wall skin in exercise M3b (tentatively set to $K_{skin} = 6.5 \cdot 10^{-9}$ m/s over a 2 m width in the tunnel wall) provides realistic inflow, but at the expense of deteriorating the agreement to measured heads. This signifies that the main flow resistance in HCDs is not located in the immediate vicinity of the tunnel wall, as the constrained tunnel inflow in M3b causes a strong, local gradient that dampens the simulated head decrease in the bedrock outside the skin zone. Inflow simulations reinforce that $K = 6.5 \cdot 10^{-9}$ m/s is a reasonable value (average approximation of the current flow regime), but simulated head indicate that the bottlenecks in the system are not confined to the tunnel wall.

This implies that simultaneous matching of inflow and heads requires balancing with some other type of additional HCD resistance (cf. inflow in M2a–c), located further away from the tunnel wall. For example, the resistance may be choking at the HCD/HSD interface, or lower effective large-scale HCD transmissivity, T_{eff}. It should be kept in mind that the HCD in the vicinity of SFR are primarily parameterised based on local, short-term hydraulic tests (falling-head data), which imply inclusion of compartmentalized transmissivity and render an upper estimate of HCD transmissivity. Measured head data is judged to provide a comparatively more reliable estimate of *large-scale HCD effective characteristics*. Alternative bottlenecks have been suggested in the conceptual modelling (e.g. low-permeable glacial clay above the Southern boundary belt, uncertain connections between Singö/sheet joints, and ZFM871/ZFMNW0805B. This is tested in exercises M5 and M6.

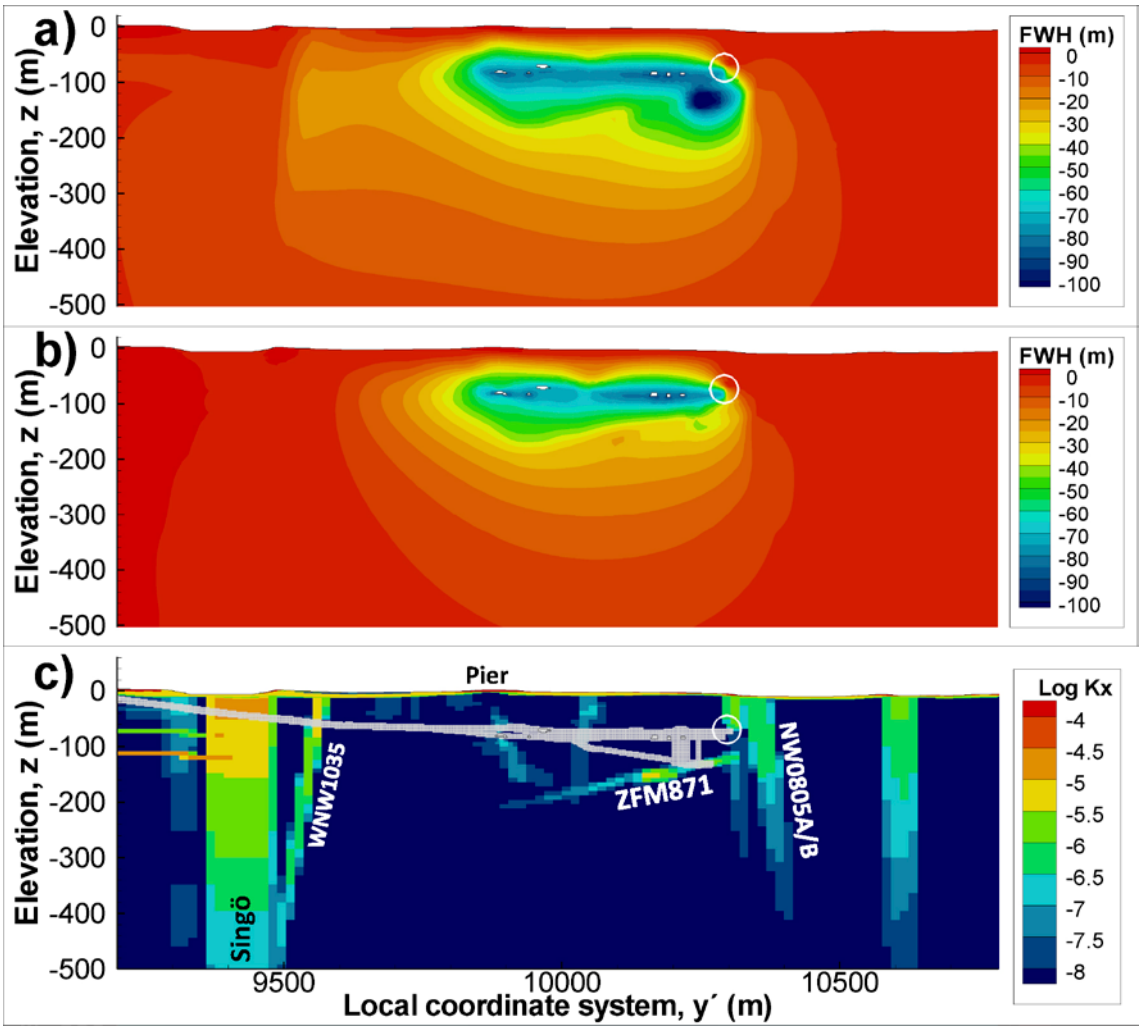

Figure C-14. *Simulated head and conductivity fields in Exercise M3; a) head for revised and conditioned HCDs, b) head for tunnel-wall skin K_{skin} = 6.5·10^{-9} m/s, and c) conductivity resulting from conditioned HCDs. Introduction of tunnel-wall skin significantly reduces the head decrease outside the tunnel wall (most clearly visible at the Silo). Conditioning the tunnel intersection of ZFMNW0805B also imposes a strong gradient across the tunnel wall (white circle; see also Figure 5-5).*

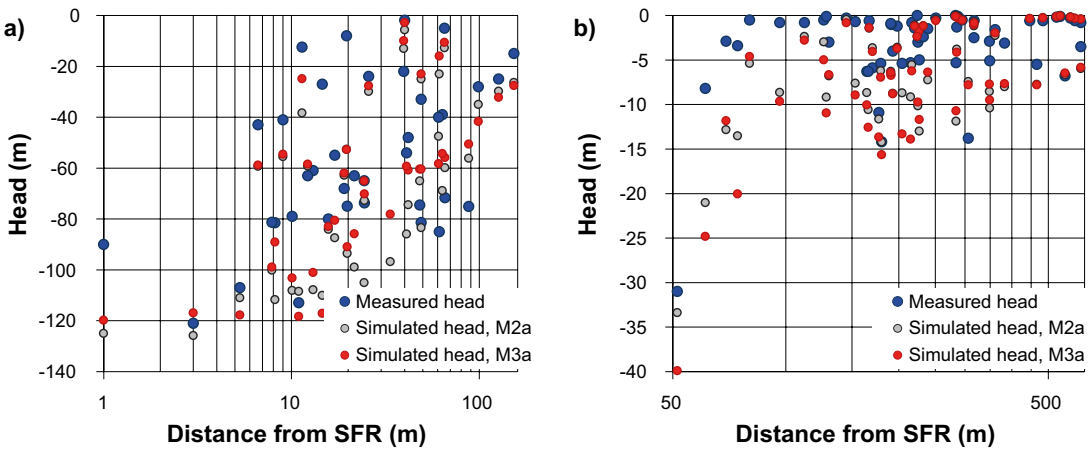

Figure C-15. *Simulated head in exercise M3a with radial distance from the SFR facility (red) versus measured head (blue) compared to the initial parameterisation in exercise M2a (grey): a) old boreholes and b) recently installed boreholes.*

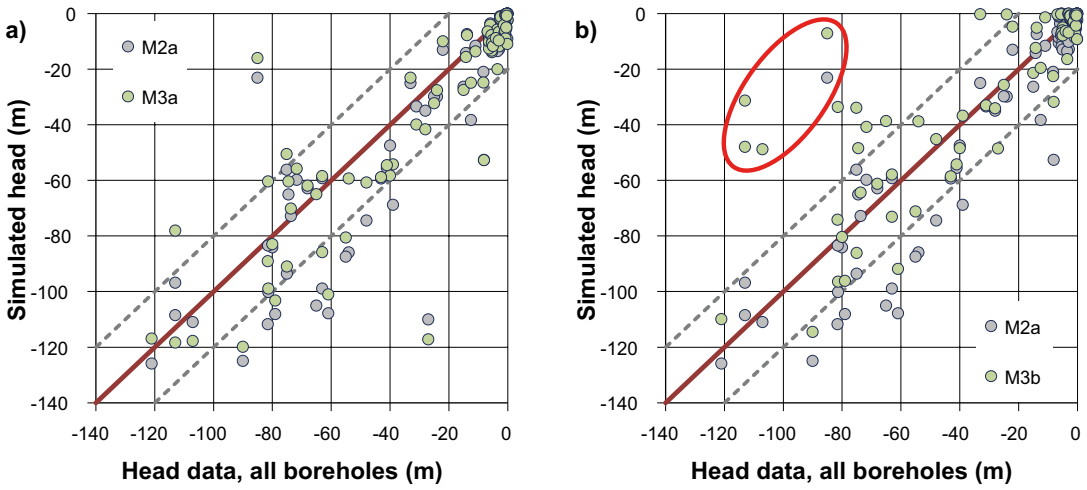

Figure C-16. *Simulated versus measured head in exercise M3 related to exercise M2a: a) revised and conditioned HCDs and b) introducing tunnel-wall skin, $K_{skin} = 6.5 \cdot 10^{-9}$ m/s. Note that no substantial improvement is achieved among the recent data set (not fully resolved in this figure).*

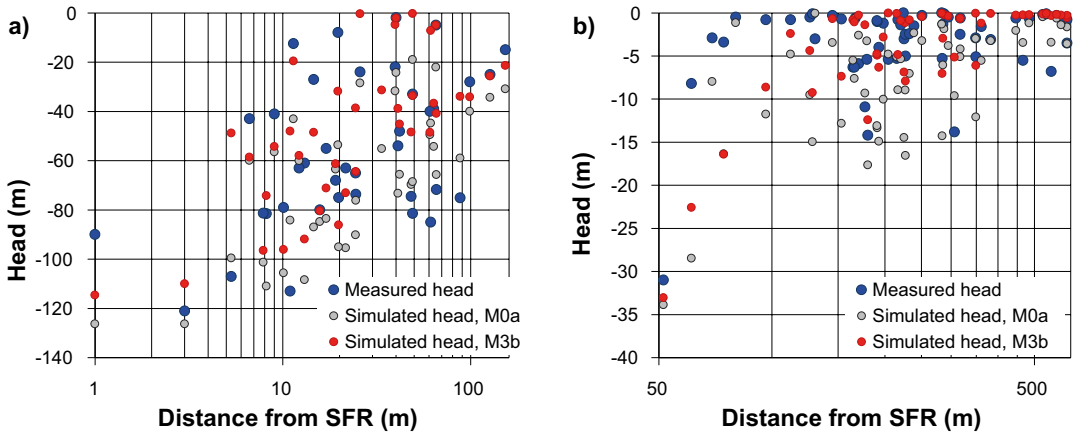

Figure C-17. *Simulated head in exercise M3b with radial distance from the SFR facility (red) compared to measured head (blue) and Initial Case M0a (grey): a) old boreholes and b) recently installed boreholes. The introduction of skin in exercise M3b reduces the extension of head decrease from SFR (cf. Figure C-15).*

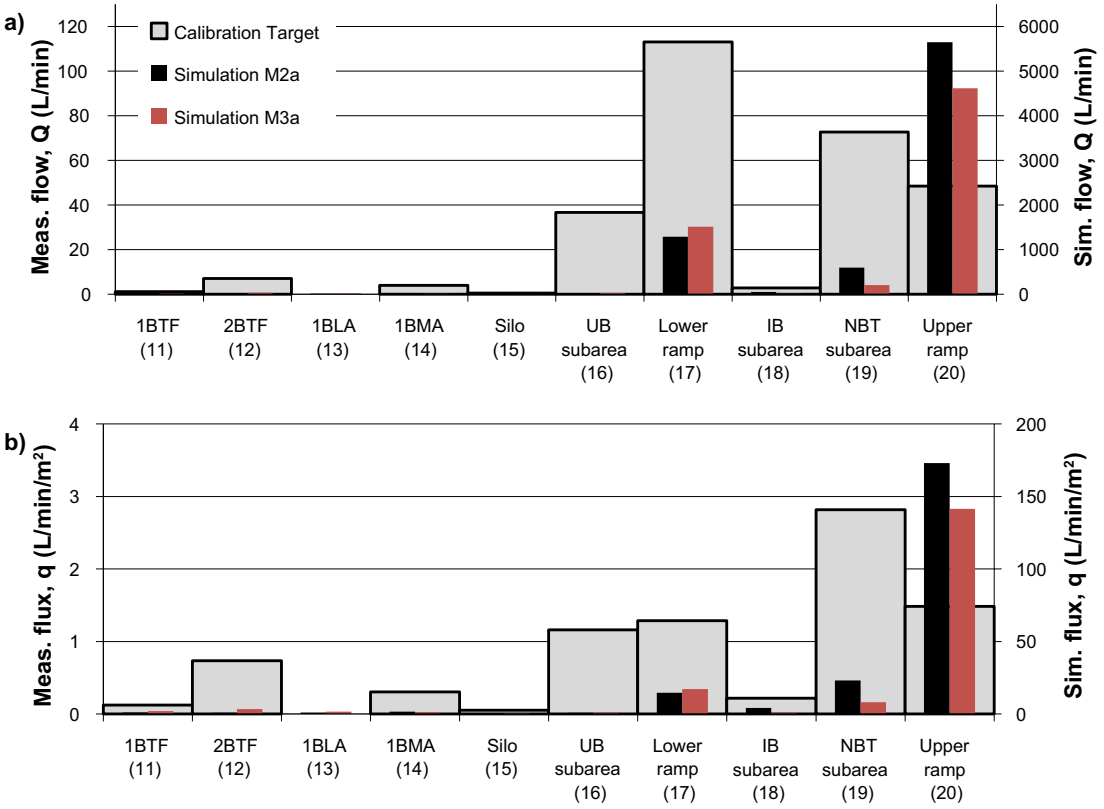

Figure C-18. *Exercise M3a simulated inflows for revised HCD parameterisation relative to initial HCD parameterisation (exercise M2a): a) tunnel inflow, Q, and b) average flux, q (normalised inflow per cross-sectional area). Simulated excessive inflow is 23 times too large (note the difference of scales and that no tunnel-skin is applied).*

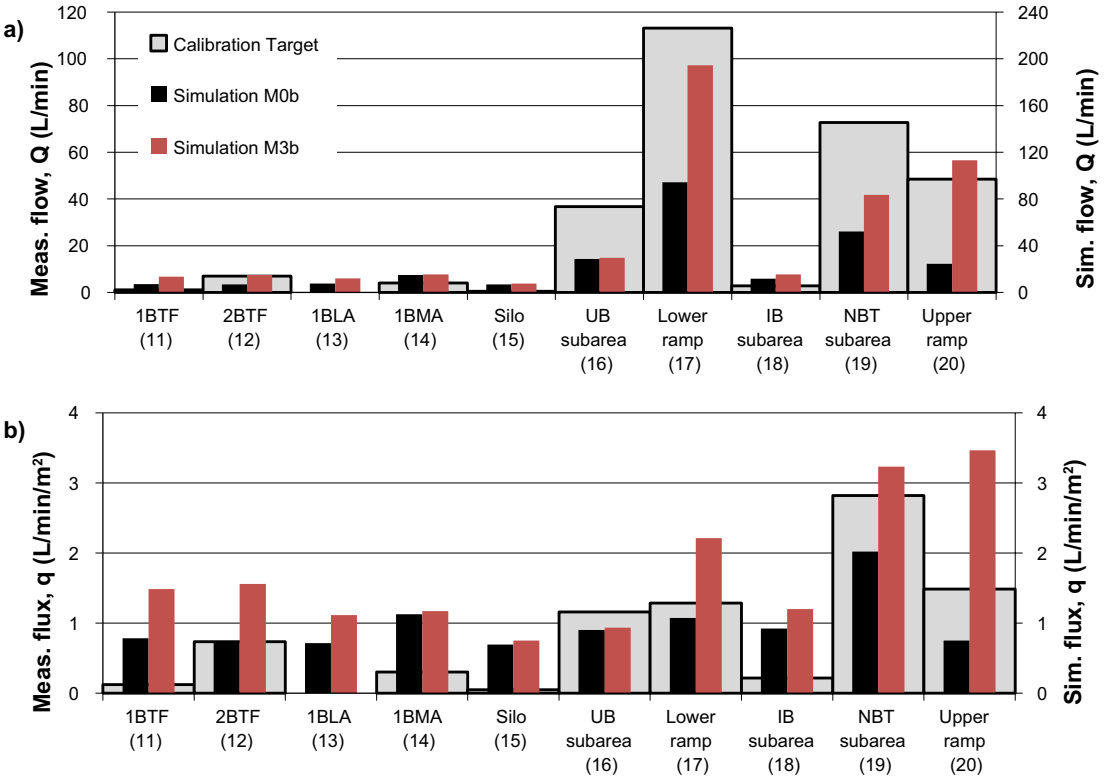

Figure C-19. *Exercise M3b simulated inflows compared to measured inflows and Initial Case M0b: a) tunnel inflow, Q, and b) specific inflow, q (inflow divided by the cross-sectional area). The total simulated inflow exceeds measurements by a factor 1.7, for constant* $K_{skin} = 6.5 \cdot 10^{-9}$ *m/s.*

Table C-4. Simulated tunnel inflow in M3.

Area code (Figure 5-1)	Reference name	Measured (L/min)	M2a (L/min)	M3a (L/min)	M3b (L/min)
11	1BTF	1.1	8.2	17.6	13.5
12	2BTF	7.0	7.8	32.4	14.9
13	1BLA	0.0	9.9	16.3	12.0
14	1BMA	4.0	20.4	15.2	15.5
15	Silo	0.5	4.0	5.4	7.6
16	UB subarea	36.7	25.4	25.0	29.5
17	Lower ramp	113.1	1,288	1,515	194.3
18	IB subarea	2.8	53.8	11.6	15.4
19	NBT subarea	72.7	596	206	83.4
20	Upper ramp	48.5	5,650	4,620	113.1
21	Rock cavern connections	NA	2.0	2.0	2.2
	TOTAL	**286.4**	**7,666**	**6,467**	**499.2**

C.5 Model Exercise M4: Introducing deterministic SBA-structures

Model Exercise M4 explores the role of the deterministic SBA-structures (SBA1 to SBA7) in current flow simulations (Section 5.5). SBA8 is not included, as it was intensively grouted during tunnel construction and therefore is expected to be insignificant for current tunnel inflow. Owing to their locations, SBA1 to SBA6 are expected to be significant for the extension of SFR, but not for the existing facility. SBA7 is located above the existing SFR. Its role in the current inflow is difficult to evaluate directly by simulations, as it neither intersects the existing facility, nor any of the monitored boreholes. Two cases are considered:

a) Introducing SBA to a simplistic model (i.e. adding SBA to M1a).
b) Introducing SBA to a complex model (i.e. adding SBA to M3b).

Thus, the impact of introducing SBA is evaluated by comparison to the reference cases M1a and M3b, as described in Sections 5.2 and 5.4, respectively. Only SBA7 is visible in the cross section of parameterised conductivity and simulated head decrease (Figure C-20 and Figure C-21). The simulated head decrease is somewhat reduced, particularly in shallow, remotely located borehole sections where the measured head decrease is low (Figure C-22). This is probably caused by SBA1, which has contact to the seafloor. SBA1 to SBA6 are modelled in the recently investigated part of the model domain, and therefore the effects are primarily found among the recent boreholes (Figure C-23b and Figure C-24b). As expected, the introduction of SBA-structures has a negligible impact on simulated tunnel inflow (Figure C-25).

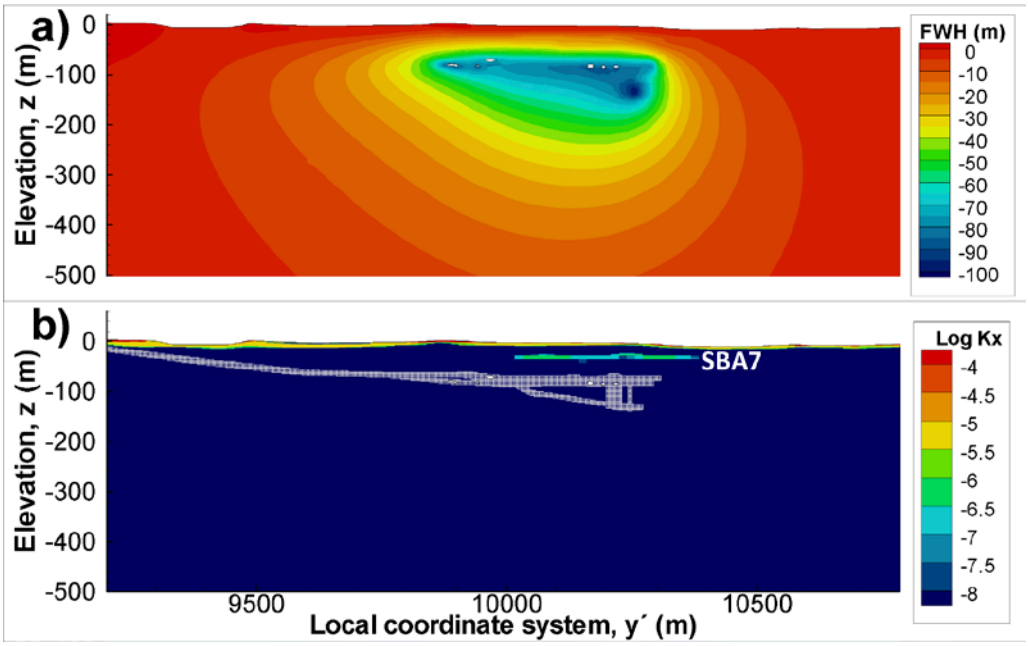

Figure C-20. *Exercise M4a: a) simulated head-field and b) conductivity field. Introducing deterministic SBA-structures (SBA1–SBA7) to simplistic model setup, reference case M1a (Figure C-7). Only SBA7 is visible in the cross-section.*

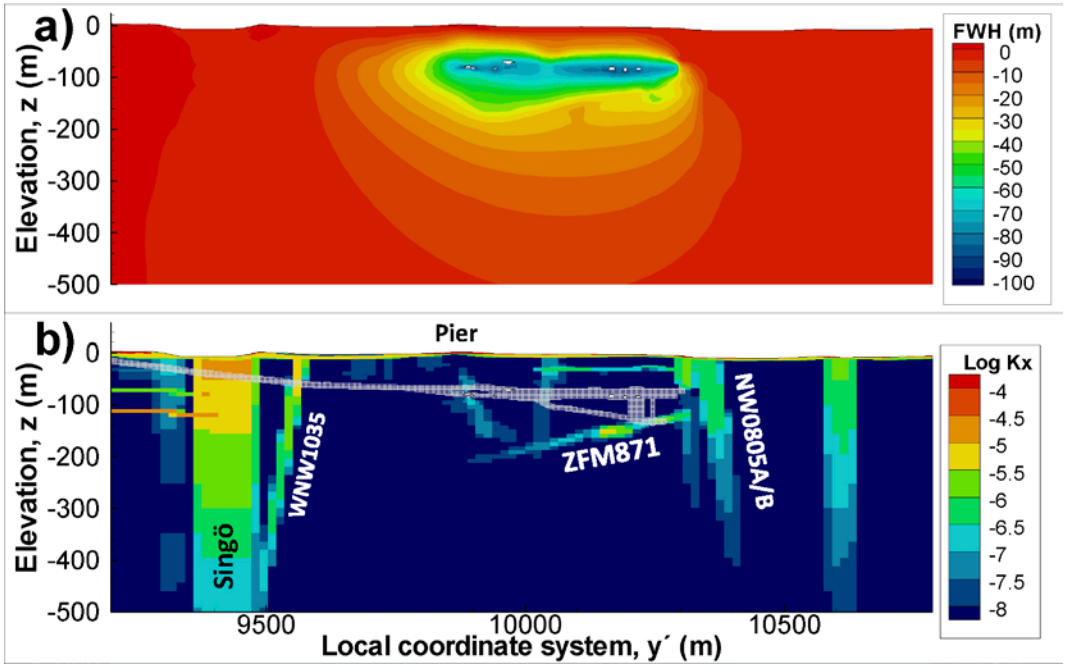

Figure C-21. *Exercise M4b: a) Simulated head-field and b) conductivity field. Introducing deterministic SBA-structures (SBA1–SBA7) causes a more complex model, reference case M3b (cf. Figure C-14).*

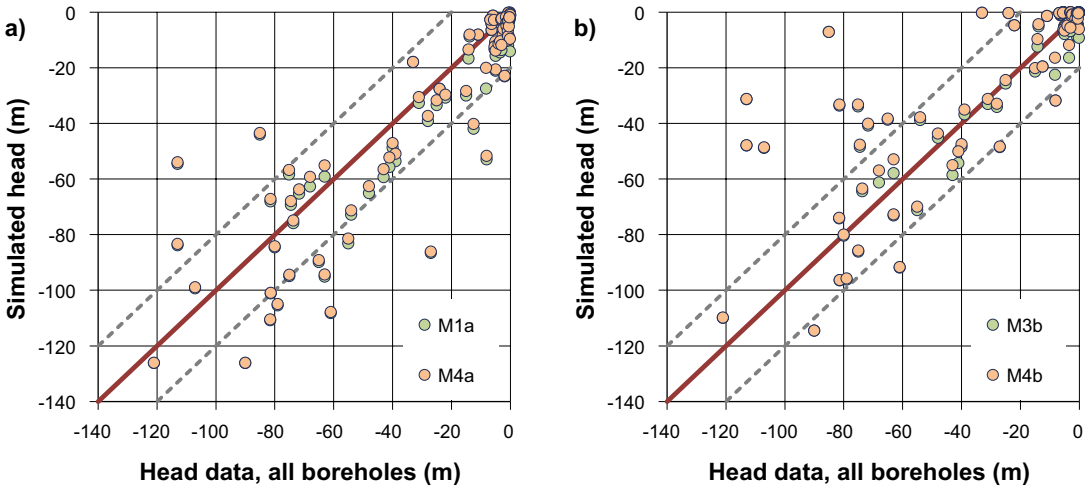

Figure C-22. *Simulated versus measured head in exercise M4. The effect of introducing SBA-structures is demonstrated by comparison to a) simple setup, reference case M1a and b) a more complex model setup, reference case M3b.*

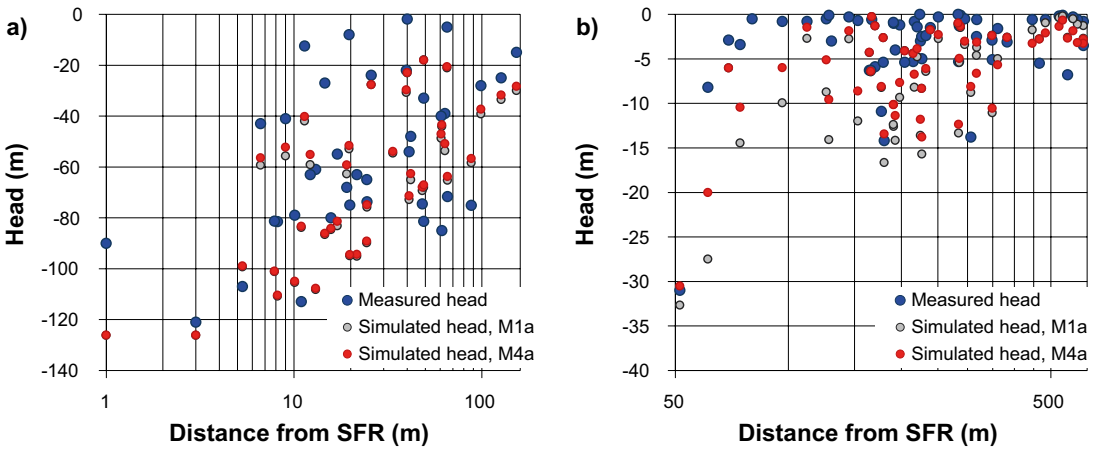

Figure C-23. *Head with radial distance from the SFR facility; a) old boreholes and b) recently installed boreholes. Simulations in exercise M4a with SBAs (red) are compared to measured head (blue) and reference case M1a without SBAs (grey).*

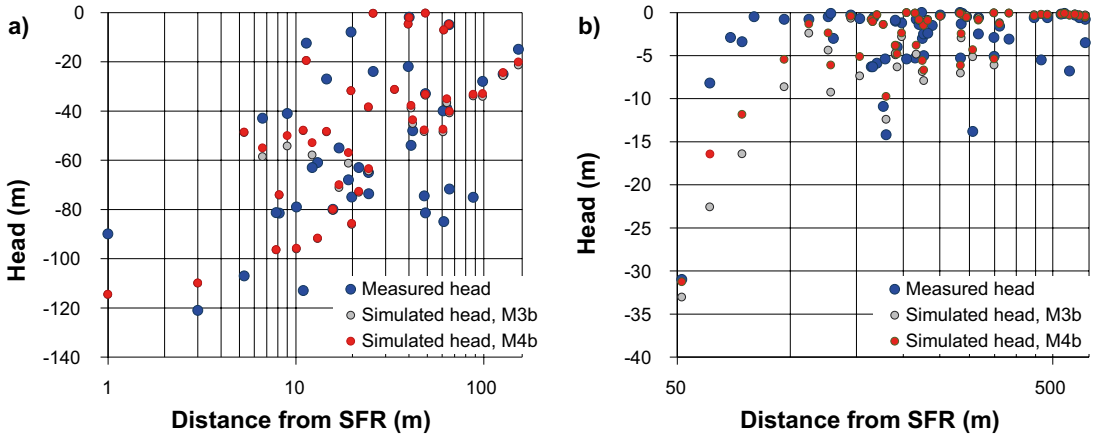

Figure C-24. *Head with radial distance from the SFR facility in a) old boreholes and b) in recently installed boreholes. Simulations in exercise M4b with SBAs (red) are compared to measured head (blue) and reference case M3b without SBAs (grey).*

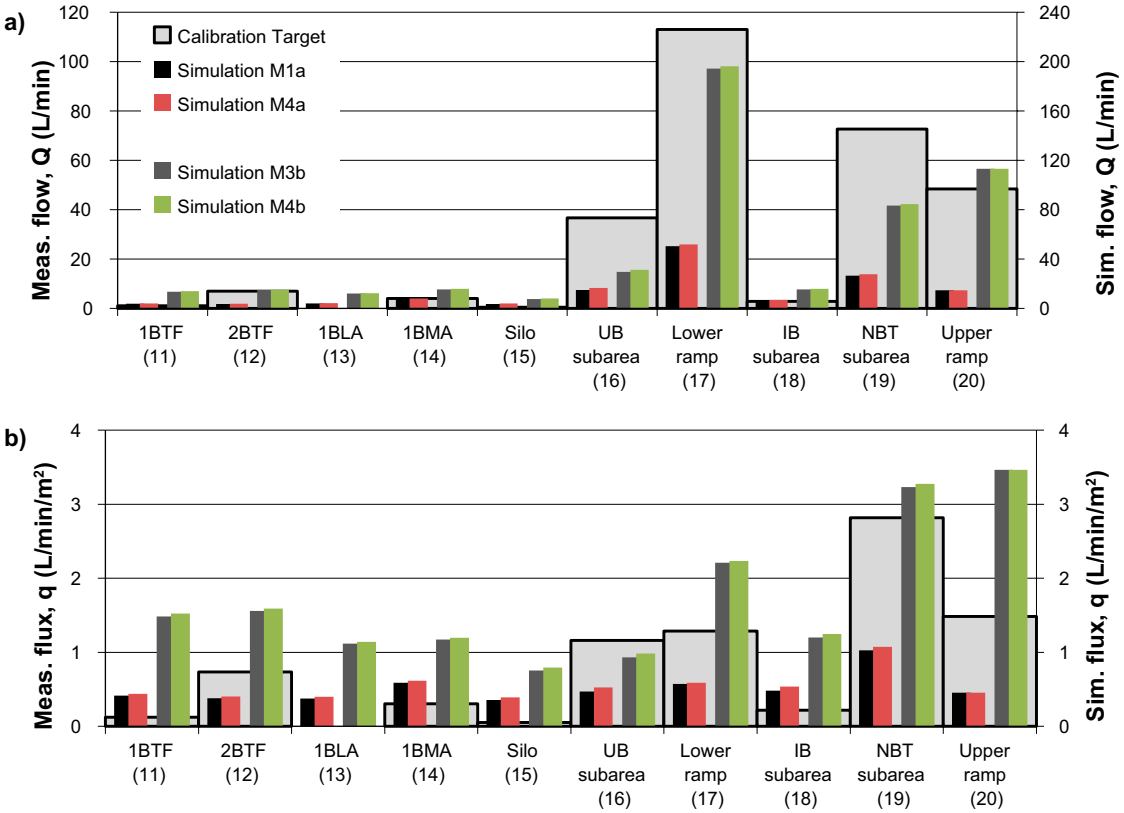

Figure C-25. *Exercise M4: the effect of SBA on simulated inflow; a) tunnel inflow, Q, and b) average flux, q (inflow divided by the cross-sectional area). The effects relative to reference cases M1a and M3b are negligible.*

However, the introduction of SBA-structures in the model slightly improves the evaluation with head data set (recent boreholes). Specifically, the SBA-structures clearly have a minor role in simulated tunnel inflow. This demonstrates the limitations of using tunnel inflow simulations for calibrating structures that are not in direct contact to the existing SFR, but nevertheless are potentially significant for the SFR extension.

C.6 Model Exercise M5: Variants of M4b

The complexity in the previous model setup (M4b) has several degrees of freedom for fine-tuning simulation results. Previous Model Exercises indicate that the constraining data are insufficient for a parameter optimisation, particularly for structures located further away from the SFR facility. Instead, Model Exercise M5 employs the previous M4b model setup to addresses the impact of four identified conceptual issues (see Öhman et al. 2012 and Appendix A). These issues are evaluated separately, and implemented as modifications of the previous model M4b setup:

a) Reduced hydraulic connection between ZFM871 and ZFMNW0805B (the conductivity is set to $6.5 \cdot 10^{-9}$ m/s along this deformation-zone junction).

b) Introducing a depth trend in HRD, according to Equation 3-6. This equation renders $K_{HRD} = 6.5 \cdot 10^{-9}$ m/s at the typical depth of disposal facilities (z = –70 m elevation).

c) Imposing global anisotropy to all hydraulic domains, HRD, HSD, and HCD. The coefficient *a* in Equation 3-5 is set to 3.0.

d) Reducing vertical conductivity of HSD by a factor of 10.

Any substantial improvement in simulation results (M5a to M5d) is taken as support for the notions raised in the conceptual modelling. Lack of substantial improvement demonstrates the non-uniqueness in applying the current tunnel-inflow configuration for tunnel-inflow model calibration.

The conductivity and the simulated head for cases M5a to M5d are shown in Figure C-26 to Figure C-29. These can be compared to the reference case M4b (Figure C-21). Note that the vertical component of conductivity is shown for M5d to resolve the contrast between HSD and HRD/HCD (Figure C-29). The anisotropy case (M5c) has the largest obvious effect on simulated head decrease (Figure C-28).

Contradictory to expectations, none of the simulation cases have major impact on simulation results. The effects in evaluated head relative to the reference case M4b are generally small (Figure C-30). The largest effect is found for the anisotropy case M5c, which provides a somewhat poorer fit to head data. Specifically, for the outlier KFR7A/B (red oval in Figure C-30) minor improvements are achieved by reduced ZFM871/ZFMNW0805B hydraulic connection, M5a, and by anisotropy, M5c. Reducing the vertical HSD conductivity by a factor 10 has essentially no impact on head or inflow. This indicates that HSD conductivity, as parameterized in the SDM-Site Forsmark model, is too high to potentially constrain bedrock recharge. Cases M5a to M5c slightly reduces inflow to the storage facilities (Table C-5; Figure C-31). The depth trend, in M5b, only reduces inflow in the deeper tunnel sections (e.g. the silo and NDB).

In summary, the absence of substantial effect in simulation results provides little guidance for improving the hydrogeological flow model (i.e. rejecting or retaining hypotheses). The insensitivity to parameterisation again demonstrates the limitations of using the tunnel inflow setup for model calibration.

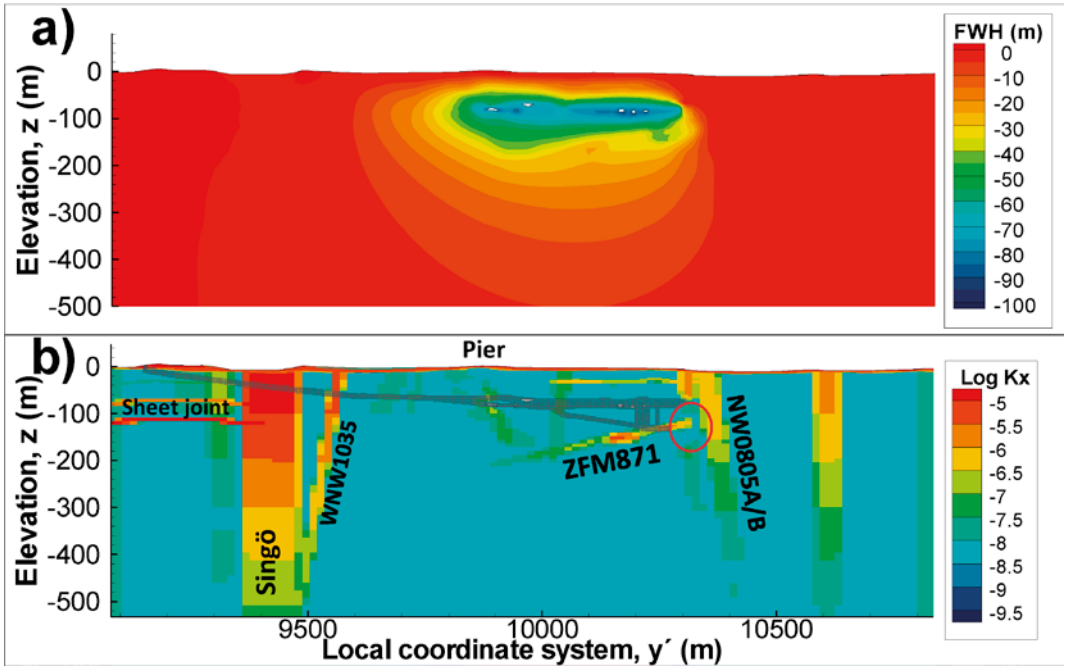

Figure C-26. *Exercise M5a: a) Simulated head and b) conductivity. Transmissivity reduction in ZFMNW0805B along junction to ZFM871 (red oval; set to the background value, K_{HRD}).*

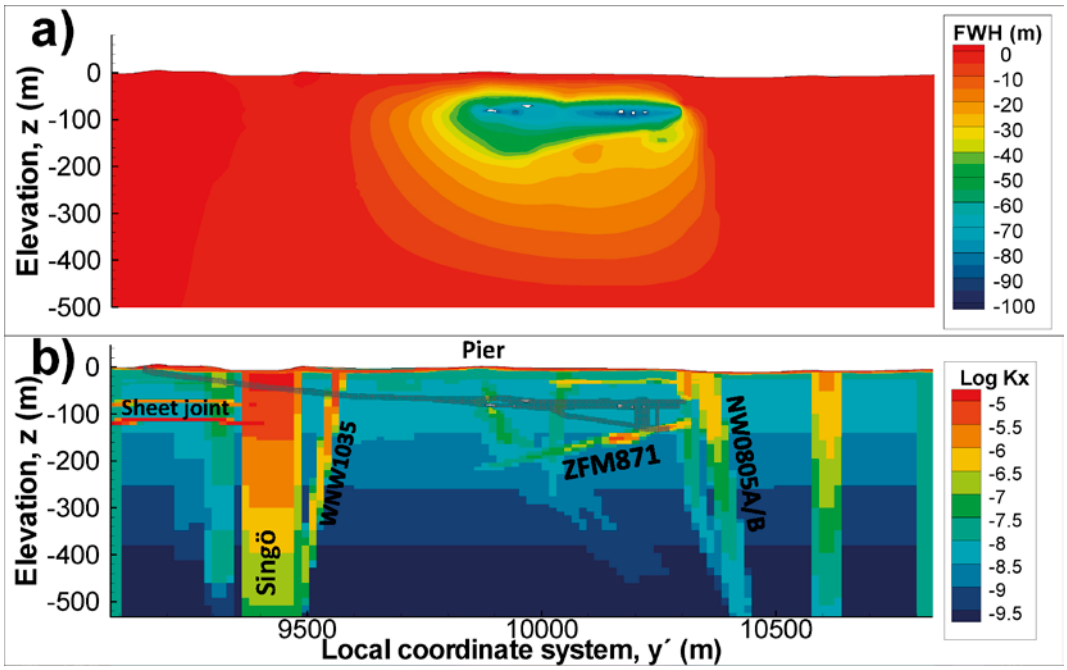

Figure C-27. *Exercise M5b: HRD depth trend; a) simulated head and b) conductivity. No depth trend is assigned outside the SFR Regional Model domain.*

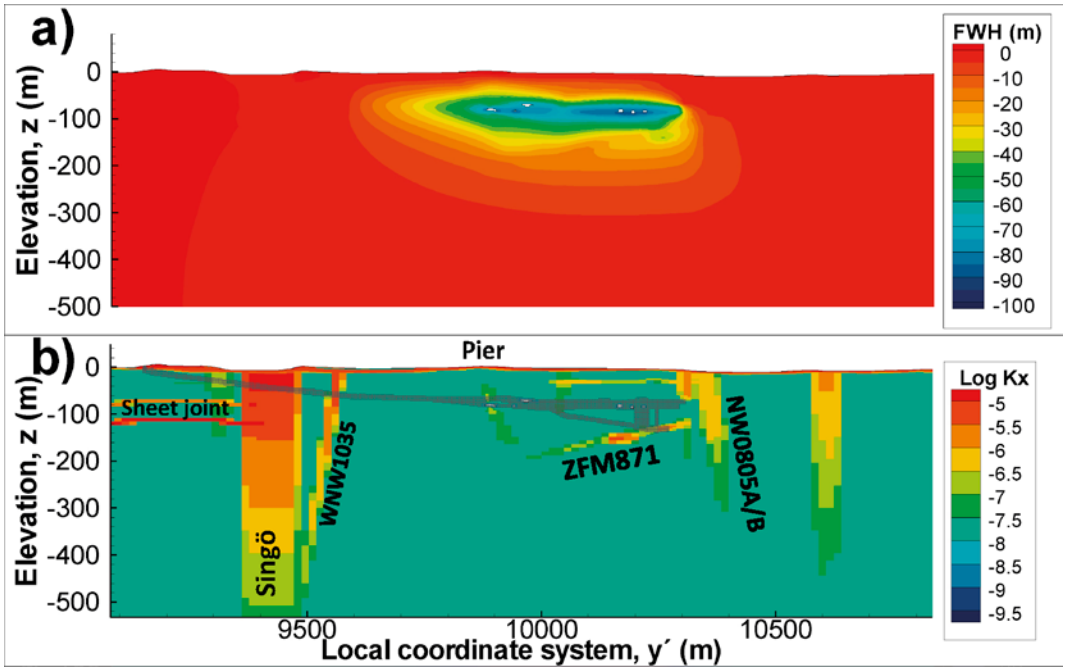

Figure C-28. *Exercise M5c: Global anisotropy in all hydraulic domains, $K_Z/K_X = 9$; a) simulated head and b) conductivity.*

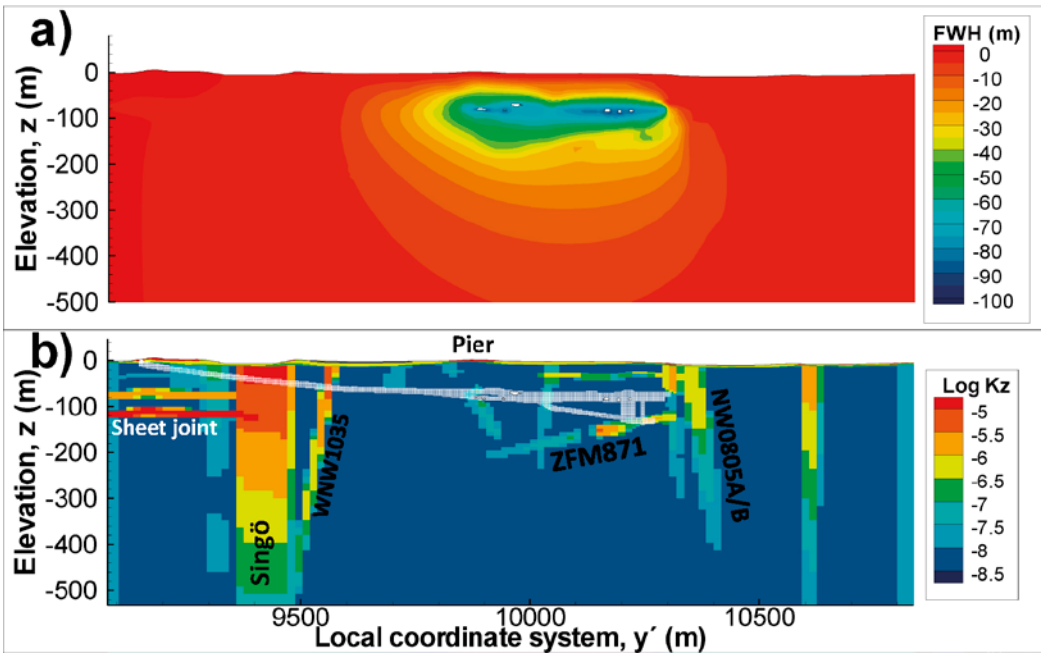

Figure C-29. *Exercise M5d: Choking sea-bottom sediments; a) simulated head and b) conductivity. K_z in HSD is reduced by a factor of 10.*

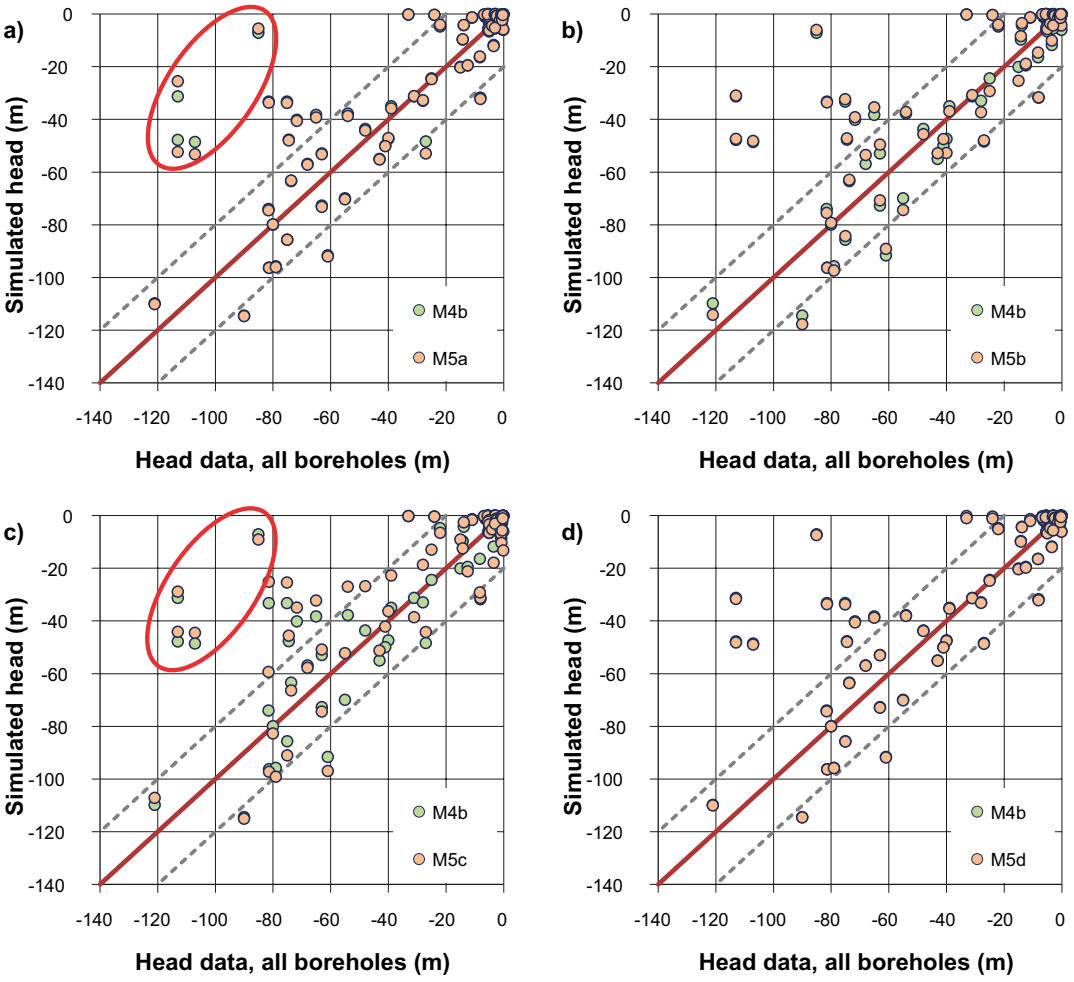

Figure C-30. *Head evaluation for tested cases in exercises M5a to M5d (orange) relative to the reference case, M4b (green). Anisotropy (M5c) has the largest notable effect. Minor improvement for the outlier KFR7A/B (red oval) are achieved by reduced hydraulic connection between ZFM871 and ZFMNW0805B (M5a) and by anisotropy (M5c).*

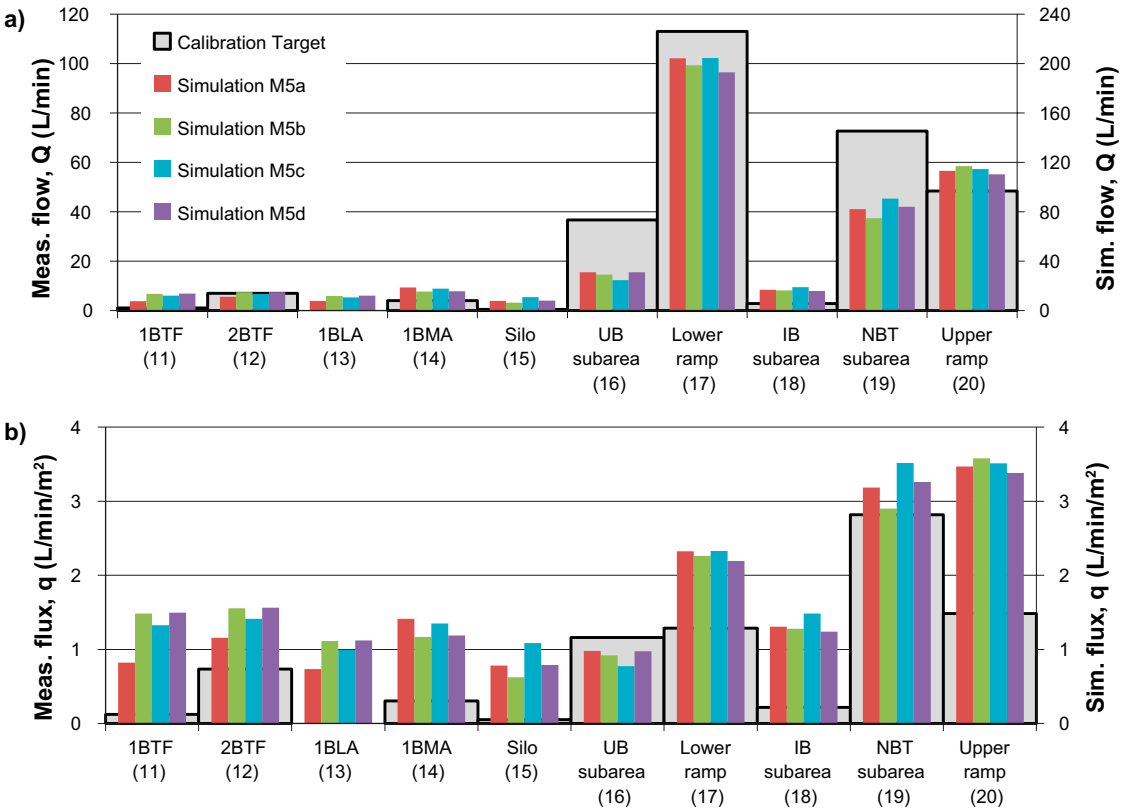

Figure C-31. *Exercise M5: Simulated inflow for variants of the reference case M4b; a) tunnel inflow, Q, and b) average flux, q (inflow divided by the cross-sectional area). The effects are negligible.*

Table C-5. Simulated tunnel inflow in exercise M5.

Area code (Figure 5-1)	Reference name	M4b (L/min)	M5a (L/min)	M5b (L/min)	M5c (L/min)	M5d (L/min)
11	1BTF	13.9	7.5	13.5	12.1	13.6
12	2BTF	15.2	11.0	14.8	13.5	14.9
13	1BLA	12.2	7.9	11.9	10.7	12.1
14	1BMA	15.8	18.6	15.4	17.8	15.6
15	Silo	8.0	7.9	6.3	10.9	7.9
16	UB subarea	31.2	31.0	29.2	24.5	30.9
17	Lower ramp	196.4	204.3	198.6	204.7	192.9
18	IB subarea	16.0	16.7	16.4	19.0	15.9
19	NBT subarea	84.4	82.1	74.8	90.7	84.1
20	Upper ramp	113.1	113.2	116.9	114.6	110.4
21	Rock cavern connections	2.3	2.3	2.1	1.5	2.2
	TOTAL	**506.1**	**500.1**	**497.9**	**518.5**	**498.3**

C.7 Model Exercise M6: Detailed calibration to measured data

Potential adjustments to improve simulation results are pursued in Model Exercise M6. In spite of the lack of model improvement in M5, all tested cases are considered realistic. Hence, the combined modifications M5a to M5d were implemented to form the starting point for exercise M6. The strategy in this exercise is to identify key discrepancies in the flow model and to sequentially test alternative parameterisations and hypotheses that improve model performance. This is done by trial-and-error, according to which successful adjustments are retained while unsuccessful adjustments are rejected. Thus, the goal of M6 is to test how far the model setup can be "optimised" at the expense of additional detail in parameterisation. Again, the level of achievement in relation to effort in refinement demonstrates the constraining power of data (or lack thereof).

It should be emphasised that the goal of M6 is *not* to establish a perfect fit to data at every data point. Firstly, the heterogeneity of the hydrogeological system can never be deterministically modelled in full detail. One such example is the wide head difference between the two adjacent sections in KFR7B (–27 and –107 m, respectively; Figure C-32a). Secondly, some limitations in the constraining power of data are known beforehand (e.g. geometric inconsistency in head evaluation and uncertainties in measured tunnel inflow, as described in Sections 2 and 4.4). The goal is to identify the most obvious discrepancies and address these based on conceptual hypotheses, while keeping the simulated inflow within realistic bounds. In this trial-and-error procedure, the model performance is evaluated for hydraulic units (for example, "Southern boundary belt"; Table D-2).

The identified key discrepancies in exercise M5 are the underestimated head decrease for the two dominant flow paths in the system, namely the Southern boundary belt and ZFM871 (see red values in Table 5-2). Hence, these two locations are here addressed in detail. Both locations are notable sink terms to the system that were intensively grouted during tunnel constructions. Three primary explanations are considered:

1) The effective transmissivity of zones, as parameterised from old borehole data, is potentially over-estimated (Section 2.4). Reducing the deformation-zone transmissivity, simultaneously as lowering the tunnel-wall resistance, will propagate head decrease further away from the tunnel wall.
2) The upstream hydraulic contact to the sea is potentially constrained (e.g. overlying sediments, or indirect contact via hydraulically significant structures). Reducing the hydraulic contact to the sea (positive hydraulic flow boundary) will increase head decrease.
3) Tunnel-wall skin is numerically implemented as a flow resistance occurring over a 2 m thick tunnel-wall cross section (Figure 2-2). This may be unrealistic in context of discussions in Sections 2.5 and 2.8. Note also that the tunnel section NDB1, which constitutes an important sink in ZFM871, was unavailable during M5 (cf. Figure C-32 and Figure C-33).

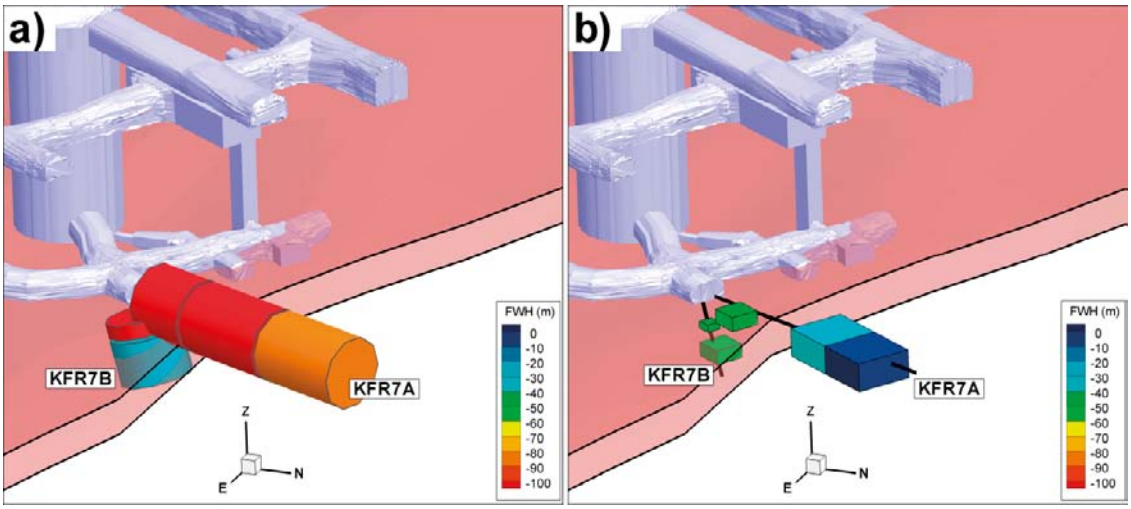

Figure C-32. *Underestimated head decrease at the ZFM871 intersection; a) measured data and b) simulation in exercise M5. Large head decrease indicates strong hydraulic connection to the SFR tunnel, relative to the connection to the sea. Note that tunnel section NDB1 was unavailable during M0 to M5 (cf. Figure 5-7).*

Actions to improve the simulations in the vicinity of ZFM871:

- **Inclusion of tunnel section NDB1**: The tunnel section became available during this study. NDB1 is an important contact between the SFR facility and ZFM871 (i.e. an important sink of the tunnel inflow setup; Figure C-33).
- **Geometric extension of ZFM871:** In the geological model, ZFM871 is terminated against ZFMNW0805B. Head decrease data in KFR7A suggests strong horizontal hydraulic, dead-end connection to SFR, poorly connected to the sea (see Öhman et al. 2012). In order to simulate the large head decrease in KFR7A, ZFM871 is at least expected to cover the midpoint of its lowest section, KFR07A_1. This is achieved by expanding ZFM871 by 15% in all directions from its geometric midpoint (cf. Figure 5-6 and Figure C-33).
- **Maintaining reduced hydraulic contact between ZFM871 and ZFMNW0805A/B:** A poor connectivity to the sea at the junction between the two zones is suggested by the large head decrease and Littorina content found in KFR7A, which is clearly different from KFR08. Therefore the vertical conductivity along their intersections with ZFM871 is reduced to equivalent of the average rock mass ($K_{HRD} = 6.5 \cdot 10^{-9}$ m/s; this is similar to M5a).
- **Grouted volume of ZFM871:** The large, widespread head decrease observed in ZFM871 cannot be attained by the simplified numerical representation of skin/grout (Figure 2-2). As an alternative, the NDB/ZFM871 intercept was modelled as a large volume of poorly grouted rock. The volume of injected grout (67 m^3) can be related to the bedrock-mass volume inside a cylinder 11 m high (i.e. ZFM871 thickness) with a radius of 14 m (assuming a porosity of 1%). However, a wider influence area is motivated by the fact that grouting is known to spread unevenly (i.e. asymmetrically) and was also performed over several tunnel sections (i.e. not originating from a single point). The best match was found for "poor grouting over a wide area" ($K_{skin} = 1.3 \cdot 10^{-7}$ m/s, r_{inf} = 55 m, x´= 6,505, y´= 10,292; see yellow area in Figure C-33).
- **Reducing the transmissivity of ZFM871:** Deformation zones close to SFR are parameterized by hydraulic data from the old data set. The old data set contain short-term measurements, which risks overestimating the effective, large-scale transmissivity of zones due to inclusion of compartmentalized transmissivity. In the current model, ZFM871 has a considerably higher transmissivity than has been used in previous modelling, e.g. Holmén and Stigsson (2001) (cf. black and dashed lines in Figure 3-4). Therefore, the transmissivity was reduced by a factor of 5, which may be more representative of its effective hydraulic property (brown line in Figure 3-4).

Actions to improve simulations in the vicinity of the Southern boundary belt are the following:

- **Adjusting the transmissivity parameterisation:** Based on the same argument as above, the effective transmissivity of ZFMWNW0001 and ZFMWNW1035 were reduced by a factor of 10, which also is more in line with previous modelling (see Table 3-2).
- **Sediment contact to the Southern boundary belt:** Modelling exercises M0 to M5 cannot reproduce the large head decrease data in the Southern boundary belt without causing excessive simulated tunnel inflow (Table 5-2). A potential reason is that its hydraulic contact to the sea is constrained by overlying sediments (clay). The uppermost part of the Southern boundary belt zones are assigned a conductivity that corresponds to overlying glacial clay. Unfortunately, this "sediment choking" is rather crudely implemented owing to coarse meshing of these zones (triangles of side length c 50 m; Figure 3-5). It should be noted that the SFR access tunnels penetrate the Southern boundary belt at c –40 to –50 m elevation and that, in reality, the sediment choking is not expected to extend to this depth.
- **Revision of Forsmark sheet joints:** A revision of the hydraulic contact between the Forsmark sheet joints and the Southern boundary belt was also explored to improve the simulated head decrease in the Southern boundary belt**.** Analysis of an interference test (performed in HFM33, subsequent to the development of sheet joints) motivates truncating the sheet joints inside the SFR Regional domain (Figure 3-10).

Further actions taken are the following:

- **Spatial differentiation of tunnel-wall skin:** Deformation-zone intercepts with the tunnel wall are assigned variable skin (Table 5-3). The Silo is assigned particularly low skin conductivity. Values are varied to improve the relation to inflow and head data.

- **Grid refinement in the shallow bedrock;** Above –200 m elevation, the computational grid inside the SFR Regional domain is refined to a minimum vertical cell side length of 4 m (Table 4-1). This modification causes a *poorer fit to head data*, which demonstrates that the model evaluation is sensitive to on the grid resolution (discussed in Section 4.4.2). Nevertheless, this modification was retained in order to enhance the ECPM translation of stochastic features in exercise M7 (anisotropy and conductivity correlation).

The final model setup is referred to as M6g. The key changes are reduction of HCD transmissivity in ZFMWNW0001, ZFMWNW1035 and ZFM871, leading to the final HCD parameterisation (Table 3-2). Also sediment-interface choking is implemented in Singö, ZFMWNW1035, and ZFMWNW3259. In the M6g exercise, the setup has a significant level of model sophistication, including the following:

- HCD: Final parameterisation (Table 3-2), conditioned intercepts (Table A-3), differentiated tunnel-wall skin (Table 5-3), and local adjustments of the ZFM871/ZFMNW0805 junction and the Singö/sheet-joint junction.
- HRD: Anisotropy, $a = 3$ in Equation 3-5 and depth trend defined by Equation 3-6.
- HSD: SR-Site Forsmark, but K_z reduced by a factor of 10.
- SBA: Implemented as deterministic structures SBA1 to SBA7.
- Refined discretisation (maximum cell size is 8 m in the upper part of the bedrock).

Some improvement is accomplished in the overall agreement in head data (cf. Figure C-34 and Figure C-30). KFR7A/B still stand out as outliers (red oval in Figure C-34; see also Figure C-33). In spite of the sequential sophistication in details of the model setup (M0 to M5) and a substantial effort to improve model results in exercise M6, the achievement is rather small compared to the Initial Case M0 (Figure C-34). The most notable improvement in simulated head is the reduction in excessive head decrease 100–350 m away from the facility (Figure C-35).

Minor achievements are accomplished in simulated inflow (Figure C-36 and Table C-6). With the introduction of variable skin (Table 5-3), the inflow to the disposal facilities has been reduced to a more realistic level (Table C-6).

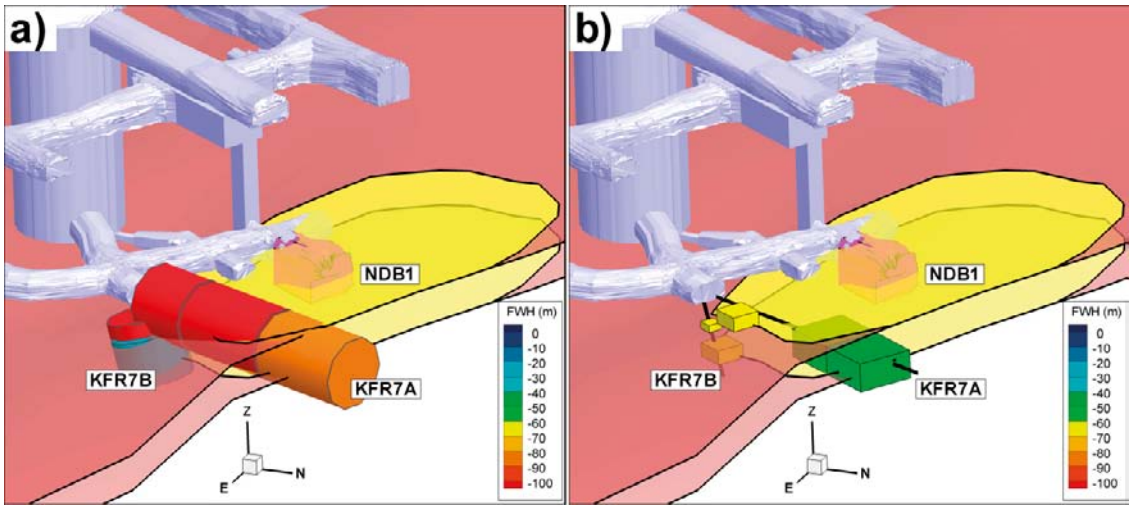

Figure C-33. *Simulating head decrease at the ZFM871 intersection; a) measured data and b) simulation in Exercise M6. ZFM871 is extended to include KFR7A, the NDB1 geometry is included as a sink (pink shade), grouting is implemented as a low resistance within a radius of 55 m (yellow) and the transmissivity of ZFMNW0805A and B is reduced locally along their intersections with ZFM871.*

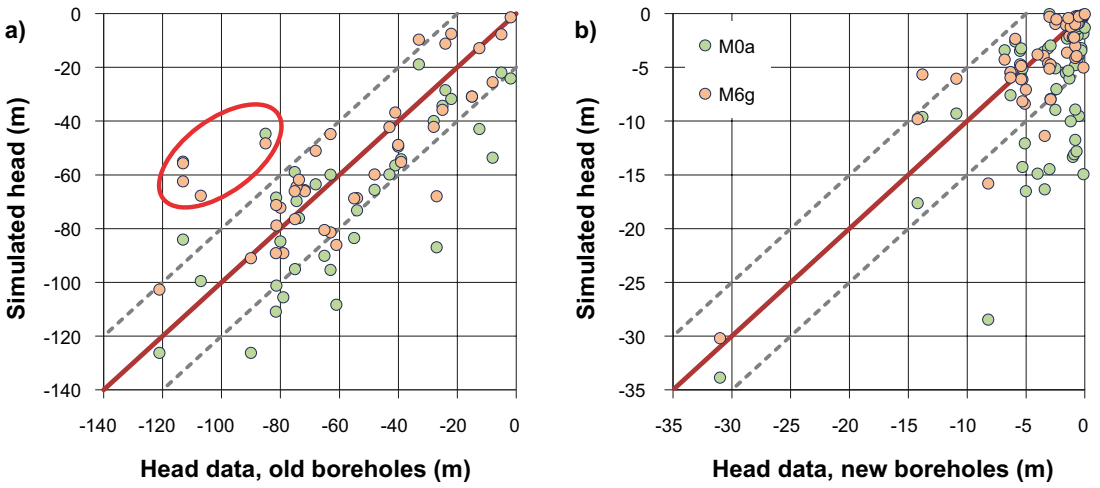

Figure C-34. *Simulated versus measured head in exercise M6 compared to the Initial Case M0; a) old boreholes and b) recently installed boreholes. Although improvement in the more complex M6 model setup is evident, the reasonable agreement in the simplistic Initial Case signifies that the system is not well-constrained by data.*

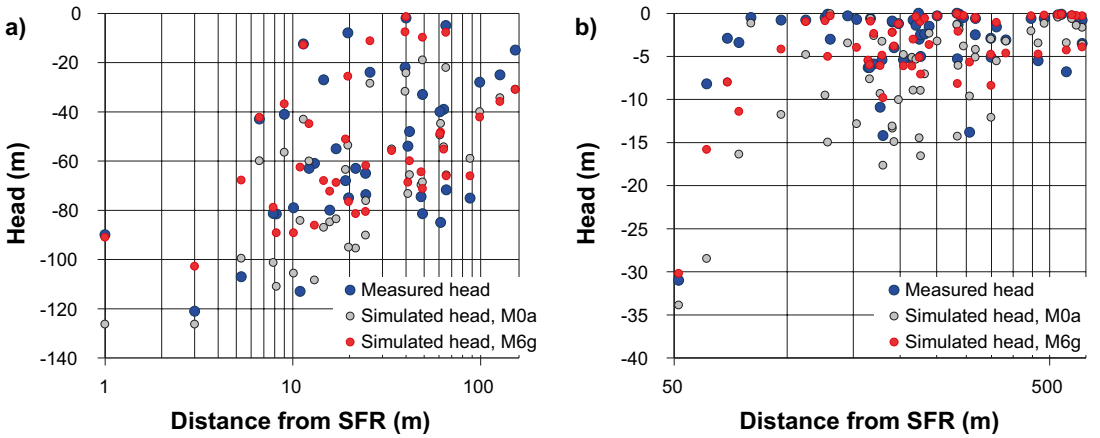

Figure C-35. *Simulated head in exercise M6 with radial distance from the SFR facility (red) compared to measured head (blue) and the Initial Case M0a (grey): a) old boreholes and b) recently installed boreholes.*

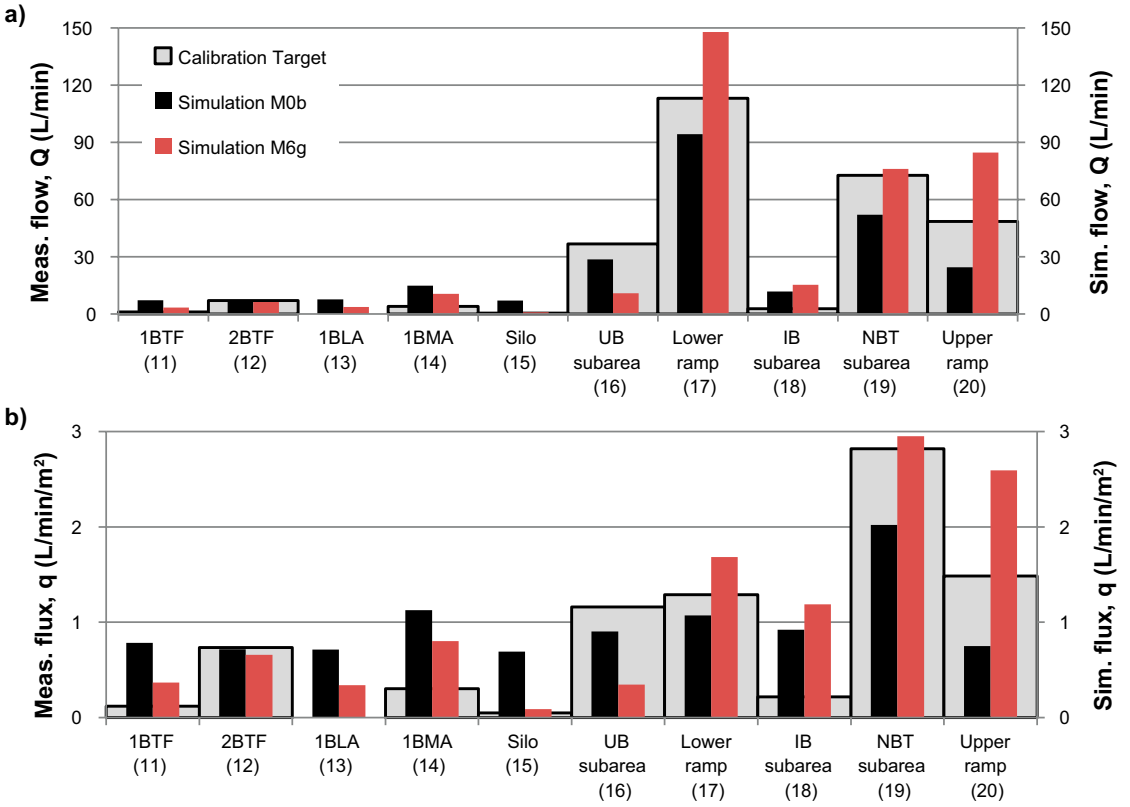

Figure C-36. Exercise M6: simulated inflow for the "optimised" case M6g compared to Initial Case M0b; a) tunnel inflow, Q, and b) average flux, q (normalised inflow per cross-sectional area). The level of model improvement relative to model complexity is minor.

Table C-6. Simulated tunnel inflow in exercise M6.

Area code (Figure 5-1)	Reference name	Measured (L/min)	M0b (L/min)	M6g (L/min)
11	1BTF	1.1	7.1	3.4
12	2BTF	7	6.8	6.3
13	1BLA	0	7.7	3.7
14	1BMA	4	14.9	10.6
15	Silo	0.5	7.0	0.9
16	UB subarea	36.7	28.6	10.9
17	Lower ramp	113.1	94.3	147.9
18	IB subarea	2.8	11.8	15.2
19	NBT subarea	72.7	52.1	76.1
20	Upper ramp	48.5	24.5	84.7
21	Rock cavern connections	NA	2.5	0.9
	TOTAL	**286.4**	**257.2**	**359.6**

C.8 Model Exercise M7: Introducing stochastic SBA-structures

Model Exercises M4 to M6 include deterministic SBA-structures SBA1 to SBA7, as defined in Öhman et al. (2012). None of them are in direct contact with the existing SFR, and owing to their location they have a negligible role in current inflow simulations. However, their spatial extension and potentially existing SBA-structures also outside borehole coverage is of key relevance to the planned SFR extension. For example, dominating horizontal hydraulic connections are indicated in the vicinity of KFR104, by means of interference-test simulations (Chapter 6). This is an area where no SBA-structures have been defined in any of the model setups.

Therefore, Model Exercise M7 was set up to explore the impact of additional SBA-type structures. This was done by complementing the deterministic SBA-structures (SBA1 to SBA7) by a stochastic representation outside borehole coverage. A highly simplified approach was taken for this purpose that does *not* follow the established DFN modelling methodology and should *not* be confused with the hydro-DFN model reported in Table 3-4. The details of this setup are lengthy and therefore summarised separately in Appendix B. The purpose of this exercise is to explore if the current tunnel-inflow setup has constraining power to provide additional indications on the existence (or absence) of SBA-structures near the existing SFR.

Deterministic SBA-structures, geometrically represented as large uniform planes in Öhman et al. (2012), are envisaged as interconnected clustered networks composed of smaller, sub-horizontal to gently dipping fractures. Their existence and hydraulic character is interpreted as intimately depending on the connectivity to the Southern and Northern boundary belts and to zone ZFMNNW1034, which are perceived as important vertical connectors to the overlying sea (Figure B-1). As the starting point, stochastically features are generated over the entire SFR Regional domain, based on the upper tail in PFL-f transmissivity data (Table B-2). Generated features in direct contact to the SFR facility are removed (Figure B-5a). Exclusion of features in direct contact with the tunnel wall is motivated by the fact that such flowing features were grouted during construction. Consequently, tunnel-wall conductivity outside deformation zones is defined by Equation 3-6.

Furthermore, stochastic features in areas with modelled geometries of SBA1 to SBA7 are removed, in order to avoid overlap between deterministic and stochastic representation (Figure B-6b; i.e. to avoid "double counting"). Following the conceptual model of Öhman et al. (2012), hydraulic choking is mimicked by assigning an *apparent transmissivity* depending on upstream contact to the Southern and Northern boundary belts and to zone ZFMNNW1034. Finally, the remaining stochastic features are merged with deterministic structures SBA1 to SBA7 (Figure B-1) for implementation in flow simulations.

Two such merged SBA realisations, M7a and M7b, are superimposed onto the previous model setup, M6. The SBA-structures are expected to cause local, horizontally anisotropic conductivity increments in the model. Unfortunately, the grid resolution (maximum vertical side length 8 m) is still too coarse to maintain anisotropy after ECPM translation. This has unfortunate consequences for the implemented conductivity reduction along the ZFM871/ZFMNW0805A/B junction (implemented as local conditioning of HCD transmissivity in M5 and M6). To uphold this hydraulic choke in presence of poorly resolved SBA-type structures even after ECPM translation, the numerical implementation methodology must be adapted. A new algorithm is added to ensure that the vertical conductivity of the ECPM grid cells along the geometric intercept, K_z, does not exceed rock-mass conductivity, as defined by Equation 3-6. This implementation is considered to be of minor relevance for the comparison between M7 and M6.

The only notable impact of stochastic SBAs occurs in head evaluation near the Silo (the KFR7A/B outliers marked by red oval in Figure C-37). Three interpretations are considered:

1) Simulations indicate local *absence* of SBA-structures near the silo, reinforcing earlier data-based interpretations of particularly low-conductive bedrock mass around the silo.
2) This does *not* prove absence of SBA-structures in the area, but instead instability in the achievement of M6g. In other words, robust model behaviour in presence of SBA requires further reduction of the vertical hydraulic contact to the sea (e.g. lower transmissivity in ZFMNW0805A/B, further geometric extension of ZFM871).
3) Results are *inconclusive*; analysis of only two realisations is insufficient for drawing any type of conclusions concerning the details of heterogeneous data, particularly given the limitations in model resolution.

As mentioned earlier, the stochastic SBA-structures are conditioned so as not to have direct contact to the SFR facility. Consequently, there is no drastic impact on simulated tunnel inflow and the difference to the Initial Case is still small (Figure C-38; Table C-7).

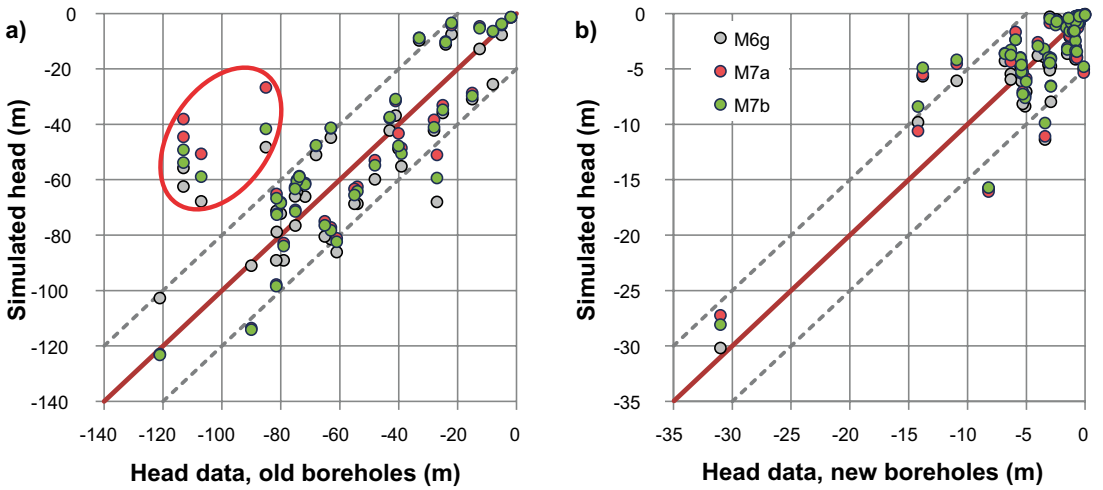

Figure C-37. *Simulated versus measured head in exercise M7. The effect of introducing SBA-structures is demonstrated by comparison to reference case M6g.*

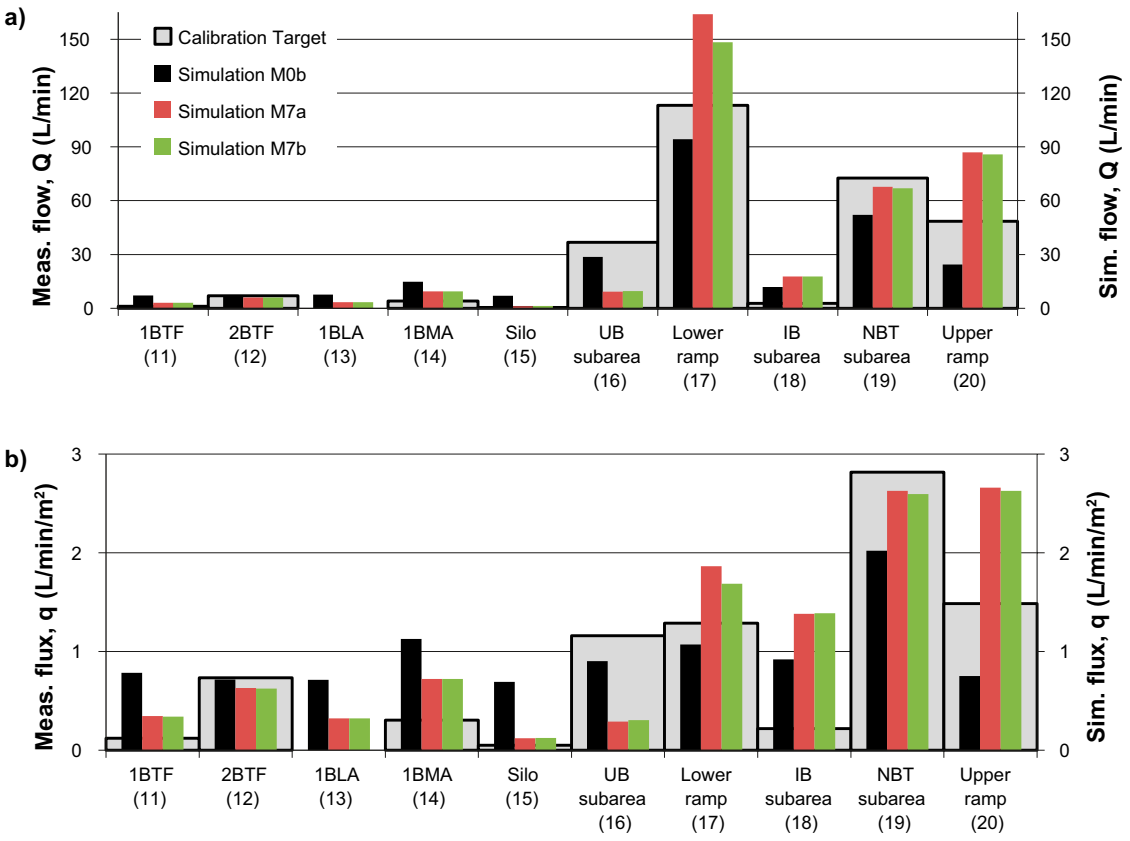

Figure C-38. *Exercise M7: Simulated inflow for case M7 compared to Initial Case M0; a) tunnel inflow, Q, and b) average flux, q (inflow divided by the cross-sectional area).*

Table C-7. Simulated tunnel inflow in exercise M7.

Area code (Figure 5-1)	Reference name	Measured (L/min)	M0b (L/min)	M7a (L/min)	M7b (L/min)
11	1BTF	1.1	7.1	3.1	3.1
12	2BTF	7	6.8	6.0	6.0
13	1BLA	0	7.7	3.5	3.5
14	1BMA	4	14.9	9.5	9.5
15	Silo	0.5	7.0	1.2	1.3
16	UB subarea	36.7	28.6	9.2	9.7
17	Lower ramp	113.1	94.3	163.9	148.3
18	IB subarea	2.8	11.8	17.7	17.8
19	NBT subarea	72.7	52.1	67.8	66.9
20	Upper ramp	48.5	24.5	86.9	85.8
21	Rock cavern connections	NA	2.5	0.8	0.8
	TOTAL	**286.4**	**257.2**	**368.8**	**351.8**

Simulating initial tunnel inflow

Simulating tunnel inflow of HCDs parameterised by borehole data, without the implementation of a skin resistance, render unrealistic results, as demonstrated in Model Exercises M2a–c and M3a. The simulated inflows did not only exceed the current measured inflow by a factor of c 25, but also its estimated upper bound of undisturbed inflow by a factor of c 7 (estimated as "theoretical initial tunnel inflow at time $t = t_0$", where the development of skin-phenomena is minimal; see Section 2.8.1). Based on this finding, resistances have sequentially been added during sequential Model Exercises M3b to M6, in terms of a) tunnel-wall skin, b) structure junctions, c) effective HCD transmissivity, d) grouting, and e) HSD contact. Limitations in constraining data and model setup cause insufficient constraining power for supporting or rejecting these adjustments. Introduction of skin had the most drastic impact on simulation results (Model Exercise M3b). In order to test the role of other resistances (b–e), it is of interest to simulate a case where the skin-resistance is reduced to only reflect grouting.

This final test was performed for cases M7a and M7b. Tunnel-wall conductivity at deformation zone intersections were assigned $K_{skin} = 10^{-6}$ m/s, for standard cement in the upper part of the facility, and $K_{skin} = 10^{-7}$ m/s for the finer grouting material in the NBT tunnel (Section 2.5). The simulated inflows are 1,100 to 1,050 L/min, which compares well to the estimated initial tunnel inflow at theoretical time t_0 (Section 2.8.1). The improvement, relative to M2 and M3a, has primarily been accomplished by: 1) lowering the effective transmissivity of ZFMWNW0001, ZFMWNW1035 and ZFM871, and 2) implementing "HSD-choking" in ZFMNW0002, ZFMWNW0001, and ZFMWNW1035.

These results reinforce the previous notions that the resistance in tunnel wall is not confined to the immediate tunnel wall.

Appendix D

Geometric input for DarcyTools model setups

The numerical model setup in DarcyTools is controlled by geometric objects. This appendix presents a list of the geometric objects used in Model Exercises M0 to M7 (Chapter 5) and the particle tracking analyses (Chapter 7). Simulations are performed within a rotated reference system (Section 4.3); the prefix "R_" denotes that the object is rotated. Geometric objects serve the following purposes:

1) Grid construction and identification of particular locations (e.g. tunnel sections; Chapter 4).
2) Hydraulic-domain parameterisation (Chapter 3). Fracture files (*.knw and *.ran) are used for the bedrock, while raster files (*.asc) are used for the HSD. A given structural geometry may have several parameterisation variants (not specified here; see Chapter 5). The HSD raster files cannot be rotated; hence the original files used, while rotation is accounted for in implementation.
3) Extraction of simulation results (inflow and borehole PWH).

The geometry files that were used are listed in Table D-1, while the geometry of monitored borehole sections used for evaluation of simulations are listed in Table D-2.

Table D-1. List of geometry files used in DarcyTools model setups.

Fracture files used in M0 to M7	Type	Varied
R_PFM_zoner_med_hål_i_mitten	knwfile	No (Figure 3-5)
R_Parameterized_SFR_BRIDGES	knwfile	No (Figure 3-5)
R_PLU_sheet_joints_truncated	knwfile	Yes (Section 3.4.1)
R_Parameterized_SFR_HCD	knwfile	Yes (Table A-1)
R_Parameterized_SFR_SBAs	knwfile	No (Section 3.4.3)
R_STOCH_SBAs_Excluding_DET_0XX	ranfile	SBA realisation XX (Appendix B)
Additional fracture files in particle tracking (Chapter 7)		
R_EXTENDED_SERCO_DFN_WITH_HOLE	knwfile	DFN outside SFR (Figure 3-9)
R_SFR_DFN_knwn	knwfile	Combined DFN + Unresolved PDZs (Figure 3-7; Figure 3-12)
Geometry objects used in grid construction (Figure 4-1)		
R_SFR_modellområde_v01.dat	SFR Regional domain	
R_WATERDIVIDE_z_1500m.dat	SFR Flow domain	
R_top_with_ridge.dat	Topography (DEM)	
R_ROCK_TOP.dat	HSD/Bedrock interface	
HSD parameterisation (Table 3-1; Figure 3-2)		
dem_20m.asc	Topography, ESRI raster	
l1.asc	L1 elevation, ESRI raster	
l2.asc	L2 elevation, ESRI raster	
l3.asc	L3 elevation, ESRI raster	
z2.asc	Z2 elevation, ESRI raster	
z1.asc	Z1 elevation, ESRI raster	
z3.asc	Z3 elevation, ESRI raster	
z4b.asc	Z4b elevation, ESRI raster	
z5.asc	Z5 elevation, ESRI raster	
z6.asc	Bedrock elevation, ESRI raster	
z7.asc	4 m depth, thin HSD coverage, ESRI raster	
koderz1_srsite.asc	Soil type distribution within Z1	
QD_codes_z5_(SDM)_with_till_from_SR-site	Soil type distribution within Z5	

Fracture files used in M0 to M7	Type	Varied
Lake geometry	**Marker ID**	
R_Lake_2-2.dat	50	
R_Lake_4-1.dat	51	
R_Lake_7-1.dat	52	
R_Lake_7-3.dat	53	
R_Lake_7-4.dat	54	
R_Lake_Lillfjarden.dat	55	
R_Lake_Marrbadet.dat	56	
R_Lake_Norra_Bassangen.dat	57	
R_Lake_Puttan.dat	58	
R_Lake_Simpviken.dat	59	
R_Lake_Stocksjon.dat	60	
R_Lake_Tallsundet.dat	61	
R_Lake_Vamborsfjarden.dat	62	
R_Lake_Bolundsfjarden.dat	63	
R_Lake_Bredviken.dat	64	
R_Lake_Eckarfjarden.dat	65	
R_Lake_Fiskarfjarden.dat	66	
R_Lake_Frakengropen.dat	67	
R_Lake_Gallsbotrasket.dat	68	
R_Lake_Graven.dat	69	
R_Lake_Gunnarsbotrasket.dat	70	
R_Lake_Gunnarsbo_Lillfjarden.dat	71	
R_Lake_Kungstrasket.dat	72	
R_Lake_Labbotrasket.dat	73	
Tunnel inflow (Figure 4-3)	**Marker (Table 4-3)**	
R_förvaring_1BTF.dat	11	
R_förvaring_2BTF.dat	12	
R_förvaring_1BLA.dat	13	
R_förvaring_1BMA.dat	14	
R_silo_del1.dat	15	
R_silo_del2.dat	15	
R_röd_BST_del1.dat	16	
R_röd_BST_del2.dat	16	
R_gulgrön_byggtunnel1.dat	17	
R_gulgrön_byggtunnel10.dat	17	
R_gulgrön_byggtunnel11.dat	17	
R_gulgrön_byggtunnel2.dat	17	
R_gulgrön_byggtunnel3.dat	17	
R_gulgrön_byggtunnel4.dat	17	
R_gulgrön_byggtunnel5.dat	17	
R_gulgrön_byggtunnel6.dat	17	
R_gulgrön_byggtunnel7.dat	17	
R_gulgrön_byggtunnel8.dat	17	
R_gulgrön_byggtunnel9.dat	17	
R_gulgrön_drifttunnel1.dat	17	
R_gulgrön_drifttunnel10.dat	17	
R_gulgrön_drifttunnel11.dat	17	
R_gulgrön_drifttunnel12.dat	17	
R_gulgrön_drifttunnel13.dat	17	
R_gulgrön_drifttunnel2.dat	17	
R_gulgrön_drifttunnel3.dat	17	
R_gulgrön_drifttunnel4.dat	17	
R_gulgrön_drifttunnel5.dat	17	
R_gulgrön_drifttunnel6.dat	17	
R_gulgrön_drifttunnel7.dat	17	

Fracture files used in M0 to M7	Type	Varied
R_gulgrön_drifttunnel8.dat	17	
R_gulgrön_drifttunnel9.dat	17	
R_gulgrön_tvärtunnel1.dat	17	
R_gulgrön_tvärtunnel2.dat	17	
R_gulgrön_tvärtunnel3.dat	17	
R_gulgrön_tvärtunnel4.dat	17	
R_gulgrön_tvärtunnel5.dat	17	
R_gulgrön_tvärtunnel6.dat	17	
R_gulgrön_tvärtunnel7.dat	17	
R_gulgrön_tvärtunnel8.dat	17	
R_blå_del.dat	18	
R_blå_del2.dat	18	
R_orange_del1_a.dat	19	
R_orange_del1_b.dat	19	
R_orange_del2.dat	19	
R_orange_del3.dat	19	
R_orange_del4.dat	19	
R_orange_del5.dat	19	
R_orange_del6.dat	19	
R_orange_del7.dat	19	
R_orange_del8.dat	19	
R_gul_byggtunnel1.dat	20	
R_gul_byggtunnel2.dat	20	
R_gul_drifttunnel1.dat	20	
R_gul_drifttunnel2.dat	20	
R_gul_drifttunnel3.dat	20	
R_gul_drifttunnel4.dat	20	
R_gul_drifttunnel5.dat	20	
R_gul_drifttunnel6.dat	20	
R_gul_drifttunnel7.dat	20	
R_singözonen_byggtunnel1.dat	20	
R_singözonen_byggtunnel2.dat	20	
R_singözonen_drifttunnel1.dat	20	
R_singözonen_drifttunnel2.dat	20	
R_singözonen_drifttunnel3.dat	20	
R_singözonen_drifttunnel4.dat	20	
R_ansl_1BLA.dat	21	
R_ansl_1BMA.dat	21	
R_ansl_1BTF.dat	21	
R_ansl_2BTF.dat	21	

Table D-2. Borehole sections with monitored head used in evaluations of model performance.

Monitored borehole section Label	Secup[1] (m)	Seclow (m)	Length (m)	Section midpoint (rotated) x´ (m)	y´ (m)	z (m)	Distance[2] r_{SFR} (m)	Head[2] 2010 (m)	Data set	Classification[3]
HFM33:1[1]	12.04	140.2	128.16	6,312	8,944	–52	224	0	New	HRD
HFM34:2	22	90	68	6,384	9,368	–48	69	–2.9	New	Southern boundary belt
HFM34:3[1]	11.99	21	9.01	6,384	9,352	–11.5	80	–0.5	New	HRD
HFM35:1	182	200.75	18.75	6,144	9,576	–144	215	–5.3	New	Southern boundary belt
HFM35:2	151	181	30	6,144	9,560	–128	204	–5.4	New	Southern boundary belt
HFM35:3	34	150	116	6,144	9,512	–72	179	–5.4	New	Southern boundary belt
HFM35:4[1]	12.04	33	20.96	6,144	9,464	–17	167	–0.6	New	HRD
HFR101:1[1]	8.04	209.3	201.26	6,528	9,864	–96	51	–31	New	NE3118/NE0870
HFR102:1	28	55.04	27.04	6,624	9,960	–34	96	–0.8	New	HRD
HFR102:2[1]	9.04	27	17.96	6,608	9,960	–13	112	–0.8	New	HRD
HFR105:1	134	200.5	66.5	6,544	9,576	–144	177	–10.9	New	Southern boundary belt
HFR105:2	107	133	26	6,544	9,560	–104	166	–6.3	New	Southern boundary belt
HFR105:3	61	106	45	6,544	9,544	–72	164	–6.3	New	Southern boundary belt
HFR105:4[1]	21.04	60	38.96	6,544	9,528	–34	170	–5.9	New	Southern boundary belt
HFR106:1	175	190.4	15.4	7,104	10,104	–144	447	–0.6	New	ZFMNNW1034
HFR106:2	47	174	127	7,136	10,120	–88	484	–0.6	New	ZFMNNW1034
HFR106:3	36	46	10	7,168	10,136	–34	527	–0.2	New	HRD
HFR106:4[1]	9.03	35	25.97	7,184	10,152	–17	538	–0.1	New	HRD
KFM11A:1	711	851.21	140.21	6,512	9,512	–660	611	–3.5	New	Southern boundary belt
KFM11A:2	690	710	20	6,512	9,448	–596	555	–6.8	New	Southern boundary belt
KFM11A:3	457	689	232	6,496	9,384	–484	466	–5.5	New	Southern boundary belt
KFM11A:4	446	456	10	6,480	9,320	–388	383	–3.1	New	Southern boundary belt
KFM11A:5	361	445	84	6,464	9,288	–356	349	–2.9	New	Southern boundary belt
KFM11A:6	131	360	229	6,448	9,224	–212	239	–1.5	New	Southern boundary belt
KFM11A:7[1]	70.8	130	59.2	6,432	9,144	–88	130	–3	New	HRD
KFR01:1	44.65	62.3	17.65	6,304	9,400	–96	49	–33	Old	Southern boundary belt
KFR01:2	11.15	43.65	32.5	6,320	9,416	–72	26	–24	Old	Southern boundary belt
KFR02:1	137.24	170.3	33.06	6,496	9,944	–240	153	–15	Old	HRD
KFR02:2	119.24	136.24	17	6,496	9,944	–216	127	–25	Old	ZFM871
KFR02:3	81.24	118.24	37	6,496	9,944	–184	99	–28	Old	ZFM871
KFR02:4	43.24	80.24	37	6,496	9,944	–144	61	–40	Old	HRD
KFR03:1	81.16	101.6	20.44	6,528	10,120	–176	88	–75.1	Old	ZFM871
KFR03:2	57.16	80.16	23	6,528	10,120	–152	66	–71.7	Old	ZFMNE0870
KFR03:3	45.16	56.16	11	6,528	10,120	–136	48	–74.5	Old	ZFMNE0870

Monitored borehole section Label	Secup[1] (m)	Seclow (m)	Length (m)	Section midpoint (rotated) x´ (m)	y´ (m)	z (m)	Distance[2] r_{SFR} (m)	Head[2] 2010 (m)	Data set	Classification[3]
KFR03:4	5.16	44.16	39	6,528	10,120	–104	24	–73.7	Old	HRD
KFR04:1	84.09	100.5	16.41	6,576	10,184	–168	41	–54	Old	ZFM871
KFR04:2	44.09	83.09	39	6,564	10,188	–138	22	–63	Old	ZFMNE0870
KFR04:3	28.09	43.09	15	6,558	10,186	–111	20	–75	Old	ZFMNE0870
KFR04:4	5.09	27.09	22	6,556	10,180	–94	16	–80	Old	ZFMNE0870
KFR05:1	97.15	131	33.85	6,528	10,216	–184	49	–81.4	Old	HRD
KFR05:2	80.15	96.15	16	6,544	10,216	–160	24	–65	Old	HRD
KFR05:3	57.15	79.15	22	6,540	10,204	–142	8	–81.5	Old	HRD
KFR05:4	12.15	56.15	44	6,547	10,193	–109	8	–81.3	Old	HRD
KFR08:1	62.95	104	41.05	6,528	10,376	–96	65	–5	Old	ZFMNW0805A
KFR08:2	35.95	61.95	26	6,512	10,344	–88	40	–22	Old	ZFMNW0805A
KFR08:3	5.95	34.95	29	6,500	10,308	–86	20	–8	Old	ZFMNW0805B
KFR09:1	0	80.24	80.24	6,288	9,960	–80	40	–1.9	Old	ZFMNNE0869
KFR101:1	279.5	341.76	62.26	6,912	10,360	–244	361	–1.6	New	ZFMNW0805B
KFR101:2	91	278.5	187.5	6,912	10,280	–144	317	–2.5	New	ZFMNW0805A/B
KFR101:3[1]	13.72	90	76.28	6,912	10,200	–42	288	–0.1	New	ZFMNNW1034
KFR102A:1	444	600.83	156.83	6,672	10,168	–468	350	–5.1	New	ZFMENE3115*
KFR102A:2	423	443	20	6,720	10,152	–388	284	–5.3	New	ZFMENE3115*
KFR102A:3	255	422	167	6,752	10,152	–304	227	–5	New	ZFMNE3112
KFR102A:4	220	254	34	6,800	10,152	–216	193	–4	New	HRD
KFR102A:5	214	219	5	6,816	10,152	–192	191	–1	New	HRD
KFR102A:6	185	213	28	6,816	10,152	–176	190	–0.9	New	HRD
KFR102A:7	103	184	81	6,832	10,152	–128	198	–1.2	New	ZFMNE3137
KFR102A:8[1]	70.38	102	31.62	6,864	10,152	–80	221	–1.4	New	HRD
KFR102B:1	146	180.08	34.08	6,832	10,232	–128	226	–2.5	New	ZFMNE3112
KFR102B:2	128	145	17	6,848	10,216	–104	232	–2.4	New	HRD
KFR102B:3[1]	13.95	127	113.05	6,880	10,184	–56	251	–0.3	New	ZFMNE3137
KFR103:1	178	200.5	22.5	6,976	10,072	–152	318	–0.6	New	ZFMWNW3262
KFR103:2	79	177	98	6,944	10,104	–104	295	–0.5	New	HRD
KFR103:3[1]	13.33	78	64.67	6,928	10,136	–34	283	0	New	HRD
KFR104:1	333	454.57	121.57	6,768	9,848	–308	307	–13.8	New	WNW3267/NE3137
KFR104:2	98	332	234	6,656	9,880	–168	180	–14.2	New	NE3112/ENE3115
KFR104:3[1]	8.73	97	88.27	6,560	9,896	–42	74	–3.4	New	ZFMNE3118
KFR105:1	265	306.81	41.81	6,832	9,848	–152	285	–1.3	New	ZFMWNW3267
KFR105:2	170	264	94	6,784	9,896	–144	217	–0.8	New	WNW8042/WNW3267/ NE3137

Monitored borehole section Label	Secup[1] (m)	Seclow (m)	Length (m)	Section midpoint (rotated) x´ (m)	y´ (m)	z (m)	Distance[2] r_{SFR} (m)	Head[2] 2010 (m)	Data set	Classification[3]
KFR105:3	138	169	31	6,752	9,944	–136	153	–0.7	New	HRD
KFR105:4	120	137	17	6,736	9,960	–128	128	–0.1	New	HRD
KFR105:5	4	119	115	6,688	10,008	–120	61	–8.2	New	NE3112/ENE3115
KFR106:1	260	300.13	40.13	7,248	10,040	–260	611	–0.8	New	ZFMNNW1034
KFR106:2	143	259	116	7,232	10,056	–184	589	–0.6	New	ZFMNNW1034
KFR106:3[1]	8.86	142	133.14	7,232	10,104	–72	574	–0.3	New	ZFMWNW3262
KFR13:1	53.75	76.6	22.85	6,608	10,168	–192	64	–39	Old	ZFM871
KFR13:2	33.75	52.75	19	6,608	10,168	–168	42	–48	Old	ZFMNE3118
KFR13:3	3.75	32.75	29	6,608	10,168	–144	17	–55	Old	PDZ
KFR19:1	95.57	110	14.43	6,532	10,220	–58	9	–41	Old	HRD
KFR19:2	77.57	94.57	17	6,534	10,202	–61	7	–43	Old	HRD
KFR19:3	66.82	76.57	9.75	6,532	10,188	–62	12	–63	Old	HRD
KFR19:4	51.82	65.82	14	6,532	10,180	–66	19	–68	Old	HRD
KFR27:1	110	501.64	391.64	6,768	10,040	–304	225	–3	New	ZFMWNW0835
KFR27:2	47	109	62	6,784	10,056	–72	126	–0.5	New	ZFMWNW0835
KFR27:3[1]	11.91	46	34.09	6,784	10,056	–27	145	–0.3	New	HRD
KFR55:1	48.53	61.89	13.36	6,543	10,213	–137	3	–121	Old	HRD
KFR55:2	39.53	47.53	8	6,553	10,209	–135	1	–90	Old	HRD
KFR55:3	21.53	38.53	17	6,566	10,202	–131	13	–61	Old	ZFMNE0870
KFR55:4	7.53	20.53	13	6,578	10,194	–129	10	–79	Old	ZFMNE0870
KFR56:1	9.55	81.7	72.15	6,524	10,316	–66	11	–12.5	Old	ZFMNW0805A/B
KFR7A:1	48.11	74.7	26.59	6,544	10,328	–136	61	–85	Old	ZFM871
KFR7A:2	20.11	47.11	27	6,544	10,312	–136	34	–113	Old	ZFM871
KFR7A:3	2.11	19.11	17	6,556	10,284	–134	11	–113	Old	ZFM871
KFR7B:1	8.6	21.1	12.5	6,556	10,276	–146	15	–27	Old	ZFM871
KFR7B:2	3.4	7.6	4.2	6,558	10,274	–139	5	–107	Old	ZFM871

1) Secup refers to upper borehole length of the monitored section. For the uppermost interval in a borehole, this value is taken as equal to the end of casing.

2) The shortest distance to SFR and the average measured head (year 2010) are coloured to facilitate data overview. Red = low values, yellow = intermediate values, and blue = low values.

3) Evaluation is facilitated by pooling the data into hydraulic units (see Table 5-2). ZFMNNW1034, ZFMNW0805A and ZFMNW0805B are pooled into “Northern boundary belt”. ZFMNE3118 and ZFMNE0870 are pooled into “ENE0870”. The single data in ZFMNNE0869 is studied separately. ZFM871 and HRD also form separate units. Remaining data in zones are pooled into “Central block HCD.